

© Copyright by Jack Jai-ick Yoh, 2001

THERMOMECHANICAL AND NUMERICAL MODELING OF ENERGETIC
MATERIALS AND MULTI-MATERIAL IMPACT

BY

JACK JAI-ICK YOH

B.S., University of California at Berkeley, 1992

M.S., University of California at Los Angeles, 1995

THESIS

Submitted in partial fulfillment of the requirements
for the degree of Doctor of Philosophy in Theoretical and Applied Mechanics
in the Graduate College of the
University of Illinois at Urbana-Champaign, 2001

Urbana, Illinois

THERMOMECHANICAL AND NUMERICAL MODELING OF ENERGETIC MATERIALS AND MULTI-MATERIAL IMPACT

Jack Jai-ick Yoh, PhD
Department of Theoretical and Applied Mechanics
College of Engineering
University of Illinois at Urbana-Champaign, 2001
D. Scott Stewart, Advisor

The aim of this thesis is the construction of a general purpose simulation tool that can simulate the elements found in an explosive system that include energetic (explosive) and inert (metal) materials. The work presented is mainly two-fold: (1) a thermomechanical model for an energetic material is developed based on a continuum model that uses two independent state variables to represent the phase transformation and the extent of chemical reaction, and (2) a high-resolution model is developed that simulates multi-material, multi-dimensional impact events (in which the energetic material of the first part can be one element) involving detonation and explosion physics. In the numerical model, we attempt to achieve high accuracy with Eulerian finite-difference methods that use essentially non-oscillatory (ENO) scheme and level sets for handling the discontinuities of the flow field, and the Runge–Kutta schemes for a high-order accurate temporal advancing.

The present continuum mechanical model of energetic material is thermodynamically self-consistent and can describe a material that undergoes phase transitions from solid to liquid to gas with exothermic chemical reaction. In various limits, the material is a classical elastic solid, a Newtonian viscous liquid, and a compressible gas.

When modeling systems with energetic material compound, one needs to consider regions where different materials are in physical contact with each other whether the neighboring material is another explosive or a non-reacting inert material. Also one must properly model the material interfaces. These interfaces are tracked by the level set function, introduced as a passive scalar that the continuous pressure and normal velocity conditions are implicitly enforced across these boundaries. Two neighboring materials of distinct equations of state can be brought to contact while their contact surface may evolve according to the local particle velocity.

Because the framework in which the simulation tool is developed is quite general, we expect a wide application of our model to many challenging multi-material physics problems. Standard shock-tube tests with distinct gases are conducted for one-dimensional validations. In multi-dimensions, we consider the Taylor impact of a copper rod and explosive rate-sticks and obtain good qualitative and quantitative agreement with the benchmark results. Other simulations are developed that simulate the explosive welding of copper and steel plates and a plate-cutting experiment.

The thesis outline is as follows: (i) derivation of continuum laws of energetic materials and examination of the model in relation to classical equilibrium thermodynamics in a quasi-static limit, (ii) specialization to simple motions and numerical analysis of dynamics and transitions of a representative explosive, HMX, (iii) development of multi-dimensional, multi-material hydrodynamic impact code using the continuum laws of energetic materials, (iv) application of the multi-material tool to a impact of ductile targets such as metals, and (v) some conclusions.

Acknowledgments

I would like to express my sincere thanks to my advisor, Prof. D. Scott Stewart, for sharing his profound knowledge in the science of mechanics. His warm character has provided a safe shelter for scientists and engineers in training, and I have benefited a great deal as a graduate research assistant in his group.

I am also thankful to Prof. Petros Sofronis for his willingness to teach and suggest basic metal plasticity to a fluid mechanician. Prof. M. Quinn Brewster, Prof. Robert D. Moser, and Prof. Mark Short have also been helpful during the preparation of this work. I also want to thank Prof. James W. Phillips for his careful reading and format checking of the thesis.

I also want to acknowledge my colleagues Aslan R. Kasimov, Igor R. Kuznetsov, Bradley L. Wescott, and Sunhee Yoo, for sharing their talents and expertise in areas outside my thesis work.

I owe a great deal of thanks to my parents, Sang-Whan Yoh and Seung-Hee Sohn, for their love and support through out my education in the States that began in 1986.

Finally my wife, Eun-Joung, has shared her deep loving for my work and amazing patience during its completion. I am also wholeheartedly grateful to her for raising our 3-year-old son, Doughyun, who persistently gave me a reason to smile each morning. I thank her most for her many prayers. I acknowledge that it was God who gave me the opportunity and privilege to engage in this endeavor.

This work was carried out with resources from the U. S. Air Force Research Laboratory, Armament Directorate, Eglin AFB, Florida, F08630-95-004 and F08630-00-1-0002.

Table of Contents

Chapter 1	Introduction	1
Chapter 2	Thermomechanical Model for Energetic Materials	7
2.1	Kinematics	12
2.2	Review of the thermomechanics for a simple model of a reactive flow	13
2.2.1	Constitutive forms and restrictions	14
2.2.2	Temperature form of the energy equation	17
2.2.3	Summary of the governing equations for a pre-mixed reactive fluid	18
2.3	Thermomechanics of a model of a material with phase changes from solid to liquid to gas	19
2.3.1	Temperature form of the energy equation	24
2.3.2	Total free-energy density and summary of constitutive forms	31
2.4	The combined model: Modifications to include chemical reaction	32
2.4.1	Material transition functions	34
2.5	Some limiting cases	35
2.5.1	Pure phases	35
2.5.2	Motionless phase transition	38
2.5.3	Relation to the simpler theory of quasi-static phase transformation	39
2.6	Special forms of the model for three simple motions	40
2.6.1	Constant volume evolution and thermal explosion	41
2.6.2	Longitudinal motion	42
2.6.3	Shear motion	44
Chapter 3	Analysis of Simple Motions	48
3.1	Mathematical formulations	49
3.1.1	Kinematics and some definitions	49
3.1.2	General formulation	50
3.1.3	Material transition functions	51
3.2	Matching material properties to HMX	54
3.3	Form of the model for three simple motions	58
3.3.1	Evolution at constant volume	58
3.3.2	Longitudinal motion	62
3.3.3	Shear motion	63
3.4	Numerical methodology	66
3.4.1	Description of low-storage semi-implicit Runge–Kutta solver	66
3.4.2	Implementation	67
3.5	Simulations of longitudinal and shear motions	68

3.5.1	One-dimensional shear motions	68
3.5.2	One-dimensional longitudinal motion: Reverse impact	70
3.6	Conclusions	80
Chapter 4	High Resolution Multi-Material Impact: EM (Explosive)	84
4.1	Numerical method	85
4.1.1	Level set and ghost-fluid-method	86
4.1.2	General ENO scheme for spatial discretization	87
4.1.3	Low-storage semi-implicit Runge–Kutta scheme	91
4.2	Mathematical formulation	93
4.2.1	One-dimensional equations	93
4.2.2	Two-dimensional equations	94
4.3	Code description	98
4.4	Numerical simulation	99
4.4.1	One-dimensional cases	99
4.4.2	Two-dimensional cases	104
Chapter 5	High Resolution Multi-Material Impact: Inert (Metal)	117
5.1	Elastic–plastic solid modeling	118
5.1.1	Preliminaries	118
5.1.2	Derivation of evolution laws of plasticity	119
5.1.3	Hardening laws	123
5.2	Mathematical formulation	124
5.2.1	Two-dimensional equations of fluid–solid interaction with reaction	124
5.2.2	Level set for interface tracking	126
5.3	Numerics	126
5.4	Interface tracking using level sets	127
5.4.1	Material–material interface tracking	127
5.4.2	Material–void stress-free interface tracking	129
5.5	Code validations	130
5.5.1	Verification of order of convergence	132
5.5.2	Validation 1: 1-D shock reflection of two different gases	134
5.5.3	Validation 2: ZND structure	135
5.5.4	Validation 3: Copper rod impact	136
5.5.5	Validation 4: Rate-stick experiment	138
5.6	Applications	141
5.6.1	HE–Cu–Void (a “challenging” rate-stick) problem	141
5.6.2	Explosive welding	145
5.6.3	Penetration of copper plate target by spherical detonation	147
Chapter 6	Conclusions	155
Appendix A	List of φ-dependent functions	156
Appendix B	Special Forms of Equations	157
B.1	Lagrangian equations (in terms of X_1)	157
B.2	Eulerian equations (in terms of x_1)	158
B.3	Conservation in Eulerian framework	159

B.4	Euler equations in spherical coordinates	161
Appendix C	Structure Analysis of Steady Phase Transformation Waves	162
C.1	Shock structures	162
C.1.1	Continuum structure of compressible N–S equations	162
C.1.2	Continuum structure of gas-phase HMX equations	165
C.1.3	Continuum structure of solid-phase HMX equations	165
C.2	Structure of phase front	167
C.2.1	Continuum structure of evaporation/condensation front	167
C.2.2	Continuum structure of melting/freezing front	173
C.3	Algebraic theory	179
C.3.1	Derivation of Rankine–Hugoniot relations	179
C.3.2	Algebraic theory of phase transition wave	183
C.3.3	Solution of algebraic theory	186
Appendix D	Thermodynamics of Energetic Materials	189
D.1	Constructing a P–V–T diagram of HMX	189
D.2	Equation of state (EOS)	192
D.2.1	Experimental isothermal data for solid HMX	192
D.2.2	Jones–Wilkins–Lee equation for vapor HMX	192
D.2.3	Hydrostatic pressure for our model	193
Appendix E	Eulerian–Lagrangian Configurations	197
E.1	Eulerian description of balance laws	198
E.1.1	Equation for displacement gradient	200
E.1.2	Displacement gradient based numerical formulation	200
E.2	Relations between spatial and referential operators	201
E.3	Lagrangian description of balance laws	203
E.3.1	Longitudinal problem	205
E.4	Two-Dimensional generalization of continuum laws	207
Appendix F	Derivation of Classical Sharp Interface Problems as Asymptotic Limits of the Phase-Field Equations	212
F.1	Introduction	212
F.2	Preliminaries	212
F.2.1	Sharp interface model problems	212
F.2.2	Phase-field model problems	213
F.3	Sharp interface limit with finite surface tension (Modified Stefan model)	214
F.4	Sharp interface limit with zero surface tension (Classical Stefan model)	220
F.5	Quasi-static limit (Hele-Shaw model)	225
Appendix G	Code Index	229
References	231
Vita	239

List of Tables

3.1	Material properties typical of HMX.	52
4.1	Running parameters of piston-driven laminate	100
5.1	Initial parameters of shock tube Case A.	132
5.2	Results of numerical test of convergence. In the table, N denotes grid points, E_1 is the L_1 norm of error measured between the grids of size N and $2N$ points, and r_c is the rate of convergence.	134
5.3	Initial parameters of shock tube Case B.	135
5.4	Initial end states of CJ detonation wave in a typical high explosive.	136
5.5	Material properties typical of copper.	138
5.6	Running parameter of rate-stick experiment of Ref. [1].	140
5.7	Material properties of high-strength steel.	145
C.1	Dimensional parameters for n -heptane evaporation/condensation [56], [72].	171
C.2	Dimensional parameters for HMX melting/freezing	176

List of Figures

2.1	Plot of ψ_2 as a function of φ with T variation.	28
2.2	Plots of transfer functions for HMX simulation and their derivatives with respect to phase variable. Shear modulus, ideal gas constant, thermal expansion coefficient, and phase diffusion coefficient are shown from top to bottom.	36
2.3	φ -dependent transfer functions (derivatives) for heat of phase transformation, β'_m and β'_v . Third figure depicts the triple-well Ginzburg–Landau potential function and its derivative.	37
2.4	T – v trajectory on an isobar ($p = 10^7$ Pa) under the quasi-static assumptions. The large volume jump from liquid to gas happens at nearly constant temperature T_v . . .	40
2.5	Phase– V trajectory of constant pressure under the thermo-quasistatic assumption. . .	41
3.1	Solid curve is melt temperature-pressure relation for β -HMX given by the semi-empirical Kraut–Kennedy law [54],[47]. Dashed line and long-dashed line are constant melt temperature and vapor temperature used in the current numerical simulation, respectively.	55
3.2	P – V isotherms at $T=300$ K and $T=900$ K. $\left \frac{dp}{dV}\right _{\varphi=0} > \left \frac{dp}{dV}\right _{\varphi=1}$ implies that the speed of sound is greater in the solid than in the liquid HMX.	56
3.3	P – V isotherms at four different temperatures for HMX vapor ($\varphi = 2$).	57
3.4	P – V isotherms for solid, liquid, and vapor HMX at $T = 300$ K, drawn to a single range of P – V axes.	57
3.5	Constant-volume phase transformation without reaction.	59
3.6	Constant-volume thermal explosion.	61
3.7	Temperature, phase, pressure, and density fields for a representative shear experiment ($v_{\text{shear}} = 600$ m/s, $T_0 = 550$ K).	72
3.8	Shear velocity (v_1), compression velocity (v_2), and displacement gradient (du_1/dX_2) fields for a representative shear experiment ($v_{\text{shear}} = 600$ m/s, $T_0 = 550$ K).	73
3.9	Snapshots of density, temperature, pressure, and phase field (from top to bottom) taken at time $t = 5, 15, 30 \mu\text{sec}$ from Figures 3.7 and 3.8 of plane shearing experiment. . .	74
3.10	Temperature, phase, pressure, and density fields for a representative shear experiment ($v_{\text{shear}} = 200$ m/s, $T_0 = 560$ K).	75
3.11	Shear velocity (v_1), compression velocity (v_2), and displacement gradient (du_1/dX_2) fields for a representative shear experiment ($v_{\text{shear}} = 200$ m/s, $T_0 = 560$ K).	76
3.12	Snapshots of density, temperature, pressure, and phase field (from top to bottom) taken at time $t = 5, 15, 30 \mu\text{sec}$ from Figures 3.10 and 3.11 of plane shearing experiment. . .	77
3.13	Velocity, phase, pressure, density and temperature fields for a representative reverse-impact (longitudinal) experiment ($v_{\text{impact}} = -500$ m/s, $T_0 = 550$ K).	78

3.14	Snapshots of density, temperature, pressure, and phase field (from top to bottom) taken at time $t = 3 \mu\text{sec}$ from Figure 3.13 of the longitudinal exercise.	79
3.15	Velocity, phase, pressure, density and temperature fields for a representative reverse-impact (longitudinal) experiment ($v_{\text{impact}} = -200 \text{ m/s}$, $T_0 = 560 \text{ K}$).	81
3.16	Snapshots of density, temperature, pressure, and phase field (from top to bottom) taken at time $t = 3 \mu\text{sec}$ from Figure 3.15 of the longitudinal experiment.	82
3.17	$d\varphi/dt$ versus φ for the two specialized reverse-impact experiments discussed. By varying the initial temperature, T_0 , meta-stable state ($\varphi \approx 0.33$) is shown as a local equilibrium point on the experiment represented by the square symbols. In contrast, the experiment shown by hollow circles suggests that $\varphi = 1$ is the only stable equilibria once the initial state is perturbed about the unstable point at $\varphi = 0$, corresponding to the solid state under the impact loading.	83
4.1	“Ring-up” test problem.	100
4.2	Space-time contour of density (kg/m^3).	101
4.3	Space-time contour of pressure (Pa).	102
4.4	Schematic of typical hot-spot ignition setup.	103
4.5	Space-time contour of pressure (Pa). ($\Delta r = 4.2 \times 10^{-8} \text{ m}$, $\Delta t = 2.0 \times 10^{-11} \text{ sec}$). . .	105
4.6	Space-time contour of phase-field. ($\Delta r = 4.2 \times 10^{-8} \text{ m}$, $\Delta t = 2.0 \times 10^{-11} \text{ sec}$). . .	106
4.7	Space-time contour of density (kg/m^3). ($\Delta r = 4.2 \times 10^{-8} \text{ m}$, $\Delta t = 2.0 \times 10^{-11} \text{ sec}$). .	107
4.8	Initial setup (top) and final velocity profile of shearing of two Blatz-Ko elastic materials of different density.	109
4.9	Temperature (Kelvin) and phase variable shown from top to bottom.	110
4.10	Two-dimensional shock-plate interaction problem.	111
4.11	Density (kg/m^3) contour at an instant when the incident shock has penetrated through the second material interface of a Blatz-Ko elastic plate. Grid of 400 by 400 points spans a physical domain of 3 cm by 3 cm.	113
4.12	Pressure (Pa) contour at an instant when the incident shock has penetrated through the second material interface of a Blatz-Ko elastic plate. Grid of 400 by 400 points spans a physical domain of 3 cm by 3 cm.	114
4.13	Density (kg/m^3) contour at an instance just before the incident shock contacts the second material interface of a Blatz-Ko elastic plate. Grid of 400 by 400 points spans a physical domain of 3 cm by 3 cm.	115
4.14	Pressure (Pa) contour at an instance just before the incident shock contacts the second material interface of a Blatz-Ko elastic plate. Grid of 400 by 400 points spans a physical domain of 3 cm by 3 cm.	116
5.1	Universal stress-strain curve from a simple tension test.	122
5.2	Schematic of material-void interface.	128
5.3	Riemann problem involving two different gases used in the validation of rate of numerical convergence.	133
5.4	Shock-tube test of shock reflection and transmission of two different gases.	135
5.5	ZND detonation structure obtained through the multi-dimensional reactive Euler solver. Δx is 0.1 mm and consequently 40 points are placed in the 4 mm reaction zone.	137
5.6	Grid comparison: (a) deformed grid at time $t = 80 \mu\text{sec}$ used in the Lagrangian FEM calculation by [19]; (b) uniform grid used in this work.	139

5.7	Comparison of effective plastic strain distribution at $80\mu\text{s}$. A 50×170 grid spans the r and z directions ($\Delta r = \Delta z = 2.0 \times 10^{-4}\text{m}$).	139
5.8	Schematic of rate-stick experiment in [1].	140
5.9	Comparison of rate-stick experiment. Shown on the left are extent of reaction and density from Ref. [1] with $\Delta x = \Delta y = 0.0074\text{ cm}$ or 54 points in the reaction zone. Computed results on the right column are based on $\Delta x = \Delta y = 0.027\text{ cm}$ or 15 points covering the reaction zone.	142
5.10	Schematic of a “challenging” rate-stick experiment.	143
5.11	Rate-stick experiment simulated on 100 by 150 grid with 0.5 cm initial thickness of copper plate. Shown are the pressure fields (taken at every $5\mu\text{sec}$) of 2 cm-thick cylinder of HE confined in a 5 mm-thick copper tube. The outer end of the copper band is a free surface.	144
5.12	Rate-stick experiment simulated on 100 by 150 grid with 0.5 cm initial thickness of copper plate. Shown are the effective plastic strain fields (taken at every $5\mu\text{sec}$) of 2 cm-thick cylinder of HE confined in a 5 mm-thick copper tube. The outer end of the copper band is a free surface.	146
5.13	Schematic of explosive welding of two metal plates.	147
5.14	Explosive welding of copper (8.93g/cc) and high-strength steel (7.85g/cc). Shown are the extent of reaction and the pressure (Pa). Simulated on a 150 by 100 grid.	148
5.15	Explosive welding of copper (8.93g/cc) and high-strength steel (7.85g/cc). Shown are the effective plastic strain and the density (kg/m^3). Simulated on a 150 by 100 grid.	149
5.16	Schematic of copper plate penetration by a point source (detonation).	150
5.17	Spherical detonation wave (ABS model) initiated at a point source located at $(x, y) = (0, 0)$ penetrating the copper plate target located at 1 cm. The right edge of the plate is at 1.5 cm, where the copper–void interface boundary is enforced. Dynamic deforming motion of the plate is illustrated through a series of snapshots at different times. Shown are the effective plastic strain field as calculated on 200 by 600 grid.	152
5.18	Spherical detonation wave (ABS model) initiated at a point source located at $(x, y) = (0, 0)$ penetrating the copper plate target located at 1 cm. The right edge of the plate is at 1.5 cm, where the copper–void interface boundary is enforced. Dynamic deforming motion of the plate is illustrated through a series of snapshots at different times. Shown are the pressure fields as calculated on 200 by 600 grid.	153
5.19	Spherical detonation wave (ABS model) initiated at a point source located at $(x, y) = (0, 0)$ penetrating the copper plate target located at 1 cm. The right edge of the plate is at 1.5 cm, where the copper–void interface boundary is enforced. Dynamic deforming motion of the plate is illustrated through a series of snapshots at different times. The reaction progress variable is shown on 200 by 600 grid.	154
C.1	Schematic of shock-attached frame.	163
C.2	Computed shock structure of compressible viscous Euler gas.	164
C.3	Computed shock structure of gas-phase HMX.	166
C.4	Computed shock structure of solid-phase HMX.	168
C.5	Evaporation wave structure based on the transformed velocity, density, phase, temperature gradient field of n -heptane.	172
C.6	Condensation wave structure based on the transformed velocity, density, phase, temperature gradient field of n -heptane.	174

C.7	Melting front structure observed from the transformed velocity, density, deformation gradient, and phase field of solid HMX.	178
C.8	Freezing front structure observed from the transformed velocity, density, deformation gradient, phase temperature gradient, and temperature field of liquid-HMX.	180
C.9	(a) Plot of $(-b + \sqrt{b^2 - 4ac})/2a$ as a function of α and Γ in the case of n -heptane evaporation/condensation. (b) Plot of $(-b + \sqrt{b^2 - 4ac})/2a$ as a function of α and Γ in the case of HMX melting/freezing.	187
D.1	Sublimation curve drawn based upon the empirical data of Rosen & Dickinson [60] and Taylor & Crookes [70]. Melt curve is estimated by semi-empirical Kraut–Kennedy law. Vapor curve is drawn from equilibrium thermodynamics using the Clausius–Clapeyron relation for idealized β -HMX vapor.	191
E.1	Lagrangian and Eulerian frames.	198

Nomenclature

Roman Symbols

A	pre-exponential factor of Arrhenius kinetic term
B	multiplication factor of $\dot{\varphi}$
\mathbf{B}	left Cauchy Green tensor, i.e. $\mathbf{B} = \mathbf{F}\mathbf{F}^\top$
\mathbf{C}	fourth-order isotropic tensor mapping \mathbf{L}
D	steady shock propagating speed
\mathbf{D}	symmetric part of \mathbf{L} , i.e. $\mathbf{D} = \frac{1}{2}(\mathbf{L} + \mathbf{L}^\top)$
E_a	reaction activation energy
$F(\varphi, T)$	Ginzburg–Landau phase free energy
\mathbf{F}	deformation gradient tensor, i.e. $\mathbf{F} = \frac{\partial \mathbf{f}(\mathbf{X}, t)}{\partial \mathbf{X}} = \frac{\partial x_i}{\partial X_j} \mathbf{e}_i \otimes \mathbf{e}_j = \mathbf{1} + \mathbf{H}$
\mathbf{F}^{-1}	inverse deformation gradient tensor, i.e. $\mathbf{F}^{-1} = \frac{\partial \mathbf{f}^{-1}(\mathbf{x}, t)}{\partial \mathbf{x}} = \frac{\partial X_j}{\partial x_i} \mathbf{e}_j \otimes \mathbf{e}_i$
$\mathbf{f}(\mathbf{X})$	deformation that is a family of functions that maps \mathcal{B} into a subset of \mathcal{E}
$\mathbf{f}(\mathbf{X}, t)$	motion that is a one-parameter (t) family of deformation
\mathbf{H}	displacement gradient tensor, i.e. $\mathbf{H} = \mathbf{Grad} \mathbf{u}(\mathbf{X}, t) = \frac{\partial \mathbf{u}(\mathbf{X}, t)}{\partial \mathbf{X}}$
I_B, II_B	first, second invariant of \mathbf{B}
III_B	third invariant or determinant of \mathbf{B} , i.e. $III_B = \left(\frac{\rho_o}{\rho}\right)^2$
J	Jacobian of \mathbf{F} , i.e. $J = \det \mathbf{F} = \frac{\rho_o}{\rho}$
k	thermal conductivity
L_m	latent heat ($L_m = -Q_m$)
\mathbf{L}	spatial velocity gradient, i.e. $\mathbf{L} = \nabla \hat{\mathbf{v}}(\mathbf{f}(\mathbf{X}, t), t) = \frac{\partial \hat{\mathbf{v}}_i}{\partial x_j} \mathbf{e}_i \otimes \mathbf{e}_j$
p	hydrostatic pressure
q	heat flux
Q_m	heat of melting (< 0)
Q_v	heat of vaporization (< 0)
Q_c	heat of combustion
Q_{heat}	artificial heat source added to drive the system
R_u	universal gas constant, $R_u = 8.3143 \text{ J}/(\text{mol K}) = 1.987 \text{ cal}/(\text{mol K})$
R	gas constant, R_u/MW
t	time
T	temperature
$\mathbf{u}(\mathbf{X}, t)$	displacement field vector
U	transformed velocity in the particle frame of reference
V	specific volume
$\mathbf{v}(\mathbf{X}, t)$	velocity field vector (equivalently, $\hat{\mathbf{v}}(\mathbf{f}(\mathbf{X}, t), t)$)

\mathbf{X}	position of material particle in reference (Lagrangian) configuration
\mathbf{x}	position occupied by the particle at time t in the spatial (Eulerian) configuration
∇	spatial gradient operator, i.e. $\nabla = \frac{\partial}{\partial \mathbf{x}}$
$\nabla \cdot$	spatial divergence operator
Grad	referential gradient operator, i.e. Grad = $\frac{\partial}{\partial \mathbf{X}}$
Div	referential divergence operator

Greek Symbols

α	thermal expansion coefficient
β_m	transfer function associated with melting
β_v	transfer function associated with vaporization
γ_φ	diffusion coefficient of phase parameter
η	V/V_o
κ	thermal diffusivity
λ	parameter of extent of chemical reaction
μ_c	shear modulus (condensed phase)
μ_s	shear modulus (solid)
μ_l	shear modulus (liquid)
μ_f	static viscosity coefficient
ν_f	bulk viscosity ($\nu_f = -2/3\mu_f$)
ν_s	Poisson's ratio
ξ	micro-stress associated with phase transition
π_φ	micro-force associated with phase transition
ρ	density
ρ_o	undeformed density
σ	stress tensor
σ^{eq}	equilibrium stress tensor
σ^{diss}	dissipative stress tensor
σ^{sph}	spherical part of σ^{eqn}
σ^{dev}	deviatoric part of σ^{eqn}
ϕ	level-set function
φ	phase variable
Ψ^{well}	depth of potential well
ψ	Helmholtz free energy

Subscripts

i	dummy index
j	dummy index
k	dummy index
c	condensed state
s	solid state
f	liquid state
o	reference state or undeformed state

Chapter 1

Introduction

Condensed phase energetic materials (EMs) are most typically room temperature organic solids that bind substantial chemical energy in molecular bonds. Upon initiation of chemical reaction between sub-molecular constituents within the solid, energy is released that is subsequently available to do work or is converted into heat. The advantage of the condensed phase explosive is that the energy per unit volume is approximately a thousand times higher than its pre-mixed, gaseous counterpart.

Fundamental scientific questions surround the phenomena of ignition and release of energy in these energetic materials subject to impact with a piston, or due to a rapid shearing motion. At high impact speeds (typically on the order of 1000 m/s), simple hydrodynamic models give an adequate description for both ignition and transition to detonation. Hydrodynamic models are expressed in the form of the Euler equations for reactive gas dynamics. At lower impact speeds (typically below 1000 m/s), one must fully take into account the solid nature of the materials. Thus, a simple Euler equations with chemical kinetics are insufficient to describe a material undergoing phase transformation, dissipation and localization of strain energy, plastic hardening, and thermal softening. A successful model must also be able to describe three-dimensional stress distributions as the material changes from solid to liquid to gas.

Modeling the phase change from solid to liquid to gas involves positing of balance laws additional to the basic continuum laws of mechanics. Gurtin [33]* has argued for a separate balance of configurational forces acting near the boundaries separating pure phases in the volumetric bulk. The argument for such configurational forces is similar to those used to explain classical surface tension forces. Those forces do work, and thus the work related to the configurational forces must

*References are listed alphabetically by author beginning on page 231.

be accounted for in the overall energy balance. Representative of three distinctly pure phases, the order parameters of phase field variables are assigned $\varphi = 0, 1$, and 2 for solid, liquid and gas phases of a material.

The second law of thermodynamics (the Clausius–Duhem inequality) restricts the form of the constitutive theory so that the rate processes are entropy increasing. In particular, the energy equation becomes so rich as to account for many additive terms of the Helmholtz free energy as posed before the second law restriction. Various parts associated with the energies are $\psi = \psi_{\text{thermal}} + \psi_{\text{reaction}} + \psi_{\text{phase}} + \psi_{\text{gradient}} + \psi_{\text{elastic}} + \psi_{\text{plastic}}$. This explicit partitioning of the Helmholtz free energy is a key aspect of the model in this work.

Previously Ruderman [61] attempted to derive the evolution equations of both phase variable, φ , and the extent of exothermic chemical reaction, λ , using the configurational balance law posited like the mass, momentum, and energy conservation laws. As we began re-deriving the continuum equations of energetic material, we found that the evolution equation of λ did not emerge from the configurational balance argument in a manner that was consistent with standard derivations in combustion theory. But it was possible to posit the evolution equation instead. As a primitive balance law, we write

$$\rho\dot{\lambda} = \nabla \cdot \mathbf{s} + \rho\Omega, \quad (1.1)$$

in the same manner as found in combustion theory. The vector \mathbf{s} is the flux of mass of reacted species per unit area per unit time and $\rho\Omega$ is the instantaneous rate of creation of mass of the reacted species per unit volume. Then λ is recognized as the mass fraction of product species for a simple exothermic reaction. Further, by direct correspondence with the standard combustion equations, one can interpret $\mathbf{s} = \rho\lambda\mathbf{V}$ where \mathbf{V} is the velocity of the product species, and where $\rho\lambda$ is the partial density fraction of the same product. Hence, in this new approach, only the evolution equation for φ , the phase order parameter, emerges from the configurational balance law, and the λ -evolution equation is instead invoked based on combustion theory.

With the combined model written down in a thermodynamically consistent framework with both φ and λ evolution laws specified, we then build a numerical study tool by which many of the interesting physics embedded in this rich model can be observed. We first considered the physical

setup of the simulations representative of actual shock impact and shear impact experiments. In the case of thermomechanical loading of EMs, we considered HMX, typically used solid propellants in explosions. Due to its vast experimental data availability, HMX is used as a baseline EM in our study. Loadings due to a low-speed impact—both longitudinal and shearing motions—are studied. In both experiments, the regions of pure phase are maintained away from the phase transition boundaries, and the material acts as a pure solid or fluid in the pure phase regions.

When EMs are placed in physical contact with other materials (both inert and reactive), the proper numerical modeling of EMs often becomes a very challenging task. In the second half of the thesis, we develop a modern approach to handle multi-material contact problems involving energetic materials, condensed gas, elasto–plastic metals, voids or vacuum, and compressible fluids. The idea of convecting a level set scalar in the flow of conservation variables is the underlying principle in tracking the material (contact) interfaces that, by definition, advect with the local particle velocity. In the final form of the unified fluid/solid code, each layer represents a different material with possibly different equations of state. Each material communicates with the neighboring materials by the continuous pressure and normal velocity. Since the code is based on the Eulerian configuration using finite differences as the basic spatial discretization, any wave that ‘crosses’ the nodes (or cells) will be captured by the high-order shock-capturing scheme (e.g. ENO scheme). Our hydrocode is capable of resolving the discontinuities of the flows in either solids or fluids, which include shocks, phase boundaries, shear bands, and detonation. This Eulerian methodology eliminates mesh distortions that are often found in the Lagrangian finite-element approach. We develop third-order temporal accuracy to resolve transients.

In the past, hydrodynamic codes have been developed that model multi-dimensional, multi-material, high-rate of deformation, strong shock wave physics [45], [38], [34], [8]. In particular, CTH is a 3-D shock wave physics code from Sandia National Laboratories, Albuquerque, New Mexico, and it has been successfully applied to a large variety of strong shock problems, such as hypervelocity impact and effects of detonating high explosives. Many of the analytic and tabular equations of state (EOS) with solid, liquid, vapor, gas–liquid mixed phase and solid–liquid mixed phase capabilities were used in the model [46]. Similar hydrocodes have been developed at Los Alamos National Laboratory. The high-speed flow models are MESA (a precursor) [34] and PAGOSA,

a multi-material hydrocode. Both simulate high-speed and high-rate material deformation and are based on finite difference approximations on an Eulerian mesh. PAGOSA is well-suited for modeling transient flows involving multiple immiscible fluids and/or distinct materials experiencing large distortion [38]. In general, the conservation of mass, momentum, and energy across the ‘fixed’ interface at each increment of time is achieved in two steps: a Lagrangian step where the cell distorts to follow the material motion followed by a rezone step where the distorted cells are mapped back to the Eulerian mesh. Benson [6] has an excellent comprehensive review on the modern high-speed flow models, and interested readers are referred to that reference.

In our current Eulerian approach to constructing a multi-material, high-rate material deformation code that can include detonating explosives, we attempt to reproduce the capabilities of the other codes in wide use. Our approach is based on high-resolution methods using fourth-order convex ENO for the spatial discretization and third-order TVD Runge–Kutta for time advancement. The treatment of interfaces is simple and made robust by the use of a level set function so that there is virtually no ‘extra’ difficulty involved in keeping the jump conditions across the material interface by solving a scalar hyperbolic equation in ϕ , the passive scalar introduced in the model. The underlying global scheme based on the method of lines enables us to treat multi-dimensional calculations without time splitting, as often used in most of the hydrocodes, and allows an easy and efficient implementation of Runge–Kutta scheme at orders higher than two. An elegant use of level sets and ghost-node-populating techniques are especially useful to handle multi-material interfaces.

The physical models in our code currently include models for compressible hydrodynamics, an ideal equation of state (EOS) for a compressible gas, high-explosive (HE) EOS using the ABS model [2], Mie–Gruneisen EOS for solid, Blatz–Ko rubber elasticity, elasto–plastic metal deformation with isotropic linear hardening and Johnson–Cook hardening laws, and chemical kinetics of energetic materials.

The capabilities of the hydrodynamics model and the high-resolution numerics with level set interface tracking are tested through several examples and validations. First, we consider validations by a pair of shock tube tests with two different gases and we demonstrate the spatial rate of convergence of the high-order scheme. To test the reactive Euler solver properly, we reproduce the

one-dimensional detonation wave structure based on the ABS model described in Ref. [2]. The third numerical validation includes a benchmark test result of rod impact. A well known Taylor copper-rod impact test is simulated by our code and the result is compared against others' results. A fourth validation computes a rate-stick experiment involving HE/Inert. The rate-stick is a stick or slab of explosive confined by inert material. The stick is initialized by a high pressure/temperature region and a curved detonation wave emerges and propagates down the axis of the stick. The steady detonation speed and the angle of inert shock transmitted through the material interface are checked against a similar benchmark computation by Aslam [1].

Following these validations, capabilities of the current multi-dimensional hydrocode are pushed to its limit by applying the model to a handful of problems of our current interest in the mechanics of detonation physics. First, we simulate a bit more ambitious rate-stick experiment involving HE, copper, and void interfaces. We can observe how the copper layer is deformed due to the strong shock. Next, we simulate explosive welding of copper and high-strength steel plates initially unbound. Upon detonating a coat of explosive on the outer layer of the copper, the two metals come in contact in both shear and impact motion to cause a Kelvin–Helmholtz instability at the material interface. The final application of the model is found in the two-dimensional metal-plate-cutting experiment. A plate of thickness 5 mm is impacted by a spherically propagating detonation wave. Intermediate and final deformations of the metal plate are of interest while the plastic strain distribution upon the penetration of the detonation wave serves to characterize the strength of the plate in this severe loading scenario.

The content of this thesis is arranged as follows. Chapter 2 deals with the thermomechanical modeling of energetic materials. Tools of thermomechanics [22] are used to derive a set of continuum equations representative of energetic materials. Chapter 3 examines the behavior of a thermomechanical model posed in Chapter 2 and specifically analyzes three simple motions: (i) Constant volume evolution, (ii) One-dimensional, time-dependent longitudinal compression (expansion), and (iii) One-dimensional, time-dependent shear. In Chapter 4, we start two-dimensional calculations of multi-material high–low speed impact by considering the Blatz–Ko rubbery material in contact with other similar materials of different density or a compressible gas. In an effort to accommodate ductile model other than the rubber elasticity of HE, we develop a metal plasticity model in

Chapter 5. In doing so, we revisit a standard derivation of incremental constitutive laws of the elasto–plasticity, which we use in addition to the conservation equations to simulate ductile impact. Basically, two additional evolution equations for effective plastic strain (a scalar) and the deviatoric stress (tensor) are developed. A very complex physics involving a point-source detonation penetrating a metal plate is simulated with the current code, illustrating many promising results that are very sensible. Finally, conclusions and suggestions for future research are given in Chapter 6.

Contents of Appendices are as follows: (A) list of φ -dependent functions, (B) special forms of continuum equations of EMs, (C) structure analysis of steady phase transformation waves, (D) thermodynamics for the energetic materials model, (E) the representation of the continuum equations of EMs in spatial configuration and a representation of the same equations in the Lagrangian configuration, (F) derivation of sharp-interface theory from the phase-field theory of our phase model.

Chapter 2

Thermomechanical Model for Energetic Materials

This chapter presents a thermodynamically self-consistent model that can describe a material that undergoes phase transitions from solid to liquid to gas with exothermic chemical reaction. The model development is quite basic and is likely to have wider application, but the motivation for the study is to describe the behavior and properties of energetic materials such as condensed explosives and solid propellants.

Condensed-phase energetic materials (EMs) are most typically room temperature organic solids that bind substantial chemical energy in molecular bonds. Upon initiation of chemical reaction between sub-molecular constituents within the solid, energy is released that is subsequently available to do work or is converted into heat. The advantage of the condensed phase explosive is that the energy per unit volume is approximately a thousand times higher than its pre-mixed, gaseous counterpart.

For the purposes of illustration and to help us develop a conceptual framework, we will consider the energetic material HMX, $[\text{CH}_2 - \text{N}(\text{NO}_2)]_4$, [52] (a solid explosive compound), to be a base-line energetic material. HMX is solid at room temperature and pressure and, when fully chemically decomposed, forms gaseous products that are simple gases such as water vapor, carbon dioxide, and molecular nitrogen. There are thousands of known energetic (explosive) compounds, so our choice of HMX is both practical (because of its wide use) and representative, in that nearly all the modeling issues considered here apply to similar materials. Fundamental scientific questions surround the phenomena of ignition and release of energy in these materials (EMs) subsequent to impact with

a piston, or due to a rapid shearing motion. At high impact speeds (typically on the order of 1000 m/sec), simple hydrodynamic models give an adequate description for both ignition and transition to detonation. Hydrodynamic models are expressed in the form of the Euler equations for reactive gasdynamics [29], which balance kinetic energy, elastic potential energy, and the chemical energy released by reaction. By virtue of the speed of collision and the short duration of the ignition event, one can justify the neglect of other types of energy and their transfer. However at lower impact speeds (typically below 1000 m/sec) one must fully take into account the solid nature of the material. In contrast, models for lower-speed impact must reflect a large number of types of energy and mechanisms by which energy in the condensed phases can be transformed, localized, and dissipated. A successful model must be able to describe three dimensional stress distributions, heat conduction, phase transformations, and chemical reaction as the material changes from solid to liquid to gas.

Thus, accounting for the change in phase and chemical reaction is essential parts of modeling the ignition of energetic solids. In a continuum modeling framework, one must add additional thermodynamic state variables that reflect the internal degrees of freedom that measure the extent of reaction and phase change in the material. Necessarily, one must posit additional balance laws and provide the required constitutive theory to complete a model formulation. One does this by using physical considerations (which may lie in the proposed model's sub-scale physics) to pose the required additional balance laws. For example in the case of classical combustion theory (see Williams [76] for a representative discussion of the derivation of the commonly used equations of combustion theory), the additional state variables that correspond to the internal degrees of freedom are the mass fractions of all the independent chemical species. The additional balance laws are literal statements of molecular mass balance for each independent species. Other constitutive forms required to describe the evolution of the mass fraction variable are based on well-known laws of collisional reaction (in the case of gaseous chemical reaction), Fickian diffusion, and so on. Importantly, the added balance laws themselves have an identifiable *molecular origin* and are directly related to physically unambiguous statements of mass balance. However, while the physics at the molecular sub-scale is clear, the continuum-scale formulation embraces the added (partial) mass conservation statements as primitive, physical laws that must be given by ansatz.

When modeling the phase changes from solid to liquid to gas, one must also have a physical understanding of the molecular origins of state variables and constitutive forms that describe the phase change. On the molecular scale a typical EM solid like HMX is comprised of nitrated hydrocarbon molecules that reside in a highly ordered crystal lattice. Large quantity of energy is released only if there is chemical reaction between smaller pieces of the molecule, juxtaposed or dislodged by deformation, which subsequently release their chemical energy through elementary exothermic reactions typical of those for the gas-phase chemistry. For example, the liquid phase of HMX is known to be very reactive and short-lived compared with the solid phase; likewise HMX vapor is extremely reactive [10], [13]. The liquid phase is molecularly less well-ordered than the solid, with larger average inter-molecular distances than the solid. If correlated to the average intermolecular spacing (say), the gas phase is even much less ordered than the liquid. Thus a state variable (sometimes called an order parameter or a phase field variable) can be introduced to reflect a continuum measure of molecular order of the condensed phases (solid crystalline and liquid phases) and the gaseous phase. We will call the order parameter, or phase field variable, simply the phase variable φ , and assume that it is normalized in such a way that $\varphi = 0$ corresponds to a solid, $\varphi = 1$ a liquid, and $\varphi = 2$ a gas.

In this formulation, the precise relationship of non-integer values of a phase variable like φ to the molecular sub-scale structure of the material is somewhat ambiguous in contrast to the unambiguous meaning of reactant mass fractions in combustion theory. In a more advanced theory it is anticipated that φ will be assigned to specific molecular coordinates. Advances in molecular dynamics of condensed phase systems do promise eventually to provide a more substantial basis for physical assignment of the phase variables, possibly based on the average molecular spacing (say) or other molecularly-based kinematic variables [20], [4].

Despite possible ambiguity in its precise physical interpretation, if a phase variable is to be used in a model to represent an independent degree of freedom, it should be constrained by standard principles found in the theory of continuum mechanics. In the regions where the phase is pure (i.e. $\varphi = 0, 1$, or 2) the material properties and the constitutive relations must describe the pure material with the properties of that phase. We require that the formulation has a sense in which it is thermodynamically and tensorially consistent. This formation allows further developments in a ra-

tional and systematic manner in three dimensions. We consider a simplified model of an EM (HMX say) which we suppose has three relevant phases, a solid phase, a liquid phase, and a gas phase. We assume that the path from solid to gas goes through the successive phase transformations, solid to liquid to gas. Phase boundaries are to be represented by (typically thin) regions across which the value of the phase variable changes from one constant to another. Also, we will use a single (lumped chemistry) progress variable λ , to describe the extent of exothermic chemical reaction λ with value $\lambda = 0$ when no reaction has occurred and $\lambda = 1$ when the reaction is completed. The model allows chemical reaction in any phase.

A key aspect of the model is explicit partitioning of the energy associated with specific internal (thermal) energy, chemical reaction energy, elastic potential (deformational) energy, and energies associated with phase change, such as the enthalpies associated with melting of the solid and evaporation of the liquid, and potential energies stored at phase boundaries. The partitioning of the energy is represented by a decomposition of the Helmholtz free energy, ψ , into the various parts associated with the energies listed above, such that $\psi = \psi_{\text{thermal}} + \psi_{\text{elastic}} + \psi_{\text{reaction}} + \psi_{\text{phase}} + \psi_{\text{grad}(\text{phase})}$. The constitutive forms used for ψ_{thermal} and ψ_{elastic} are found in discussions of thermo-elastic materials. The constitutive forms for ψ_{phase} and $\psi_{\text{grad}(\text{phase})}$ contain the energies of phase change and energies stored near phase change interfaces. The constitutive form for ψ_{reaction} can be found in discussion of pre-mixed combustible materials. The free energies and other constitutive variables are allowed to depend on both the phase variable, φ , and the reaction progress variable, λ , as well as the temperature, T , and the deformation gradient, \mathbf{F} , and the gradient of φ , $\vec{\nabla}\varphi$. The governing equations are formulated by statements of conservation of mass, momentum, energy, and evolution equations for the change in phase and progress of chemical reaction.

The treatment we use to describe the evolution of the phase variable follows classical treatments that have arisen in the discussion of solidification (for example see [15]) but specifically follows a consistent formulation pioneered by Gurtin [32]. Gurtin has argued for a separate continuum balance of configurational forces acting near the boundaries separating pure phases in the volumetric bulk. The arguments for including these additional forces may be justified by consideration of short-range van der Waals forces, which typically are generated near phase boundaries due to local changes in the intermolecular distances between molecules. The argument for such configurational

forces is similar to those used to explain classical surface tension forces. The hypothesis is that if the configurational forces act in the vicinity of the boundary near the change in phase and in the bulk, they can be in balance, and if so they must not affect the overall (conventional) momentum balances. Hence the force is posited as a basic law. However, with the postulate of a balance of configurational forces comes the consequence that those forces do work. The working rate is accounted for explicitly in the overall energy balance.

The second law of thermodynamics (the Clausius–Duhem inequality) restricts the form of the constitutive theory so that the rate processes are dissipative and entropy-increasing. An important outcome of these arguments is the derivation of an evolution equation for the phase variable φ that is essentially a Ginzburg–Landau equation with additional forcing terms. The evolution equation for φ is a time-dependent, reaction diffusion equation that is amply capable of describing the pattern formation associated with phase transformation. The richness of the resulting theory becomes evident in the energy equation. Due to the decomposition of the Helmholtz free energy, the energy equation contains contributions from all the different terms in the partition, and reflects the fact that in the energetic material, energy is converted and distributed to many different forms such as elastic, kinetic, internal, and phase gradient energy (stored in interfaces).

In the sections that follow, the development of the model is given, based on the continuum-thermodynamic formulation described above. In Section 1 we review the continuum thermodynamic formulation consistent with conventional combustion theory [76], [14], [50], [11], which specifically includes a reaction progress variable. A (nonstandard) presentation of the Helmholtz energy decomposition is given and the attendant standard arguments for restrictions placed by the second law are given. In Section 2 we present a model for a material that changes from solid to liquid to gas and present a Helmholtz free energy decomposition that is suitable to describe such a material, subject to second-law restrictions. In Section 3, the combined model for an EM (with both phase change and chemical reaction) is then presented. In Section 4 we discuss various limiting cases of the model. We discuss the relationship of the model to classical quasi-static thermodynamics, and illustrate examples based on fits to HMX properties to illustrate the dynamics of a phase change that would be calculated in the classical theory. Section 5 presents special formulations of the model equation for three important simple motions. These cases are: (i) Constant volume

evolution (which is a generalization of the classical constant volume explosion formulation found in combustion theory), (ii) One-dimensional, time-dependent longitudinal compression (expansion), and (iii) One-dimensional, time-dependent shear motion. The solution of the equations for these three important cases for an HMX-like material is the subject of Chapter 3.

In what follows, a “c” subscript denotes a condensed phase, solid or liquid, an “f” subscript denotes fluid—either liquid or gas, an “s” subscript denotes solid, an “l” subscript denotes liquid and a “g” subscript denotes gas. The spelled out subscripts “solid”, “liquid” and “gas” refer to constant values for that pure phase. The notation is kept as simple as possible in an attempt make the thesis easier to read. Boldface quantities can either be vectors or tensors. If obvious, the constant arguments during differentiation are dropped. Our notation is standard, insofar as possible, and follows a well-known text such as Bowen [11].

2.1 Kinematics

Let the Eulerian (spatial) coordinates of position in the lab frame be given by \mathbf{x} and the Lagrangian (material) coordinates initial position of the particles (or particle coordinates) be given by \mathbf{X} . For simplicity we will assume that \mathbf{X} represents the initial position of material particles. Then the mapping of the deformations that define the particle trajectory paths is given by

$$\mathbf{x} = \mathbf{x}(\mathbf{X}, t). \quad (2.1)$$

The deformation gradient \mathbf{F} is defined by the derivative

$$\mathbf{F} = \frac{\partial \mathbf{x}}{\partial \mathbf{X}}, \quad (2.2)$$

and the velocity of particles \mathbf{v} is defined by the time derivative of the particle trajectories $\mathbf{v} = (\partial \mathbf{x} / \partial t)_{\mathbf{X}}$. The velocity gradient is $\mathbf{L} = \vec{\nabla} \mathbf{v}$. Let the dot notation, $\dot{(\)}$, refer to the material derivative. A standard identity, which can be verified by the previous definitions and the chain rule, gives the material (particle-fixed) time derivative of the deformation gradient as $\dot{\mathbf{F}} = \mathbf{L}\mathbf{F}$. A statement of conservation of mass in the material frame is that the ratio of the instantaneous

density ρ of the particle to a reference (ambient) density of the solid ρ_0 is equal to the determinant of the deformation gradient:

$$\det(\mathbf{F}) = \frac{\rho_0}{\rho} . \quad (2.3)$$

2.2 Review of the thermomechanics for a simple model of a reactive flow

The standard combustion model, for a pre-mixed mixture that can explode or burn, can be derived from a simple mixture theory: see references [76], [14], [50], [11]. The combined model that we introduce later incorporates the features of the standard combustion model, so we review its derivation. Importantly, the reaction progress variable λ represents a product reactant mass flux. Hence λ is treated differently than the phase variable φ , which is introduced later to describe the change in phase from solid to liquid to gas.

For the purpose of discussion, one assumes that there are only two distinct species, fuel and product (say). The corresponding chemical reaction is written as $F \rightarrow P + Q_{\text{hc}}$ (heat). All physical properties of the two species, such as the molecular weights, specific heats, conductivities, etc., are assumed to be identical, save the heats of formation, the weighted difference of which is a heat of combustion.

We start with the balance laws for conservation of mass, linear momentum and energy

$$\dot{\rho} + \rho(\vec{\nabla} \cdot \mathbf{v}) = 0 , \quad (2.4)$$

$$\rho \dot{\mathbf{v}} = \vec{\nabla} \cdot \boldsymbol{\sigma} + \rho \mathbf{f} , \quad (2.5)$$

$$\rho \dot{e} = \boldsymbol{\sigma} : \vec{\nabla} \mathbf{v} - \vec{\nabla} \cdot \mathbf{q} + \rho r . \quad (2.6)$$

In the energy equation, r is a volumetric energy production term that typically represents radiation or volumetric heating (or cooling) in combustion theory. The body force is given by \mathbf{f} . In addition

we invoke a primitive evolution law for the reaction progress variable λ :

$$\rho \dot{\lambda} = \vec{\nabla} \cdot \mathbf{s} + \rho \Omega. \quad (2.7)$$

The vector \mathbf{s} is the flux of mass of reacted species per unit area per unit time and $\rho \Omega$ is the instantaneous rate of creation of mass of the reacted species per unit volume. Then λ is recognized as the mass fraction of the product species. Further, by direct correspondence with the standard combustion equations, one can interpret $\mathbf{s} = \rho \lambda \mathbf{V}$ where \mathbf{V} is the velocity of the product species (say), and where $\rho \lambda$ is the partial density fraction of the same product.

To these basic laws we add the second law of thermodynamics, the Clausius–Duhem inequality

$$\rho \dot{\eta} \geq -\vec{\nabla} \cdot \left(\frac{\mathbf{q}}{T} \right) + \vec{\nabla} \cdot \left(\frac{Q_{\text{hc}} \mathbf{s}}{T} \right) + \frac{\rho r}{T}, \quad (2.8)$$

where Q_{hc} , the heat of combustion, is the exothermic energy release per unit mass, and the term $\vec{\nabla} \cdot (Q_{\text{hc}} \mathbf{s}/T)$ represents the entropy flux per unit volume per unit time associated with chemical reaction.

2.2.1 Constitutive forms and restrictions

Next consider the classical forms and assumptions that lead to the combustion equations of premixed materials found in such texts as [76] and [14]. The formulation uses the Helmholtz free energy, which is defined in terms of the internal energy and entropy as $\psi = e - T\eta$. We start with the assumption that ψ is specified by

$$\psi = \psi(\mathbf{F}, T, \lambda) \quad (2.9)$$

and we assume similar dependencies for e , η , and all other thermodynamic variables. Next we consider the implication of the entropy inequality and deduce various restrictions imposed by it on the constitutive formulation.

If we use the definition of the Helmholtz free energy to get an expression for the entropy, as $\eta = (e - \psi)/T$, and take the material derivative, we obtain $\dot{\eta} = (\dot{e} - \dot{\psi} - \eta \dot{T})/T$. Using the form

assumed above, the derivative $\dot{\psi}$ appears as

$$\dot{\psi} = \frac{\partial \psi}{\partial \mathbf{F}} \mathbf{F}^\top : \vec{\nabla} \mathbf{v} + \frac{\partial \psi}{\partial T} \dot{T} + \frac{\partial \psi}{\partial \lambda} \dot{\lambda}. \quad (2.10)$$

Using this expression for $\dot{\psi}$ and using the energy equation to replace \dot{e} in the entropy inequality lead to an intermediate result

$$\left(\boldsymbol{\sigma} - \rho \frac{\partial \psi}{\partial \mathbf{F}} \mathbf{F}^\top \right) : \vec{\nabla} \mathbf{v} - \rho \left(\eta + \frac{\partial \psi}{\partial T} \right) \dot{T} - (\mathbf{q} - Q_{\text{hc}} \mathbf{s}) \cdot \frac{\vec{\nabla} T}{T} - \rho \frac{\partial \psi}{\partial \lambda} \dot{\lambda} - Q_{\text{hc}} \vec{\nabla} \cdot \mathbf{s} \geq 0. \quad (2.11)$$

We restrict our choice in constitutive theory to forms that will automatically satisfy this dissipation inequality as the physical processes in the material range over all admissible deformations and temperature fields. For example, since $\vec{\nabla} \mathbf{v}$ can be regarded as an independent field, then in the standard way we restrict the form of the stress tensor such that

$$\boldsymbol{\sigma} = \rho \frac{\partial \psi}{\partial \mathbf{F}} \mathbf{F}^\top + \boldsymbol{\sigma}^{\text{diss}}, \quad (2.12)$$

where the dissipative stress $\boldsymbol{\sigma}^{\text{diss}}$, satisfies $\boldsymbol{\sigma}^{\text{diss}} : \vec{\nabla} \mathbf{v} \geq 0$. This last requirement is clearly satisfied by the classical choice for a viscous fluid

$$\boldsymbol{\sigma}^{\text{diss}} = \nu_g (\vec{\nabla} \cdot \mathbf{v}) \mathbf{I} + 2\mu_g \mathbf{D}, \quad (2.13)$$

where $\mathbf{D} = (\vec{\nabla} \mathbf{v} + \vec{\nabla} \mathbf{v}^\top)/2$ and ν_g, μ_g are positive and are identified as the gas-phase bulk and shear viscosities. The assumed form of the stress becomes

$$\boldsymbol{\sigma} = \rho \frac{\partial \psi}{\partial \mathbf{F}} \mathbf{F}^\top + \nu_g (\vec{\nabla} \cdot \mathbf{v}) \mathbf{I} + 2\mu_g \mathbf{D}. \quad (2.14)$$

In a similar fashion, since \dot{T} is independent, we require that the Helmholtz free energy must satisfy the Gibbs relation

$$\frac{\partial \psi}{\partial T} = -\eta. \quad (2.15)$$

The entropy inequality is now satisfied if the following reduced inequality is satisfied:

$$-(\mathbf{q} - Q_{\text{hc}}\mathbf{s}) \cdot \frac{\vec{\nabla}T}{T} - \rho \frac{\partial \psi}{\partial \lambda} \dot{\lambda} - Q_{\text{hc}} \vec{\nabla} \cdot \mathbf{s} \geq 0. \quad (2.16)$$

If we assume that the change in the Helmholtz free energy with respect to the progress variable is related to the heat of combustion (which also can be verified and put into direct correspondence with forms derived in mixture theory of reacting gases, see [14], [50], [11]), that is,

$$\frac{\partial \psi}{\partial \lambda} = -Q_{\text{hc}}, \quad (2.17)$$

and use the evolution equation for the progress variable $\rho \dot{\lambda} - \vec{\nabla} \cdot \mathbf{s} = \rho \Omega$, then the reduced inequality can be recast as

$$-(\mathbf{q} - Q_{\text{hc}}\mathbf{s}) \cdot \frac{\vec{\nabla}T}{T} + \rho Q_{\text{hc}} \Omega \geq 0. \quad (2.18)$$

Finally we make the choice that the energy flux vector is the sum of a Fourier heat conductive flux and a energy flux associated with the diffusion of the product species

$$\mathbf{q} = -k \vec{\nabla}T + Q_{\text{hc}} \mathbf{s}, \quad (2.19)$$

and require that, for an exothermic chemical reaction with $Q_{\text{hc}} > 0$, the reaction rate must be positive with $\Omega \geq 0$. With these restrictions the second law is automatically satisfied. Recall that \mathbf{s} represented the mass flux vector of the product species, $\mathbf{s} = \rho \lambda \mathbf{V}$, where \mathbf{V} is the diffusion velocity of that species. Without further restriction we can make a standard assumption that the diffusion velocity is related to the gradient of the species concentration through a Fick's law relation by

$$\mathbf{s} = \rho \lambda \mathbf{V} = d \vec{\nabla} \lambda, \quad (2.20)$$

where $d \geq 0$ is a diffusion coefficient.

2.2.2 Temperature form of the energy equation

We present the temperature form of the energy equation in terms of a specification of the Helmholtz free energy, in order to set the stage for later discussions. We use the definition of the specific internal energy in terms of the temperature and the entropy, $e = \psi + T\eta$, to obtain $\dot{e} = \dot{\psi} + \eta\dot{T} + T\dot{\eta}$. Next we use the form of the Helmholtz energy $\psi(\mathbf{F}, T, \lambda)$ and the Gibbs relation $\eta = -\partial\psi/\partial T$ to generate expressions for $\dot{\psi}$ and $\dot{\eta}$ as

$$\dot{e} = \frac{\partial\psi}{\partial\mathbf{F}}\mathbf{F}^\top : \vec{\nabla}\mathbf{v} + \frac{\partial\psi}{\partial T}\dot{T}, \quad \dot{\eta} = -\frac{\partial^2\psi}{\partial T\partial\mathbf{F}}\mathbf{F}^\top : \vec{\nabla}\mathbf{v} - \frac{\partial^2\psi}{\partial T^2}\dot{T}. \quad (2.21)$$

We then insert these expression into (2.6) and make some further simplifications. A collection of terms appears that is associated with the stress-related dissipation

$$\left(\boldsymbol{\sigma} - \rho \frac{\partial\psi}{\partial\mathbf{F}}\mathbf{F}^\top\right) : \vec{\nabla}\mathbf{v} = \boldsymbol{\sigma}^{\text{diss}} : \vec{\nabla}\mathbf{v}.$$

Using the classical definition of the specific heat at constant deformation (volume)

$$c_v \equiv T \frac{\partial\eta}{\partial T} \Big|_{\mathbf{F}} = -T \left(\frac{\partial^2\psi}{\partial T^2} \right) \Big|_{\mathbf{F}}, \quad (2.22)$$

we can re-write the energy equation as

$$\rho c_v \dot{T} = -\vec{\nabla} \cdot \mathbf{q} + \boldsymbol{\sigma}^{\text{diss}} : \vec{\nabla}\mathbf{v} + \rho T \frac{\partial^2\psi}{\partial T\partial\mathbf{F}}\mathbf{F}^\top : \vec{\nabla}\mathbf{v}. \quad (2.23)$$

The term $\rho T (\partial^2\psi/\partial T\partial\mathbf{F})\mathbf{F}^\top : \vec{\nabla}\mathbf{v}$ is a stress work term classically associated with thermal stresses. As we will see below in the case of gaseous combustion for ideal gases, this term is proportional to the pressure work term $-p(\vec{\nabla} \cdot \mathbf{v})$, where $p = \rho R_g T$, and R_g is the ideal gas constant.

The form of the Helmholtz free energy from classical combustion theory

To complete the classical formulation for pre-mixed combustion, one must specify the form of the Helmholtz free energy. The forms can be extracted from the correct forms found in the binary mixture theory of premixed gases, see [11], [76], [14], [50]. Let $\mathbf{B} = \mathbf{F}\mathbf{F}^\top$ be the left Cauchy–

Green tensor and let $III_B = (\rho_0/\rho)^2$ be the third invariant of \mathbf{B} . Then the form of the Helmholtz free energy for a thermally ideal material, with the additional term required for the change in enthalpy associated with combustion, is comprised of three parts: A thermal energy density $\psi_1 = c_v[(T - T_0) - T \ln(T/T_0)]$, a strain energy density associated with the temperature (which defines the pressure in terms of the density and temperature) $\psi_2 = -1/2 R_g T \ln(III_B)$ and the chemical enthalpy $\psi_3 = -Q_{hc}\lambda$. Thus the total free energy $\psi = \psi_1 + \psi_2 + \psi_3$ is

$$\psi = c_v(T - T_0) - c_v T \ln(T/T_0) - \frac{1}{2} R_g T \ln(III_B) - Q_{hc}\lambda. \quad (2.24)$$

It follows that the elastic part of the stress can be computed from this form of the free energy and identifies the classical thermodynamic pressure p . In particular, we have that $\rho(\partial\psi/\partial\mathbf{F})\mathbf{F}^T = 2\rho(\partial\psi/\partial\mathbf{B})\mathbf{B} = -\rho R_g T \mathbf{I} \equiv -p\mathbf{I}$, which leads to the identification of the pressure p by the ideal gas law, $p = \rho R_g T$. Also the thermal stress work term is re-written $\rho(\partial\psi/\partial\mathbf{F})\mathbf{F}^T : \vec{\nabla}\mathbf{v} = -p(\vec{\nabla} \cdot \mathbf{v})$. The corresponding form of the entropy and the internal energy (obtained from the definition of the Helmholtz free energy and the Gibbs relation) are given by

$$e = c_v(T - T_0) - Q_{hc}\lambda, \quad \eta = c_v \ln(T/T_0) + \frac{R}{2} \ln(III_B). \quad (2.25)$$

2.2.3 Summary of the governing equations for a pre-mixed reactive fluid

Here we summarize the results of the last section, which reduce to the classical form of the combustion equations for a premixed combustible fluid. These equations incorporate the various restrictions and constitutive forms that we assumed and are suitable for solving initial-value problems ordinarily associated with the theory of pre-mixed combustion. The entropy (dissipation) inequality is not included in our list since it is automatically satisfied by construction of the model. The equations

for ρ, \mathbf{v}, T and λ are

$$\dot{\rho} + \rho \vec{\nabla} \cdot \mathbf{v} = 0, \quad (2.26)$$

$$\rho \dot{\mathbf{v}} = \vec{\nabla} \cdot \boldsymbol{\sigma} + \rho \mathbf{f}, \quad (2.27)$$

$$\rho c_v \dot{T} = \vec{\nabla} \cdot (k \vec{\nabla} T) + \boldsymbol{\sigma}^{diss} : \vec{\nabla} \mathbf{v} - p(\vec{\nabla} \cdot \mathbf{v}) + \rho Q_{hc} \Omega, \quad (2.28)$$

$$\rho \dot{\lambda} = \vec{\nabla} \cdot (d \vec{\nabla} \lambda) + \rho \Omega, \quad (2.29)$$

with the constitutive relation for the stress given by $\boldsymbol{\sigma} = -\rho R_g T \mathbf{I} + \nu_g \vec{\nabla} \cdot \mathbf{v} \mathbf{I} + 2\mu_g \mathbf{D}$, with $\boldsymbol{\sigma}^{diss} = \nu_g \vec{\nabla} \cdot \mathbf{v} \mathbf{I} + 2\mu_g \mathbf{D}$, and with $\mathbf{D} = (\vec{\nabla} \mathbf{v} + \vec{\nabla} \mathbf{v}^T)/2$.

2.3 Thermomechanics of a model of a material with phase changes from solid to liquid to gas

Here we develop a model for a material that can undergo a phase change from solid to liquid to gas, in preparation for the development of the combined model, which includes chemical reaction and exothermic energy release. The important difference in the development in this section from that in Section 2 is the introduction of a phase variable that is used to describe and delineate the separate phases. In order to describe the phase transitions we introduce the (normalized) variable φ so that $\varphi = 0$ corresponds to the solid phase, $\varphi = 1$ to the liquid phase, and $\varphi = 2$ to the vapor phase. In its pure phases, solid, liquid and gas, the material is prescribed by classical models for that pure phase, i.e. a compressible elastic solid, a compressible Newtonian liquid, and a gas, respectively.

A consistent thermodynamic formulation for the model is developed through an extension of a formulation proposed by Gurtin [32]. Energy expended by the system during phase change is associated with configurational forces of two types, a configurational stress that acts at or near the boundaries between phases, which is balanced by a configurational force distributed in the bulk. The power expenditure of these forces must be accounted for in the energy balance. If one assumes that the configurational forces in the material are balanced separately (this is a posited balance) then the evolution of the phase field φ is constrained by the entropy inequality to be dissipative and further considerations lead to the derivation of an evolution law for φ . This is in contrast to

the formulation of the last section, where we considered the evolution law for the progress variable λ as posited. Presumably, (and we have considered this in some detail that is not presented here) an alternative to deriving the equation for φ is to pose an evolution equation as fundamental and then derive the consequence of local balance for the configurational forces. Either way one comes to similar physical conclusions. The consequences of this choice, in absence of better, physically-based arguments, need to be judged against the forms of the resulting equation that allow us to solve interesting initial-value problems.

The starting point is the form of the general laws. The differential form of the general law for mass (2.4) and momentum (2.5) are unchanged from the previous section. We turn to the more unfamiliar considerations of the force balance law associated with the phase change and corresponding changes in the energy balance next.

Force balances associated with change in phase

Associated with the evolution of the phase variable φ , we introduce a balance of configurational stress $\boldsymbol{\xi}$, a configurational internal force density π_φ . The integral form of the balance law for a body in region \mathcal{B} with boundary $\partial\mathcal{B}$ is

$$\int_{\partial\mathcal{B}} \boldsymbol{\xi} \cdot \mathbf{n} \, dA + \int_{\mathcal{B}} (\pi_\varphi) \, dV = 0, \quad (2.30)$$

and with the use of the divergence theorem, the corresponding differential form of the balance law is

$$\vec{\nabla} \cdot \boldsymbol{\xi} + \pi_\varphi = 0. \quad (2.31)$$

Rate of work

The rate of work expended on \mathcal{B} is due to the external forces acting on the surface and within the volume of \mathcal{B} . Gurtin [32] shows that the correct form for the rate of work due to all stresses is

$$\mathcal{W}(\mathcal{P}) = \int_{\partial\mathcal{B}} (\boldsymbol{\sigma} \mathbf{n} \cdot \mathbf{v} + \boldsymbol{\xi} \cdot (\dot{\varphi} \mathbf{n})) \, dA + \int_{\mathcal{B}} \mathbf{b} \cdot \mathbf{v} \, dV. \quad (2.32)$$

The integral form of the energy balance can be written in the standard way as the material derivative of the total energy (internal and kinetic) equated to the rate of work minus the energy flux out of the body plus the rate of heating by any other source; thus

$$\frac{D}{Dt} \int_{\mathcal{B}} \rho(e + \tfrac{1}{2}|\mathbf{v}|^2) dV + = \mathcal{W} - \int_{\partial\mathcal{B}} \mathbf{q} \cdot \mathbf{n} dA + \int_{\mathcal{B}} \rho r dV. \quad (2.33)$$

To obtain the differential form we convert the surface integrals into volume integrals and use the divergence theorem. The resulting integral must hold everywhere for all sub-volumes, so the resulting integrand is set to zero, which leads to an intermediate differential form (not shown). We then use the momentum equations and take its dot product with the velocity \mathbf{v} to get the standard work-energy statement on a material path and subtract that result from the above-mentioned intermediate form to get the following form of the energy equation:

$$\rho \dot{e} = -\vec{\nabla} \cdot \mathbf{q} + \boldsymbol{\sigma} : \vec{\nabla} \mathbf{v} + \boldsymbol{\xi} \cdot \vec{\nabla}(\dot{\varphi}) - \pi_{\varphi} \dot{\varphi} + \rho r. \quad (2.34)$$

The main difference from the classical form is the appearance of the two work terms $\boldsymbol{\xi} \cdot \vec{\nabla}(\dot{\varphi})$ and $-\pi_{\varphi} \dot{\varphi}$ that derive from the configurational forces. For upcoming considerations of the entropy inequality, it is useful to use identities (which can be verified easily in Cartesian index notation) to rewrite the term $\boldsymbol{\xi} \cdot \vec{\nabla}(\dot{\varphi})$ as

$$\boldsymbol{\xi} \cdot \vec{\nabla}(\dot{\varphi}) = \overline{\vec{\nabla} \dot{\varphi}} \cdot \boldsymbol{\xi} + \vec{\nabla} \varphi \otimes \boldsymbol{\xi} : \mathbf{L}, \quad (2.35)$$

so that the revised energy equation reads

$$\rho \dot{e} = -\vec{\nabla} \cdot \mathbf{q} + \boldsymbol{\sigma} : \vec{\nabla} \mathbf{v} + \overline{\vec{\nabla} \dot{\varphi}} \cdot \boldsymbol{\xi} + \vec{\nabla} \varphi \otimes \boldsymbol{\xi} : \vec{\nabla} \mathbf{v} - \pi_{\varphi} \dot{\varphi} + \rho r. \quad (2.36)$$

The entropy inequality

Finally, to these basic laws we must add the second law of thermodynamics, the Clausius–Duhem inequality

$$\rho \dot{\eta} \geq -\vec{\nabla} \cdot \left(\frac{\mathbf{q}}{T} \right) + \frac{\rho r}{T}. \quad (2.37)$$

Note that since φ is not assumed to be related to a partial mass density of material, there is no entropy flux term such as $\vec{\nabla} \cdot (Q_{\text{hc}} \mathbf{s}/T)$ that appears in the combustion-based entropy inequality (2.8). Equation (2.37) is the classical (inert) form of the entropy inequality.

Constitutive forms and restrictions from the entropy inequality

We restrict our attention to a general class of constitutive equations and start with a very general assumption that the free-energy density ψ , the Cauchy stress $\boldsymbol{\sigma}$, the configurational stresses $\boldsymbol{\xi}$, the internal configurational force π_φ , the entropy density η , and the heat flux \mathbf{q} at any point (\mathbf{x}, t) are dependent on the deformation gradient \mathbf{F} , the temperature T , the phase field φ , the gradients $\vec{\nabla} T$, $\vec{\nabla} \varphi$, and the velocity gradient \mathbf{L} , such that we can write

$$\psi = \psi(\mathbf{F}, T, \varphi, \vec{\nabla} T, \vec{\nabla} \varphi, \mathbf{L}). \quad (2.38)$$

We assume that $\boldsymbol{\sigma}$, $\boldsymbol{\xi}$, π_φ , η , and \mathbf{q} all depend on the same argument list, $(\mathbf{F}, T, \varphi, \vec{\nabla} T, \vec{\nabla} \varphi, \mathbf{L})$. We use the definition of the Helmholtz free energy to get an expression for the entropy, $\eta = (e - \psi)/T$, take the material derivative, then use the energy equation to replace \dot{e} , and use the chain rule to replace $\dot{\psi}$. These substitutions into the entropy inequality leads to the intermediate result

$$\begin{aligned} & \left(\boldsymbol{\sigma} - \rho \frac{\partial \psi}{\partial \mathbf{F}} \mathbf{F}^\top + \vec{\nabla} \varphi \otimes \boldsymbol{\xi} \right) : \vec{\nabla} \mathbf{v} - \rho \left(\eta + \frac{\partial \psi}{\partial T} \right) \dot{T} - \left(\pi_\varphi + \rho \frac{\partial \psi}{\partial \varphi} \right) \dot{\varphi} \\ & - \rho \frac{\partial \psi}{\partial \vec{\nabla} T} \cdot \dot{\vec{\nabla} T} - \left(\rho \frac{\partial \psi}{\partial \vec{\nabla} \varphi} - \boldsymbol{\xi} \right) \cdot \dot{\vec{\nabla} \varphi} - \rho \left(\frac{\partial \psi}{\partial \mathbf{L}} \right) : \dot{\mathbf{L}} - \mathbf{q} \cdot \frac{\vec{\nabla} T}{T} \geq 0. \end{aligned} \quad (2.39)$$

Again we restrict our choice of constitutive forms to those that automatically satisfy this dis-

sipation inequality as the physical process in the material ranges over all admissible deformations and temperature and phase fields. We restrict the form of the stress tensor such that

$$\boldsymbol{\sigma} = \rho \frac{\partial \psi}{\partial \mathbf{F}} \mathbf{F}^\top - \vec{\nabla} \varphi \otimes \boldsymbol{\xi} + \boldsymbol{\sigma}^{diss}, \quad (2.40)$$

where again $\boldsymbol{\sigma}^{diss}$ must be chosen to satisfy $\boldsymbol{\sigma}^{diss} : \vec{\nabla} \mathbf{v} \geq 0$. Later we will take $\boldsymbol{\sigma}^{diss}$ to be given by (2.13), where the shear and bulk viscosities are taken to be functions of the phase field variable φ . We require that the Gibbs relation be satisfied and that the configurational force $\boldsymbol{\xi}$ be defined by the derivative of the Helmholtz free energy with respect to the gradient of φ such that

$$\eta = -\frac{\partial \psi}{\partial T}, \quad \text{and} \quad \boldsymbol{\xi} = \rho \frac{\partial \psi}{\partial \vec{\nabla} \varphi}. \quad (2.41)$$

We also assume that the Helmholtz free energy is independent of $\mathbf{L} = \vec{\nabla} \mathbf{v}$ and the temperature gradient $\vec{\nabla} T$ so that

$$\frac{\partial \psi}{\partial \mathbf{L}} = 0, \quad \text{and} \quad \frac{\partial \psi}{\partial \vec{\nabla} T} = 0, \quad (2.42)$$

hold. We also suppose that the energy flux vector is described by a Fourier heat conduction law, $\mathbf{q} = -k \vec{\nabla} T$, and insist that k is a positive constant that can be a function of the temperature and the order parameter, i.e. $k(\varphi, T) \geq 0$. Then the reduced dissipation inequality now has the form

$$-\left(\pi_\varphi + \rho \frac{\partial \psi}{\partial \varphi}\right) \dot{\varphi} \geq 0. \quad (2.43)$$

The final form of the reduced dissipation inequality is satisfied if we require that the phase changes be dissipative and if we allow π_φ to take the form

$$-\left(\pi_\varphi + \rho \frac{\partial \psi}{\partial \varphi}\right) = B \dot{\varphi}, \quad (2.44)$$

where $B \geq 0$. Equation (2.44) is an evolution equation for the phase variable φ . Note that the configurational force balance (2.31) defines $\pi_\varphi = -\vec{\nabla} \cdot \boldsymbol{\xi}$, and with the configurational force identified

by $\boldsymbol{\xi} = \rho(\partial\psi/\partial\vec{\nabla}\varphi)$, leads to $\pi_\varphi = -\vec{\nabla} \cdot (\rho\partial\psi/\partial\vec{\nabla}\varphi)$. Thus (2.44) can be re-expressed as

$$B\dot{\varphi} = \vec{\nabla} \cdot \left(\rho \frac{\partial\psi}{\partial\vec{\nabla}\varphi} \right) - \rho \frac{\partial\psi}{\partial\varphi}. \quad (2.45)$$

Given appropriate forms for ψ (such as quadratic dependence of ψ on $\vec{\nabla}\psi$, (2.45) is recognized as an advection, reaction–diffusion equation, which given an assumed form for ψ , can generate a Ginzburg–Landau equation. The coefficient B^{-1} is then recognized as a kinetic rate constant for the phase transformation.

2.3.1 Temperature form of the energy equation

In order to show the coupling between the thermal (temperature) field, the stress field, and the phase field, we present an alternative form of the energy equation. Starting with the energy balance (2.36) we use the definition of the specific internal energy in terms of the temperature and the entropy, $e = \psi + T\eta$, to obtain $\dot{e} = \dot{\psi} + \eta\dot{T} + T\dot{\eta}$. Next we use the form of the Helmholtz energy $\psi(\varphi, T, \vec{\nabla}\varphi, \mathbf{F})$ and the Gibbs relation $\eta = -\partial\psi/\partial T$ to generate expressions for $\dot{\psi}$ and $\dot{\eta}$:

$$\dot{\psi} = \frac{\partial\psi}{\partial\mathbf{F}} \mathbf{F}^\top : \vec{\nabla}\mathbf{v} + \frac{\partial\psi}{\partial T} \dot{T} + \frac{\partial\psi}{\partial\varphi} \dot{\varphi} + \frac{\partial\psi}{\partial\vec{\nabla}\varphi} \cdot \frac{\dot{\vec{\nabla}\varphi}}{\vec{\nabla}\varphi}, \quad (2.46)$$

$$\dot{\eta} = -\frac{\partial^2\psi}{\partial T \partial \mathbf{F}} \mathbf{F}^\top : \vec{\nabla}\mathbf{v} - \frac{\partial^2\psi}{\partial T^2} \dot{T} - \frac{\partial^2\psi}{\partial T \partial \varphi} \dot{\varphi} - \frac{\partial^2\psi}{\partial T \partial \vec{\nabla}\varphi} \cdot \frac{\dot{\vec{\nabla}\varphi}}{\vec{\nabla}\varphi}. \quad (2.47)$$

We then insert these expression into (2.36) and make some further simplifications. In the resulting collection, terms proportional to \dot{T} drop out because of the Gibbs relation $\eta = -\partial\psi/\partial T$. Likewise terms proportional to $\frac{\dot{\vec{\nabla}\varphi}}{\vec{\nabla}\varphi}$ drop out because of the relation for the configurational stress $\boldsymbol{\xi} = \rho(\partial\psi/\partial\vec{\nabla}\varphi)$. A collection of terms appears that is associated with the stress-related dissipation

$$\left(\boldsymbol{\sigma} - \rho \frac{\partial\psi}{\partial\mathbf{F}} \mathbf{F}^\top + \vec{\nabla}\varphi \otimes \boldsymbol{\xi} \right) : \vec{\nabla}\mathbf{v} = \boldsymbol{\sigma}^{\text{diss}} : \vec{\nabla}\mathbf{v}$$

and a collection of terms appears associated with the dissipation induced by the phase transforma-

tion

$$-\left(\rho \frac{\partial \psi}{\partial \varphi} + \pi_\varphi\right) \dot{\varphi} = B \dot{\varphi}^2.$$

Using the classical definition of the specific heat at constant deformation (volume) $c_v \equiv T(\partial \eta / \partial T)_{\mathbf{F}} = -T(\partial^2 \psi / \partial T^2)_{\mathbf{F}}$, we can re-write the energy equation as

$$\begin{aligned} \rho c_v \dot{T} = & -\vec{\nabla} \cdot \mathbf{q} + \boldsymbol{\sigma}^{\text{diss}} : \vec{\nabla} \mathbf{v} + B \dot{\varphi}^2 + \rho T \frac{\partial^2 \psi}{\partial T \partial \mathbf{F}} \mathbf{F}^\top : \vec{\nabla} \mathbf{v} + \\ & \rho T \frac{\partial^2 \psi}{\partial T \partial \varphi} \dot{\varphi} + \rho T \frac{\partial^2 \psi}{\partial T \partial \vec{\nabla} \varphi} \cdot \frac{\vec{\nabla} \dot{\varphi}}{\vec{\nabla} \varphi} + \rho r. \end{aligned} \quad (2.48)$$

Some straightforward physical interpretations can be made for the various terms. The term $\boldsymbol{\sigma}^{\text{diss}} : \vec{\nabla} \mathbf{v}$ is the viscous dissipation associated with the stress. The term $B \dot{\varphi}^2$ is a dissipation associated with the phase change. The term $\rho T(\partial^2 \psi / \partial T \partial \varphi) \dot{\varphi}$ is an energy source term that is associated with enthalpic changes in phase (similar to those associated with the heat of combustion for reacting flows). The term $\rho T(\partial^2 \psi / \partial T \partial \mathbf{F}) \mathbf{F}^\top : \vec{\nabla} \mathbf{v}$ is (again) a stress work term classically associated with thermal stresses. Similarly, the term $\rho T(\partial^2 \psi / \partial T \partial \vec{\nabla} \varphi) \cdot \frac{\vec{\nabla} \dot{\varphi}}{\vec{\nabla} \varphi}$ is a thermal stress work term associated with the configurational stress of the phase change.

Invariance requirements and isotropy

Most energetic solids are encountered as fine-grained polycrystalline aggregates and are often modeled with conventional isotropic liquid and gaseous forms. We now restrict our attention to isotropic materials and we ignore possible anisotropic properties in this model. As is conventional we require that the material response be invariant under superposed rigid changes of observer. It can be shown in a standard way that the constitutive dependence on the deformation gradient \mathbf{F} can be replaced by the left Cauchy–Green tensor $\mathbf{B} = \mathbf{F} \mathbf{F}^\top$ and that the dependence on the velocity gradient is replaced by the symmetric stretching tensor $\mathbf{D} = (\mathbf{L} + \mathbf{L}^\top)/2$. Furthermore, isotropy requires that the dependence on \mathbf{B} appears through its principal scalar invariants $I_{\mathbf{B}} = \text{trace} \mathbf{B}$, $II_{\mathbf{B}} = \frac{1}{2}((\text{trace} \mathbf{B})^2 - \text{trace}(\mathbf{B}^2))$ and $III_{\mathbf{B}} = \det \mathbf{B}$.

Constitutive specification of the Helmholtz free energy

Having made arguments that constrain the general form of the constitutive description, we next specialize the forms to extend the phase field constitutive forms and to capture commonly used classical forms for the pure solid, liquid, and gas phases. Without regard to exothermic chemical reaction, we will assume that the Helmholtz free energy is composed of four parts, such that we can write

$$\psi = \psi_1 + \psi_2 + \psi_3 + \psi_4 . \quad (2.49)$$

The first two, ψ_1 and ψ_2 , are to be associated with the formulation of the phase transformations—the phase gradient energy density and the enthalpies associated with the phase transition. The latter, ψ_3 and ψ_4 are of classical origins—the thermal energy density and the strain energy density.

We assume that the Helmholtz free energy depends on $\vec{\nabla}\varphi$ only through ψ_1 and that the phase gradient energy density is specified with the explicit quadratic dependence

$$\psi_1 = \frac{1}{2}\gamma_\varphi |\vec{\nabla}\varphi|^2 . \quad (2.50)$$

It follows from (2.41) that the configurational force ξ is determined by the formula

$$\xi = \rho \frac{\partial \psi}{\partial \vec{\nabla}\varphi} = \rho \gamma_\varphi \vec{\nabla}\varphi . \quad (2.51)$$

The physical interpretation of the phase-configurational stress ξ is as a traction that acts near or in the phase transition region in the direction of the gradient of $\vec{\nabla}\varphi$, i.e. perpendicular to contours of constant φ .

Next we consider the contribution ψ_2 , the phase transition energy density that reflects enthalpy changes during phase transition, specified as

$$\psi_2 = \frac{1}{2}\Psi^{\text{well}}\mathcal{F}(\varphi) + \beta_m(\varphi)Q_m\left(\frac{T}{T_m} - 1\right) + \beta_v(\varphi)Q_v\left(\frac{T}{T_v} - 1\right) . \quad (2.52)$$

The constants $\Psi^{\text{well}} > 0$, $Q_m < 0$, and $Q_v < 0$ represent a potential well depth and the heats of

melting and vaporization. The constants $T_m > 0$ and $T_v > 0$ represent temperatures of melting and vaporization. The triple-well potential $\mathcal{F}(\varphi)$ can be described by a smooth positive definite function whose isolated zeroes are at $\varphi = 0, 1$, and 2 , representing three local minima. In addition, $\mathcal{F}(\varphi)$ is assumed to be locally quadratic near the zeroes at $\varphi = 0, 1$, and 2 , i.e. near $\varphi = 0$, $\mathcal{F} \sim \varphi^2$, near $\varphi = 1$, $\mathcal{F} \sim (\varphi - 1)^2$, and near $\varphi = 2$, $\mathcal{F} \sim (\varphi - 2)^2$. As an illustration, $\mathcal{F} = [\varphi(\varphi - 1)(\varphi - 2)]^2$ has this property. The function $\beta_m(\varphi)$ is assumed to be smooth and monotonically increasing and has values from 0 to 1 on the range $0 \leq \varphi \leq 1$ with zero derivative elsewhere. The function $\beta_v(\varphi)$ is similarly assumed to be monotonically increasing with values from 0 to 1 on the range $1 \leq \varphi \leq 2$. Note that the derivative of transition-energy density $\partial\psi_2/\partial\varphi$ generates source terms in both the energy and phase equations represented as

$$\frac{\partial\psi_2}{\partial\varphi} = \frac{1}{2}\Psi^{\text{well}}\frac{\partial\mathcal{F}}{\partial\varphi}(\varphi) + \beta'_m(\varphi)Q_m\left(\frac{T}{T_m} - 1\right) + \beta'_v(\varphi)Q_v\left(\frac{T}{T_v} - 1\right). \quad (2.53)$$

Figure 2.1 illustrates the assumed dependence of $\psi(\varphi, T)$ on φ and T . Starting from (a) through (d), temperature T is raised from below T_m to above T_v , representing a standard melting–evaporation process. The transition energy density in case (a) has its minimum at $\varphi = 0$. As T is increased through T_m and then T_v , we see a shift in the global minima from pure solid to solid–liquid and to liquid–vapor. As T eventually exceeds T_v as shown in (d), the energy minimizing well shifts to a vapor state at $\varphi = 2$. The coefficients and functions $\Psi^{\text{well}}, \beta_m, \beta_v$ can be adjusted (if needed) to reflect more accurately the physical properties observed in accordance with the phase transformation. Here we have chosen very simple forms.

We again assume the classical form for the thermal energy density and choose ψ_3 (which has the same form as ψ_1 in Section 2) to be

$$\psi_3 = c_v [(T - T_0) - T \ln(T/T_0)] \quad (2.54)$$

where c_v is the specific heat at constant deformation. This assumption is consistent with simple ideal models for solids, liquids and gases.

Finally we choose a form for ψ_4 , the strain energy density. We assume that it is composed

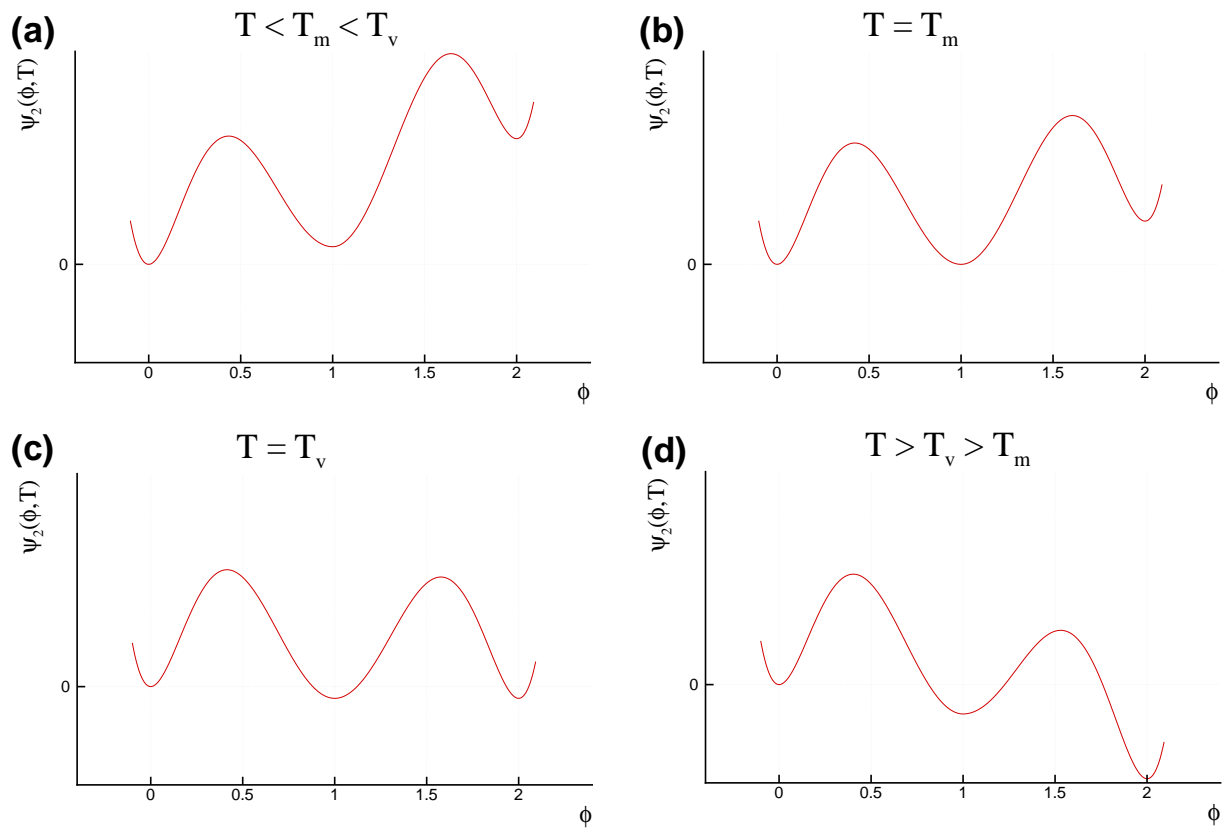


Figure 2.1: Plot of ψ_2 as a function of ϕ with T variation.

of three sub-parts. The first part is associated with the thermal expansion stresses commonly identified in the condensed phase

$$\psi_{4a} = -\frac{\alpha_c(\varphi)K}{2\rho_0}(T - T_0) \ln(\mathbb{I}\mathbb{I}\mathbb{I}_{\mathbf{B}}), \quad (2.55)$$

where K is the solid bulk modulus and α_c is the linear coefficient of thermal expansion. We again take $\alpha_c(\varphi)$ to be a smooth, non-zero function in the condensed phases, solid and liquid, and zero in the gas phase. For example, $\alpha_c(0) = \alpha_{\text{solid}}$, $\alpha_c(1) = \alpha_{\text{liquid}}$, and $\alpha_c(2) = 0$. The second part of ψ_4 is associated with the pressure commonly identified in an ideal gas that we encountered in the previous section on gaseous combustion:

$$\psi_{4b} = -\frac{1}{2}R_g(\varphi)T \ln(\mathbb{I}\mathbb{I}\mathbb{I}_{\mathbf{B}}). \quad (2.56)$$

Here $R_g(\varphi)$ plays the role of the ideal gas constant except that it is assumed to be non-zero in the gas phase and at or near zero in the solid and liquid condensed phases such that $R_g(0) = 0$, $R_g(1) = 0$, $R_g(2) = R_{\text{gas}}$.

The third part, ψ_{4c} , is based on properties of a compressible neo-Hookean, Blatz–Ko solid [25], which is given as

$$\psi_{\text{BK}} = \frac{\mu}{2\rho_0}(I_{\mathbf{B}} - 3) + \frac{\mu(1 - 2\nu)}{2\rho_0\nu} \left(\mathbb{I}\mathbb{I}\mathbb{I}_{\mathbf{B}}^{-\nu/(1-2\nu)} - 1 \right). \quad (2.57)$$

The constants ν and μ here represent the Poisson's ratio of the material and the elastic Lamé parameter μ . The contribution to the stress associated with this potential is

$$\boldsymbol{\sigma}_{\text{BK}} = 2\rho \frac{\partial \psi_{\text{BK}}}{\partial \mathbf{B}} \mathbf{B} = \mu \frac{\rho}{\rho_0} \mathbf{B} - \mu \frac{\rho}{\rho_0} \mathbb{I}\mathbb{I}\mathbb{I}_{\mathbf{B}}^{-\nu/(1-2\nu)} \mathbf{I}. \quad (2.58)$$

We use this to model the elastic deformation of the solid, but for the liquid we pose a slightly altered form of this potential based on purely isotropic deformations. Consider the isotropic (either uniform contraction or expansion) mapping given by $\mathbf{x} = s\mathbf{X}$, where s is the stretch ratio of material line segments. It follows simply that $\mathbf{F} = s\mathbf{I}$, $\mathbf{B} = s^2\mathbf{I}$, $\mathbb{I}\mathbb{I}\mathbb{I}_{\mathbf{B}} = \det(\mathbf{B}) = (\rho_0/\rho)^2 = s^6$, $s = (\rho_0/\rho)^{1/3}$, $\mathbf{B} = (\rho_0/\rho)^{1/3}\mathbf{I}$, and $(\rho_0/\rho)^{1/3} = \mathbb{I}\mathbb{I}\mathbb{I}_{\mathbf{B}}^{1/6}$. For the Blatz–Ko solid, the isotropic stress

is related to the volume ratio by

$$\boldsymbol{\sigma} = -\mu \frac{\rho}{\rho_0} \left[\left(\frac{\rho}{\rho_0} \right)^{-\frac{2\nu}{1-2\nu}} - \left(\frac{\rho}{\rho_0} \right)^{-\frac{1}{3}} \right] \mathbf{I}. \quad (2.59)$$

We choose our model for the strain energy of the liquid to have the same functional form for the isotropic stress dependence on the density ratio as that for the solid, and merely note that we can replace the dependence on ρ_0/ρ by $\text{III}_{\mathbf{B}}^{1/2}$ and work backwards. The corresponding Helmholtz free energy for the liquid would take the form

$$\psi_{\text{BK(liquid)}} = \frac{3}{2} \frac{\mu}{\rho_0} \text{III}_{\mathbf{B}}^{1/3} + \frac{\mu(1-2\nu)}{2\rho_0\nu} \left(\text{III}_{\mathbf{B}}^{-\nu/(1-2\nu)} - 1 \right). \quad (2.60)$$

We can combine the two potentials for the solid and the liquid in the following way. Let $\mu_s(\varphi)$ be a coefficient such that $\mu_s(0) = \mu_{\text{solid}}$ and is zero for $\varphi \geq 1$. Let $\mu_l(\varphi)$ be a smooth function such that $\mu_l(1) = \mu_{\text{liquid}}$ with $\mu_l(0) = \mu_l(2) = 0$. One makes similar definitions for ν_s and ν_l . Let μ_c be defined as the sum $\mu_c = \mu_l + \mu_s$, and $\nu_c = \nu_l + \nu_s$. Then the combined solid, liquid elastic potential can be written as

$$\psi_{4c} = \frac{\mu_s}{2\rho_0} (I_{\mathbf{B}} - 3) + \frac{3}{2} \frac{\mu_l}{\rho_0} \text{III}_{\mathbf{B}}^{1/3} + \frac{\mu_c(1-2\nu_c)}{2\rho_0\nu_c} \left(\text{III}_{\mathbf{B}}^{-\nu_c/(1-2\nu_c)} - 1 \right). \quad (2.61)$$

Note that other functional forms for the strain energy density could have been chosen for ψ_{4c} , but we chose the Blatz–Ko form since it has a simple reduction to compressible linear elasticity in the limit of small strain, which is deemed convenient for our purposes. We anticipate that as the solid become significantly nonlinearly elastic, a phase transformation will occur, so that the specific choice of the Blatz–Ko form is not a sensitive one for the properties of the model. The deformational portion of stress associated with this strain energy is

$$\boldsymbol{\sigma}^{\text{def}} \equiv 2\rho \frac{\partial \psi_{4c}}{\partial \mathbf{B}} \mathbf{B} = \mu_s \frac{\rho}{\rho_0} \mathbf{B} - \mu_c \frac{\rho}{\rho_0} \text{III}_{\mathbf{B}}^{-\nu_s/(1-2\nu_s)} \mathbf{I} + \mu_l \frac{\rho}{\rho_0} \text{III}_{\mathbf{B}}^{1/3} \mathbf{I}. \quad (2.62)$$

2.3.2 Total free-energy density and summary of constitutive forms

The form of $\psi = \psi_1 + \psi_2 + \psi_3 + \psi_{4a} + \psi_{4b} + \psi_{4c}$ is written as

$$\begin{aligned}
\psi = & \frac{\mu_s(\varphi)}{2\rho_0}(I_B - 3) + \frac{\mu_c(\varphi)(1 - 2\nu_s)}{2\rho_0\nu_s} \left(\text{III}_B^{-\nu_s/(1-2\nu_s)} - 1 \right) & + \frac{3\mu_l(\varphi)}{2\rho_o} \text{III}_B^{1/3} \\
& - \frac{\alpha_c(\varphi)K}{2\rho_0}(T - T_0) \ln(\text{III}_B) - \frac{1}{2}R_g(\varphi)T \ln(\text{III}_B) & \text{Strain energy density} \\
& - c_v(\varphi) [T \ln(T/T_0) - (T - T_0)] & \text{Thermal energy density} \\
& + \frac{1}{2}\Psi^{\text{well}}\mathcal{F}(\varphi) + \beta_m(\varphi) \left(\frac{T}{T_m} - 1 \right) Q_m + \beta_v(\varphi) \left(\frac{T}{T_v} - 1 \right) Q_v & \text{Phase transition energy density} \\
& + \frac{1}{2}\gamma_\varphi |\vec{\nabla}\varphi|^2. & \text{Gradient energy density}
\end{aligned} \tag{2.63}$$

The constitutive theory is essentially complete. The stress is given by the general expression

$$\boldsymbol{\sigma} = \rho \frac{\partial \psi}{\partial \mathbf{B}} \mathbf{B} - \vec{\nabla}\varphi \otimes \boldsymbol{\xi} + \boldsymbol{\sigma}^{\text{diss}} \tag{2.64}$$

with $\boldsymbol{\xi}$ given by $\boldsymbol{\xi} = \rho\gamma_\varphi \vec{\nabla}\varphi$ and $\boldsymbol{\sigma}^{\text{diss}}$ given by $\boldsymbol{\sigma}^{\text{diss}} = \mu_f(\vec{\nabla} \cdot \mathbf{v})\mathbf{I} + 2\mu_f\mathbf{D}$. The stress formula becomes

$$\begin{aligned}
\boldsymbol{\sigma} = & \mu_s \frac{\rho}{\rho_0} \mathbf{B} - \mu_c \frac{\rho}{\rho_0} \text{III}_B^{-(\nu_s/1-2\nu_s)} \mathbf{I} + \mu_l \frac{\rho}{\rho_o} \text{III}_B^{1/3} \mathbf{I} \\
& - \alpha_c(\varphi)K \frac{\rho}{\rho_0}(T - T_0)\mathbf{I} - \rho R_g(\varphi)T \mathbf{I} \\
& - \rho\gamma_\varphi \vec{\nabla}\varphi \otimes \vec{\nabla}\varphi + \nu_f(\vec{\nabla} \cdot \mathbf{v})\mathbf{I} + 2\mu_f\mathbf{D}.
\end{aligned} \tag{2.65}$$

The energy flux vector remains $\mathbf{q} = -k\vec{\nabla}T$. The various source terms in the energy equation and the phase equation can be computed from the forms given in (2.63).

We can now summarize the governing equations for the phase change model as

$$\dot{\rho} + \rho \vec{\nabla} \cdot \mathbf{v} = 0, \quad (2.66)$$

$$\rho \dot{\mathbf{v}} = \vec{\nabla} \cdot \boldsymbol{\sigma} + \rho \mathbf{f}, \quad (2.67)$$

$$\begin{aligned} \rho c_v \dot{T} = & \vec{\nabla} \cdot (k \vec{\nabla} T) + \boldsymbol{\sigma}^{\text{diss}} : \vec{\nabla} \mathbf{v} + B \dot{\varphi}^2 + \rho T \frac{\partial^2 \psi}{\partial T \partial \mathbf{F}} \mathbf{F}^\top : \vec{\nabla} \mathbf{v} + \\ & \rho T \frac{\partial^2 \psi}{\partial T \partial \varphi} \dot{\varphi} + \rho T \frac{\partial^2 \psi}{\partial T \partial \vec{\nabla} \varphi} \cdot \frac{\dot{\vec{\nabla}}}{\vec{\nabla}} \varphi + \rho r, \end{aligned} \quad (2.68)$$

$$B \dot{\varphi} = \vec{\nabla} \cdot (\rho \gamma_\varphi \vec{\nabla} \varphi) - \rho \frac{\partial \psi}{\partial \varphi}, \quad (2.69)$$

$$\dot{\mathbf{F}} = \mathbf{L} \mathbf{F} \quad (2.70)$$

where $B, c_v, \gamma_\varphi, k$, etc. are constitutive scalars that could be regarded as functions of both φ and T . We have added the kinematic identity (2.70) in order to compute the evolution of the displacement gradients.

2.4 The combined model: Modifications to include chemical reaction

Here we list the modifications required to combine both models into one. First we take the phase change model as the starting point and we retain all the assumptions and assumed forms of the previous section, specifically in regards to the appearance of φ . The configurational force balance (2.31) is retained as a fundamental balance law (the consequence of which leads to the derivation of the evolution equation for φ , equation (2.69)).

Next we assume that in addition to φ , which measures the molecular order of the phase, the mass fraction λ simultaneously measures the amount of exothermic chemical reaction that has taken place. So λ is added to all the argument lists; in particular in the expression for ψ we assume the dependence

$$\psi = \psi(\mathbf{F}, T, \varphi, \lambda, \vec{\nabla} \varphi, \mathbf{L}). \quad (2.71)$$

A statement of conservation of λ is added in the form of (2.7), which reflects a molecularly based

conservation of species. The second law must be modified to include the entropy flux associated with the heat of combustion (so it takes the same form as (2.8)):

$$\rho \dot{\eta} \geq -\vec{\nabla} \cdot \left(\frac{\mathbf{q}}{T} \right) + \vec{\nabla} \cdot \left(\frac{Q_{\text{hc}} \mathbf{s}}{T} \right) + \frac{\rho r}{T}. \quad (2.72)$$

One argues the entropy inequality in exactly the same manner as in the previous section, with the same assumptions and conclusions of Section 3, with the additional exception that one uses the evolution equation for λ , (2.7), to reduce the dissipation inequality in the manner explained in Section 2. The energy flux vector is identified by the requirement of positivity of the left-hand side of (2.18), which leads to

$$\mathbf{q} = -k \vec{\nabla} T + Q_{\text{hc}} \mathbf{s}. \quad (2.73)$$

The vector \mathbf{s} can be chosen according to Fick's law such that

$$\mathbf{s} = d \vec{\nabla} \lambda. \quad (2.74)$$

The Helmholtz free energy is designated as $\psi = \psi_1 + \psi_2 + \psi_3 + \psi_{4a} + \psi_{4b} + \psi_{4c} + \psi_5$, where ψ_{1-4c} are defined in the previous section and ψ_5 is the chemical enthalpy $\psi_5 = -Q_{\text{hc}} \lambda$. The configurational stress is again of the form $\boldsymbol{\xi} = \rho \gamma_\varphi \vec{\nabla} \varphi$. The representation of the stress is

$$\begin{aligned} \boldsymbol{\sigma} = & \mu_s \frac{\rho}{\rho_0} \mathbf{B} - \mu_c \frac{\rho}{\rho_0} \text{III}_{\mathbf{B}}^{-(\nu_s/(1-2\nu_s))} \mathbf{I} + \mu_l \frac{\rho}{\rho_0} \text{III}_{\mathbf{B}}^{1/3} \mathbf{I} \\ & - \alpha_c(\varphi) K \frac{\rho}{\rho_0} (T - T_0) \mathbf{I} - \rho R_g(\varphi) T \mathbf{I} \\ & - \rho \gamma_\varphi \vec{\nabla} \varphi \otimes \vec{\nabla} \varphi + \nu_f (\vec{\nabla} \cdot \mathbf{v}) \mathbf{I} + 2\mu_f \mathbf{D}. \end{aligned} \quad (2.75)$$

The various scalar material properties identified previously, such as c_v and γ_φ , now can also have explicit dependence on λ as well as φ and T .

A revised list of the governing equations for combined model with reaction and phase change is

$$\dot{\rho} + \rho \vec{\nabla} \cdot \mathbf{v} = 0, \quad (2.76)$$

$$\rho \dot{\mathbf{v}} = \vec{\nabla} \cdot \boldsymbol{\sigma} + \rho \mathbf{f}, \quad (2.77)$$

$$\begin{aligned} \rho c_v \dot{T} &= \vec{\nabla} \cdot (k \vec{\nabla} T) + \boldsymbol{\sigma}^{\text{diss}} : \vec{\nabla} \mathbf{v} + B \dot{\varphi}^2 + \rho T \frac{\partial^2 \psi}{\partial T \partial \mathbf{F}} \mathbf{F}^\top : \vec{\nabla} \mathbf{v} \\ &+ \rho T \frac{\partial^2 \psi}{\partial T \partial \varphi} \dot{\varphi} + \rho T \frac{\partial^2 \psi}{\partial T \partial \vec{\nabla} \varphi} \cdot \vec{\nabla} \dot{\varphi} + \rho Q_{\text{hc}} \Omega + \rho r, \end{aligned} \quad (2.78)$$

$$B \dot{\varphi} = \vec{\nabla} \cdot (\rho \gamma_\varphi \vec{\nabla} \varphi) - \rho \frac{\partial \psi}{\partial \varphi}, \quad (2.79)$$

$$\rho \dot{\lambda} = \vec{\nabla} \cdot (d \vec{\nabla} \lambda) + \rho \Omega, \quad (2.80)$$

$$\dot{\mathbf{F}} = \mathbf{L} \mathbf{F}. \quad (2.81)$$

With the specific constitutive forms chosen for ψ the energy equation becomes

$$\begin{aligned} \rho c_v \dot{T} &= \vec{\nabla} \cdot (k \vec{\nabla} T) + \nu_f (\vec{\nabla} \cdot \mathbf{v})^2 + 2\mu_f \mathbf{D} : \mathbf{D} + B \dot{\varphi}^2 - \alpha_c(\varphi) K \frac{\rho}{\rho_0} T (\vec{\nabla} \cdot \mathbf{v}) - \rho R_g(\varphi) T (\vec{\nabla} \cdot \mathbf{v}) \\ &+ \left\{ -\frac{\alpha'_c(\varphi)}{2} K \frac{\rho}{\rho_0} T \ln(\text{III}_B) - \rho \frac{R'_g(\varphi)}{2} T \ln(\text{III}_B) - \rho c'_v(\varphi) T \ln(T/T_0) \right. \\ &\quad \left. + \rho \left[\beta'_m(\varphi) \frac{T}{T_m} Q_m + \beta'_v(\varphi) \frac{T}{T_v} Q_v \right] \right\} \dot{\varphi} + \rho Q_{\text{hc}} \Omega + \rho r, \end{aligned} \quad (2.82)$$

and the evolution law for φ becomes

$$\begin{aligned} B \dot{\varphi} &= \vec{\nabla} \cdot (\rho \gamma_\varphi \vec{\nabla} \varphi) + \rho c'_v(\varphi) [T \ln(T/T_0) - (T - T_0)] \\ &- \frac{\mu'_s(\varphi)}{2} \frac{\rho}{\rho_0} (I_B - 3) - \frac{\mu'_c(\varphi)}{2} \frac{\rho}{\rho_0} \frac{(1 - 2\nu_s)}{\nu_s} \left(\text{III}_B^{-\nu_s/(1-2\nu_s)} - 1 \right) + \frac{3\mu'_l(\varphi)}{2} \frac{\rho}{\rho_o} \text{III}_B^{1/3} \\ &+ \frac{\alpha'_c(\varphi)}{2} K \frac{\rho}{\rho_0} (T - T_0) \ln(\text{III}_B) + \frac{1}{2} \rho R'_g(\varphi) T \ln(\text{III}_B) \\ &- \rho \frac{1}{2} \Psi^{\text{well}} \frac{\partial \mathcal{F}}{\partial \varphi} - \rho \left[\beta'_m(\varphi) \left(\frac{T}{T_m} - 1 \right) Q_m + \beta'_v(\varphi) \left(\frac{T}{T_v} - 1 \right) Q_v \right]. \end{aligned} \quad (2.83)$$

2.4.1 Material transition functions

An important ingredient of our model is the use of φ -dependent material properties, or material transition functions. Earlier in Section 2.4.2, we encountered $\beta_m(\varphi), \beta_v(\varphi)$ in the specification of the phase transition energy density, $\mu_c(\varphi), \mu_l(\varphi), \mu_s(\varphi), \alpha_c(\varphi), R_g(\varphi)$ in the specification of the

strain energy density, $c_v(\varphi)$ in the specification of the thermal energy density as well as functions associated with dissipative processes like $\nu_f(\varphi)$. The model assumes that these functions have limiting pure-phase values when $\varphi = 0, 1, 2$. The structure of these functions has an influence on the exact details of the spatial structure of the transition layers and their dynamics when particular problems are solved. However one makes an implicit assumption that when the transitions occur in thin layers relative to other geometric lengths the structure within the layer does not strongly influence the information transmitted across the layer. This modeling precept is consistent with the use of viscous dissipation to describe continuum shock structure when the shock is molecularly thin.

For illustration sake, Figure 2.2 and 2.3 show typical transition functions that we have used to carry out representative simulations discussed in [81]. These functions are constructed from simple polynomials in φ and their smooth extensions. The figures clearly show the basic properties that are required. For example, in Fig. 2.2c, the representation of the thermal expansion parameter $\alpha_c(\varphi)$ which has the same (constant) value in the solid and liquid phase is zero in the gas phase. Another example is that $\beta'_m(\varphi)$ is zero for all values of φ except those between 0 and 1, and terms that multiply $\beta'_m(\varphi)$ are only involved in solid to liquid transition of melting or freezing, and are totally absent in the liquid gas transition of evaporation and condensation.

2.5 Some limiting cases

2.5.1 Pure phases

The results for pure phase can be identified by the constitutive forms for the stress tensor. First we will consider the solid, $\varphi = 0$ in the additional limit of small strain. The small strain limit is represented in terms of the displacement gradient $\mathbf{H} = \mathbf{F} - \mathbf{I}$, where $|\mathbf{H}| \ll 1$. Define the small strain tensor $\mathbf{E} = (\mathbf{H} + \mathbf{H}^\top)/2$ and the left Cauchy–Green tensor can be written as $\mathbf{B} = \mathbf{F}\mathbf{F}^\top = \mathbf{I} + 2\mathbf{E} + \mathbf{H}\mathbf{H}^\top$. Our limiting form for the stress relation reduces to

$$\boldsymbol{\sigma} = -\alpha_{\text{solid}} \frac{\rho}{\rho_0} K(T - T_0) \mathbf{I} + \frac{2\mu_{\text{solid}} \nu_{\text{solid}}}{1 - 2\nu_{\text{solid}}} I_{\mathbf{E}} \mathbf{I} + 2\mu_{\text{solid}} \mathbf{E}, \quad (2.84)$$

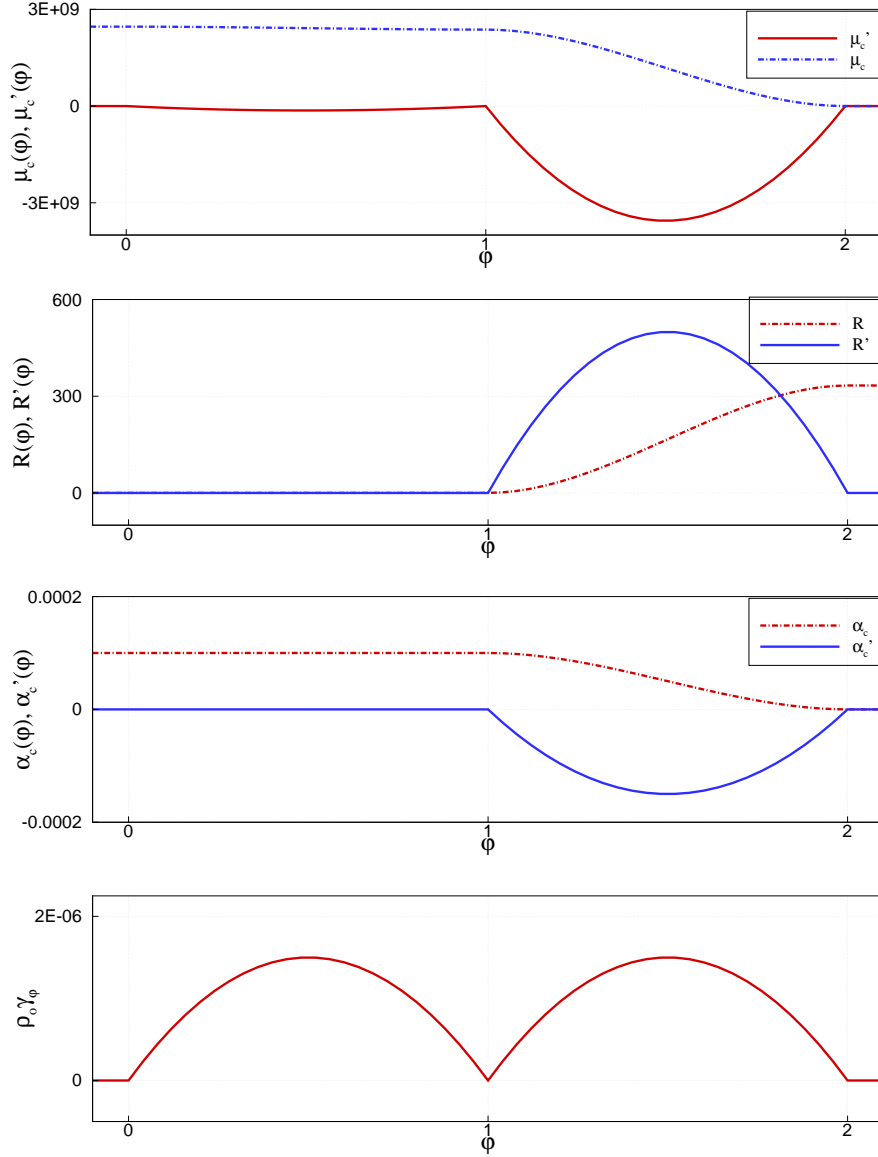


Figure 2.2: Plots of transfer functions for HMX simulation and their derivatives with respect to phase variable. Shear modulus, ideal gas constant, thermal expansion coefficient, and phase diffusion coefficient are shown from top to bottom.

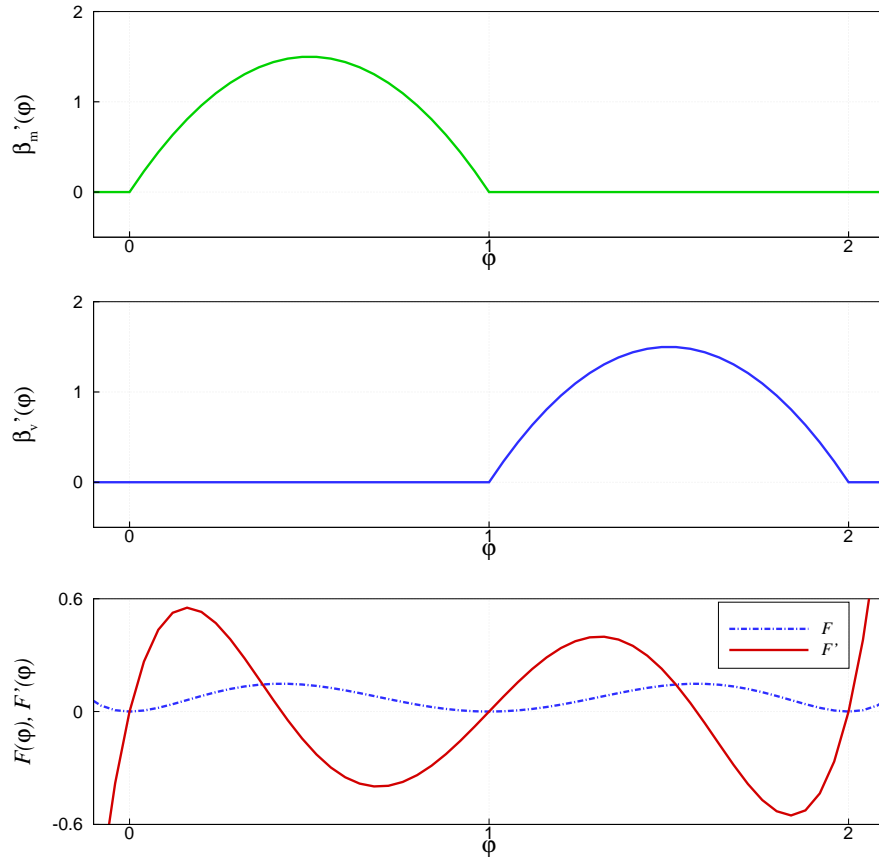


Figure 2.3: ϕ -dependent transfer functions (derivatives) for heat of phase transformation, β'_m and β'_v . Third figure depicts the triple-well Ginzburg–Landau potential function and its derivative.

When one considers the limit of a liquid, $\varphi = 1$, the expression for the stress becomes

$$\begin{aligned} \boldsymbol{\sigma} = & -\alpha_{\text{liquid}} K \frac{\rho}{\rho_0} (T - T_0) \mathbf{I} - \mu_{\text{liquid}} \frac{\rho}{\rho_0} \left(\left(\frac{\rho}{\rho_0} \right)^{2\nu_{\text{liquid}}/(1-2\nu_{\text{liquid}})} - \left(\frac{\rho}{\rho_0} \right)^{1/3} \right) \mathbf{I} \\ & + \nu_{\text{liquid}} (\vec{\nabla} \cdot \mathbf{v}) \mathbf{I} + 2\mu_{\text{liquid}} \mathbf{D}, \end{aligned} \quad (2.85)$$

similarly for the limit of the gas, $\varphi = 2$ one obtains the expression for the stress becomes

$$\boldsymbol{\sigma} = -\rho R_{\text{gas}} T \mathbf{I} + \nu_{\text{gas}} (\vec{\nabla} \cdot \mathbf{v}) \mathbf{I} + 2\mu_{\text{gas}} \mathbf{D}. \quad (2.86)$$

2.5.2 Motionless phase transition

In this case we simply assume that the system is nearly motionless with $\mathbf{v} \approx 0$ and consider the pure phase-change from solid to liquid with no chemical reaction. In addition, we neglect thermal expansion configurational forces, consistent with a nearly zero velocity field and the thermal dissipation associated with the phase transition. Further we assume that φ is in the range $0 \leq \varphi \leq 1$ and $\mathcal{F}(\varphi)$ is effectively a double-well potential. We take the specific heat to be constant and are left with a thermal-diffusional model for the temperature and phase-field given by the equations

$$\rho c_v \dot{T} = \vec{\nabla} \cdot (k \vec{\nabla} T) + \rho \beta'_m(\varphi) \frac{T}{T_m} Q_m \dot{\varphi}, \quad (2.87)$$

and

$$B \dot{\varphi} = \vec{\nabla} \cdot (\rho \gamma_\varphi \vec{\nabla} \varphi) - \rho \frac{1}{2} \Psi^{\text{well}} \frac{\partial \mathcal{F}}{\partial \varphi} - \rho \beta'_m(\varphi) \left(\frac{T}{T_m} - 1 \right) Q_m. \quad (2.88)$$

These equations are a generalized form of a thermally-dependent Ginzburg–Landau theory of phase transitions often cited in discussions of solidification of binary alloys (see Wright et al, for example [73].) Simple systems of this form, with a double-well potential and a single latent heat term, have been analyzed in the literature have been shown to correspond to various forms of the classical (sharp interface) description of phase transitions. Further analysis leads to modified Stefan problems that incorporate surface tension and kinetic undercooling, [15].

2.5.3 Relation to the simpler theory of quasi-static phase transformation

Here we briefly discuss the manner in which our model relates to the theory of quasi-static phase transformations that is part of classical equilibrium thermodynamics. We assume that the changes in the state in the material happen so slowly that all inertial effects can be neglected and that the material only undergoes isotropic volume changes that are measured by changes in the density. The stress is spherical so that $\boldsymbol{\sigma} = -p\mathbf{I}$. The deformation is homogeneous such that $\mathbf{x} = s\mathbf{X}$, with $\mathbf{F} = s\mathbf{I}$, $\det(\mathbf{F}) = s = (\rho_0/\rho)$, $\mathbf{B} = (\rho_0/\rho)^2\mathbf{I}$, and strain invariants $\text{III}_{\mathbf{B}} = (\rho_0/\rho)^2$ and $I_{\mathbf{B}} - 3 = 3[(\rho_0/\rho)^2 - 1]$. One neglects all spatial gradients.

Next we consider the volume changes that occur as the temperature rises when the material is subjected to constant volumetric heating (given by constant r), under isobaric (constant pressure) conditions. For simplicity, we will also assume that the specific heat is constant in all phases. Then the change in the thermodynamic states would be controlled by a simplified version of the energy equation (for the temperature) and the phase evolution equation. These are written as

$$\rho c_v \frac{\partial T}{\partial t} = \rho \left(\beta'_m(\varphi) \frac{T}{T_m} Q_m + \beta'_v(\varphi) \frac{T}{T_v} Q_v \right) \frac{\partial \varphi}{\partial t} + \rho r, \quad (2.89)$$

$$B \frac{\partial \varphi}{\partial t} = -\rho \frac{1}{2} \Psi^{\text{well}} \frac{\partial \mathcal{F}}{\partial \varphi} - \rho \left[\beta'_m(\varphi) \frac{T - T_m}{T_m} Q_m + \beta'_v(\varphi) \frac{T - T_v}{T_v} Q_v \right], \quad (2.90)$$

and for the purpose of illustration, (2.75) is simplified by linearizing ρ about ρ_0 in the solid and liquid phases to obtain the thermal equation of state, a relation between p, ρ, T and φ

$$p = \frac{6\mu_c(\varphi)\nu_s}{1-2\nu_s} \left(\frac{\rho}{\rho_0} - 1 \right) + \alpha_c K \frac{\rho}{\rho_0} (T - T_0) - \rho R_g T. \quad (2.91)$$

The above equations are solved subject to the initial condition that the material is initially solid and at the reference temperature, $\varphi(0) = 0$ and $T(0) = T_0$. For constant pressure, a specified temperature and φ , equation (2.91) determines the specific volume, $V = 1/\rho$. The solution of the initial value problem for T and φ determines a trajectory in T, V, φ -space at fixed p . A typical solution shows that as the temperature rises in the solid, the volume increases along the isobar. A phase transition (change in φ) does not take place till the temperature nears the melting temperature, T_m .

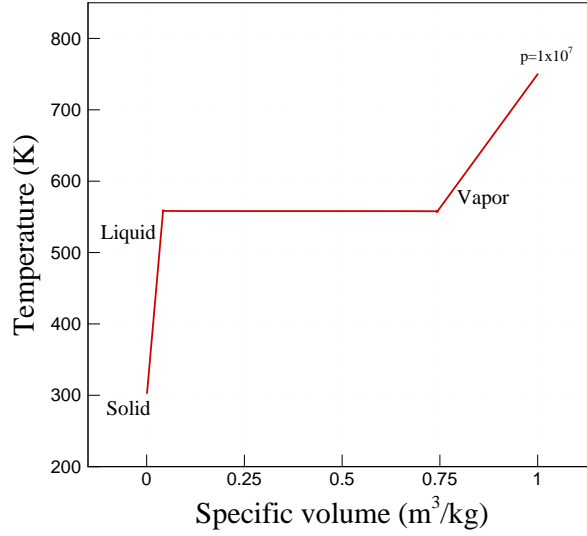


Figure 2.4: T - v trajectory on an isobar ($p = 10^7$ Pa) under the quasi-static assumptions. The large volume jump from liquid to gas happens at nearly constant temperature T_v .

Above that temperature local analysis shows that a change in stability of the state $\varphi = 0$ occurs and then the transition from $\varphi = 0$ to $\varphi = 1$ occurs. Since the volumetric change is small (4 % or less) the deviation in a T, v isobar is not large in some sense. As the temperature continues to rise then the second phase transition occurs near the vaporization temperature T_v . Since the thermal equation of state is effectively modeled by the ideal gas law, a rather large change in the specific volume occurs. Finally after the phase transition to vapor is completed and $\varphi = 2$ is reached, the temperature continues to climb on the gas-phase isobar with increasing volume. Figure 5.1 show plots of a T, V -trajectory for a isobaric phase transition for the HMX-like material described in Chapter 3. Figure 5.2 shows the corresponding φ, V - trajectory at different pressures. Again the purpose here is simply to illustrate that conventional notions of quasi-static phase transformations described in classical thermodynamics are embedded in this model.

2.6 Special forms of the model for three simple motions

In this concluding section we write out special and exact forms of the differential equations for the model when the material undergoes three simple motions, i) evolution at constant volume,

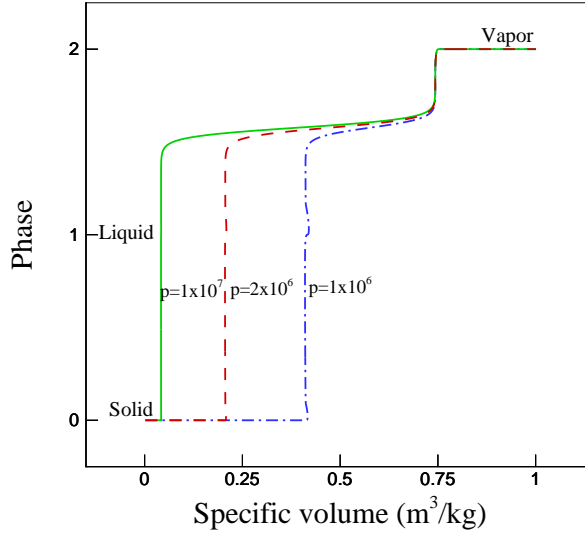


Figure 2.5: Phase– V trajectory of constant pressure under the thermo-quasistatic assumption.

ii) one-dimensional, time-dependent, longitudinal motion and iii) one-dimensional, time-dependent shear motion. All three are very important in the analysis of ignition of energetic materials. The three cases are the exclusive subject of Chapter 3, where numerical simulation and the properties of the model are discussed further.

2.6.1 Constant volume evolution and thermal explosion

A simple but extremely important sub-case that is studied extensively in combustion theory describes the constant volume thermal explosion, where the velocity \mathbf{v} and all spatial gradients are exactly zero. The density is constant hence the volume of a material particle is constant. For illustration, we neglect thermal expansion, and assume constant specific heat and gas constant. We are left with three ordinary differential equations in time for the temperature, phase-change and reaction progress,

$$\rho c_v \frac{\partial T}{\partial t} = \rho \left(\beta'_m(\varphi) \frac{T}{T_m} Q_m + \beta'_v(\varphi) \frac{T}{T_v} Q_v \right) \frac{\partial \varphi}{\partial t} + \rho Q_{\text{hc}} \Omega + \rho r, \quad (2.92)$$

$$B \frac{\partial \varphi}{\partial t} = -\rho \frac{1}{2} \Psi^{\text{well}} \frac{\partial \mathcal{F}}{\partial \varphi} - \rho \left[\beta'_m(\varphi) \frac{T - T_m}{T_m} Q_m + \beta'_v(\varphi) \frac{T - T_v}{T_v} Q_v \right], \quad (2.93)$$

$$\frac{\partial \lambda}{\partial t} = \Omega. \quad (2.94)$$

If one discards phase change we recover the equations from standard combustion theory for constant volume thermal explosion, $c_v(\partial T/\partial t) = Q_{\text{hc}} \Omega$, $(\partial \lambda/\partial t) = \Omega$. Of course, the more interesting behavior occurs when phase change is included. The typical dynamics of these ordinary differential equations are discussed at length in Chapter 3.

2.6.2 Longitudinal motion

Next we turn to specializations of the equations to simplified motions that lead to PDEs in one space dimension and one time dimension, particularly suited to the study of ignition phenomena in energetic materials (which is one of our main concerns). First we consider longitudinal compression associated with a flyer-plate impact test. In this idealization, an infinite slab experiences a displacement loading normal to its surface. Specifically we consider the following one-dimensional motion

$$x_1 = X_1 + f_1(X_1, t), \quad x_2 = X_2, \quad x_3 = X_3, \quad (2.95)$$

where f_1 is the 1 displacement.

For this motion, there is one nonzero velocity component, $v_1 = \partial f_1/\partial t|_{\mathbf{X}}(X_1, t)$, and \mathbf{F} is diagonal with $F_{11} = \partial x_1/\partial X_1 = 1 + f'_1$, and $F_{22} = F_{33} = 1$. The density is related to the single strain gradient by $1 + f'_1 = \rho_0/\rho$. Also \mathbf{B} is diagonal with $B_{11} = (1 + f'_1)^2$, $B_{22} = 1$, $B_{33} = 1$. The first and third invariants of \mathbf{B} are $I_{\mathbf{B}} = 2 + (1 + f'_1)^2$ and $III_{\mathbf{B}} = (1 + f'_1)^2$, with $III_{\mathbf{B}} = (\rho_0/\rho)^2$ and $I_{\mathbf{B}} - 3 = (\rho_0/\rho)^2 - 1$. Hence we use the density as the independent strain measure and replace f'_1 . The one nonzero component of the velocity gradient and rate of strain tensor are respectively, $L_{11} = D_{11} = \partial v_1/\partial x_1$. Also $(\vec{\nabla} \varphi \otimes \vec{\nabla} \varphi)_{11} = (\partial \varphi/\partial x_1)^2$. It then follows that all the shear stresses

are zero, $\sigma_{12} = \sigma_{23} = \sigma_{13} = 0$, and the normal stresses σ_{11} is given by

$$\begin{aligned} \sigma_{11} = -\mu_c \left(\frac{\rho}{\rho_0} \right) \left[\left(\frac{\rho}{\rho_0} \right)^{\frac{2\nu_s}{1-2\nu_s}} - \left(\frac{\rho}{\rho_0} \right)^{-2} \right] - \alpha_c K \frac{\rho}{\rho_0} (T - T_0) \\ - \rho R_g T - \rho \gamma_\varphi \left(\frac{\partial \varphi}{\partial x_1} \right)^2 + (\nu_f + 2\mu_f) \frac{\partial v_1}{\partial x_1}. \end{aligned} \quad (2.96)$$

The other normal stress are the same as the σ_{11} stress, minus the phase stress, i.e. $\sigma_{22} = \sigma_{33} = \sigma_{11} + \rho \gamma_\varphi (\partial \varphi / \partial x_1)^2$.

The specific governing equations for longitudinal compression are the mass and momentum equations

$$\frac{\partial \rho}{\partial t} + v_1 \frac{\partial \rho}{\partial x_1} + \rho \frac{\partial v_1}{\partial x_1} = 0, \quad (2.97)$$

$$\begin{aligned} \rho \left(\frac{\partial v_1}{\partial t} + v_1 \frac{\partial v_1}{\partial x_1} \right) = \frac{\partial}{\partial x_1} \left\{ -\mu_c \left(\frac{\rho}{\rho_0} \right) \left[\left(\frac{\rho}{\rho_0} \right)^{\frac{2\nu_s}{1-2\nu_s}} - \left(\frac{\rho}{\rho_0} \right)^{-2} \right] \right. \\ \left. - \alpha_c K \frac{\rho}{\rho_0} (T - T_0) - \rho R_g T - \rho \gamma_\varphi \left(\frac{\partial \varphi}{\partial x_1} \right)^2 + (\nu_f + 2\mu_f) \frac{\partial v_1}{\partial x_1} \right\} \end{aligned} \quad (2.98)$$

and the energy balance, phase evolution, and reaction progress evolution equations, which take the specific forms

$$\begin{aligned} \rho c_v \left(\frac{\partial T}{\partial t} + v_1 \frac{\partial T}{\partial x_1} \right) = \frac{\partial}{\partial x_1} \left(k \frac{\partial T}{\partial x_1} \right) + (\nu_f + 2\mu_f) \left(\frac{\partial v_1}{\partial x_1} \right)^2 + B \dot{\varphi}^2 - \left[\alpha_c K \frac{\rho}{\rho_0} T + \rho R_g(\varphi) T \right] \frac{\partial v_1}{\partial x_1} \\ + \left\{ -\frac{1}{2} \alpha'_c(\varphi) K \frac{\rho}{\rho_0} T \ln(\mathcal{I}\mathcal{I}\mathcal{I}_B) - \frac{1}{2} \rho R'_g(\varphi) T \ln(\mathcal{I}\mathcal{I}\mathcal{I}_B) - \rho c'_v(\varphi) T \ln(T/T_0) \right. \\ \left. + \rho \left[\beta'_m(\varphi) \frac{T}{T_m} Q_m + \beta'_v(\varphi) \frac{T}{T_v} Q_v \right] \right\} \dot{\varphi} + \rho Q_{\text{hc}} \Omega + \rho r, \end{aligned} \quad (2.99)$$

$$\begin{aligned}
B \left(\frac{\partial \varphi}{\partial t} + v_1 \frac{\partial \varphi}{\partial x_1} \right) &= \frac{\partial}{\partial x_1} \left(\rho \gamma_\varphi \frac{\partial \varphi}{\partial x_1} \right) + \rho c'_v(\varphi) [T \ln(T/T_0) - (T - T_0)] \\
&\quad - \frac{\mu'_s(\varphi)}{2} \frac{\rho}{\rho_0} (I_B - 3) - \frac{\mu'_c(\varphi)}{2} \frac{\rho}{\rho_0} \frac{(1 - 2\nu_s)}{\nu_s} \left(\text{III}_B^{-\nu_s/(1-2\nu_s)} - 1 \right) - \frac{3\mu'_l(\varphi)}{2} \frac{\rho}{\rho_o} \text{III}_B^{1/3} \\
&\quad + \frac{\alpha'_c(\varphi)}{2} K \frac{\rho}{\rho_0} (T - T_0) \ln(\text{III}_B) + \frac{1}{2} \rho R'_g(\varphi) T \ln(\text{III}_B) \\
&\quad - \frac{1}{2} \rho \Psi^{\text{well}} \frac{\partial \mathcal{F}}{\partial \varphi} - \rho \left[\beta'_m(\varphi) \frac{T - T_m}{T_m} Q_m + \beta'_v(\varphi) \frac{T - T_v}{T_v} Q_v \right], \quad (2.100)
\end{aligned}$$

and

$$\rho \left(\frac{\partial \lambda}{\partial t} + v_1 \frac{\partial \lambda}{\partial x_1} \right) = \frac{\partial}{\partial x_1} \left(d \frac{\partial \lambda}{\partial x_1} \right) + \rho \Omega. \quad (2.101)$$

2.6.3 Shear motion

Now we turn to specialization of the equations to shear motion, which again leads to PDEs in one space dimension, transverse to the motion and one time dimension. A nominal geometry is a slab of fixed thickness loaded one surface with constant velocity, while the other is fixed. The bottom surface is taken to be fixed (zero displacement) for the entire duration of the test. Specifically we consider the following one-dimensional motion

$$x_1 = X_1 + f_1(X_2, t), \quad x_2 = X_2 + f_2(X_2, t), \quad x_3 = X_3, \quad (2.102)$$

where f_1 and f_2 are the in-plane displacements, which can also be regarded as functions of the spatial coordinate and time x_2, t . Corresponding to this motion one has the velocities with dependencies $v_1(x_2, t), v_2(x_2, t)$, and $v_3 = 0$, and $\partial/\partial x_1 = \partial/\partial x_3 = 0$. The expression of the material time derivative is given by $\dot{(\cdot)} = \partial/\partial t + v_2 \partial/\partial x_2$.

The shear deformation is described by

$$(\mathbf{F})_{ij} = \frac{\partial x_i}{\partial X_j} = \begin{bmatrix} 1 & f'_1 & 0 \\ 0 & 1 + f'_2 & 0 \\ 0 & 0 & 1 \end{bmatrix}_{ij}, \quad (\mathbf{B})_{ij} = (\mathbf{F}\mathbf{F}^\top)_{ij} = \begin{bmatrix} 1 + f_1'^2 & f'_1(1 + f'_2) & 0 \\ f'_1(1 + f'_2) & (1 + f'_2)^2 & 0 \\ 0 & 0 & 1 \end{bmatrix}_{ij}, \quad (2.103)$$

$$(\mathbf{L})_{ij} = (\vec{\nabla} \mathbf{v})_{ij} = \frac{\partial v_i}{\partial x_j} = \begin{bmatrix} 0 & \frac{\partial v_1}{\partial x_2} & 0 \\ 0 & \frac{\partial v_2}{\partial x_2} & 0 \\ 0 & 0 & 0 \end{bmatrix}, \quad (\mathbf{D})_{ij} = \begin{bmatrix} 0 & \frac{1}{2} \frac{\partial v_1}{\partial x_2} & 0 \\ \frac{1}{2} \frac{\partial v_1}{\partial x_2} & \frac{\partial v_2}{\partial x_2} & 0 \\ 0 & 0 & 0 \end{bmatrix}_{ij}, \quad (2.104)$$

The invariants of \mathbf{B} are computed as $I_{\mathbf{B}} = 1 + f_1'^2 + (1 + f_2')^2 + 1$ and $III_{\mathbf{B}} = (1 + f_2')^2 = (\rho_0/\rho)^2$ with $1 + f_2' = \rho_0/\rho$. Also $I_{\mathbf{B}} - 3 = (\rho_0/\rho)^2 - 1 + f_1'^2$. In addition from the kinematic identity, $\dot{\mathbf{F}} = \mathbf{L}\mathbf{F}$ we obtain two nontrivial relations $\dot{f}_1' = (1 + f_2')\partial v_1/\partial x_2$ and $\dot{f}_2' = (1 + f_2')\partial v_2/\partial x_2$, where the material derivative is $\dot{(\cdot)} = \partial/\partial t + v_2 \partial/\partial x_2$. The second of the two results is just a re-statement of the mass conservation, and is equivalent to replacing $1 + f_2'$ with ρ_0/ρ . But the first is an independent expression for the shear strain which can be recast in terms of the density and transverse velocity gradient as

$$\dot{(\frac{1}{f_1'})} = \left(\frac{\rho_0}{\rho}\right) \frac{\partial v_1}{\partial x_2}. \quad (2.105)$$

Finally, the contribution to the configurational stress has only one nonzero component, $(\vec{\nabla} \varphi \otimes \vec{\nabla} \varphi)_{22} = (\partial \varphi / \partial x_2)^2$.

Using the density, ρ and the shear strain f_1' as the two independent kinematic variables, we can now write down expressions for the components of the stress tensor. The cross plane shear stresses are zero, i.e., $\sigma_{13} = \sigma_{23} = 0$. The in-plane shear stress σ_{12} is given by the expression

$$\sigma_{12} = \mu_s f_1' + \mu_f \frac{\partial v_1}{\partial x_2}. \quad (2.106)$$

The in-plane normal stress σ_{22} is given by

$$\sigma_{22} = -\mu_c \left(\frac{\rho}{\rho_0} \right) \left[\left(\frac{\rho}{\rho_0} \right)^{\frac{2\nu_s}{1-2\nu_s}} - \left(\frac{\rho}{\rho_0} \right)^{-2} \right] - \alpha_c K \frac{\rho}{\rho_0} (T - T_0) - \rho R_g T - \rho \gamma_\varphi \left(\frac{\partial \varphi}{\partial x_2} \right)^2 + (\nu_f + 2\mu_f) \frac{\partial v_2}{\partial x_2}. \quad (2.107)$$

The specific governing equations for the shear motion for the full model are

$$\frac{\partial \rho}{\partial t} + v_2 \frac{\partial \rho}{\partial x_2} + \rho \frac{\partial v_2}{\partial x_2} = 0, \quad (2.108)$$

$$\rho \left(\frac{\partial v_1}{\partial t} + v_2 \frac{\partial v_1}{\partial x_2} \right) = \frac{\partial}{\partial x_2} \left[\mu_s f'_1 + \mu_f \frac{\partial v_1}{\partial x_2} \right], \quad (2.109)$$

$$\rho \left(\frac{\partial v_2}{\partial t} + v_2 \frac{\partial v_2}{\partial x_2} \right) = \frac{\partial}{\partial x_2} \left\{ -\mu_c \left(\frac{\rho}{\rho_0} \right) \left[\left(\frac{\rho}{\rho_0} \right)^{\frac{2\nu_s}{1-2\nu_s}} - \left(\frac{\rho}{\rho_0} \right)^{-2} \right] - \alpha_c(\varphi) K \frac{\rho}{\rho_0} (T - T_0) - \rho R_g(\varphi) T - \rho \gamma_\varphi \left(\frac{\partial \varphi}{\partial x_2} \right)^2 + (\nu_f + 2\mu_f) \frac{\partial v_2}{\partial x_2} \right\}, \quad (2.110)$$

$$\begin{aligned} \rho c_v \left(\frac{\partial T}{\partial t} + v_2 \frac{\partial T}{\partial x_2} \right) &= \frac{\partial}{\partial x_2} \left(k \frac{\partial T}{\partial x_2} \right) + \left[\mu_f \left(\frac{\partial v_1}{\partial x_2} \right)^2 + (\nu_f + 2\mu_f) \left(\frac{\partial v_2}{\partial x_2} \right)^2 \right] \\ &\quad + B \dot{\varphi}^2 - \left[\alpha_c K \frac{\rho}{\rho_0} T + \rho R_g T \right] \frac{\partial v_2}{\partial x_2} \\ &\quad + \left\{ -\frac{1}{2} \alpha'_c(\varphi) K \frac{\rho}{\rho_0} T \ln(\mathcal{I}\!\!\mathcal{I}\!\!\mathcal{I}_{\mathbf{B}}) - \frac{1}{2} \rho R'_g(\varphi) T \ln(\mathcal{I}\!\!\mathcal{I}\!\!\mathcal{I}_{\mathbf{B}}) - \rho c'_v(\varphi) T \ln(T/T_0) \right. \\ &\quad \left. + \rho \left[\beta'_m(\varphi) \frac{T}{T_m} Q_m + \beta'_v(\varphi) \frac{T}{T_v} Q_v \right] \right\} \dot{\varphi} + \rho Q_{\text{hc}} \Omega + \rho r, \end{aligned} \quad (2.111)$$

$$\begin{aligned}
B \left(\frac{\partial \varphi}{\partial t} + v_2 \frac{\partial \varphi}{\partial x_2} \right) &= \frac{\partial}{\partial x_2} \left(\rho \gamma_\varphi \frac{\partial \varphi}{\partial x_2} \right) + \rho c'_v(\varphi) [T \ln(T/T_0) - (T - T_0)] \\
&\quad - \frac{\mu'_s(\varphi)}{2} \frac{\rho}{\rho_0} (I_B - 3) - \frac{\mu'_c(\varphi)}{2} \frac{\rho}{\rho_0} \frac{(1 - 2\nu_s)}{\nu_s} \left(\text{III}_B^{-\nu_s/(1-2\nu_s)} - 1 \right) - \frac{3\mu'_l(\varphi)}{2} \frac{\rho}{\rho_o} \text{III}_B^{1/3} \\
&\quad + \frac{\alpha'_c(\varphi)}{2} K \frac{\rho}{\rho_0} (T - T_0) \ln(\text{III}_B) + \frac{1}{2} \rho R'_g(\varphi) T \ln(\text{III}_B) \\
&\quad - \frac{1}{2} \rho \Psi^{\text{well}} \frac{\partial \mathcal{F}}{\partial \varphi} - \rho \left[\beta'_m(\varphi) \frac{T - T_m}{T_m} Q_m + \beta'_v(\varphi) \frac{T - T_v}{T_v} Q_v \right], \quad (2.112)
\end{aligned}$$

and for chemical reaction,

$$\rho \left(\frac{\partial \lambda}{\partial t} + v_2 \frac{\partial \lambda}{\partial x_2} \right) = \frac{\partial}{\partial x_2} \left(d \frac{\partial \lambda}{\partial x_2} \right) + \rho \Omega. \quad (2.113)$$

Finally the kinematic relation (2.105) for the shear strain (which must be included) is expressed as

$$\frac{\rho}{\rho_0} \left(\frac{\partial f'_1}{\partial t} + v_2 \frac{\partial f'_1}{\partial x_2} \right) = \frac{\partial v_1}{\partial x_2}. \quad (2.114)$$

Chapter 3

Analysis of Simple Motions

This chapter describes a continuum model for the behavior of a condensed phase energetic material that undergoes phase transformation. Such materials are often used in explosive and pyrotechnic systems and are commonly known as solid explosives. Explosive materials are usually stable solids at room temperature and pressure, and when subjected to sufficiently strong mechanical or thermal stimulus they undergo transitions to liquid and gas before releasing the bulk of their stored energy by chemical reaction mainly in the gas phase. Chapter 2 presented the continuum formulation that describes phase transitions from solid to liquid to gas. The model also includes energy-release due to chemical reaction. The state of the phase and the progress of the chemical reaction are represented by two thermodynamically independent variables, φ and λ . The phase variable φ takes on the values 0 for a pure solid, 1 for a pure liquid and 2 for a pure gas. The progress of the (exothermic) chemical reaction is represented by λ which ranges from 0 (unreacted) to 1 (completely reacted).

Most of Chapter 2 explains the model's formulation, assumptions and the restricted form of the constitutive theory based on standard arguments from the second law of thermodynamics. Following Gurtin's suggestion [32], configurational forces are assumed to be in global and local balance and further arguments lead to the derivation of an evolution law for φ , which is of the advection, diffusion, reaction type. Following combustion theory for a reactive mixture, an evolution law for the reaction progress variable λ is posited as a fundamental law.

Hence, our model is fully three-dimensional and is thermodynamically and tensorially consistent. Specialization of the model and limiting forms are examined in Chapter 2 and the equations for the special cases of constant volume evolution, one-dimensional, time-dependent longitudinal compression motion and time-dependent shear motion are obtained. Solutions to initial boundary-

value problems for the equations for these simple motions illustrate the behavior of the model and reveal its properties. The results testify to the model's potential suitability for modeling complex phenomena that involve both phase transformation and chemical reaction in one combined framework. Material constants and properties of the energetic material (solid explosive) HMX are used to determine representative values for the model. These include properties such as (but not limited to) the elastic properties, viscosities, specific heats, gas constant, heats of melting (fusion), vaporization (condensation), and combustion (detonation).

In Section 1 the equations for the three dimensional model is given. In Section 2 we discuss how we assigned the material properties of HMX to the model. In Section 3 the special forms of the equations for the three simple motions are given. We also solve the case for constant volume evolution and discuss the properties of the underlying ordinary differential equations and their dynamics. In Section 4 the numerical methodology is given for longitudinal and shear motions. Section 5 presents representative numerical solutions for mechanically induced phase transformation and includes examples of interesting properties of the model such as shear localization and shock melting.

3.1 Mathematical formulations

3.1.1 Kinematics and some definitions

The coordinates of position in the lab-frame are given by \mathbf{x} and the initial position of the material particles are given by \mathbf{X} . The mapping of the deformations is given by $\mathbf{x} = \mathbf{x}(\mathbf{X}, t)$. The deformation gradient \mathbf{F} is defined by the derivative $\mathbf{F} = \partial \mathbf{x} / \partial \mathbf{X}$. The left Cauchy-Green tensor $\mathbf{B} = \mathbf{F} \mathbf{F}^T$ is used to describe finite deformations. The velocity is defined by the time derivative of the particle trajectories $\mathbf{v} = (\partial \mathbf{x} / \partial t)_{\mathbf{X}}$. The velocity gradient is the gradient of the velocity field defined by the tensor $\mathbf{L} = \vec{\nabla} \mathbf{v}$. Let the dot notation, $\dot{(\)}$, refer to the material derivative. The rate of stretching tensor appears is given by $\mathbf{D} = [\vec{\nabla} \mathbf{v} + (\vec{\nabla} \mathbf{v})^T] / 2$. The time derivative of the deformation gradient is $\dot{\mathbf{F}} = \mathbf{L} \mathbf{F}$. Consideration of conservation of mass relates the instantaneous density ρ to a reference (ambient) density of the solid, ρ_0 by $\det(\mathbf{F}) = \rho_0 / \rho$ as well as $\det(\mathbf{B}) = (\rho_0 / \rho)^2$.

3.1.2 General formulation

The derivation of the model and its constitutive specification was the principal subject of Ref. [62] or Chapter 2. The arguments in that paper, developed a φ -dependent constitutive expression for the stress $\boldsymbol{\sigma}$ as

$$\begin{aligned}\boldsymbol{\sigma} = & \mu_s \frac{\rho}{\rho_0} \mathbf{B} - \mu_c \frac{\rho}{\rho_0} \text{III}_{\mathbf{B}}^{-[\nu_c/(1-2\nu_c)]} \mathbf{I} + \mu_l \frac{\rho}{\rho_0} \text{III}_{\mathbf{B}}^{1/3} \mathbf{I} \\ & - \alpha_c K \frac{\rho}{\rho_0} (T - T_0) \mathbf{I} - \rho R_g T \mathbf{I} \\ & - \rho \gamma_\varphi \vec{\nabla} \varphi \otimes \vec{\nabla} \varphi + \nu_f (\vec{\nabla} \cdot \mathbf{v}) \mathbf{I} + 2\mu_f \mathbf{D} .\end{aligned}\tag{3.1}$$

The material properties μ_c , μ_s , μ_l , α_c , R_g , γ_φ , ν_f and μ_f are assumed to be functions of φ such that they are non-zero in the appropriate phase and are zero otherwise. The shear modulus μ_s is associated with a Blatz-Ko compressible solid and μ_l is associated with liquid. The function μ_c represents the shear modulus of the condensed phase such that $\mu_c = \mu_s + \mu_l$, with the properties that $\mu_c(0) = \mu_s(0) = \mu_{solid}$, $\mu_l(0) = 0$, $\mu_s(1) = 0$, $\mu_c(1) = \mu_l(1) = \mu_{liquid}$ and $\mu_c(2) = \mu_s(2) = \mu_l(2) = 0$. The function α_c is associated with a thermal expansion stress, R_g is associated with the ideal gas constant in a gas, ν_f and μ_f are associated with strain rate generated viscous stress, and γ_φ is associated with phase change induced stresses that act in regions with nonzero phase gradients. Derivatives of the φ -dependent functions that appear represented are by derivatives like $\alpha'(\varphi, T) = \partial\alpha/\partial\varphi|_T$. The s -subscript refers to the solid phase, l -subscript refers to the liquid phase, and c -subscript refers to the condensed phase. Similarly the f -subscript refers to the fluid properties for both liquid and gas phases. If spelled out the subscript, ‘solid’, ‘liquid’, or ‘gas’, refers to a constant material property. The various scalar material properties, such as c_v , γ_φ could have explicit dependence on λ as well as φ and T . The governing equations for the model with

reaction and phase change (without body forces) are

$$\dot{\rho} + \rho \vec{\nabla} \cdot \mathbf{v} = 0, \quad (3.2)$$

$$\rho \dot{\mathbf{v}} = \vec{\nabla} \cdot \boldsymbol{\sigma}, \quad (3.3)$$

$$\begin{aligned} \rho c_v \dot{T} &= \vec{\nabla} \cdot (k \vec{\nabla} T) + \nu_f (\vec{\nabla} \cdot \mathbf{v})^2 + 2\mu_f \mathbf{D} : \mathbf{D} + B \dot{\phi}^2 \\ &- \alpha_c K \frac{\rho}{\rho_0} T (\vec{\nabla} \cdot \mathbf{v}) - \rho R_g T (\vec{\nabla} \cdot \mathbf{v}) \\ &+ \left\{ -\frac{\alpha'_c(\varphi)}{2} K \frac{\rho}{\rho_0} T \ln(\mathcal{I}_B) - \rho \frac{R'_g(\varphi)}{2} T \ln(\mathcal{I}_B) - \rho c'_v(\varphi) T \ln(T/T_0) \right. \\ &\left. + \rho \left[\beta'_m(\varphi) \frac{T}{T_m} Q_m + \beta'_v(\varphi) \frac{T}{T_v} Q_v \right] \right\} \dot{\phi} + \rho Q_{hc} \Omega + \rho r, \end{aligned} \quad (3.4)$$

$$\begin{aligned} B \dot{\phi} &= \vec{\nabla} \cdot (\rho \gamma_\varphi \vec{\nabla} \phi) + \rho c'_v(\varphi) [T \ln(T/T_0) - (T - T_0)] \\ &- \frac{\mu'_s(\varphi)}{2} \frac{\rho}{\rho_0} (I_B - 3) - \frac{\mu'_c(\varphi)}{2} \frac{\rho}{\rho_0} \frac{(1 - 2\nu_c)}{\nu_c} \left(\mathcal{I}_B^{-\nu_c/(1-2\nu_c)} - 1 \right) + \frac{3\mu'_l(\varphi)}{2} \frac{\rho}{\rho_0} \mathcal{I}_B^{1/3} \\ &+ \frac{\alpha'_c(\varphi)}{2} K \frac{\rho}{\rho_0} (T - T_0) \ln(\mathcal{I}_B) + \frac{1}{2} \rho R'_g(\varphi) T \ln(\mathcal{I}_B) \\ &- \rho \frac{1}{2} \Psi^{\text{well}} \frac{\partial F}{\partial \phi} - \rho \left[\beta'_m(\varphi) \left(\frac{T}{T_m} - 1 \right) Q_m + \beta'_v(\varphi) \left(\frac{T}{T_v} - 1 \right) Q_v \right], \end{aligned} \quad (3.5)$$

$$\rho \dot{\lambda} = \vec{\nabla} \cdot (d \vec{\nabla} \lambda) + \rho \Omega, \quad (3.6)$$

$$\dot{\mathbf{F}} = \mathbf{L} \mathbf{F}. \quad (3.7)$$

Table 3.1 gives the values for material properties that appear in equations (3.1-3.7). The values are based upon HMX along with references to the data source or a notation that we have used a model value.

3.1.3 Material transition functions

An important ingredient of our model is the use of φ -dependent material properties, or material transition functions. Their most prominent use is in the definition of the source terms in the φ -evolution equation and the energy (temperature) equation. Also, functions such as $\mu_c(\varphi)$, $\mu_s(\varphi)$, $\mu_l(\varphi)$, $\alpha_c(\varphi)$, $R_g(\varphi)$, $c_v(\varphi)$ all change with the phase variable φ . The model assumes that these are defined in such a way so that they take on proper values for pure phases when the material has the limiting pure-phase values for φ . The φ -dependent material transition functions used for this paper are listed in the Appendix A and are made up of simple, smooth or piece-wise smooth,

Material Property	Value	Refs.
Density of β -HMX (ρ_0)	1.71 g/cm ³	[47]
Density of liquid-HMX	1.65 g/cm ³	[4]
Specific heat at constant volume (c_v)	1.5×10^3 J/kg K	[47]
Isothermal Bulk modulus ($K = \rho \left. \frac{\partial p}{\partial \rho} \right _T$)	13.5 GPa	[47]
Shear modulus (μ_{solid})	2.46 GPa	modeled
Shear modulus (μ_{liquid})	2.37 GPa	modeled
Poisson's ratio (ν_c)	0.414	calculated
Viscosity coefficient (μ_f)	0.45 N s/m ²	[24]
Bulk viscosity coefficient (ν_f)	$-2/3 \mu_f$	Stokes hypothesis
Thermal expansion coefficient (α_{solid})	0.000134 1/K [47]	
Thermal conductivity (k)	.36 W/m K	[47]
Phase diffusion coefficient ($\rho\gamma_\varphi$)	1.0×10^{-6} m kg/s ²	modeled
Universal gas constant (R_u)	8313 J/kmole K	
Molar weight of β -HMX	296.2 kg/kmole	[24]
Gas constant per unit mass (R_{gas})	300 J/kg K	modeled
Melting temperature (T_m)	558 K	[24]
Vaporization temperature (T_v)	588 K	modeled
Heat of melting (Q_m)	-200×10^3 J/kg	[24]
Heat of vaporization (Q_v)	-100×10^3 J/kg	modeled
Heat of combustion (Q_{hc})	5.0×10^6 J/kg	[69]
Rate of heat source (ρr)	5000 J/m ³ s	modeled
Frequency of Arrhenius kinetic (A)	9.3×10^{16} 1/s	[69]
Activation temperature (E_a/R_u)	24660 K	[69]
Depth of phase well (Ψ^{well})	550 J/kg	modeled
Multiplication factor of $\dot{\varphi}$ (B)	1.5 kg/m s	modeled

Table 3.1: Material properties typical of HMX.

polynomials in φ .

Figure 2.3 shows the material transition functions $\beta'_m(\varphi)$, $\beta'_v(\varphi)$ that are used to construct ψ_2 , which represents free energy changes during phase transition and is given by

$$\psi_2 = \frac{1}{2}\Psi^{\text{well}}F(\varphi) + \beta_m(\varphi)Q_m\left(\frac{T}{T_m} - 1\right) + \beta_v(\varphi)Q_v\left(\frac{T}{T_v} - 1\right), \quad (3.8)$$

where $\Psi^{\text{well}} > 0$ is a constant that describes the potential, and $Q_m < 0$ and $Q_v < 0$ are constants representing the heats of melting and vaporization. The constants $T_m > 0$ and $T_v > 0$ are melting and vaporization temperatures. Here we assume a specific form for $F(\varphi)$ (listed in the Appendix A) that is a smooth positive definite function with isolated zeroes at $\varphi = 0, 1$, and 2 , representing three local minima. In addition, $F(\varphi)$ is assumed to be locally quadratic near the zeroes at $\varphi = 0, 1$ and 2 , i.e. near $\varphi = 0, F \sim \varphi^2$, near $\varphi = 1, F \sim (\varphi - 1)^2$, and near $\varphi = 2, F \sim (\varphi - 2)^2$. The function $\beta_m(\varphi)$ is assumed to be smooth and monotonically increasing and has values from 0 to 1 on the range $0 \leq \varphi \leq 1$ with zero derivative elsewhere. Similarly the function $\beta_v(\varphi)$ is similarly assumed to be monotonically increasing with values from 0 to 1 on the range $1 \leq \varphi \leq 2$. The derivative of transition-energy density $\partial\psi_2/\partial\varphi$ generates source terms in the phase equation represented as

$$\frac{\partial\psi_2}{\partial\varphi} = \frac{1}{2}\Psi^{\text{well}}\frac{\partial F}{\partial\varphi}(\varphi) + \beta'_m(\varphi)Q_m\left(\frac{T}{T_m} - 1\right) + \beta'_v(\varphi)Q_v\left(\frac{T}{T_v} - 1\right), \quad (3.9)$$

Figure 2.1 illustrates the assumed dependence of $\psi_2(\varphi, T)$ on φ and T . Starting from (a) through (d), the temperature T , is raised from below T_m to above T_v , representing a standard melting-evaporation process. The transition energy density in case (a) has its minimum at $\varphi = 0$. As T is increased through T_m and then T_v , we see a shift in the global minima from pure solid to solid-liquid and to liquid-vapor. As T eventually exceeds T_v as shown in (d), the energy minimizing well shifts to a vapor state at $\varphi = 2$. Figure 2.2 shows examples of the other material transition functions and their derivatives.

3.2 Matching material properties to HMX

Here we discuss our fit of the model's material properties to mimic an energetic material like HMX. Figure 3.1 shows a pressure-temperature plane that indicates regions where, from classical and experimental considerations, HMX can be considered to be a static solid, liquid or a gas in thermodynamic equilibrium. Some of the boundaries (specifically the solid/liquid boundary) are known from experiment. Note that solid phases of HMX are not differentiated here and it is assumed that the β -phase of solid HMX is representative. The solid/liquid boundary is of particular interest and is computed via a Kraut–Kennedy law. It is well known that HMX liquid is quite unstable, [13] and once the liquid phase appears it quickly evolves into gas, partly from exothermic energy released by chemical reaction in the condensed phase. For the purpose of our early modeling efforts we have decided to match the HMX melt temperature to the experimental melt temperature $T = 558$ K and the evaporation temperature at $T = 588$ K. Figure 3.1 shows a shaded box that represents the range of temperatures and pressures (level of stress) predicted by computation with model.

In our model (p, V) -isotherms (where $V = 1/\rho$) can be obtained directly from (3.1) by setting all derivatives equal to zero and by assuming a homogeneous deformation such that $\mathbf{B} = (\rho_0/\rho)^{2/3}\mathbf{I}$ and $\boldsymbol{\sigma} = -p\mathbf{I}$, (where p is the pressure) to obtain

$$p = \mu_c \left(\frac{\rho}{\rho_0} \right) \left[\left(\frac{\rho}{\rho_0} \right)^{\frac{2\nu_c}{1-2\nu_c}} - \left(\frac{\rho}{\rho_0} \right)^{-\frac{2}{3}} \right] + \alpha_c K \frac{\rho}{\rho_0} (T - T_0) - \rho R_g T. \quad (3.10)$$

HMX liquid is approximately 4% less dense than HMX solid [4]. Figure 3.2 shows a plot of an isotherm computed from (3.10) with values shown in Table 3.1. Experimental data points on the solid isotherms obtained by Yoo and Cynn [85], are shown for comparison. Since HMX liquid is so chemically unstable, experimental data for the liquid isotherm is not available. One implication of the lower density for HMX-liquid is that the isothermal sound speed (the negative slope of the $p - V$ isotherm) is greater in the solid than in the liquid. Figure 3.3 shows a plot of an isotherm computed from (3.10) for the ideal gas term that is proportional to R_g . Figure 3.4 shows a representative isotherm on log-scales at 300 K, for the full range of values for the model, when the material is solid, liquid or gas, as computed from (3.10).

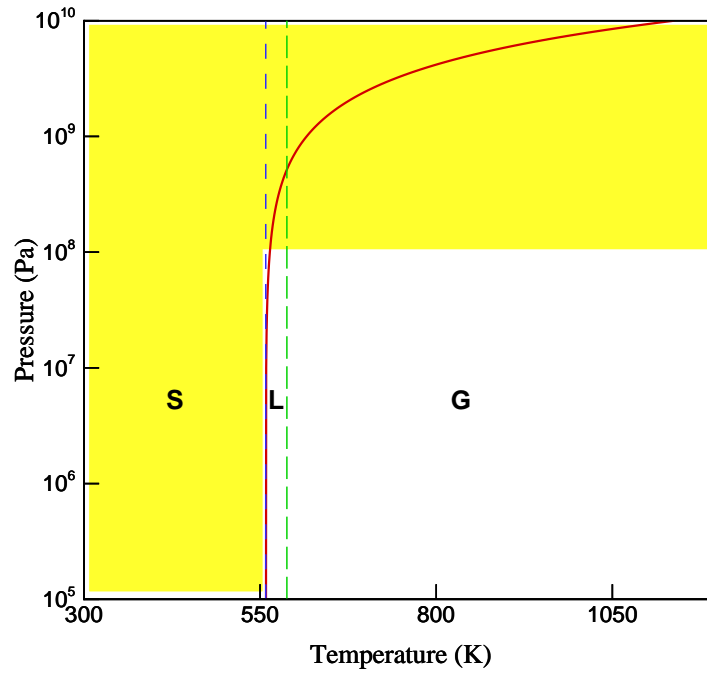


Figure 3.1: Solid curve is melt temperature-pressure relation for β -HMX given by the semi-empirical Kraut–Kennedy law [54],[47]. Dashed line and long-dashed line are constant melt temperature and vapor temperature used in the current numerical simulation, respectively.

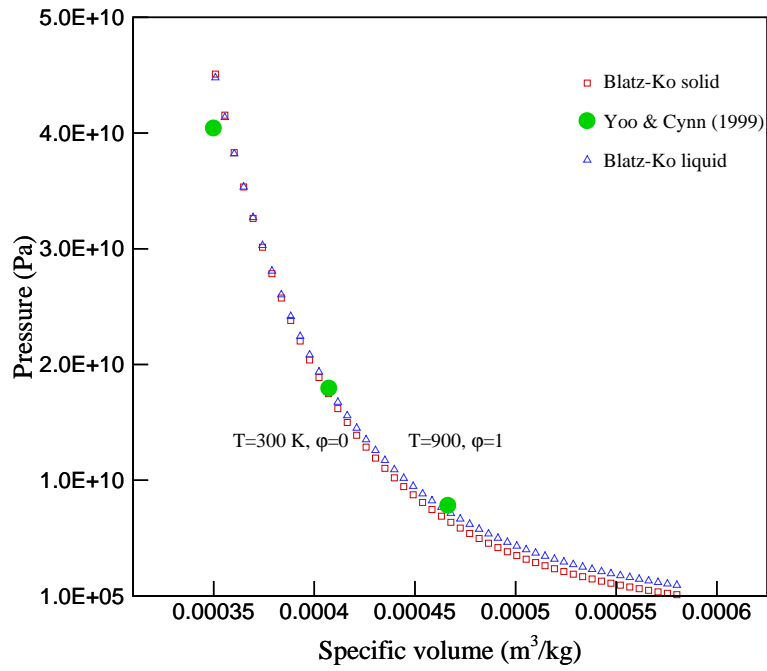


Figure 3.2: P - V isotherms at $T=300$ K and $T=900$ K. $\left| \frac{dp}{dV} \right|_{\varphi=0} > \left| \frac{dp}{dV} \right|_{\varphi=1}$ implies that the speed of sound is greater in the solid than in the liquid HMX.

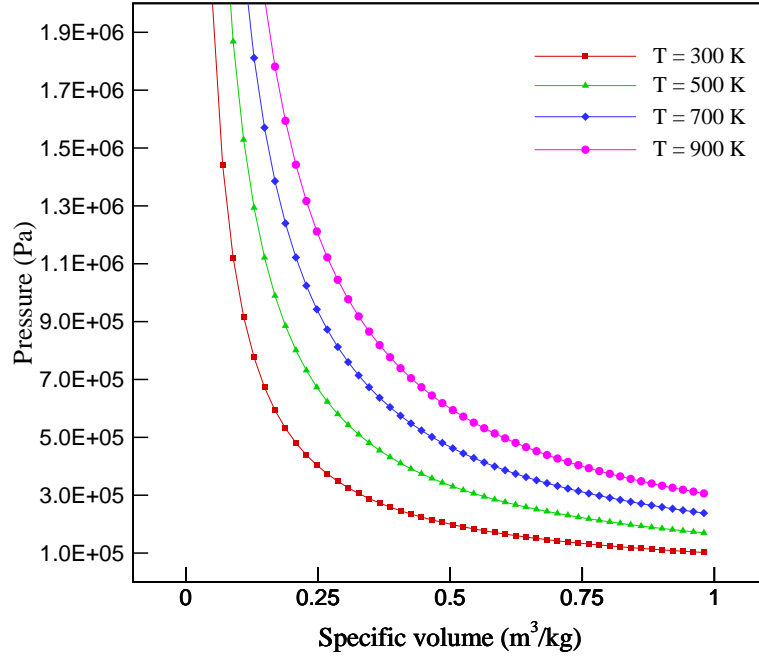


Figure 3.3: P - V isotherms at four different temperatures for HMX vapor ($\varphi = 2$).

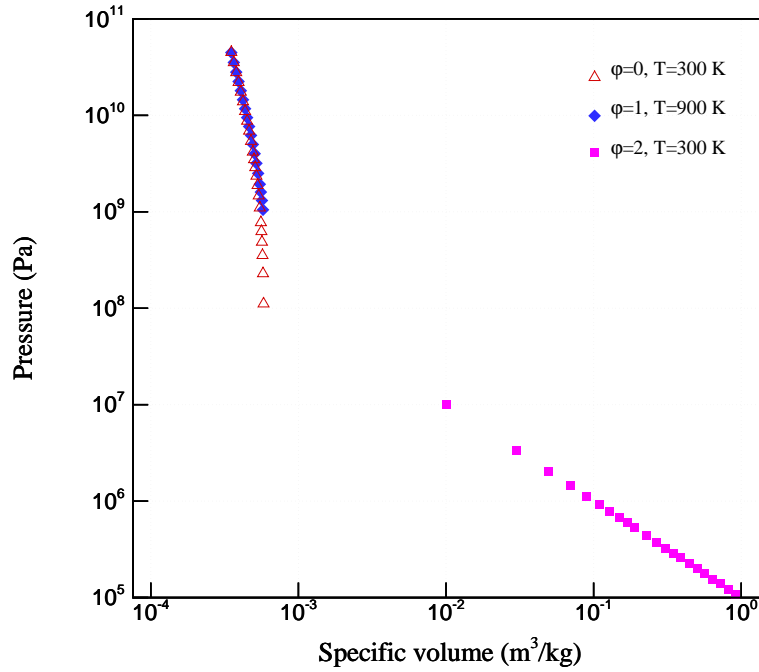


Figure 3.4: P - V isotherms for solid, liquid, and vapor HMX at $T = 300$ K, drawn to a single range of P - V axes.

3.3 Form of the model for three simple motions

Here we consider the differential equations for the model when the material undergoes three simple motions: (i) evolution at constant volume, (ii) time-dependent longitudinal motion and (iii) one-dimensional, time-dependent shear motion. All three cases are amenable to extensive computational and theoretical analysis and their discussion reveals the underlying mathematical properties of the model. All three are very important in the traditional analysis of ignition of energetic materials. The reduction for the three special motions follow directly from the general form of equations (3.2–3.7) and were derived in the last section of Chapter 2.

3.3.1 Evolution at constant volume

An important simple case often considered in combustion theory describes constant volume thermal explosion, where the velocity \mathbf{v} as well as all spatial gradients are exactly zero and the density is constant. For illustration (in this section only) we neglect thermal expansion, and assume a constant specific heat and gas constant. We are left with three ordinary differential equations in time for the temperature, T , phase variable φ , and reaction progress variable λ ,

$$\rho c_v \frac{\partial T}{\partial t} = \rho \left(\beta'_m(\varphi) \frac{T}{T_m} Q_m + \beta'_v(\varphi) \frac{T}{T_v} Q_v \right) \frac{\partial \varphi}{\partial t} + \rho Q_{hc} \Omega + \rho r, \quad (3.11)$$

$$B \frac{\partial \varphi}{\partial t} = -\rho \frac{1}{2} \Psi^{\text{well}} \frac{\partial F}{\partial \varphi} - \rho \left[\beta'_m(\varphi) \left(\frac{T}{T_m} - 1 \right) Q_m + \beta'_v(\varphi) \left(\frac{T}{T_v} - 1 \right) Q_v \right], \quad (3.12)$$

$$\frac{\partial \lambda}{\partial t} = \Omega. \quad (3.13)$$

If phase change is discarded we recover the equations from standard combustion theory for constant volume thermal explosion, $c_v(\partial T/\partial t) = Q_{hc} \Omega$, $(\partial \lambda/\partial t) = \Omega$. Of course, the more interesting behavior occurs when phase change is included.

Figure 3.5 shows an example of the time evolution of constant volume heating without chemical reaction starting from a solid ($\varphi = 0$) at an initial temperature of $T = 300$ K. The heating rate

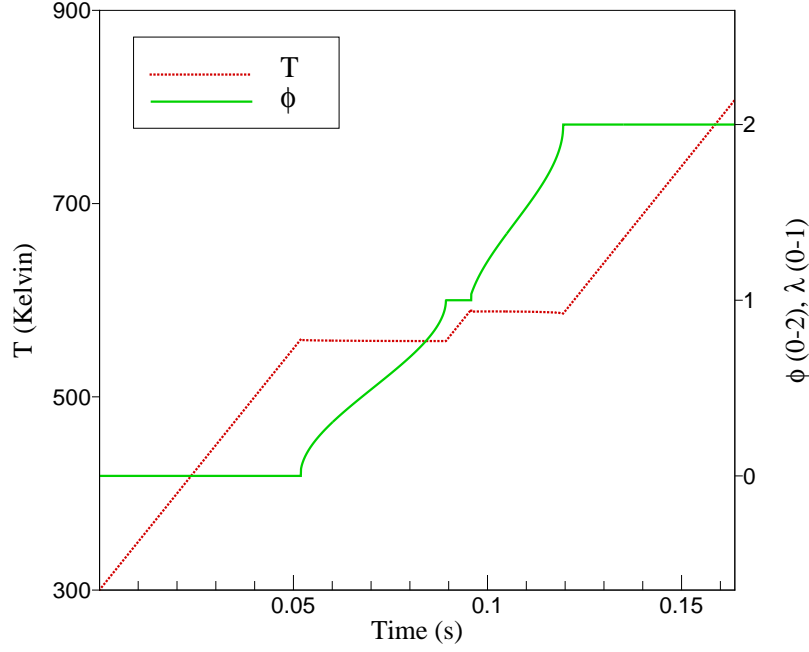


Figure 3.5: Constant-volume phase transformation without reaction.

r and the kinetic parameter B , control the transformation rates. It is possible to see (at least qualitatively) all of the phase change behaviors expected during constant volume heating. As heat is first applied, the temperature increases linearly. As the temperature increases further, the material begins to melt and the endothermic process absorbs heat from the system. (In Figure 3.5 the slight temperature decrease is barely visible in the nearly constant temperature interval). At the completion of the phase transformation to liquid, the temperature rises in the liquid at a constant rate until the vaporization temperature is reached and second phase transition from liquid to gas phase occurs. After that, constant rate heating in the gas occurs.

The sharp transitions that are apparent in Fig 3.5 (for example near the times $t = 0.05$ and $t = 0.09$ sec) are the result of a bifurcation and a change of stability in the ODEs near the transition temperatures, T_m and T_v . To see this clearly, consider the stability of the solid phase during constant rate heating. The temperature and the phase variable can be represented to leading order as $T = T_0 + r t / c_v$ and $\varphi = 0$, (with $\lambda = 0$ for all time), so that a stability analysis assumes

that T and φ take the form

$$T = T_0 + \frac{r}{c_v}t + T'(t) + \dots \quad \varphi = \varphi'(t) + \dots \quad (3.14)$$

where T' and φ' are assumed to be small. The linearization of (3.11), (3.12) with $\beta'_m \approx 6\varphi'$ and $\partial F/\partial \varphi \approx 8\varphi'$ is straightforward and leads to equations for T', φ'

$$\frac{dT'}{dt} = 0, \quad (3.15)$$

$$\frac{d\varphi'}{dt} = -\frac{\rho}{B} \left\{ 4\Psi^{\text{well}} - 6Q_m \left(1 - \frac{T^{(0)}}{T_m} \right) \right\} \varphi', \quad (3.16)$$

where $T^{(0)}$ is the leading order temperature found from simple constant rate heating

$$T^{(0)} = T_0 + \frac{r}{c_v}t. \quad (3.17)$$

The stability properties of the solution for φ' are governed by the sign of $d\varphi'/dt$ found on the right hand side of (3.16). For early times, the argument is always negative, since $T^{(0)} < T_m$ and $Q_m < 0$. Consequently, the solution is exponentially stable. (It is a simple matter to right down the exact solution of (3.16)). As the temperature rises, the stability changes as $d\varphi'/dt$ changes sign, and this time is found by setting the right hand sign of (3.16) exactly equal to zero. In which case the leading order temperature is

$$T^{(0)} = T_m - \frac{2}{3} \frac{\Psi^{\text{well}}}{Q_m} T_m. \quad (3.18)$$

For the case where $|\Psi^{\text{well}}/Q_m| \ll 1$, the phase transition temperature associated with this simple change of stability is close to T_m . So we find that below the melt temperature the perturbations are stable, but near the melt temperature the stability changes type and becomes unstable. Any perturbation grows and subsequently an abrupt transition occurs from $\varphi = 0$. Another point is that our assumed properties for F strictly requires a nonzero perturbation of φ , to be combined with heating, in order to observe a phase transition. In other cases than constant volume evolution,

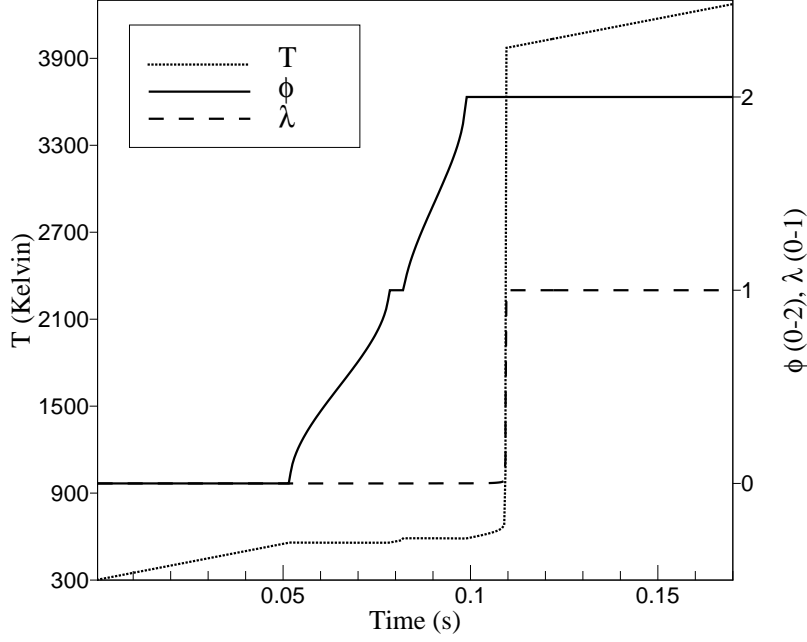


Figure 3.6: Constant-volume thermal explosion.

other source terms exist in the φ -evolution equation (specifically those related to derivatives of the Helmholtz free energy associated with deformation) and those can be the source of thermomechanical disturbances that can grow when the phase becomes dynamically unstable.

Figure 3.6 show a representative solution to (3.11-3.13) with an Arrhenius form assumed for $\Omega = A(\varphi)(1 - \lambda) \exp[-E_a/(R_u T)]$. The function $A(\varphi)$ is chosen to be zero in the solid phase and takes the value listed in Table 3.1 in the gas phase. Initially the material is solid and cold and heated at a uniform rate. So the phase transformations from solid to liquid to gas occur in the same way as shown in Fig. 4.1. However, for this example, once the gas is in abundance, the chemical reaction starts and the gas undergoes a classically well-understood constant volume thermal explosion. If we had chosen to adopt a more complex kinetic form for Ω , reaction could take place first in the liquid phase. In the near future, we plan to use more realistic kinetic scheme for HMX. Clearly there is the flexibility within this formulation to model many aspects of condensed phase energy release.

3.3.2 Longitudinal motion

Next we consider simple longitudinal motion. Typically, explosives are tested by subjecting them to impact with a flyer-plate. In an idealization of this experiment, an infinite slab experiences a displacement loading normal to its surface. As a computational matter, the same flow can be modeled as a reverse impact experiment, where the sample is set into uniform motion and suddenly comes to rest at the origin. We must consider following one-dimensional motion

$$x_1 = X_1 + f_1(X_1, t), \quad x_2 = X_2, \quad x_3 = X_3, \quad (3.19)$$

where f_1 is the displacement in the 1-direction. There is one nonzero velocity component, $v_1 = \partial f_1 / \partial t|_{\mathbf{X}}(X_1, t)$, and \mathbf{F} and \mathbf{B} are both diagonal and $B_{11} = (1 + f_1')^2$, $B_{22} = 1$, $B_{33} = 1$. The first and third invariants of \mathbf{B} are $I_{\mathbf{B}} = 2 + (1 + f_1')^2$ and $III_{\mathbf{B}} = (1 + f_1')^2 = (\rho_0/\rho)^2$. Then $I_{\mathbf{B}} - 3 = (\rho_0/\rho)^2 - 1$. Hence we use the density as the independent strain measure and replace f_1' . The one nonzero component of the rate of strain tensor is, $D_{11} = \partial v_1 / \partial x_1$. Also $(\vec{\nabla} \varphi \otimes \vec{\nabla} \varphi)_{11} = (\partial \varphi / \partial x_1)^2$. It follows that all the shear stresses are zero, $\sigma_{12} = \sigma_{23} = \sigma_{13} = 0$, and the normal stress σ_{11} , is given by

$$\begin{aligned} \sigma_{11} = -\mu_c \left(\frac{\rho}{\rho_0} \right) \left[\left(\frac{\rho}{\rho_0} \right)^{\frac{2\nu_c}{1-2\nu_c}} - \left(\frac{\rho}{\rho_0} \right)^{-2} \right] - \alpha_c K \frac{\rho}{\rho_0} (T - T_0) - \rho R_g T \\ - \rho \gamma_\varphi \left(\frac{\partial \varphi}{\partial x_1} \right)^2 + (\nu_f + 2\mu_f) \frac{\partial v_1}{\partial x_1}. \end{aligned} \quad (3.20)$$

The governing equations for longitudinal compression are the mass and momentum equations

$$\frac{\partial \rho}{\partial t} + v_1 \frac{\partial \rho}{\partial x_1} + \rho \frac{\partial v_1}{\partial x_1} = 0, \quad (3.21)$$

$$\begin{aligned} \rho \left(\frac{\partial v_1}{\partial t} + v_1 \frac{\partial v_1}{\partial x_1} \right) = \frac{\partial}{\partial x_1} \left\{ -\mu_c \left(\frac{\rho}{\rho_0} \right) \left[\left(\frac{\rho}{\rho_0} \right)^{\frac{2\nu_c}{1-2\nu_c}} - \left(\frac{\rho}{\rho_0} \right)^{-2} \right] \right. \\ \left. - \alpha_c K \frac{\rho}{\rho_0} (T - T_0) - \rho R_g T - \rho \gamma_\varphi \left(\frac{\partial \varphi}{\partial x_1} \right)^2 + (\nu_f + 2\mu_f) \frac{\partial v_1}{\partial x_1} \right\}, \end{aligned} \quad (3.22)$$

the energy equation (written in temperature form)

$$\begin{aligned}
\rho c_v \left(\frac{\partial T}{\partial t} + v_1 \frac{\partial T}{\partial x_1} \right) &= \frac{\partial}{\partial x_1} \left(k \frac{\partial T}{\partial x_1} \right) + (\nu_f + 2\mu_f) \left(\frac{\partial v_1}{\partial x_1} \right)^2 \\
&\quad + B \dot{\varphi}^2 - \left[\alpha_c K \frac{\rho}{\rho_0} T + \rho R_g(\varphi) T \right] \frac{\partial v_1}{\partial x_1} \\
&\quad + \left\{ -\frac{1}{2} \alpha'_c(\varphi) K \frac{\rho}{\rho_0} T \ln(\text{III}_B) - \frac{1}{2} \rho R'_g(\varphi) T \ln(\text{III}_B) - \rho c'_v(\varphi) T \ln(T/T_0) \right. \\
&\quad \left. + \rho \left[\beta'_m(\varphi) \frac{T}{T_m} Q_m + \beta'_v(\varphi) \frac{T}{T_v} Q_v \right] \right\} \dot{\varphi} + \rho Q_{hc} \Omega + \rho r, \quad (3.23)
\end{aligned}$$

and the phase and reaction progress evolution equations, given by

$$\begin{aligned}
B \left(\frac{\partial \varphi}{\partial t} + v_1 \frac{\partial \varphi}{\partial x_1} \right) &= \frac{\partial}{\partial x_1} \left(\rho \gamma_\varphi \frac{\partial \varphi}{\partial x_1} \right) + \rho c'_v(\varphi) [T \ln(T/T_0) - (T - T_0)] \\
&\quad - \frac{\mu'_s(\varphi)}{2} \frac{\rho}{\rho_0} (I_B - 3) - \frac{\mu'_c(\varphi)}{2} \frac{\rho}{\rho_0} \frac{(1 - 2\nu_c)}{\nu_c} \left(\text{III}_B^{-\nu_c/(1-2\nu_c)} - 1 \right) - \frac{3\mu'_l(\varphi)}{2} \frac{\rho}{\rho_0} \text{III}_B^{1/3} \\
&\quad + \frac{\alpha'_c(\varphi)}{2} K \frac{\rho}{\rho_0} (T - T_0) \ln(\text{III}_B) + \frac{1}{2} \rho R'_g(\varphi) T \ln(\text{III}_B) \\
&\quad - \frac{1}{2} \rho \Psi^{\text{well}} \frac{\partial F}{\partial \varphi} - \rho \left[\beta'_m(\varphi) \left(\frac{T}{T_m} - 1 \right) Q_m + \beta'_v(\varphi) \left(\frac{T}{T_v} - 1 \right) Q_v \right], \quad (3.24)
\end{aligned}$$

and

$$\rho \left(\frac{\partial \lambda}{\partial t} + v_1 \frac{\partial \lambda}{\partial x_1} \right) = \frac{\partial}{\partial x_1} \left(d \frac{\partial \lambda}{\partial x_1} \right) + \rho \Omega. \quad (3.25)$$

This special formulation is a set of five PDEs for the dependent variables ρ, v_1, T, φ and λ in terms of the independent variables x_1 and t .

3.3.3 Shear motion

The specialization of the equations to shear motion lead to PDEs in one space variable and time. The nominal geometry is a slab of fixed thickness loaded at one surface with constant velocity. The other surface is taken to be fixed (zero displacement) for the entire duration of the test. We consider the following shear motion

$$x_1 = X_1 + f_1(X_2, t), \quad x_2 = X_2 + f_2(X_2, t), \quad x_3 = X_3, \quad (3.26)$$

where f_1 and f_2 are the in-plane displacements, which can also be regarded as functions of the spatial coordinate x_2 and time t . Corresponding to this motion one has the velocities with $v_1(x_2, t), v_2(x_2, t), v_3 = 0$, and $\partial/\partial x_1 = \partial/\partial x_3 = 0$. The expression of the material time derivative is given by $\dot{(\cdot)} = \partial/\partial t + v_2 \partial/\partial x_2$. The shear deformation is described by

$$(\mathbf{F})_{ij} = \frac{\partial x_i}{\partial X_j} = \begin{bmatrix} 1 & f'_1 & 0 \\ 0 & 1 + f'_2 & 0 \\ 0 & 0 & 1 \end{bmatrix}_{ij}, \quad (\mathbf{B})_{ij} = (\mathbf{F}\mathbf{F}^\top)_{ij} = \begin{bmatrix} 1 + f_1'^2 & f'_1(1 + f'_2) & 0 \\ f'_1(1 + f'_2) & (1 + f'_2)^2 & 0 \\ 0 & 0 & 1 \end{bmatrix}_{ij}, \quad (3.27)$$

$$(\mathbf{L})_{ij} = (\vec{\nabla}\mathbf{v})_{ij} = \frac{\partial v_i}{\partial x_j} = \begin{bmatrix} 0 & \frac{\partial v_1}{\partial x_2} & 0 \\ 0 & \frac{\partial v_2}{\partial x_2} & 0 \\ 0 & 0 & 0 \end{bmatrix}, \quad (\mathbf{D})_{ij} = \begin{bmatrix} 0 & \frac{1}{2} \frac{\partial v_1}{\partial x_2} & 0 \\ \frac{1}{2} \frac{\partial v_1}{\partial x_2} & \frac{\partial v_2}{\partial x_2} & 0 \\ 0 & 0 & 0 \end{bmatrix}_{ij}. \quad (3.28)$$

The invariants of \mathbf{B} are computed as $I_{\mathbf{B}} = 1 + f_1'^2 + (1 + f_2')^2 + 1$ and $III_{\mathbf{B}} = (1 + f_2')^2 = (\rho_0/\rho)^2$ with $1 + f_2' = \rho_0/\rho$. Also $I_{\mathbf{B}} - 3 = (\rho_0/\rho)^2 - 1 + f_1'^2$. In addition from the kinematic identity, $\dot{\mathbf{F}} = \mathbf{L}\mathbf{F}$ we obtain two nontrivial relations $\dot{f}'_1 = (1 + f'_2)\partial v_1/\partial x_2$ and $\dot{f}'_2 = (1 + f'_2)\partial v_2/\partial x_2$, where the material derivative is $\dot{(\cdot)} = \partial/\partial t + v_2 \partial/\partial x_2$. The second of the two results is equivalent to replacing $1 + f_2'$ with ρ_0/ρ . The first is an independent expression for the shear strain which can be recast in terms of the density and transverse velocity gradient as

$$\dot{\left(\frac{f'_1}{\rho}\right)} = \left(\frac{\rho_0}{\rho}\right) \frac{\partial v_1}{\partial x_2}. \quad (3.29)$$

Finally, $\vec{\nabla}\varphi \otimes \vec{\nabla}\varphi$ has only one nonzero component, $(\vec{\nabla}\varphi \otimes \vec{\nabla}\varphi)_{22} = (\partial\varphi/\partial x_2)^2$.

We use the density ρ and the shear strain f'_1 , as the two independent kinematic variables. We can now write down expressions for the components of the stress tensor. The cross plane shear stresses are zero, i.e., $\sigma_{13} = \sigma_{23} = 0$. The in-plane shear stress σ_{12} is given by the expression

$$\sigma_{12} = \mu_s f'_1 + \mu_f \frac{\partial v_1}{\partial x_2}. \quad (3.30)$$

The in-plane normal stress σ_{22} is given by

$$\sigma_{22} = -\mu_c \left(\frac{\rho}{\rho_0} \right) \left[\left(\frac{\rho}{\rho_0} \right)^{\frac{2\nu_c}{1-2\nu_c}} - \left(\frac{\rho}{\rho_0} \right)^{-2} \right] - \alpha_c K \frac{\rho}{\rho_0} (T - T_0) - \rho R_g T - \rho \gamma_\varphi \left(\frac{\partial \varphi}{\partial x_2} \right)^2 + (\nu_f + 2\mu_f) \frac{\partial v_2}{\partial x_2}. \quad (3.31)$$

The specific governing equations for the shear motion are

$$\frac{\partial \rho}{\partial t} + v_2 \frac{\partial \rho}{\partial x_2} + \rho \frac{\partial v_2}{\partial x_2} = 0, \quad (3.32)$$

$$\rho \left(\frac{\partial v_1}{\partial t} + v_2 \frac{\partial v_1}{\partial x_2} \right) = \frac{\partial}{\partial x_2} \left[\mu_s f'_1 + \mu_f \frac{\partial v_1}{\partial x_2} \right], \quad (3.33)$$

$$\rho \left(\frac{\partial v_2}{\partial t} + v_2 \frac{\partial v_2}{\partial x_2} \right) = \frac{\partial}{\partial x_2} \left\{ -\mu_c \left(\frac{\rho}{\rho_0} \right) \left[\left(\frac{\rho}{\rho_0} \right)^{\frac{2\nu_c}{1-2\nu_c}} - \left(\frac{\rho}{\rho_0} \right)^{-2} \right] - \alpha_c(\varphi) K \frac{\rho}{\rho_0} (T - T_0) - \rho R_g(\varphi) T - \rho \gamma_\varphi \left(\frac{\partial \varphi}{\partial x_2} \right)^2 + (\nu_f + 2\mu_f) \frac{\partial v_2}{\partial x_2} \right\}, \quad (3.34)$$

$$\begin{aligned} \rho c_v \left(\frac{\partial T}{\partial t} + v_2 \frac{\partial T}{\partial x_2} \right) &= \frac{\partial}{\partial x_2} \left(k \frac{\partial T}{\partial x_2} \right) + \left[\mu_f \left(\frac{\partial v_1}{\partial x_2} \right)^2 + (\nu_f + 2\mu_f) \left(\frac{\partial v_2}{\partial x_2} \right)^2 \right] \\ &\quad + B \dot{\varphi}^2 - \left[\alpha_c K \frac{\rho}{\rho_0} T + \rho R_g T \right] \frac{\partial v_2}{\partial x_2} \\ &\quad + \left\{ -\frac{1}{2} \alpha'_c(\varphi) K \frac{\rho}{\rho_0} T \ln(\mathcal{I}\mathcal{I}\mathcal{I}_{\mathbf{B}}) - \frac{1}{2} \rho R'_g(\varphi) T \ln(\mathcal{I}\mathcal{I}\mathcal{I}_{\mathbf{B}}) - \rho c'_v(\varphi) T \ln(T/T_0) \right. \\ &\quad \left. + \rho \left[\beta'_m(\varphi) \frac{T}{T_m} Q_m + \beta'_v(\varphi) \frac{T}{T_v} Q_v \right] \right\} \dot{\varphi} + \rho Q_{hc} \Omega + \rho r, \end{aligned} \quad (3.35)$$

$$\begin{aligned}
B \left(\frac{\partial \varphi}{\partial t} + v_2 \frac{\partial \varphi}{\partial x_2} \right) &= \frac{\partial}{\partial x_2} \left(\rho \gamma_\varphi \frac{\partial \varphi}{\partial x_2} \right) + \rho c'_v(\varphi) [T \ln(T/T_0) - (T - T_0)] \\
&\quad - \frac{\mu'_s(\varphi)}{2} \frac{\rho}{\rho_0} (I_B - 3) - \frac{\mu'_c(\varphi)}{2} \frac{\rho}{\rho_0} \frac{(1 - 2\nu_c)}{\nu_c} \left(\text{III}_B^{-\nu_c/(1-2\nu_c)} - 1 \right) - \frac{3\mu'_l(\varphi)}{2} \frac{\rho}{\rho_0} \text{III}_B^{1/3} \\
&\quad + \frac{\alpha'_c(\varphi)}{2} K \frac{\rho}{\rho_0} (T - T_0) \ln(\text{III}_B) + \frac{1}{2} \rho R'_g(\varphi) T \ln(\text{III}_B) \\
&\quad - \frac{1}{2} \rho \Psi^{\text{well}} \frac{\partial F}{\partial \varphi} - \rho \left[\beta'_m(\varphi) \frac{T - T_m}{T_m} Q_m + \beta'_v(\varphi) \frac{T - T_v}{T_v} Q_v \right], \quad (3.36)
\end{aligned}$$

$$\rho \left(\frac{\partial \lambda}{\partial t} + v_2 \frac{\partial \lambda}{\partial x_2} \right) = \frac{\partial}{\partial x_2} \left(d \frac{\partial \lambda}{\partial x_2} \right) + \rho \Omega. \quad (3.37)$$

Finally the kinematic relation (3.29) for the shear strain (which must be included) is expressed as

$$\frac{\rho}{\rho_0} \left(\frac{\partial f'_1}{\partial t} + v_2 \frac{\partial f'_1}{\partial x_2} \right) = \frac{\partial v_1}{\partial x_2}. \quad (3.38)$$

This special formulation is a set of seven PDEs for the dependent variables $\rho, v_1, v_2, T, \varphi, \lambda$ and f'_1 in terms of the independent variables x_2 and t .

3.4 Numerical methodology

We have implemented an efficient high-order temporal scheme for stiff equations based on the method of lines (MOL) to solve for longitudinal and shear motions. The MOL method can be implemented for various choices of spatial discretization. For discretization of convective terms we use a fourth-order convex essentially non-oscillatory (ENO) method [42] combined with a third-order, low-storage, semi-implicit Runge–Kutta method [82] for the MOL-ODEs. We will describe the ENO discretization in Chapter 4.

3.4.1 Description of low-storage semi-implicit Runge–Kutta solver

A more comprehensive discussion of the temporal scheme can be found in [82], and only a brief description of the method is given below. To solve a system of autonomous ODEs of the form $\mathbf{u}' = \mathbf{f}(\mathbf{u}) + \mathbf{g}(\mathbf{u})$, we use an explicit scheme for the non-stiff term \mathbf{f} and use an implicit scheme for the stiff term \mathbf{g} . We solve the system in an explicit/implicit hybrid fashion to achieve high-order

accuracy and stiffly stable calculation. A typical third-order method of this kind is given below:

$$\begin{aligned}
\mathbf{k}_j &= a_j \mathbf{k}_{j-1} + h[\mathbf{f}(\mathbf{u}_{j-1}) + \mathbf{g}(\mathbf{u}_{j-1} + \bar{c}_j \mathbf{k}_{j-1} + c_j \mathbf{k}_j)] \\
\mathbf{u}_j &= \mathbf{u}_{j-1} + b_j \mathbf{k}_j \\
(j &= 1, \dots, 3)
\end{aligned} \tag{3.39}$$

where h is the time increment, and the coefficients of the scheme are as follows:

$$\begin{aligned}
b_1 &= \frac{1}{3} & b_2 &= \frac{15}{16} & b_3 &= \frac{8}{15} & a_2 &= -\frac{5}{9} & a_3 &= -\frac{153}{128} \\
c_1 &= \frac{1}{5} & c_2 &= \frac{49}{75} & c_3 &= \frac{143}{600} & \bar{c}_2 &= -\frac{59}{135} & \bar{c}_3 &= -\frac{5283}{25600}
\end{aligned} \tag{3.40}$$

with $a_1 = 0, \bar{c}_1 = 0$.

In many instances where implicit calculation is not required, one can simply assign zero to the stiff vector \mathbf{g} and assign the entire source as a non-stiff vector \mathbf{f} and the standard explicit Runge–Kutta scheme is recovered.

3.4.2 Implementation

Before starting the computation one writes the governing PDEs in a conservative form such that limiting forms of the equations admit discontinuous solutions which are also admitted by the numerical approximation. Further, the stiff and nonstiff terms must be intelligently separated. In particular, convective terms, which are a priori discretized in space via fourth-order convex ENO scheme, are always treated as non-stiff terms. The viscous stress terms of momentum equations are treated as non-stiff, and are discretized by a fourth-order central differencing. Only the reaction source term, Ω , is treated as stiff and is subjected to the implicit numerical procedure. Otherwise the explicit method solves all the remaining terms of the equations.

We consider the shear motion to illustrate the numerical implementation. After converting the equations into a conservative form and separating the stiff and non-stiff terms, we can write the

conservative variables and the fluxes as follows:

$$\mathbf{u} = \begin{bmatrix} \rho \\ \rho v_1 \\ \rho v_2 \\ \rho c_v T \\ \rho \varphi \\ \rho f'_1 \\ \rho \lambda \end{bmatrix}, \mathbf{f} = \begin{bmatrix} -\frac{\partial}{\partial x} (\rho v_2) \\ -\frac{\partial}{\partial x} (\rho v_1 v_2 + \sigma_{12}) \\ -\frac{\partial}{\partial x} (\rho v_2 v_2 + \sigma_{22}) \\ -\frac{\partial}{\partial x} (\rho c_v T v_2) + \omega_1 \\ -\frac{\partial}{\partial x} (\rho \varphi v_2) + \omega_2 \\ -\frac{\partial}{\partial x} (\rho f'_1 v_2) + \rho_0 \frac{\partial v_1}{\partial x} \\ -\frac{\partial}{\partial x} (\rho \lambda v_2) \end{bmatrix}, \text{ and } \mathbf{g} = \begin{bmatrix} 0 \\ 0 \\ 0 \\ 0 \\ 0 \\ 0 \\ \rho \Omega \end{bmatrix} \quad (3.41)$$

where ω_1 and ω_2 are the right hand side source terms of T and φ . The convective terms are discretized by the fourth-order convex ENO scheme [42] and the resulting semi-discretized equation $\mathbf{u}_t = \mathbf{f} + \mathbf{g}$ are a system of autonomous ODEs in \mathbf{u} are integrated in time via the third-order Runge–Kutta method as discussed earlier.

3.5 Simulations of longitudinal and shear motions

We have validated the code written for the full model through a series of graduated tests. Since equations that correspond to classical elastodynamics and classical gasdynamics can be obtained simply by suppressing the appropriate terms, limiting versions of the code be used to solve problems with exact solutions, like standard Riemann problems, or small amplitude linear wave propagation. For example, Riemann problems have been computed for a special case of an ideal gas. In the special limiting case of small-displacement elasticity for shear motions, with the assumption of constant material properties, one can show that there are dilatation waves that travel at $\sqrt{(\lambda_s + 2\mu_s)/\rho_0}$ and shear waves that travel at $\sqrt{\mu_s/\rho_0}$, where $\lambda_s = 2\mu_s\nu_c/(1 - 2\nu_c)$.

3.5.1 One-dimensional shear motions

Here we discuss representative solutions to initial boundary-value problem that represents numerical experiments for shear motion. The problem set up as follows: A slab of material 15 mm thick in the x_2 direction is initially at an elevated temperature and suddenly subjected to a constant velocity shearing motion at the edge $x_2 = 15$ mm while the edge at $x_2 = 0$ is held fixed. The

material is thermally insulated. For the purpose of these experiments, the gas phase is suppressed and does not appear; hence the transitions documented here occur only between solid and liquid. We show representative results for two different initial conditions. First, we consider the initial temperature at 550 K with the constant shear velocity of 600 m/s, dubbed Shear Case A. In the second case, the initial temperature is slightly above the melting transition temperature at 560 K with a lower shearing velocity of 200 m/s, dubbed Shear Case B. Shear Case B exhibits more complex dynamics associated with multiple regions of phase change. Both cases show generic elastic wave interactions and reflections within solid-fluid regions. The computational domain has 500 points spread uniformly over 15 mm.

Figures 3.7 and 3.8 show x_2 - t contour plots of the thermodynamic variables T, φ, p, ρ , the velocities v_1 and v_2 , and the displacement gradient $f'_1(X_2)$. Initially the hot sample, just below the melting temperature at 550 K is exposed to the wall shear at 600 m/s. The rapid shearing at $x_2 = 15$ mm produces sufficient heating to cause rapid melting in a thin layer near the moving boundary. This is easily observed in Figure 3.7a and 3.7b for the temperature T , and phase variable φ , respectively. The shearing motion is then confined mostly to a thin shear layer as seen in Figure 3.8a for velocity v_1 , (in the direction of the imposed motion at $x_2 = 15$ mm). Note that the shear wave in the solid associated with v_1 is clearly observed as a wave that initially enters the domain at $x_2 = 15$ mm and travels toward $x_2 = 0$ mm and subsequently reflects off the stationary wall.

Figure 3.8b, for v_2 , displays waves that travel at the dilatational wave speed which is approximately twice the shear wave speed. The dilatational waves are generated by the initial growth of the melted layer and are associated with pressure waves of magnitude of approximately 10^8 Pa = 1 KBar. Note that the initial stress in the system is elevated due to the effect of thermal expansion at the initially raised temperature. Close inspection of the temperature and pressure fields shown in Figure 3.7a,c shows evidence of high frequency acoustic waves that can be traced to reflections and transmissions of waves through the solid/liquid interface near $x_2 = 15$ mm.

Figure 3.9 shows computed profiles for Shear Case A for ρ, T, p , and φ at times 5, 15, and 30 μ sec, which represents time cuts across Figure 3.7a-d. The profiles show elevated temperatures and phase change (melting) confined to the layer near the $x_2 = 15$ mm boundary. The fluctuations in the pressure, density and temperature profiles are the result of the acoustic disturbances propagating

through the solid and across the solid/liquid layer.

Note that the layer of liquid that develops at $x_2 = 15$ mm is a localized shear layer and can be thought of as a shear band. The material in the melt layer has very large v_1 -velocities and subsequently undergoes large deformation. The material in the solid phase essentially remains fixed in place as the fluid layer slides across it.

Shear Case B has the solid with its initial temperature slightly above the melt temperature, suddenly subjected to a (lower) constant shear motion of 200 m/s. As in Case A, a melt layer forms near $x_2 = 15$ mm and the dilation wave travels across the slab. After reflection at the fixed wall, a second melt layer develops near $x_2 = 0$ mm. Figures 3.10 and 3.11 show the additional complexity in the x_2-t record. The second melt layer causes additional scatter of waves generated near the $x_2 = 15$ mm boundary, and in turn the growth of the layer generates additional disturbances which transmit through the regions. One recalls that there are additional terms in the φ evolution equation that are associated with the deformational part of the stress. We clearly see that the stress waves (by themselves) can induce the phase transformation. One sees transient phase generation carried on the sub-characteristics in the phase variable plot Figure 3.10b. The next set of experiments for longitudinal motions, illustrate shock melting.

3.5.2 One-dimensional longitudinal motion: Reverse impact

The results discussed next are for two different longitudinal motions where a HMX specimen of thickness 15 mm is initially solid at the melt temperature ($T = 558$ K) and subjected to a reverse impact at speed -500 m/s for Longitudinal Case A and -200 m/s for Longitudinal Case B. The computational domain spans the 0.015 m with 500 mesh points.

For Longitudinal Case A, Figures 3.13 and 3.14 illustrate the phenomena of shock melting as predicted by the model. Figure 3.13a-e clearly shows the emergence of a shock wave from the stationary wall into the oncoming stream. Ahead of the shock, the material is solid, with $\varphi = 0$, behind the shock the material is liquid with $\varphi = 1$. The model predicts a shock with definite spatial structure as illustrated by the structure profiles taken at $t = 3 \mu\text{sec}$ and shown in Figure 3.14. In the shocked state, where the material has liquefied, there is a significant pressure increase to about 2.8 GPa (28 KBar) a 20 % density increase, and a drop in the temperature due to the

endothermic nature of the phase transformation. The pressure and density rise monotonically across the shock structure. The temperature increases slightly, then drops with the onset of the phase transformation from solid to liquid. Throughout the structure, the phase changes monotonically from solid to liquid.

Longitudinal Case B corresponds to a reverse impact experiment where the impact speed is reduced to -200 m/s but the initial temperature is raised slightly to 560 K, just two degrees above the melt temperature. Figure 3.15 shows the x_1-t contour plots. Figure 3.16 shows corresponding line cuts taken at time $t = 3 \mu\text{sec}$. Similar to Longitudinal Case A, shock induced phase transformation occurs, however a stable intermediate phase is produced behind the shock front with $\varphi = 0.33$. Interestingly, the model can be shown to allow these intermediate states in φ due to the contributions of the other stress-dependent source terms proportional to $\mu'_s(\varphi), \mu'_c(\varphi), \alpha'_c(\varphi)$, etc. as found in equation (3.5). A complete analysis of all possible φ -states and their stability is beyond the scope of this paper. However, we can illustrate the stability of the intermediate state for Longitudinal Case B by a numerical evaluation as follows. We take the evolution equation for φ , (3.24) to be rewritten as $\frac{\partial \varphi}{\partial t} = -v_1 \frac{\partial \varphi}{\partial x_1} + w_2$ where w_2 is the source term for the material derivative of φ . We then take the shock structure as obtained numerically at $t = 3 \mu\text{sec}$ for both Longitudinal Case A and B and plot $\partial \varphi / \partial t$ versus φ in Figure 3.17. Stable equilibria points (in φ) are found by the zeroes of $\partial \varphi / \partial t$. For Longitudinal Case A, only $\varphi = 0$, and $\varphi = 1$ are stable with $\partial \varphi / \partial t = 0$. But for Longitudinal Case B, the intermediate state $\varphi = 0.33$ is found to be stable. Our numerical experiments suggest that increasing the intensity of the reverse impact causes the intermediate states to disappear with $\varphi = 0, 1$ as the only stable equilibria.

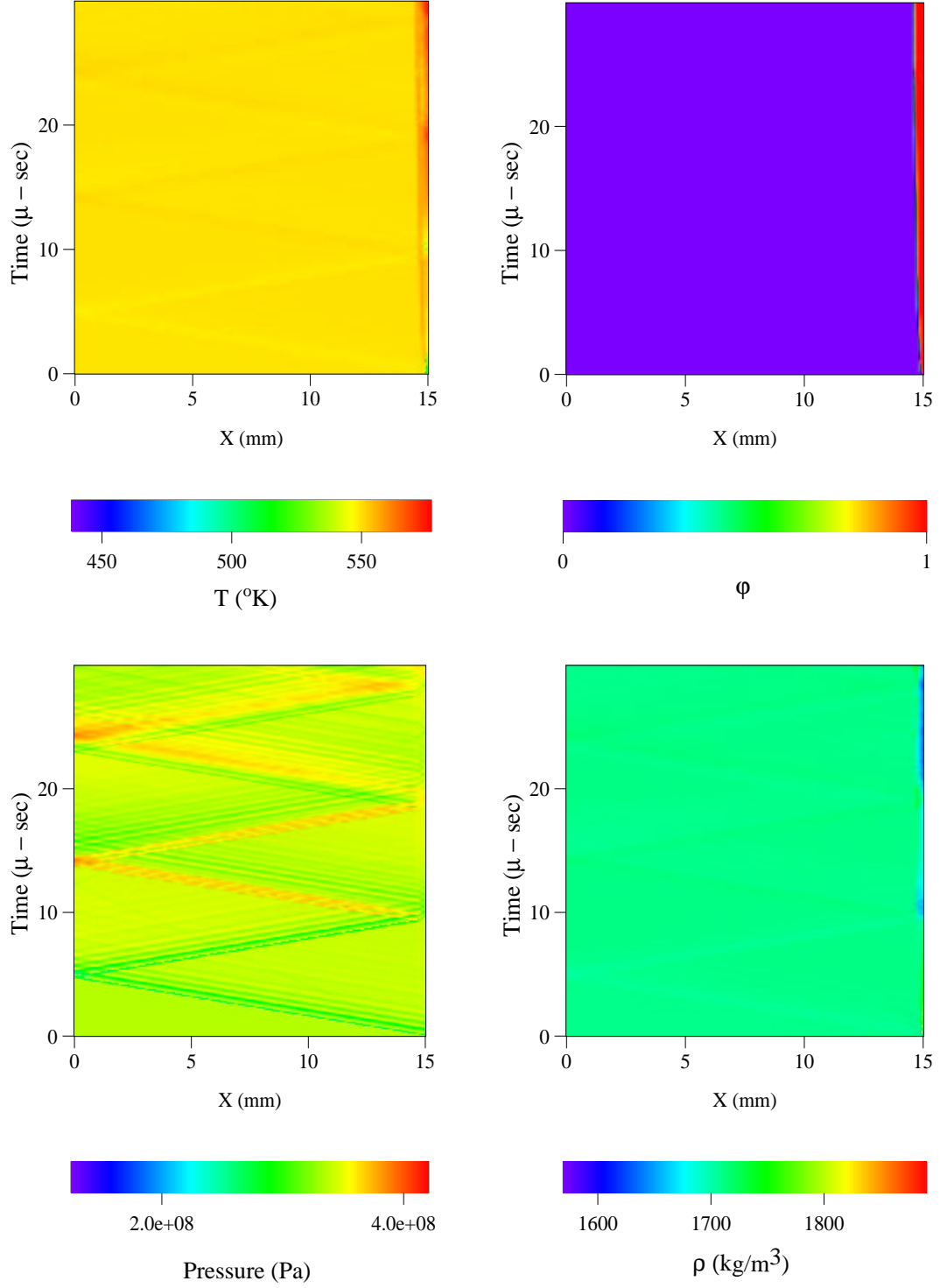


Figure 3.7: Temperature, phase, pressure, and density fields for a representative shear experiment ($v_{\text{shear}} = 600 \text{ m/s}$, $T_0 = 550 \text{ K}$).

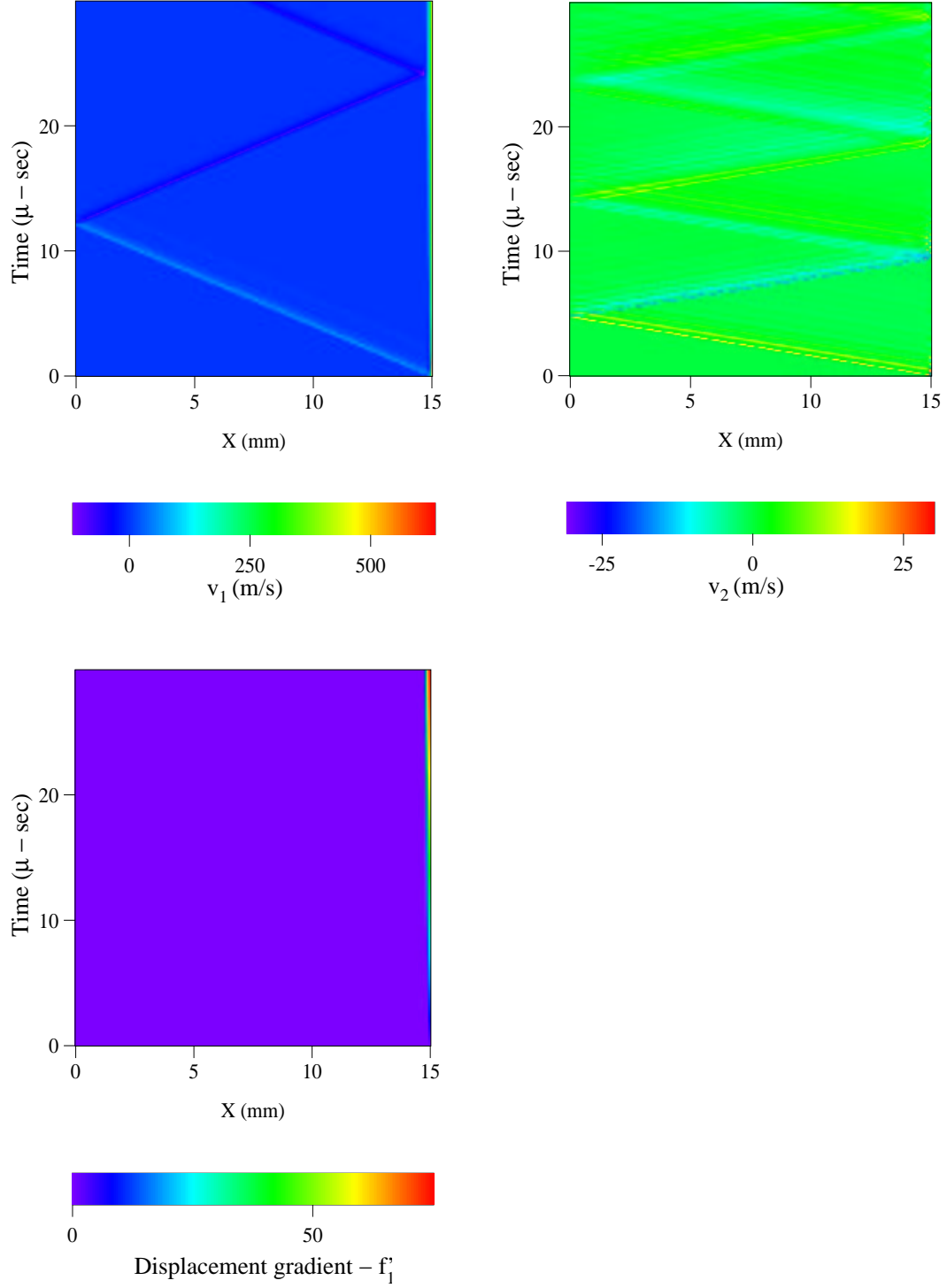


Figure 3.8: Shear velocity (v_1), compression velocity (v_2), and displacement gradient (du_1/dX_2) fields for a representative shear experiment ($v_{\text{shear}} = 600$ m/s, $T_0 = 550$ K).

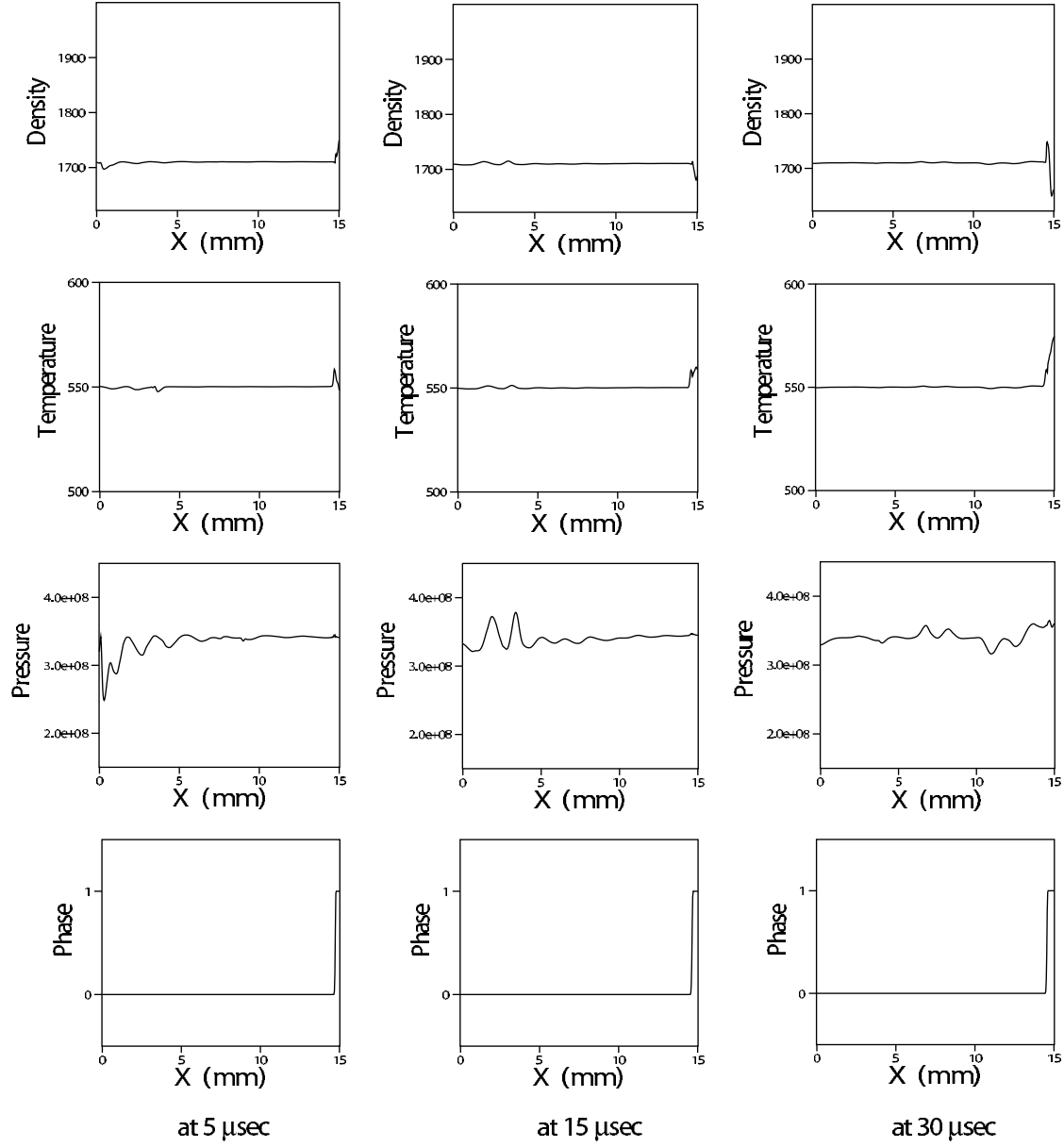


Figure 3.9: Snapshots of density, temperature, pressure, and phase field (from top to bottom) taken at time $t = 5, 15, 30 \mu\text{sec}$ from Figures 3.7 and 3.8 of plane shearing experiment.

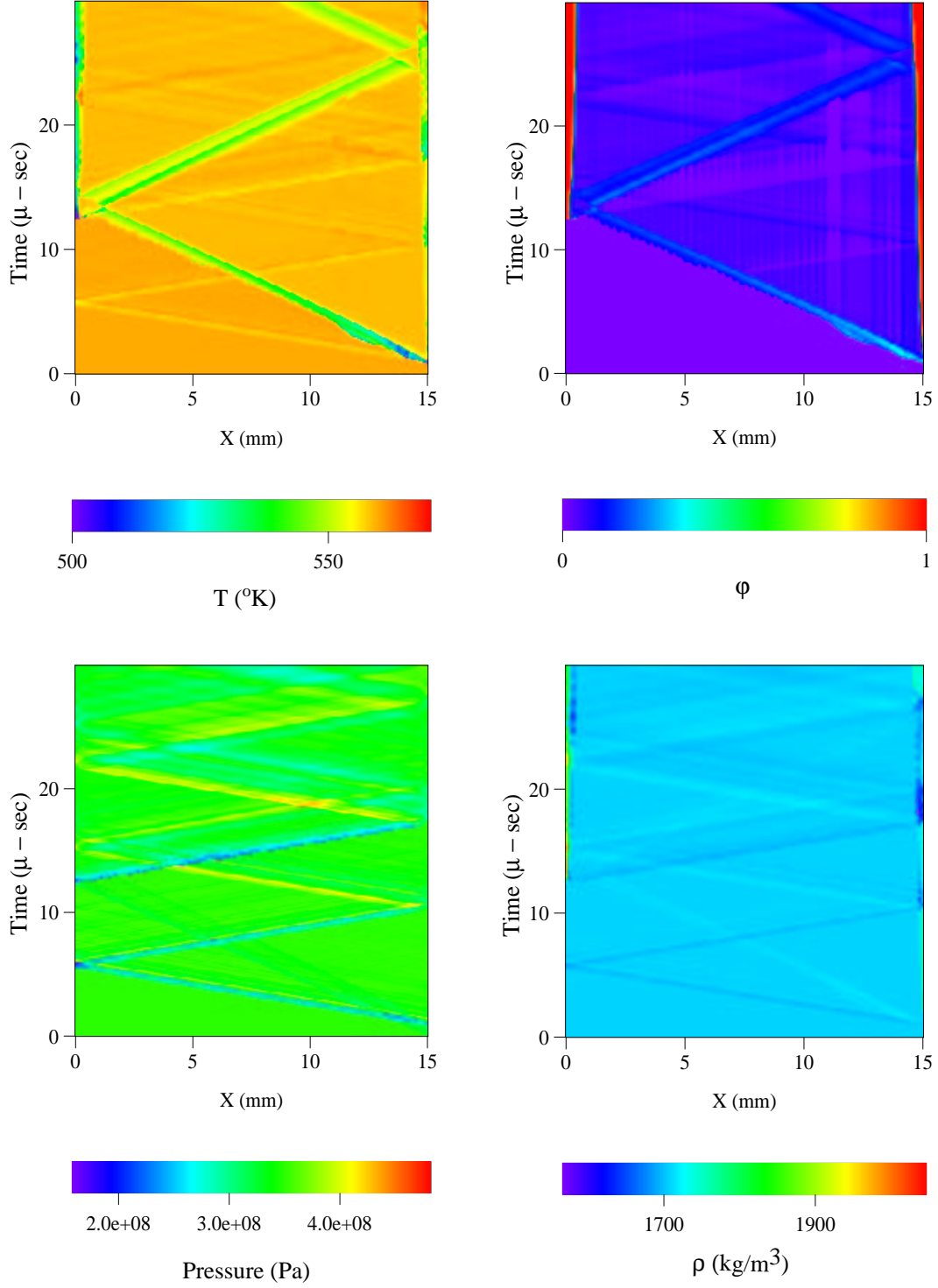


Figure 3.10: Temperature, phase, pressure, and density fields for a representative shear experiment ($v_{\text{shear}} = 200$ m/s, $T_0 = 560$ K).

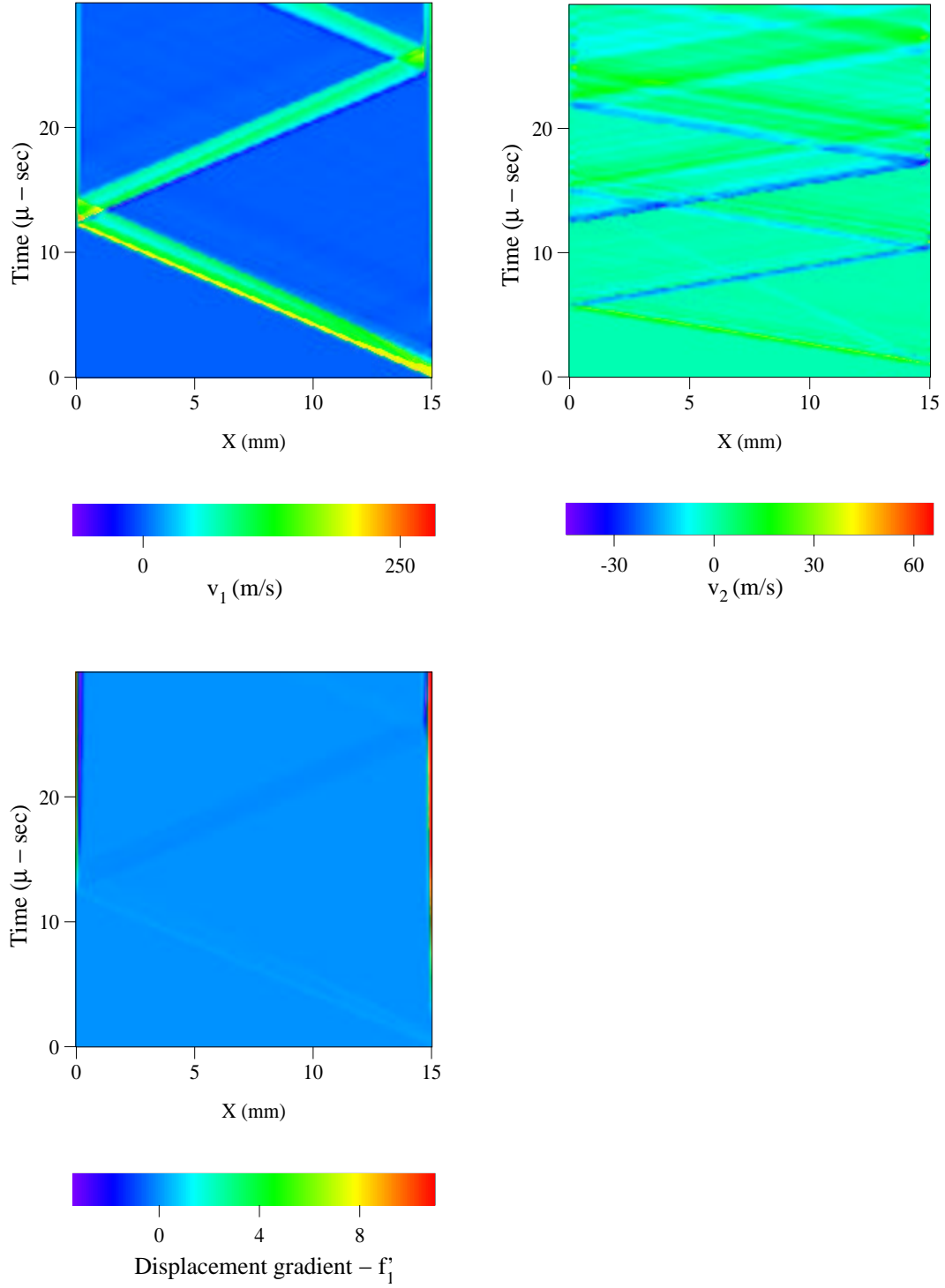


Figure 3.11: Shear velocity (v_1), compression velocity (v_2), and displacement gradient (du_1/dX_2) fields for a representative shear experiment ($v_{\text{shear}} = 200$ m/s, $T_0 = 560$ K).

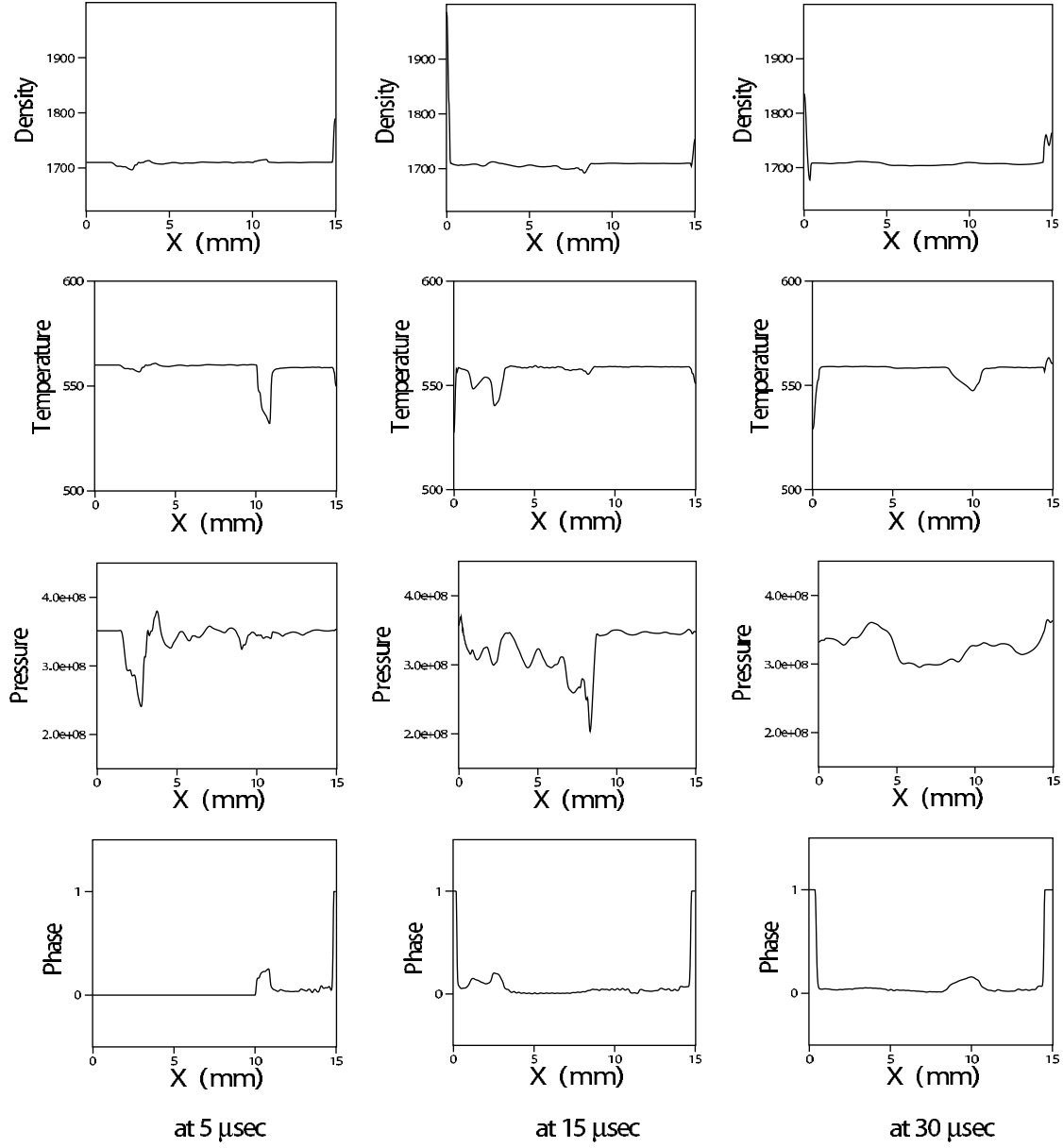


Figure 3.12: Snapshots of density, temperature, pressure, and phase field (from top to bottom) taken at time $t = 5, 15, 30 \mu\text{sec}$ from Figures 3.10 and 3.11 of plane shearing experiment.

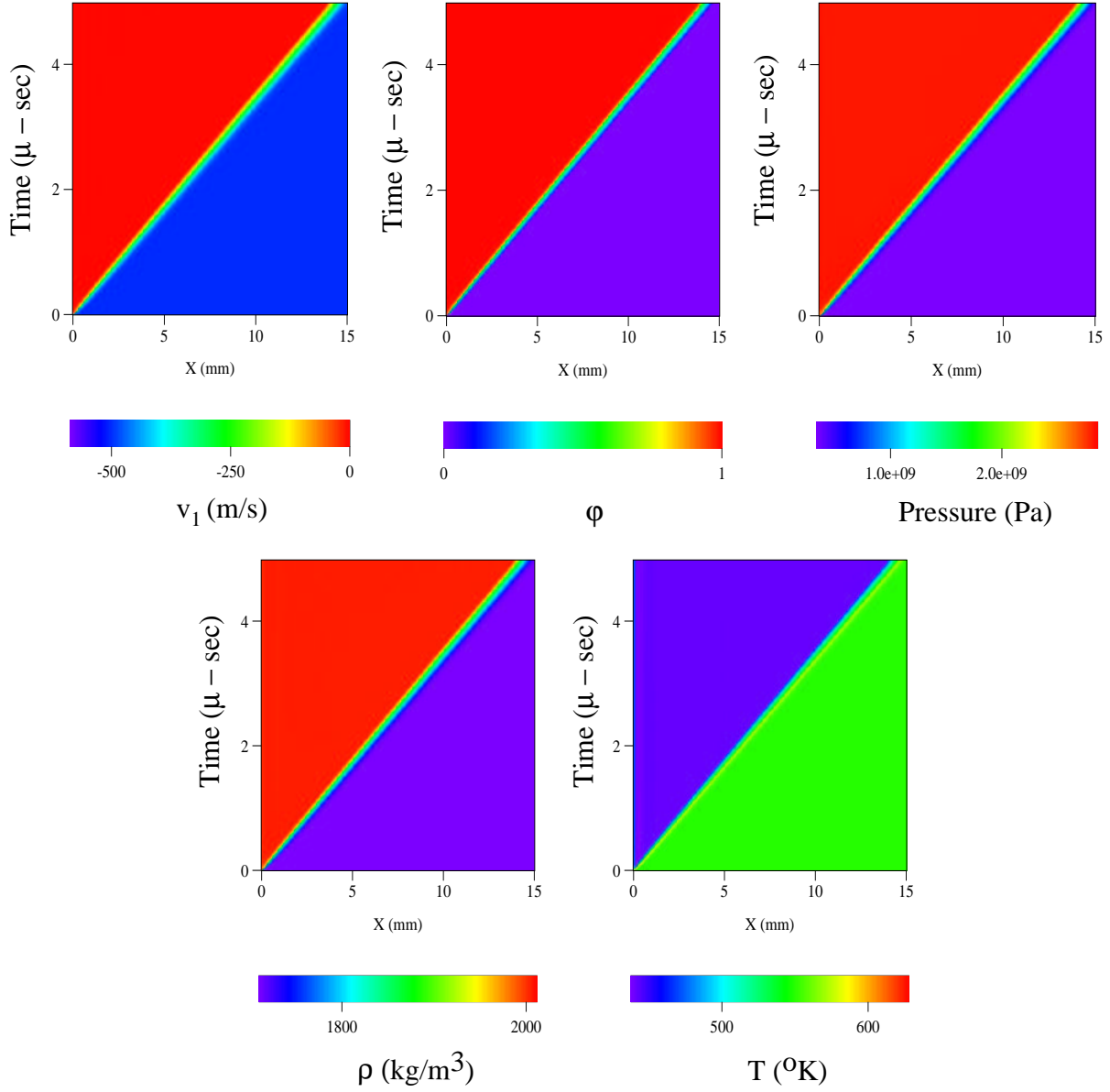


Figure 3.13: Velocity, phase, pressure, density and temperature fields for a representative reverse-impact (longitudinal) experiment ($v_{\text{impact}} = -500$ m/s, $T_0 = 550$ K).

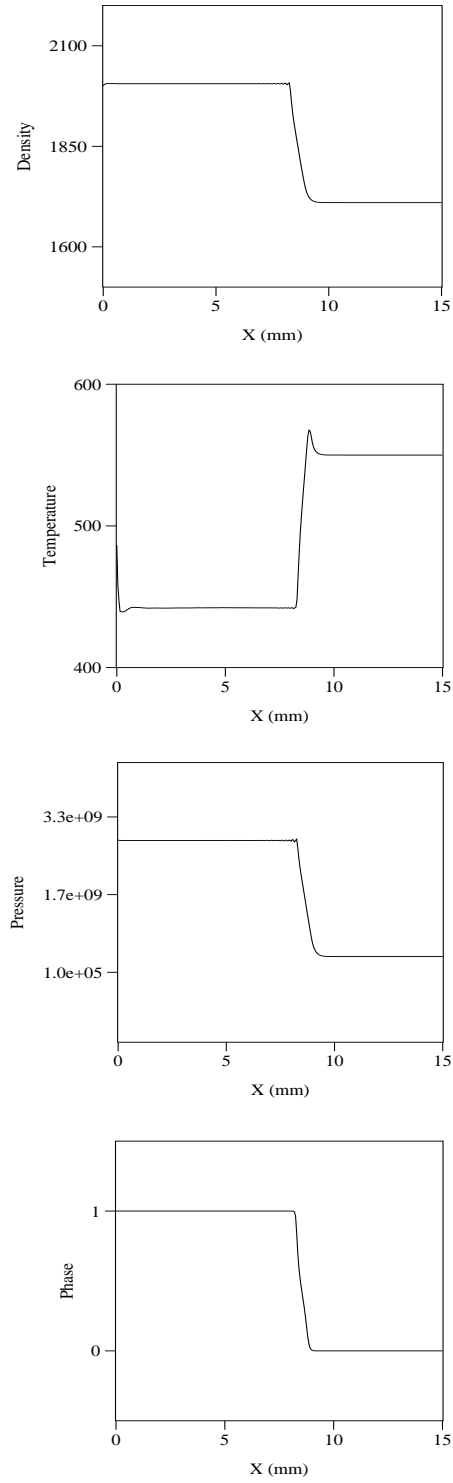


Figure 3.14: Snapshots of density, temperature, pressure, and phase field (from top to bottom) taken at time $t = 3\mu\text{sec}$ from Figure 3.13 of the longitudinal exercise.

3.6 Conclusions

We have illustrated that our model, fit to a real material, leads to predictions of simple motions (constant volume evolution, shear motion, and longitudinal motion) that are plausible. The model has the property that the constitutive theory automatically changes with the phase and is consistent with classical properties of that phase. We have shown that it is possible to fit the model to the known behavior of a real material.

Although idealized, the representative numerical experiments exhibit extremely rich behaviors. Strain localization phenomena occurred via melting in thin layers in many of the trials we have conducted. The phase change phenomenon is directly coupled to the material loading through the change in material type and changes in properties that are carried with the phase. We are ready to apply this new continuum model to more complex physical problems of interest to us. Of course extremely interesting and varied mathematical problems, such as steady traveling waves and their multidimensional stability, will arise that can profitably be analyzed by asymptotic means. The models embedded within this larger model may have greater application to the general theory of phase transformation. Of specific near term interest to us is a detailed study of the mechanically induced ignition of an energetic solid. We also plan to pursue a simplified version of this model to more fully examine the processes of classical melting/freezing and vaporization/condensation in the context of the model. We also anticipate the near term application of the model to problems of vaporizing fuels and condensed phase propellant combustion.

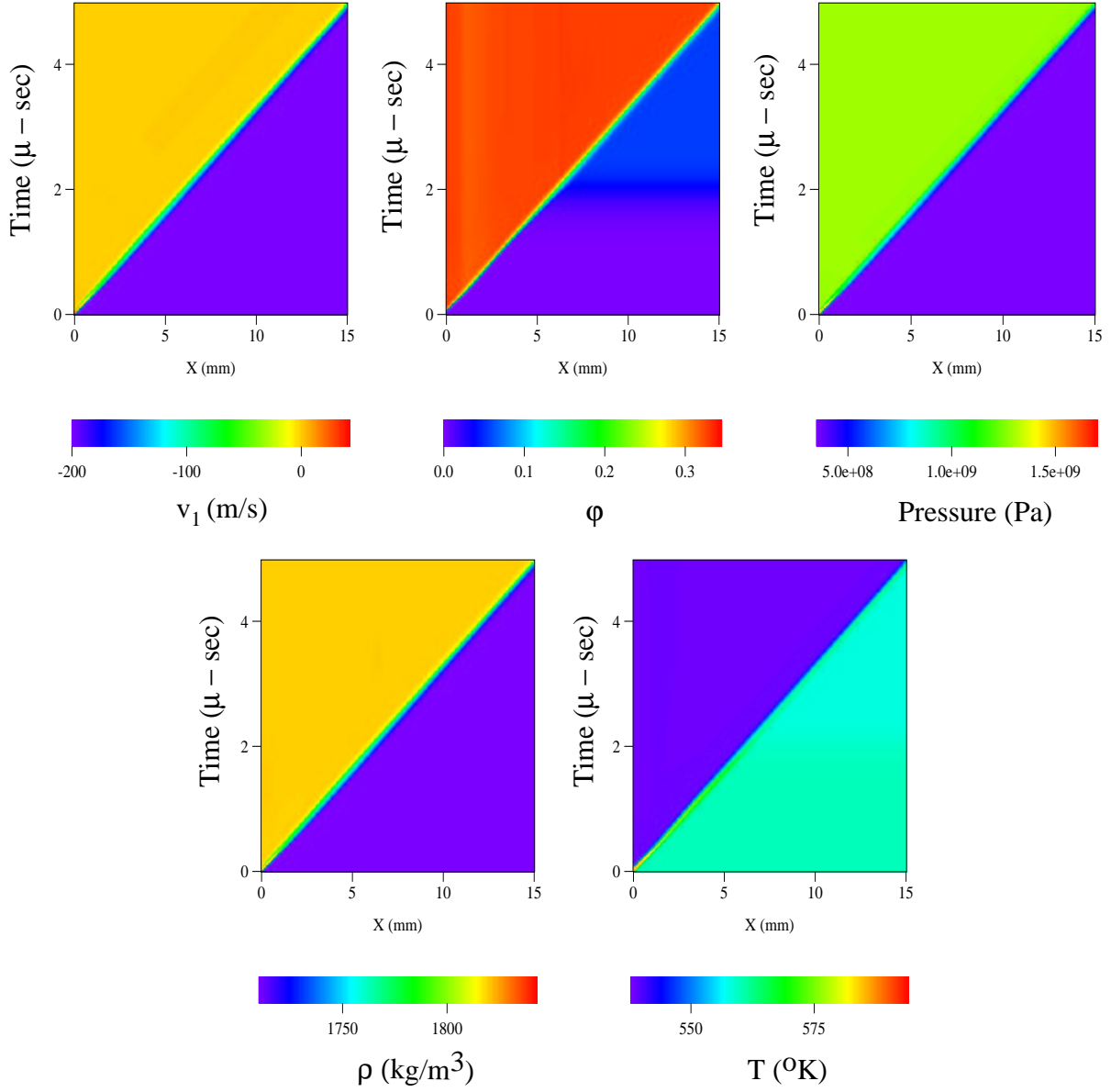


Figure 3.15: Velocity, phase, pressure, density and temperature fields for a representative reverse-impact (longitudinal) experiment ($v_{\text{impact}} = -200$ m/s, $T_0 = 560$ K).

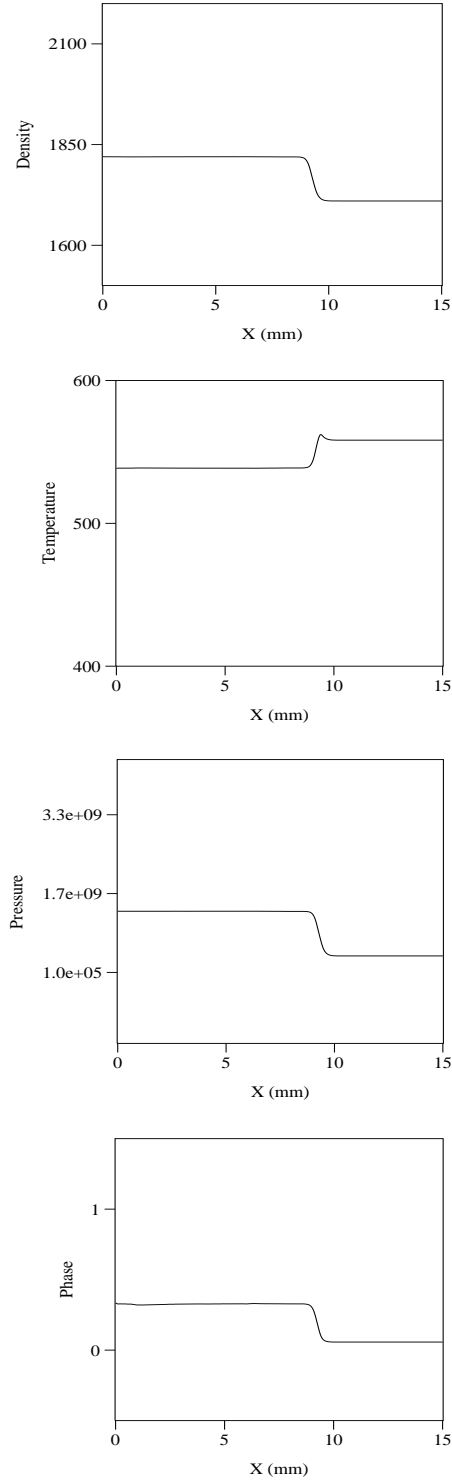


Figure 3.16: Snapshots of density, temperature, pressure, and phase field (from top to bottom) taken at time $t = 3\mu\text{sec}$ from Figure 3.15 of the longitudinal experiment.

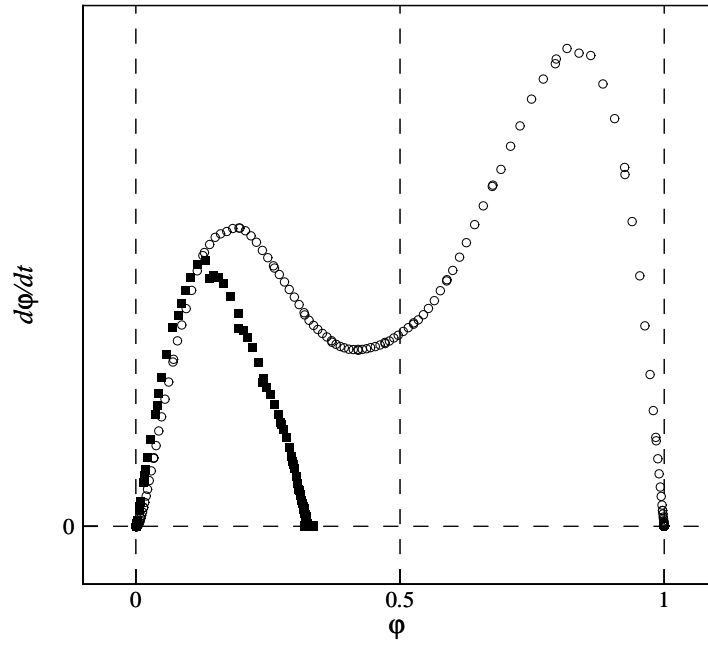


Figure 3.17: $d\varphi/dt$ versus φ for the two specialized reverse-impact experiments discussed. By varying the initial temperature, T_0 , meta-stable state ($\varphi \approx 0.33$) is shown as a local equilibrium point on the experiment represented by the square symbols. In contrast, the experiment shown by hollow circles suggests that $\varphi = 1$ is the only stable equilibria once the initial state is perturbed about the unstable point at $\varphi = 0$, corresponding to the solid state under the impact loading.

Chapter 4

High Resolution Multi-Material Impact: EM (Explosive)

In this chapter, we describe the development of the multi-material shock dynamics code aimed to solve the system of three dimensional multi-phase continuum equations. The major goal of the simulation was to capture the essential physical phenomena that take place in a material undergoing solid-liquid-gas phase transitions and chemical reaction when sharp discontinuities, such as shock waves and material interfaces are present. The two general methods are implemented to account for the discontinuities. One of them, the ghost-fluid-method (GFM), is used to track the material boundaries, while the ENO takes care of discretizing the governing equations in a manner suitable for capturing the sharp shock fronts. The code is fully parallelized for any shared memory processor (SMP) machines.

When dealing with deformations in complex materials, it is standard practice to use a Lagrangian representation of the solid, allowing computational grids to deform with the material, and there is no ambiguity associated with the convection between nodes and points. Finite-element methods that use this approach are considered to be a suitable spatial scheme to calculate both elastic and plastic material deformations. An Eulerian approach, however, is preferred in the field of high-speed gas dynamics. The reason for that is the extent to which gases and fluids are more apt to deformations when compared to solids. Instead of calculating the shape of deforming material by mapping the spatial configuration on the displaced meshes, Eulerian approach leaves the shape to be accounted for by means of either interface tracking or capturing techniques. The latter approach is more favorable in presence of high rate of deformations or complex geometries. Over the years,

a wide range of multi-material shock capturing techniques emerged (see [7], [31], [34], [38], [46]). In most cases, the solid phase calculations are performed with the finite element approach, while the hydrodynamics code is used to resolve the gas phase. These codes were capable of capturing a number of significant effects, such as material deformations, and for the large load rates, inter facial debonding and void formation. Yet, the nature of the material treatment simplifications made in these models inadvertently made them unable to reproduce many other interesting and important material behavior features.

We use our continuum description of energetic materials to create a model that is able to represent a material that may behave as solid, gas or liquid, depending on the dynamic phase transformations that take place. The model adopts itself and given the state of the material it has to account for, produces the sub-models to describe deformed solid or, when the solid is shocked and melts (or evaporates), to bring up the system of reactive Euler equations. In addition, the equation state has similar adaptive capabilities. In order to define the regions of applicability of each sub-model, the method uses a modified version of level set technique. This way, solid and gas media can be placed in ‘layers’, such that we can allow flow variables to connect between the fixed mesh points and work with added geometrical complexity.

In what follows, we will elaborate on the techniques we use to perform the high-order robust parallel computation.

4.1 Numerical method

Multi-material wave interaction problems may involve sharp material interfaces, contact surfaces, shocks, phase-transformation fronts, and detonation surfaces. there are two basic approaches to resolve the sharp evolving fronts. The first approach is tracking of the surface. In this approach, one would need to track the location of the jump and satisfy the local boundary conditions across the jump. An alternative and most widely used approach to treat sharp fronts is the capturing approach. Instead of maintaining the sharp profile, one would assign a best smooth curve across the grid nodes of the jump and eliminate the necessity to apply the jump conditions across the fronts completely. Most of modern shock treating schemes are of the latter kind as well as the essentially non-oscillatory (ENO) schemes.

We will use the ghost fluid method [27] for treating the sharp material interface and high-order convex ENO scheme for capturing other discontinuities of the flow field.

4.1.1 Level set and ghost-fluid-method

We use the level set equation

$$\frac{\partial \phi}{\partial t} + v_1 \frac{\partial \phi}{\partial x} + v_2 \frac{\partial \phi}{\partial y} = 0 \quad (4.1)$$

to track the location of the material interface represented by the zero level curve of $\phi(x, y)$. Initially, ϕ starts out as the normal distance function to the boundary represented by $\phi(x, y) = 0$, and in time the function will be evolved with the local velocities v_1 and v_2 . Resolving the advection of ϕ allows to track the exact location of material interface as a position of moving distant function where its value is equal to some specific value. So, as we further discuss how the other jumps in the flow field are treated, we want to emphasize that the material interfaces are tracked with the level set function.

Once the mechanism of tracking the location of interface is written down unambiguously, we look into the actual multi-material treatment in the light of GFM technique. First, one needs to identify that there is the real fluid (material) and the ghost fluid. Behaving like the real fluid in every way, the ghost fluid is represented by the nodes included beyond the material interface, and looks just like another fluid. In other words, both pressure and velocity of the ghost fluid of fluid 1 are the same as those of fluid 1, whereas the entropy is of fluid 2. And the opposite is true for the ghost fluid of fluid 2. In this way, one is able to prescribe the interface conditions in an elegant fashion without any explicit boundary jump conditions. Of course, entropy may not be always computed either density or temperature can alternatively be chosen as the thermodynamic variable which makes the fluid ‘look’ ghost.

In particular, the term, ‘isobaric-fix’ variable is reserved for entropy, density, or temperature, and is the variable under one-sided extrapolation from the real fluid side to the ghost zone. Under a constant pressure, the ideal EOS admits hyperbola on a ρ - T plot. Depending on p , each isobar represents a possible value of ρ and T . It is shown in [28] that spurious oscillations near a rigid wall (or a piston) can be avoided by properly modifying the either ρ or T of the ghost points representing

the wall interior while other flow variables are calculated from the differential equations. For instance, ρ is the isobaric-fix variable and its value in the ghost region are obtained by the one-sided extrapolation from the real fluid region.

4.1.2 General ENO scheme for spatial discretization

Details of this section can be found in [64, 42]. The conservative form of a one-dimensional hyperbolic system of differential equations takes the form

$$\frac{dq}{dt} + \frac{1}{\Delta x}(\hat{f}_{j+\frac{1}{2}} - \hat{f}_{j-\frac{1}{2}}) = 0. \quad (4.2)$$

The numerical fluxes, \hat{f} as they are called in the general ENO methods, are the determining ingredient of order of accuracy, and different versions of ENO (or earlier versions of TVD) schemes emerge depending on the kind of numerical fluxes constructed. Below, we will describe the general ENO construction of these fluxes to a high-order. The special version of high-order scheme called convex ENO will be explained later.

The fluxes in (4.2) are generated from the combination of the upwind and downwind portions represented by

$$\begin{aligned} f_{j+\frac{1}{2}}^+(q) &= \frac{1}{2}(f(q) + \alpha_{j+\frac{1}{2}}q) \\ f_{j+\frac{1}{2}}^-(q) &= \frac{1}{2}(f(q) - \alpha_{j+\frac{1}{2}}q). \end{aligned} \quad (4.3)$$

We note that variation of definition of α which controls the amount of viscosity or diffusion of a scheme results in different variations of these fluxes. In this work, the local Lax–Friedrichs fluxes are considered by specifying

$$\alpha_{j+\frac{1}{2}} = \max_{\min(q_j, q_{j+1}) \leq q \leq \max(q_j, q_{j+1})} \left| \frac{df}{dq} \right|, \quad (4.4)$$

to consider the largest eigenvalue of the flux Jacobian, df/dq , on the local computational domain

of (q_j, q_{j+1}) . The first order local Lax–Friedrichs flux is defined as follows:

$$\hat{f}_{j+\frac{1}{2}}^{LLF} = f_{j+\frac{1}{2}}^+(q_j) + f_{j+\frac{1}{2}}^-(q_{j+1}). \quad (4.5)$$

The second order flux is written as

$$\begin{aligned} \hat{f}_{j+\frac{1}{2}}^{LLF} &= \frac{1}{2}[f(q_{j+1}) + f(q_j) - \alpha_{j+\frac{1}{2}}(q_{j+1} - q_j)] \\ &+ \frac{1}{4}[\ell(r_j^+)(\Delta_+ f(q_j) + \alpha_{j+\frac{1}{2}}\Delta_+ q_j) - \ell(r_{j+1}^-)(\Delta_+ f(q_{j+1}) - \alpha_{j+\frac{1}{2}}\Delta_+ q_{j+1})] \end{aligned} \quad (4.6)$$

where

$$\begin{aligned} \Delta_{\pm} q_j &= \pm(q_{j\pm 1} - q_j) \\ r_j^+ &= \frac{(\Delta_- f(q_j) + \alpha_{j+\frac{1}{2}}\Delta_- q_j)}{(\Delta_+ f(q_j) + \alpha_{j+\frac{1}{2}}\Delta_+ q_j)} \\ r_{j+1}^- &= \frac{(\Delta_- f(q_{j+1}) - \alpha_{j+\frac{1}{2}}\Delta_- q_{j+1})}{(\Delta_+ f(q_{j+1}) - \alpha_{j+\frac{1}{2}}\Delta_+ q_{j+1})} \end{aligned} \quad (4.7)$$

and for ℓ , we chose the minmod limiter, given by

$$\ell(r) = \max(1, \min(r, 1)). \quad (4.8)$$

High-order convex ENO scheme

Here we describe the high-order convex ENO scheme [42]. We want to build a high-order (≥ 3) approximation to the local Lax–Friedrichs flux $\hat{f}(x)$. To do this, we first define a function $H(x)$, whose derivative with respect to x_j represents a non-oscillatory approximation to the flux $\hat{f}(x)$ at each grid points. For the clarity of discussion, we choose the upwinding procedure as $H_{\nu}^{(n)+}(x)$ involving the points (x_{j-1}, x_j) . Here (n) represents the order of approximation and ν labels the candidate interpolants as they are constructed in the section below. The downwinding version can be derived in an analogous way.

The first order polynomial interpolant to the upwind flux is

$$H^{(1)+}(x) = H[x_{j-1}] + H[x_{j-1}, x_j](x - x_{j-1}) \quad (4.9)$$

where we use the square bracket to denote the divided difference coefficient of the Newton interpolating polynomial. A table of these coefficients for each points in the computing grids can be constructed in a straight forward manner, and below we list those for up to the fourth-order polynomial:

$$\begin{aligned} H[x_j] &= H(x_j), \\ H[x_j, x_{j+1}] &= \frac{H[x_{j+1}] - H[x_j]}{x_{j+1} - x_j}, \\ H[x_j, x_{j+1}, x_{j+2}] &= \frac{H[x_{j+1}, x_{j+2}] - H[x_j, x_{j+1}]}{x_{j+2} - x_j}, \\ H[x_j, x_{j+1}, x_{j+2}, x_{j+3}] &= \frac{H[x_{j+1}, x_{j+2}, x_{j+3}] - H[x_j, x_{j+1}, x_{j+2}]}{x_{j+3} - x_j}. \end{aligned} \quad (4.10)$$

Differentiating (4.9) with respect to x and evaluating it at x_j gives the first order approximation

$$H^{(1)'+}(x_j) = H[x_{j-1}, x_j]. \quad (4.11)$$

Now, the second order interpolants are of two kinds involving the points (x_{j-2}, x_{j-1}, x_j) and (x_{j-1}, x_j, x_{j+1}) . In other words, we find that

$$\begin{aligned} H_1^{(2)+}(x) &= H[x_{j-2}] + H[x_{j-2}, x_{j-1}](x - x_{j-2}) \\ &\quad + H[x_{j-2}, x_{j-1}, x_j](x - x_{j-2})(x - x_{j-1}) \\ H_2^{(2)+}(x) &= H[x_{j-1}] + H[x_{j-1}, x_j](x - x_{j-1}) \\ &\quad + H[x_{j-1}, x_j, x_{j+1}](x - x_{j-1})(x - x_j). \end{aligned} \quad (4.12)$$

As in the first-order case, we evaluate the derivative of the second-order interpolants at x_j and find,

$$\begin{aligned} H_1^{(2)'+}(x_j) &= H[x_{j-2}, x_{j-1}] + H[x_{j-2}, x_{j-1}, x_j](3\Delta x) \\ H_2^{(2)'+}(x_j) &= H[x_{j-1}, x_j] + H[x_{j-1}, x_j, x_{j+1}](\Delta x). \end{aligned} \quad (4.13)$$

Here, we make the convex combination of $H_1^{(2)'+}(x_j)$ and $H_2^{(2)'+}(x_j)$ which is closest to the lower order approximation $H^{(1)'+}(x_j)$. So the second order interpolant based on this decision process is found as $H^{(2)'+}(x_j)$.

As for third-order, there are three interpolants involving points from $(x_{j-3}, x_{j-2}, x_{j-1}, x_j)$, $(x_{j-2}, x_{j-1}, x_j, x_{j+1})$, to $(x_{j-1}, x_j, x_{j+1}, x_{j+2})$. They are

$$\begin{aligned}
H_1^{(3)+}(x) &= H[x_{j-3}] + H[x_{j-3}, x_{j-2}](x - x_{j-3}) \\
&+ H[x_{j-3}, x_{j-2}, x_{j-1}](x - x_{j-3})(x - x_{j-2}) \\
&+ H[x_{j-3}, x_{j-2}, x_{j-1}, x_j](x - x_{j-3})(x - x_{j-2})(x - x_{j-1}) \\
H_2^{(3)+}(x) &= H[x_{j-2}] + H[x_{j-2}, x_{j-1}](x - x_{j-2}) \\
&+ H[x_{j-2}, x_{j-1}, x_j](x - x_{j-2})(x - x_{j-1}) \\
&+ H[x_{j-2}, x_{j-1}, x_j, x_{j+1}](x - x_{j-2})(x - x_{j-1})(x - x_j) \\
H_3^{(3)+}(x) &= H[x_{j-1}] + H[x_{j-1}, x_j](x - x_{j-1}) \\
&+ H[x_{j-1}, x_j, x_{j+1}](x - x_{j-1})(x - x_j)
\end{aligned} \tag{4.14}$$

$$+ H[x_{j-1}, x_j, x_{j+1}, x_{j+2}](x - x_{j-1})(x - x_j)(x - x_{j+1}) \tag{4.15}$$

whose derivative evaluated at x_j becomes

$$\begin{aligned}
H_1^{(3)'+}(x_j) &= H[x_{j-3}, x_{j-2}] + H[x_{j-3}, x_{j-2}, x_{j-1}](5\Delta x) \\
&+ H[x_{j-3}, x_{j-2}, x_{j-1}, x_j](11(\Delta x)^2) \\
H_2^{(3)'+}(x_j) &= H[x_{j-2}, x_{j-1}] + H[x_{j-2}, x_{j-1}, x_j](3\Delta x) \\
&+ H[x_{j-2}, x_{j-1}, x_j, x_{j+1}](2(\Delta x)^2) \\
H_3^{(3)'+}(x_j) &= H[x_{j-1}, x_j] + H[x_{j-1}, x_j, x_{j+1}](\Delta x) \\
&+ H[x_{j-1}, x_j, x_{j+1}, x_{j+2}](-(\Delta x)^2)
\end{aligned} \tag{4.16}$$

Now, using these interpolants, we will illustrate how a third-order convex ENO scheme is constructed. Similar procedure will apply for any orders higher than three. The weighted difference d_ν is evaluated between all candidate interpolants ($\nu = 1 \dots 3$) for third order ($n = 3$) and the second

order $(n - 1)$ interpolant. For illustration purpose, the convex-weighted differences are tabulated for $n = 3$ involving three possible interpolants labeled $\nu = 1 \dots 3$ as follows:

$$\begin{aligned} d_1 &= c_1(H_1^{(3)'+}(x_j) - H^{(2)'+}(x_j)) \\ d_2 &= c_2(H_2^{(3)'+}(x_j) - H^{(2)'+}(x_j)) \\ d_3 &= c_3(H_3^{(3)'+}(x_j) - H^{(2)'+}(x_j)) \end{aligned}$$

If all are of the same sign, we find the smallest of these difference and denote it $d_{\nu 0}$ with

$$H^{(3)'+}(x_j) = H_{\nu 0}^{(3)'+}(x_j). \quad (4.17)$$

Otherwise, the lower ordered interpolant is chosen so that

$$H^{(3)'+}(x_j) = H^{(2)'+}(x_j). \quad (4.18)$$

Values of c_ν are $c_1 = 1.0, c_2 = 0.7, c_3 = 1.0$ for third order and $c_1 = 1.0, c_2 = 0.7, c_3 = 0.7, c_4 = 1.0$ for fourth order.

Thus, we construct the third-order local Lax–Friedrichs flux by adding the upwind portion as outlined above and the downwind portion analogously derived:

$$\hat{f}_{j+\frac{1}{2}}^{LLF} = H'^+(x_{j+\frac{1}{2}}) + H'^-(x_{j+\frac{1}{2}}). \quad (4.19)$$

Substituting this into (4.2) sets up the differential equations for the Runge–Kutta scheme discussed in the next section. In the calculations included in this paper, we have used the fourth-order local Lax–Friedrichs convex ENO scheme with the third order Runge–Kutta scheme.

4.1.3 Low-storage semi-implicit Runge–Kutta scheme

A detailed discussion of this temporal scheme can be found in [83], [84], so only a brief description of the method will be given here. To solve a system of non-autonomous ODEs of the form $\mathbf{u}' = \mathbf{f}(\mathbf{u}, t) + \mathbf{g}(\mathbf{u}, t)$, we like to use an explicit scheme for the non-stiff term \mathbf{f} and use an implicit

scheme for the stiff term \mathbf{g} . Essentially, we solve the system in an explicit/implicit hybrid fashion to achieve high-order accuracy and stiffly stable calculation. A typical third order method of this kind are given below:

$$\left\{ \begin{array}{l} \mathbf{k}_1 = h[\mathbf{f}(t_o, \mathbf{u}_o) + \mathbf{g}(t_o + s_1 h, \mathbf{u}_o + c_1 \mathbf{k}_1)] \\ \mathbf{u}_1 = \mathbf{u}_o + b_1 \mathbf{k}_1 \\ \mathbf{k}_2 = a_2 \mathbf{k}_1 + h[\mathbf{f}(t_o + r_2 h, \mathbf{u}_1) + \mathbf{g}(t_o + s_2 h, \mathbf{u}_1 + \bar{c}_2 \mathbf{k}_1 + c_2 \mathbf{k}_2)] \\ \mathbf{u}_2 = \mathbf{u}_1 + b_2 \mathbf{k}_2 \\ \mathbf{k}_3 = a_3 \mathbf{k}_2 + h[\mathbf{f}(t_o + r_3 h, \mathbf{u}_2) + \mathbf{g}(t_o + s_3 h, \mathbf{u}_2 + \bar{c}_3 \mathbf{k}_2 + c_3 \mathbf{k}_3)] \\ \mathbf{u}_3 = \mathbf{u}_2 + b_3 \mathbf{k}_3 \\ \mathbf{k}_4 = a_4 \mathbf{k}_3 + h[\mathbf{f}(t_o + r_4 h, \mathbf{u}_3) + \mathbf{g}(t_o + s_4 h, \mathbf{u}_3 + \bar{c}_4 \mathbf{k}_3 + c_4 \mathbf{k}_4)] \\ \mathbf{u}_4 = \mathbf{u}_3 + b_4 \mathbf{k}_4 \end{array} \right.$$

where h is the time increments, and the coefficients of the scheme are given as follows:

$$\begin{array}{lll} b_1 = 3/4 & b_2 = -2/27 & b_3 = 2 \\ b_4 = 2/3 & a_2 = 23/4 & a_3 = -1/9 \\ a_4 = -5/2 & r_2 = 3/4 & r_3 = 1/4 \\ r_4 = 3/4 & s_1 = 2 & s_2 = 79/28 \\ s_3 = 127/84 & s_4 = 11/84 & c_1 = 2 \\ c_2 = 10901/12096 & c_3 = 7601/1344 & c_4 = 3/4 \\ \bar{c}_2 = -1027/256 & \bar{c}_3 = -817/36288 & \bar{c}_4 = -605/168. \end{array}$$

In many instances where implicit calculation is not required, one may simply assign zero to the stiff vector \mathbf{g} and assign the entire source as a non-stiff vector \mathbf{f} ; the standard explicit Runge–Kutta scheme is recovered. Several other versions of the low-storage hybrid Runge–Kutta scheme can be found in [78], [77], [67], [26].

4.2 Mathematical formulation

In this section, we describe the governing equations for a compressible gas and a Blatz–Ko solid. The following two subsections list the one-dimensional and two-dimensional form of the equations as they are used in the multi-material shock-physics simulation.

4.2.1 One-dimensional equations

The basic compressible gas equations can be written as

$$\begin{pmatrix} \rho \\ \rho v \\ \rho E \end{pmatrix}_t + \begin{pmatrix} \rho v \\ \rho v^2 + p \\ \rho E v + p v \end{pmatrix}_x = 0. \quad (4.20)$$

Here v represents velocity and E is the total energy per unit mass, while p is the pressure. The total energy is the sum of the internal and kinetic energy

$$E = e + \frac{1}{2}v^2 \quad (4.21)$$

where e is the internal energy per unit mass. Using the gamma law, one can express the internal energy as

$$e = \frac{p}{\rho(\gamma - 1)} \quad (4.22)$$

with the ratio of specific heats, γ . Thus two gases with different γ would essentially represent distinct materials with unequal entropy.

When no phase change occurs, the continuum equations for energetic materials in the general tensorial form from the earlier sections can now be written in the one-dimensional formulation. The single component of the displacement gradient shall be denoted by f' :

$$\begin{pmatrix} \rho \\ \rho v \\ \rho c_v T \end{pmatrix}_t + \begin{pmatrix} \rho v \\ \rho v^2 - \sigma \\ \rho c_v T v \end{pmatrix}_x = \begin{pmatrix} 0 \\ 0 \\ w \end{pmatrix} \quad (4.23)$$

where the Cauchy stress σ and the energy source w take the following one-dimensional form:

$$\sigma = \mu_c \frac{\rho}{\rho_o} (1 + f')^2 - \mu_c \left(\frac{\rho}{\rho_o} \right)^{\frac{1}{1-2\nu_s}} - \rho RT - \alpha \kappa \frac{\rho}{\rho_o} (T - T_o) + \nu_f \left(\frac{\partial v}{\partial x} \right) + 2\mu_f \frac{\partial v}{\partial x} \quad (4.24)$$

and

$$w = \kappa \frac{\partial^2 T}{\partial x_1^2} + (\nu_f + 2\mu_f) \left(\frac{\partial v}{\partial x} \right)^2 - \rho RT \frac{\partial v}{\partial x} - \frac{\rho}{\rho_o} \alpha \kappa T \frac{\partial v}{\partial x} \quad (4.25)$$

with

$$\frac{\rho}{\rho_o} = \frac{1}{1 + f'}. \quad (4.26)$$

Hence, we use the density as the independent strain measure and replace f' . Pressure can be deduced from the stress term as the negative of the non-deviatoric part, such that

$$\bar{p} = \mu_s (1 + f')^{-\frac{1}{1-2\nu_s}} - \frac{\mu_s (1 + f')^{-1}}{3} ((1 + f')^2 + 2) + \rho RT + \alpha \kappa \frac{\rho}{\rho_o} (T - T_o) \quad (4.27)$$

4.2.2 Two-dimensional equations

In two dimensions, the governing equations for both the compressible gas and the Blatz–Ko solid can be expressed by a system of hyperbolic PDE

$$\frac{\partial \mathbf{U}}{\partial t} + \frac{\partial \mathbf{F}}{\partial x} + \frac{\partial \mathbf{G}}{\partial y} = \mathbf{S}, \quad (4.28)$$

where \mathbf{U} is an array of the conservation variables, \mathbf{F} , \mathbf{G} represent the spatial fluxes, and \mathbf{S} represents the source.

In the case of a compressible gas in two dimensions,

$$\begin{pmatrix} \rho \\ \rho v_1 \\ \rho v_2 \\ \rho E \end{pmatrix}_t + \begin{pmatrix} \rho v_1 \\ \rho v_1^2 + p \\ \rho v_2 v_1 \\ \rho E v_1 + p v_1 \end{pmatrix}_x + \begin{pmatrix} \rho v_2 \\ \rho v_1 v_2 \\ \rho v_2^2 + p \\ \rho E v_2 + p v_2 \end{pmatrix}_y = 0 \quad (4.29)$$

where v_1 and v_2 are velocities in x and y -directions, respectively and E is the total energy per unit mass, and p is the pressure. The total energy is the sum of the internal energy and the kinetic energy, such that

$$E = e + \frac{1}{2}(v_1^2 + v_2^2) \quad (4.30)$$

with e being the internal energy per unit mass.

The two-dimensional equations of Blatz-Ko solid are considered without the phase-field equations. In two dimensions, the solid may deform in both x and y directions. Following the descriptions of the full continuum laws of energetic materials of the earlier chapter, we find

$$\begin{pmatrix} \rho \\ \rho v_1 \\ \rho v_2 \\ \rho c_v T \\ \rho H_{11} \\ \rho H_{12} \\ \rho H_{22} \\ \rho H_{21} \end{pmatrix}_t + \begin{pmatrix} \rho v_1 \\ \rho v_1^2 - \sigma_{11} \\ \rho v_2 v_1 - \sigma_{21} \\ \rho c_v T v_1 \\ \rho H_{11} v_1 \\ \rho H_{12} v_1 \\ \rho H_{22} v_1 \\ \rho H_{21} v_1 \end{pmatrix}_x + \begin{pmatrix} \rho v_2 \\ \rho v_1 v_2 - \sigma_{12} \\ \rho v_2^2 - \sigma_{22} \\ \rho c_v T v_2 \\ \rho H_{11} v_2 \\ \rho H_{12} v_2 \\ \rho H_{22} v_2 \\ \rho H_{21} v_2 \end{pmatrix}_y = \begin{pmatrix} 0 \\ 0 \\ 0 \\ w \\ \rho \left(\frac{\partial v_1}{\partial x} (1 + H_{11}) + \frac{\partial v_1}{\partial y} H_{21} \right) \\ \rho \left(\frac{\partial v_1}{\partial x} H_{12} + \frac{\partial v_1}{\partial y} (1 + H_{22}) \right) \\ \rho \left(\frac{\partial v_2}{\partial y} (1 + H_{22}) + \frac{\partial v_2}{\partial x} H_{12} \right) \\ \rho \left(\frac{\partial v_2}{\partial y} H_{21} + \frac{\partial v_2}{\partial x} (1 + H_{11}) \right) \end{pmatrix}, \quad (4.31)$$

where c_v is the specific heat at a constant volume, and H_{11}, H_{22} are the x and y component of longitudinal deformation gradient while H_{12} and H_{21} are the shear components of the displacement gradient tensor \mathbf{H} . Furthermore, the source of the internal energy $\rho c_v T$ is

$$\begin{aligned} w = & \kappa \left(\frac{\partial^2 T}{\partial x_1^2} + \frac{\partial^2 T}{\partial y^2} \right) + \nu_f \left(\frac{\partial v_1}{\partial x} + \frac{\partial v_2}{\partial y} \right)^2 + 2\mu_f \left[\left(\frac{\partial v_1}{\partial x} \right)^2 + \frac{1}{2} \left(\frac{\partial v_1}{\partial y} + \frac{\partial v_2}{\partial x} \right)^2 + \left(\frac{\partial v_2}{\partial y} \right)^2 \right] \\ & - \rho R T \left(\frac{\partial v_1}{\partial x} + \frac{\partial v_2}{\partial y} \right) - \frac{\rho}{\rho_o} \alpha \kappa T \left(\frac{\partial v_1}{\partial x} + \frac{\partial v_2}{\partial y} \right), \end{aligned} \quad (4.32)$$

where

$$\frac{\rho}{\rho_o} = \frac{1}{\sqrt{((1 + H_{11})^2 + H_{12}^2)(H_{21}^2 + (1 + H_{22})^2) - ((1 + H_{11})H_{21} + H_{12}(1 + H_{22}))^2}}. \quad (4.33)$$

The components of Cauchy stress are defined as follows:

$$\begin{aligned} \sigma_{11} = & \mu_s \frac{\rho}{\rho_o} [(1 + H_{11})^2 + H_{12}^2] - \mu_s \left(\frac{\rho}{\rho_o} \right)^{\frac{1}{1-2\nu_s}} \\ & - \rho RT - \alpha \kappa \frac{\rho}{\rho_o} (T - T_o) + \nu_f \left(\frac{\partial v_1}{\partial x} + \frac{\partial v_2}{\partial y} \right) + 2\mu_f \frac{\partial v_1}{\partial x} \end{aligned} \quad (4.34)$$

$$\sigma_{12} = \mu_s \frac{\rho}{\rho_o} [(1 + H_{11})H_{21} + H_{12}(1 + H_{22})] + \mu_f \left(\frac{\partial v_1}{\partial y} + \frac{\partial v_2}{\partial x} \right) \quad (4.35)$$

$$\sigma_{21} = \sigma_{12} \quad (4.36)$$

$$\begin{aligned} \sigma_{22} = & \mu_s \frac{\rho}{\rho_o} [(1 + H_{22})^2 + H_{21}^2] - \mu_s \left(\frac{\rho}{\rho_o} \right)^{\frac{1}{1-2\nu_s}} \\ & - \rho RT - \alpha \kappa \frac{\rho}{\rho_o} (T - T_o) + \nu_f \left(\frac{\partial v_1}{\partial x} + \frac{\partial v_2}{\partial y} \right) + 2\mu_f \frac{\partial v_2}{\partial y} \end{aligned} \quad (4.37)$$

As in one-dimensional case, ‘pressure’ of this two-dimensional formulation can be derived as the non-deviatoric part of the stress with a minus sign, such that

$$\begin{aligned} \bar{p} = & \mu_s \left(\frac{\rho}{\rho_o} \right)^{\frac{1}{1-2\nu_s}} - \frac{1}{3} \mu_s \frac{\rho}{\rho_o} [(1 + H_{11})^2 + (1 + H_{22})^2 + H_{12}^2 + H_{21}^2 + 1] \\ & + \rho RT + \alpha \kappa \frac{\rho}{\rho_o} (T - T_o). \end{aligned} \quad (4.38)$$

Thus far, two-dimensional equations of the compressible gas and the Blatz–Ko solid are described. To carry out the multi-material simulation involving both gas and solid, we list a complete set of governing equations in a flux form by defining the arrays \mathbf{U} , \mathbf{F} , \mathbf{G} , and \mathbf{S} . For an illustration purpose, we consider a Blatz–Ko plate in contact with two different compressible gases on either side. Below, each array represents three distinct materials in contact with two level set functions

representing the material interfaces:

$$\begin{array}{c}
\mathbf{U} = \left[\begin{array}{c} \tilde{\rho} \\ \tilde{\rho}\tilde{v}_1 \\ \tilde{\rho}\tilde{v}_2 \\ \tilde{\rho}\tilde{E} \\ - - - \\ \rho \\ \rho v_1 \\ \rho v_2 \\ \rho c_v T \\ \rho H_{11} \\ \rho H_{12} \\ \rho H_{22} \\ \rho H_{21} \\ - - - \\ \hat{\rho} \\ \hat{\rho}\hat{v}_1 \\ \hat{\rho}\hat{v}_2 \\ \hat{\rho}\hat{E} \\ - - - \\ \tilde{\rho}\phi_1 \\ \rho\phi_2 \end{array} \right]
\end{array}
\begin{array}{c}
\mathbf{F} = \left[\begin{array}{c} \tilde{\rho}\tilde{v}_1 \\ \tilde{\rho}\tilde{v}_1^2 + \tilde{p} \\ \tilde{\rho}\tilde{v}_2\tilde{v}_1 \\ \tilde{\rho}\tilde{E}\tilde{v}_1 + \tilde{p}\tilde{v}_1 \\ - - - \\ \rho v_1 \\ \rho v_1^2 - \sigma_{11} \\ \rho v_2 v_1 - \sigma_{21} \\ \rho c_v T v_1 \\ \rho H_{11} v_1 \\ \rho H_{12} v_1 \\ \rho H_{22} v_1 \\ \rho H_{21} v_1 \\ - - - \\ \hat{\rho}\hat{v}_1 \\ \hat{\rho}\hat{v}_1^2 + \hat{p} \\ \hat{\rho}\hat{v}_2\hat{v}_1 \\ \hat{\rho}\hat{E}\hat{v}_1 + \hat{p}\hat{v}_1 \\ - - - \\ \tilde{\rho}\phi_1\tilde{v}_1 \\ \rho\phi_2 v_1 \end{array} \right]
\end{array}
\begin{array}{c}
\mathbf{G} = \left[\begin{array}{c} \tilde{\rho}\tilde{v}_2 \\ \tilde{\rho}\tilde{v}_1\tilde{v}_2 \\ \tilde{\rho}\tilde{v}_2^2 + \tilde{p} \\ \tilde{\rho}\tilde{E}\tilde{v}_2 + \tilde{p}\tilde{v}_2 \\ - - - \\ \rho v_2 \\ \rho v_1 v_2 - \sigma_{12} \\ \rho v_2^2 - \sigma_{22} \\ \rho c_v T v_2 \\ \rho H_{11} v_2 \\ \rho H_{12} v_2 \\ \rho H_{22} v_2 \\ \rho H_{21} v_2 \\ - - - \\ \hat{\rho}\hat{v}_2 \\ \hat{\rho}\hat{v}_1\hat{v}_2 \\ \hat{\rho}\hat{v}_2^2 + \hat{p} \\ \hat{\rho}\hat{E}\hat{v}_2 + \hat{p}\hat{v}_2 \\ - - - \\ \tilde{\rho}\phi_1\tilde{v}_2 \\ \rho\phi_2 v_2 \end{array} \right]
\end{array}
\begin{array}{c}
\mathbf{S} = \left[\begin{array}{c} 0 \\ 0 \\ 0 \\ 0 \\ - - - \\ 0 \\ 0 \\ 0 \\ w \\ \rho \left(\frac{\partial v_1}{\partial x} (1 + H_{11}) + \frac{\partial v_1}{\partial y} H_{21} \right) \\ \rho \left(\frac{\partial v_1}{\partial y} (1 + H_{22}) + \frac{\partial v_1}{\partial x} H_{12} \right) \\ \rho \left(\frac{\partial v_2}{\partial y} (1 + H_{22}) + \frac{\partial v_2}{\partial x} H_{12} \right) \\ \rho \left(\frac{\partial v_2}{\partial x} (1 + H_{11}) + \frac{\partial v_2}{\partial y} H_{21} \right) \\ - - - \\ 0 \\ 0 \\ 0 \\ 0 \\ - - - \\ 0 \\ 0 \end{array} \right]
\end{array}$$

Of the 18 conservative variables, the first four describe high-explosive Euler gas, the next eight are for the material modeled after a Blatz–Ko material, the next four Euler variables model a light gas next to a Blatz–Ko material, and the last two are for the level-set passive scalars. One can also keep only 16 variables as the conservative variables by excluding the level set functions and do an independent time marching for convecting the passive scalars.

4.3 Code description

The code is written in Fortran 90. Though it has been optimized extensively for one processor calculations, the code further benefits from the parallelization. We chose the Open MP paradigm in its standardized use on a shared memory processor like the SGI Power Challenge 10000. Unlike the MPI (message passing interface), where each processor communicates by means of message passing, Open MP communicates through the variables (addresses). In this way, tasks that first developed in sequential pattern can be parallelized with placing Open MP directives wherever parallelizable.

We take the full advantage of Open MP supports for incremental parallelization of the sequential program developed a priori. The most fundamental task of optimization is the loop parallelization where each of the total number of processors divides the outer most coarsest do-loops into pieces. This is in most cases beneficial provided that the maximum loop count is greater than 500. Below, a sample Runge–Kutta step routine is written in Fortran with Open MP directives to illustrate the parallelization implementation:

```
*****
      SUBROUTINE CONVEXENO4-RK3
*****
#include <common.hd>

! - STAGE 1 -
C$OMP PARALLEL SECTIONS DEFAULT(SHARED)
C$OMP SECTION
      CALL fill_f(U)          ! assigning flux in x-direction
      CALL f_flux_llf(U)      ! making ENO fluxes in x-direction
C$OMP SECTION
      CALL fill_s(U)          ! assigning flux in y-direction
      CALL s_flux_llf(U)      ! making ENO fluxes in y-direction
C$OMP SECTION
      CALL fill_g(U)          ! assigning sources
C$OMP END PARALLEL SECTIONS

C$OMP PARALLEL DO PRIVATE(i,j,k)! performing j-loop in parallel
```

```

do 20 j = 0, ymesh
do k = 1, SYSDIM
do i = 0, xmesh
    U1(k,i,j) = U(k,i,j)
&          - (deltat/deltax)*(f_flux(k,i,j)-f_flux(k,i-1,j))
&          - (deltat/deltay)*(s_flux(k,i,j)-s_flux(k,i,j-1))
&          + deltat*(g(k,i,j))
end do
end do
20 CONTINUE
C$OMP END PARALLEL DO

! Likewise stage 2 and 3 can also be parallelized in this fashion

RETURN
END

```

In addition to loop parallelization, one can also assign different tasks to each available processor. Three independent flux assigning and calculating ENO fluxes are task-parallelized in the step before entering the do loop process in the sample code. In other instances, where entering of a parallel region by each thread (processor) must be controlled, one can take an advantage of the following directive to allow just one thread passing at a time.

```

C$OMP CRITICAL
    parallel region
C$OMP END CRITICAL

```

Here each tread will wait for the previous thread to complete the task within the parallel region before entering the region considered.

4.4 Numerical simulation

4.4.1 One-dimensional cases

“Ring-up” problem.

One possible testing of multi-material capability is to perform the classical “ring-up” problem: two different gases with different densities are in contact while the left boundary is driven by a piston at 500 m/s and the right boundary is open to a compliant boundary, modeling a vacuum (see Fig. 4.1). Table 4.4.1 lists the running parameters of this experiment. An incident shock generated

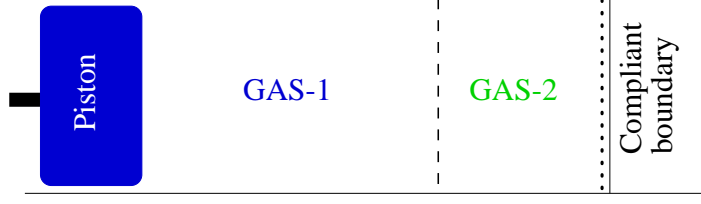


Figure 4.1: “Ring-up” test problem.

by the right-running piston travels in a lighter gas medium ($\rho = 0.01 \text{ kg/m}^3$) whose thickness is 1.436 cm. Using level set function to track the material interface in the GFM fashion, we expect to observe the incident, transmitted, and reflected states of the piston-generated shock.

By keeping track of the characteristic invariants, it is straight forward to find out the velocity of the incident shock which is generated by the right-running piston at 500 m/s. The analytically obtained value of the shock speed is 4041 m/s. Inspecting the numerically obtained result, we can approximate the calculated shock speed by taking the slope of the incident wave observed on the $x-t$ contour. Figs. 4.2 and 4.3 are the numerically obtained results during the transients. By inspection, the shock speed is approximately 4080 m/s, suggesting a good agreement with the exact value.

As the shock from the piston driver is incident on a material interface separating the two different gases, additional shocks and expansion waves are generated in both sides of the material. The motion of the material interface between the two gases as seen in the density contour is essentially the particle trajectory as it is typically referred to. The simulation is run until all three interfaces of the problem are parallel to each other at time ≈ 40 microseconds, when the initial state before the start of the ring-up is recovered. We can deduce from the result that the global energy balance which began as a stationary potential energy has transformed to a mainly kinetic

	Piston	Gas1 (1.436 cm)	Gas2 (0.5 cm)	Vacuum model
γ		1.4	1.4	1.4
$\rho \text{ (kg/m}^3\text{)}$		0.01	0.0128	0.0128
$p \text{ (Pascal)}$		1.0×10^5	1.0×10^5	$p_{interface}$
$v \text{ (m/s)}$	500	0	0	$v_{interface}$

Table 4.1: Running parameters of piston-driven laminate

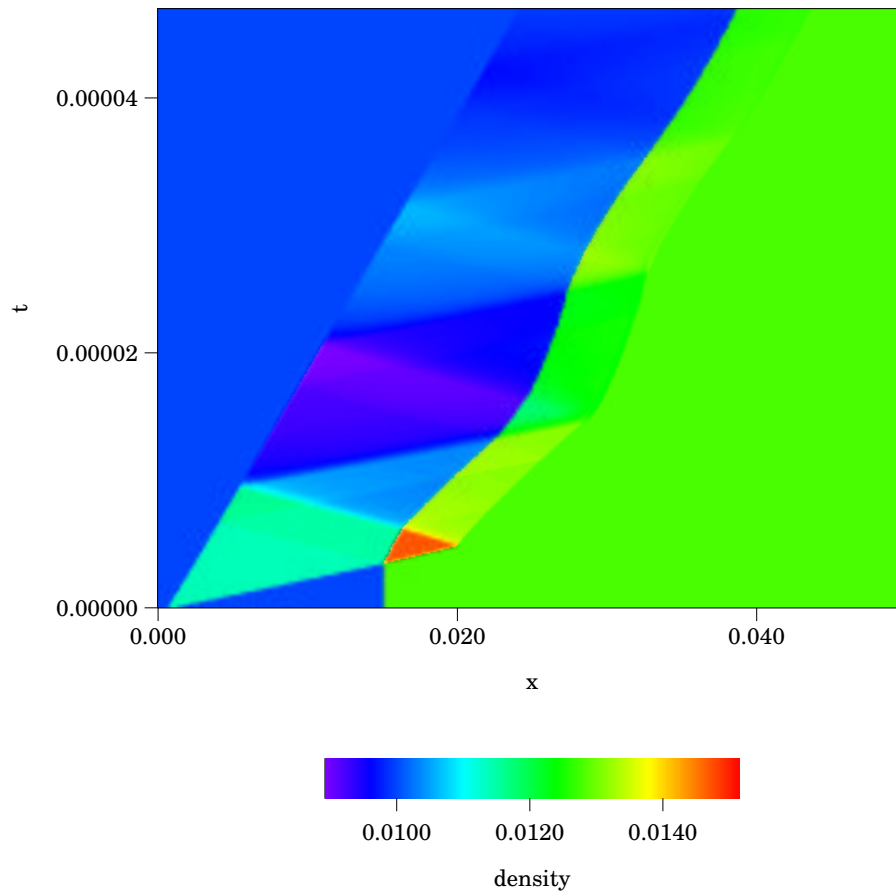


Figure 4.2: Space-time contour of density (kg/m^3).

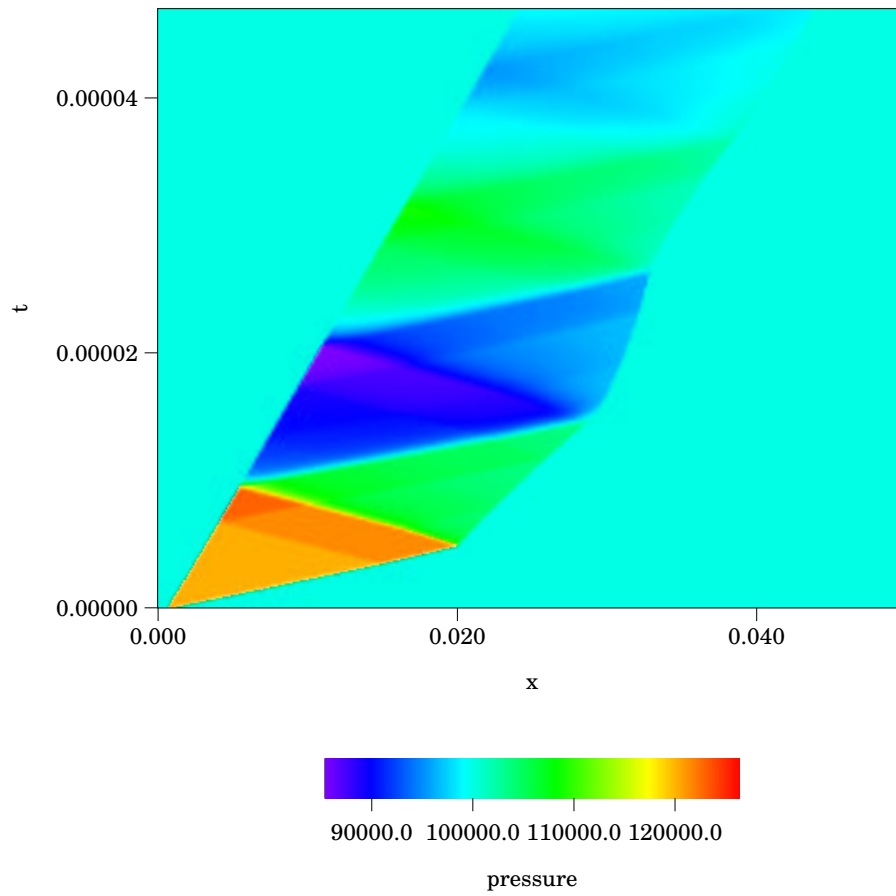


Figure 4.3: Space-time contour of pressure (Pa).

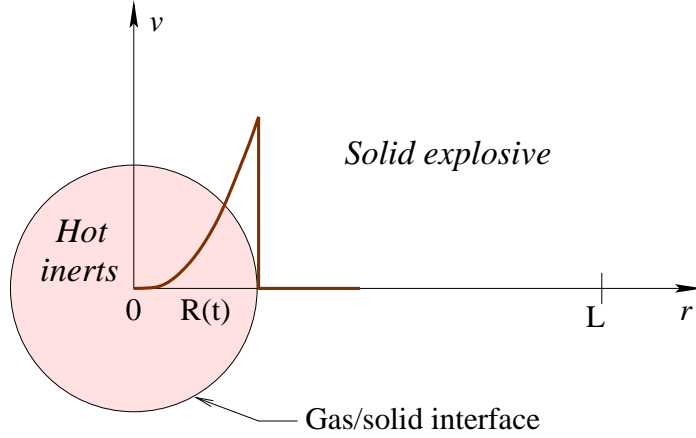


Figure 4.4: Schematic of typical hot-spot ignition setup.

energy during the busy ringing stage. Once the ringing shock interactions die out such that the layer propagate uniformly at the piston velocity, density and pressure of the initial phase are back to their initial values. Thus the ring-up test problem has been used to validate the mathematical formulations and also the multi-material simulation.

Hot-spot ignition of HMX

Another application of the multi-material shock physics code can be drawn from the hot-spot ignition of explosives (see Fig. 4.4). Vacancies and irregularities of a single HMX grain is modeled by hot inerts with detonation pressure of a typical high explosive. As the hot gas expands toward the neighboring unreacted solid explosive, a shock is transmitted into the solid unreacted explosive, and a material interface separating the inert and reactive HMX follows the local thermomechanical conditions. Depending on the size of the pore, detonation pressure, and the kind of solid propellant, go-no-go ignition criteria can be constructed for the explosive.

We model the hot inerts by the mock-up high explosive products gas as discussed in [2] and the solid explosive with the continuum equations for HMX. Then the interface between the two materials is computed with the GFM technique. The initial high pressure of the inert is set to 300 kbar to resemble a typical detonation pressure. We further assume the spherical symmetry with a (r, θ, ϕ) coordinate representation.

Figures 4.5, 4.6, and 4.7 are the space-time contours, expressing the wave structures within the

solid media as they interact with the incident detonation wave. One can distinguish the material interface (or contact surface) from the shock by comparing the pressure and density contours. Because of the complexity of the nature of the continuum equations for energetic materials, a wide spectrum of shock reflections are observed in these figures. In one instance close to the time at 1.25×10^{-2} micro-second, an isolated regions of a liquid can vaporize a-priori at a point or in a small region before the *arrival* of the evaporation front. In the phase contour in Fig. 4.6, three distinct colors (regions) are shown to represent the three phases of the materials, from the reacted product (or vapor), melt region (liquid) and the unreacted region (solid). The displacement gradient field is also calculated through out the Eulerian description as the non-elastic HMX undergoes strain deformation. Regions with high strains are also marked by the location where the pronounced wave interactions occur.

Since the experimental evidence suggest the onset of chemical reaction takes place well after the phase transformation of melting of HMX, we have computed these results without the reaction mechanism. We do predict that the inclusion of the detailed reaction mechanism of HMX will further enrich the behavior of multi-material ignition simulation.

4.4.2 Two-dimensional cases

Shear induced melting

The purpose of this two-dimensional numerical experiment is essentially to simulate the melting behavior of two different materials modeled by the continuum equations derived in the earlier chapters. The case of two pieces of nonlinear elastic materials under a severe shearing motion has its industrial applications in the explosive welding [48]. Two plates of different densities (8.9 g/cc and 7.8 g/cc) are initially separated by an air gap on the order of micron. The outer layer of one Blatz–Ko material is coated with an explosive which is ignited to initiate shock wave traveling at the speeds typical of detonation waves. As the shock wave traverses the top layer, the transmitted shock wave forces the upper layer to collide against the receptor in the shearing motion. Experimental observations support the fact that intially elastic solid materials under heavy shearing motion can undergo a melting transition and further the mixing or binding of the two different materials can occur by means of an instability develops around the contact surface. Upon cooling of the materials,

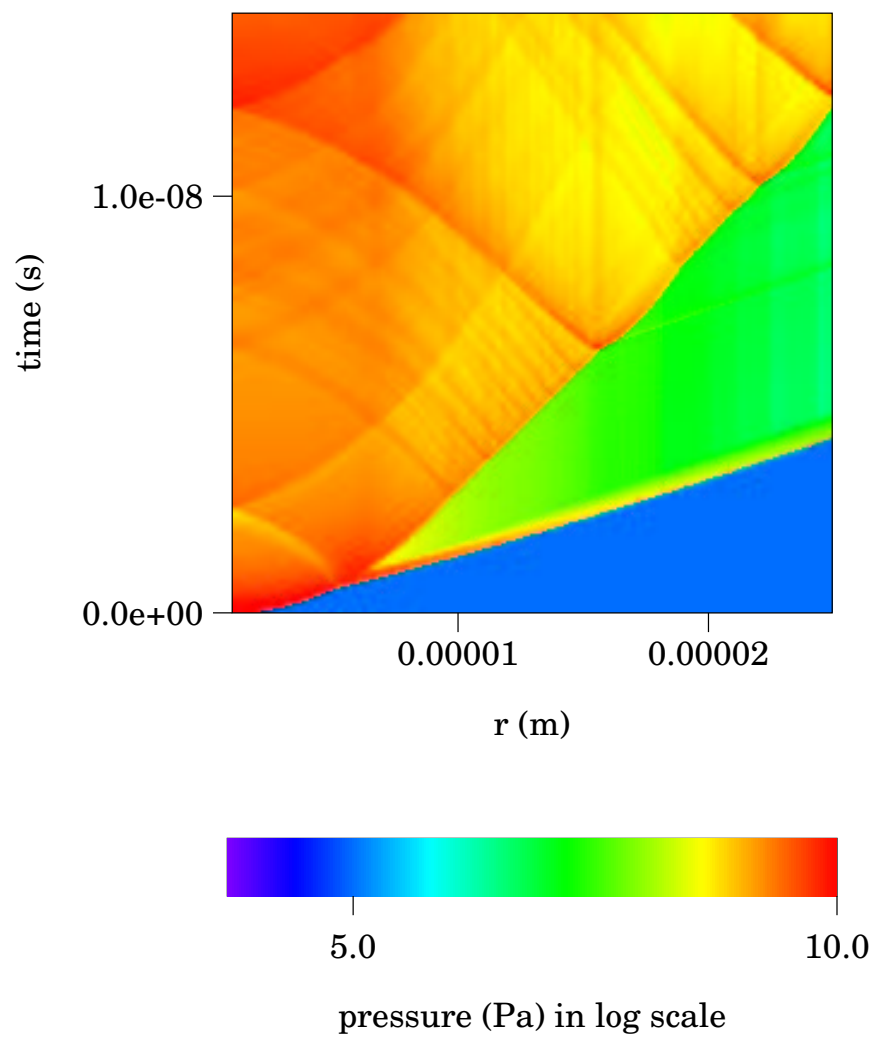


Figure 4.5: Space-time contour of pressure (Pa). ($\Delta r = 4.2 \times 10^{-8}$ m, $\Delta t = 2.0 \times 10^{-11}$ sec).

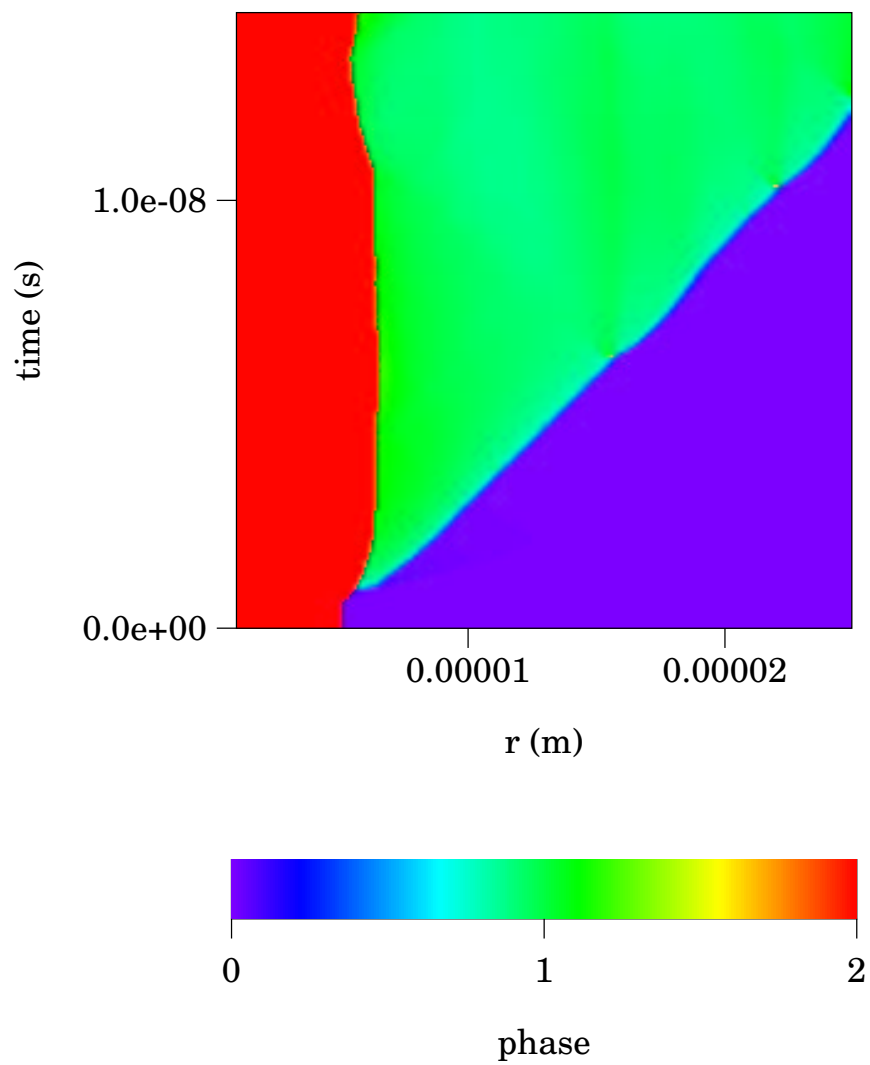


Figure 4.6: Space-time contour of phase-field. ($\Delta r = 4.2 \times 10^{-8}$ m, $\Delta t = 2.0 \times 10^{-11}$ sec).

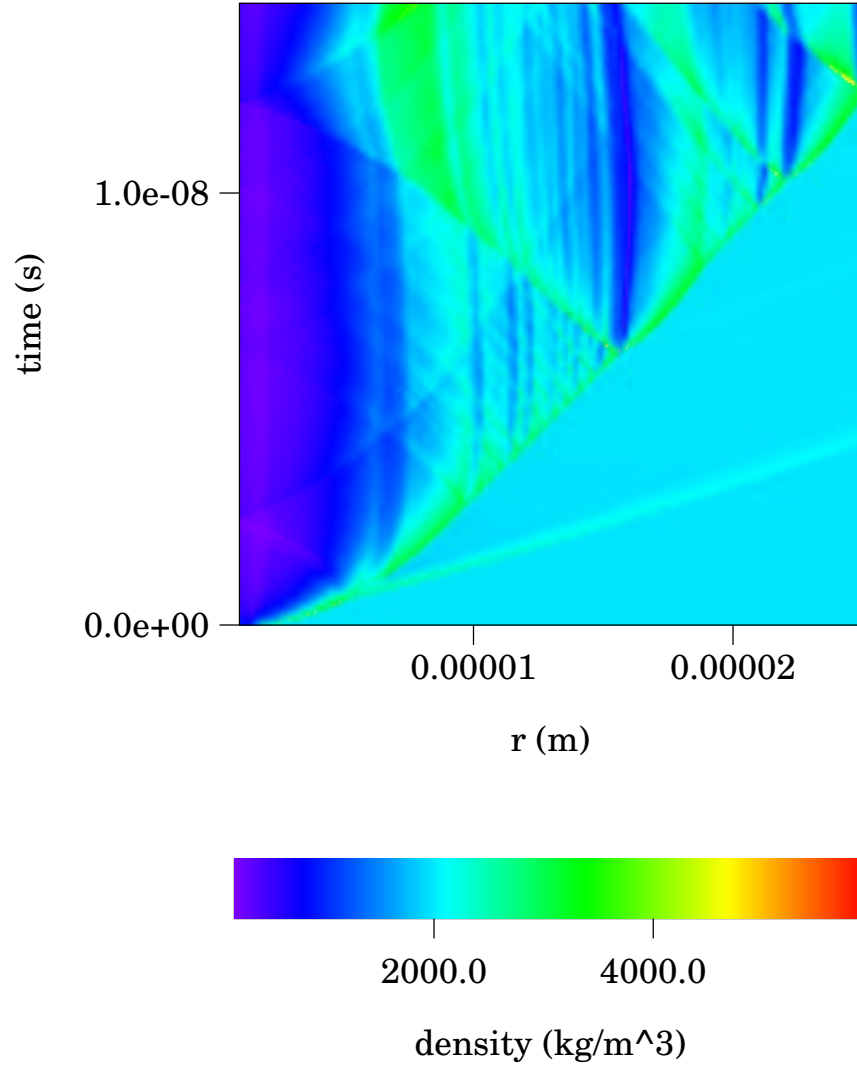


Figure 4.7: Space-time contour of density (kg/m^3). ($\Delta r = 4.2 \times 10^{-8} \text{ m}$, $\Delta t = 2.0 \times 10^{-11} \text{ sec}$).

the liquid layer goes back to its solid state and the final product of the experiment is a welded single piece of what initially was two different materials.

We simulate this two-dimensional dynamic melting and shearing motion between the two materials using our equations for a material that supports phase transitions. Shown in the Fig. 4.8 is the initial set of two materials before applying the shearing motion. The computational grid is 100 by 50 in x and y directions, respectively. A large shearing motion of 6000 m/s in is imposed on the materials. With time, we start to observe the propagating phase fronts separating melt layers from the solid media. Fig. 4.9 shows a band of liquid phase where the two materials are under heavy shearing motion. The x -directional velocity in Fig. 4.8 shows the unstable nature of the slip line between the two *liquidus* materials, where the rolling up of the interface resembles the classical Kelvin–Helmholtz instability in the liquids and gases.

Although the numerical experiment is performed just as far as the initiation of the mixing motion between the two materials, our model can in fact simulate the freezing process in which the liquid-banded region can undergo another phase transition back to the solid phase by forcing the temperature to go down well below the melting temperatures. Basically, we have accomplished two things from performing the particular experiment. We have first properly modeled the multi-dimensional melting, likewise the evaporation, of energetic materials under hard straining. Furthermore, by the evidence provided by the presence of Kelvin–Helmholtz-like instability, the fluid characteristics of the liquidus materials are also modeled by our overall continuum equations.

Detonation shock interaction with Blatz-Ko elastic plate

Figure 4.10 depicts the two-dimensional multi-material interaction experiment: two detonators (sources) are placed vertically three centimeters apart and a plate of thickness one centimeter is placed at one centimeter away from these sources. To the right of the plate, there is a lighter fluid, modeled by an Euler gas with density close to 1 g/cc (i.e. water).

The condensed phase explosive gas resembling the HMX products is placed on the left side of a solid plate under consideration. For simplicity, we assume that there are no phase transformations in the plate and that no reaction occurs in the explosive region. Instead, we initialize a hot-spot, filled with inert product gas with $p = 300$ kbar, $\rho = 2$ g/cc, $\gamma = 3$, and simulate a strong pressure

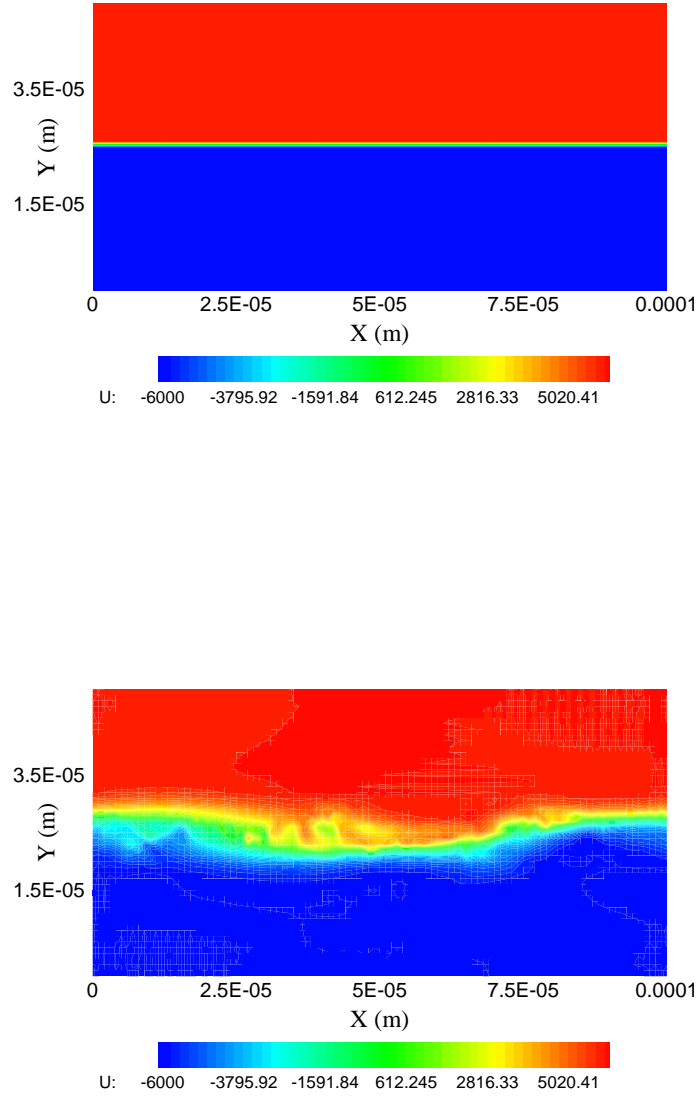


Figure 4.8: Initial setup (top) and final velocity profile of shearing of two Blatz-Ko elastic materials of different density.

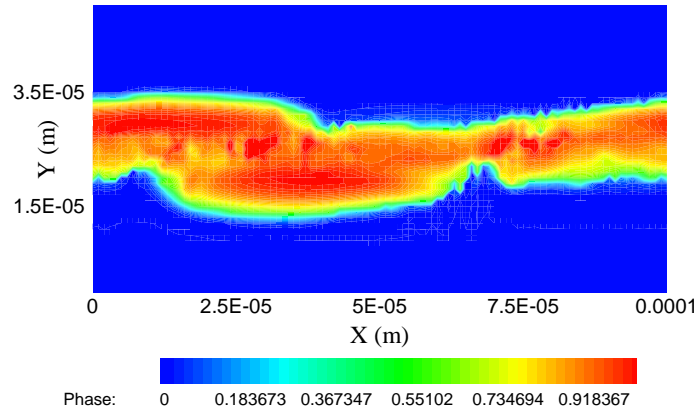
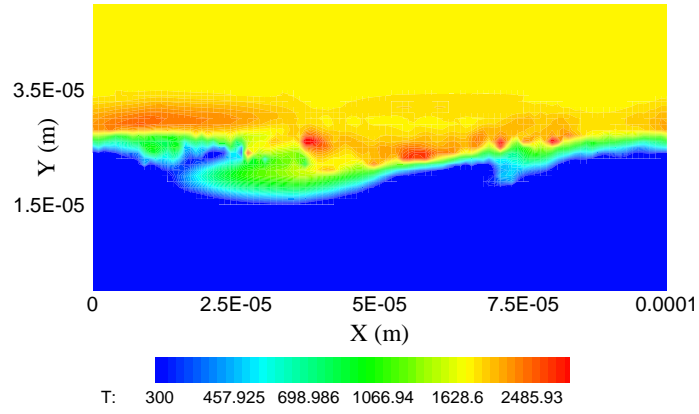


Figure 4.9: Temperature (Kelvin) and phase variable shown from top to bottom.

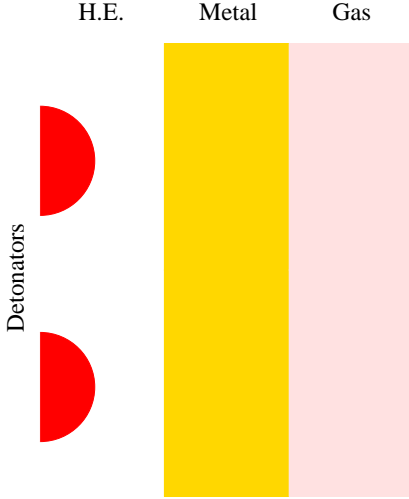


Figure 4.10: Two-dimensional shock-plate interaction problem.

wave propagating in the radial direction.

As for the material representing a plate, the shear modulus μ_s for copper is used, whose value is on the order of GPa. The strain energy of the plate is of the classical Blatz-Ko material form for solid whose undeformed density is 7.9 g/cc.

Unlike the previous case involving phase changes in the solid HMX, the Blatz-Ko plate simulation of this section is rather simplified. The numerical experiment is a simplified model and melting/freezing is precluded. Instead, the focus is on shock formation, generation of high strains in the shocked solid material. Finally, to the right of the plate, we place a lighter dense fluid, modeled by an Euler gas with $\gamma = 1.4$ and $\rho = 1$ g/cc.

Figs. 4.11 and 4.12 depict the x - y contour density and pressure field at an instant when the incident detonation bow shock has made its way into, and beyond both material interfaces of the plate. As pressure field does not show the material interfaces separating the gases from the solid, one can observe the deformed shape of the material as internal boundaries exactly tracked by means of level set functions. Transmitted, reflected, and Mach shocks are all present inside the solid medium where a pair of triple points is generated as these waves interact with each other. The kind of shock structures observed in the material is classical in a sense that any two-dimensional shock traveling down the channel will develop triple points. This means that the equation of state of the material modeled through our constitutive equations are capable of transforming into an compressible Euler gas in the presence of a strong shock. Figs. 4.13 and 4.14 show earlier snap

shots of both density and pressure fields. Similar shock structures are observed within the solid.

Peak density within the solid field is about twice the undeformed density. With only 200 mesh points in both directions, we were able to resolve shocks, rolling-up slip lines separating the Mach stems and reflections. However, we still suffer from consequences of using the Eulerian fixed grids, so that a great improvement in the resolution is possible in the regions of main interest with the help of adaptive refinement techniques. At this stage, though, we are taking the maximum benefit of the multi-processor computations by dividing the task within the calculations and the elegant treatment of the material interface within the Eulerian approach. With added features of the current version of multi-material code, we will be able not only to resolve the shock structures, but also to simulate the pinching-off behavior of the material interface.

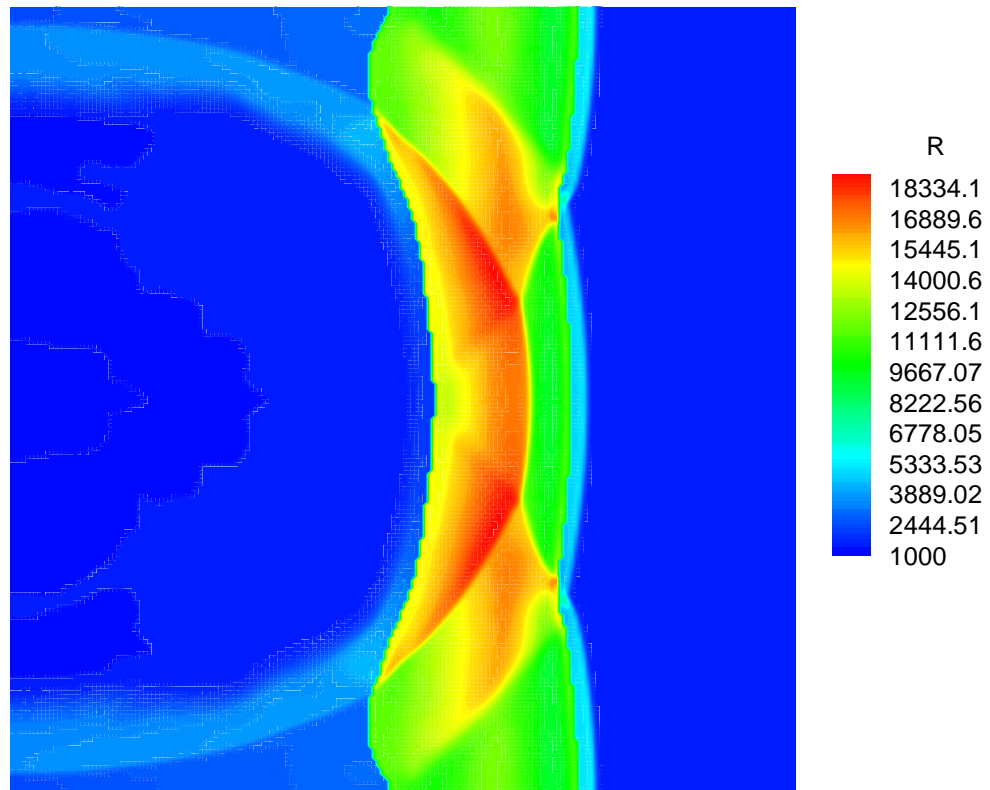


Figure 4.11: Density (kg/m^3) contour at an instant when the incident shock has penetrated through the second material interface of a Blatz-Ko elastic plate. Grid of 400 by 400 points spans a physical domain of 3 cm by 3 cm.

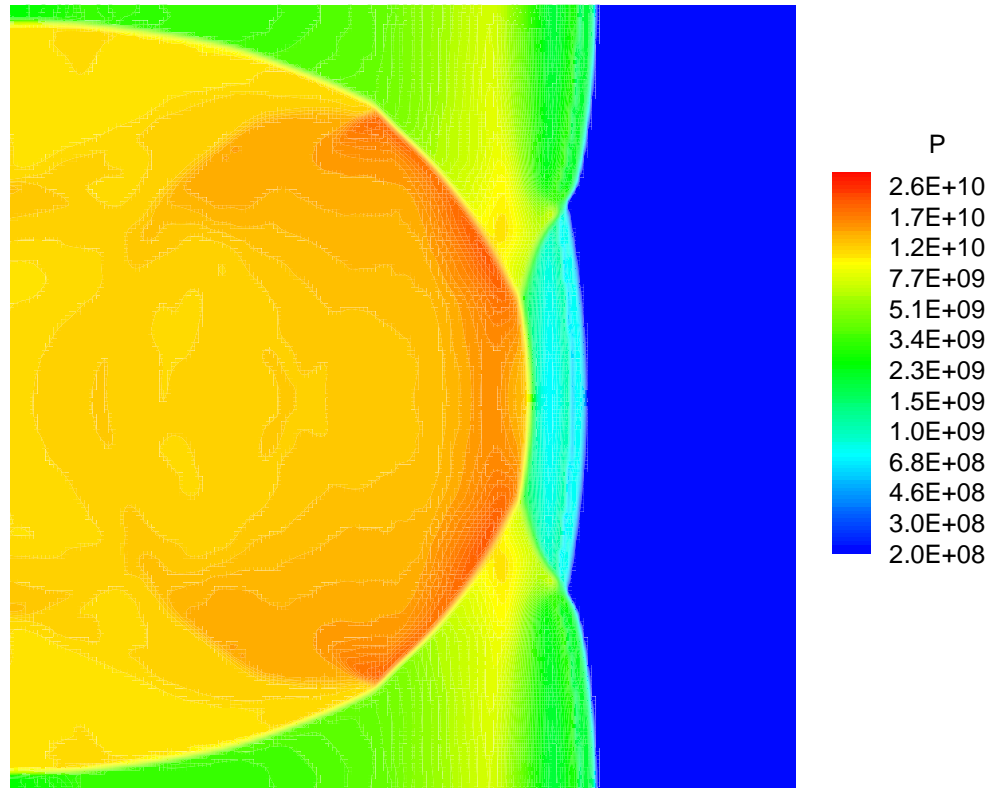


Figure 4.12: Pressure (Pa) contour at an instant when the incident shock has penetrated through the second material interface of a Blatz-Ko elastic plate. Grid of 400 by 400 points spans a physical domain of 3 cm by 3 cm.

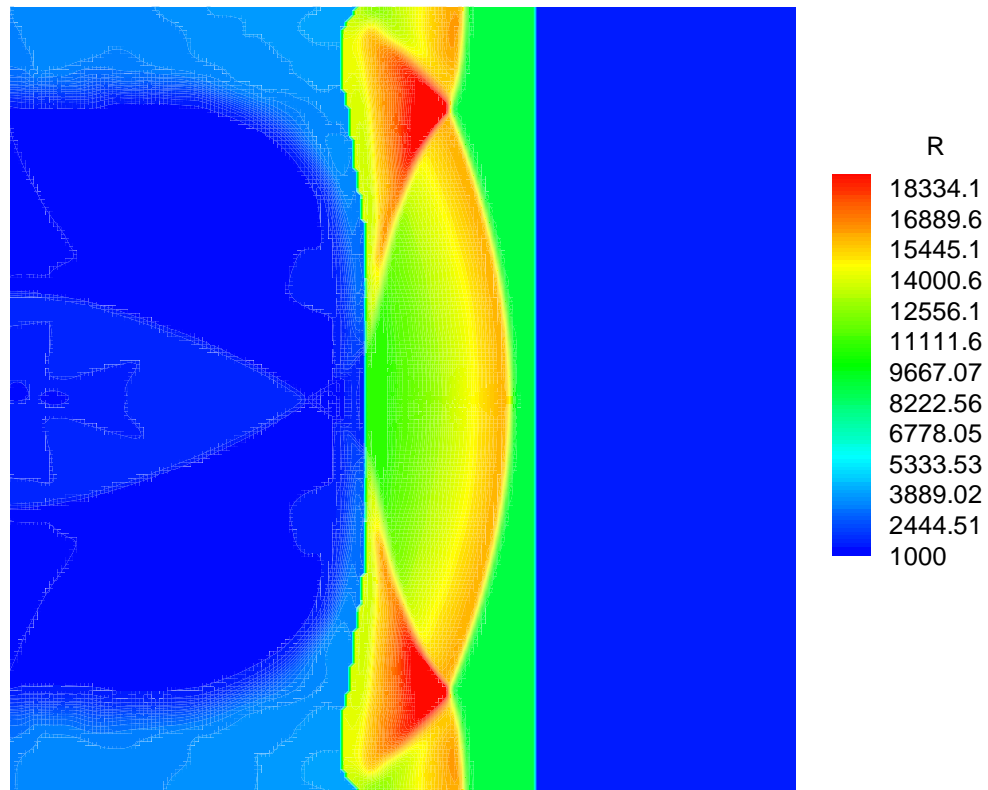


Figure 4.13: Density (kg/m^3) contour at an instance just before the incident shock contacts the second material interface of a Blatz-Ko elastic plate. Grid of 400 by 400 points spans a physical domain of 3 cm by 3 cm.

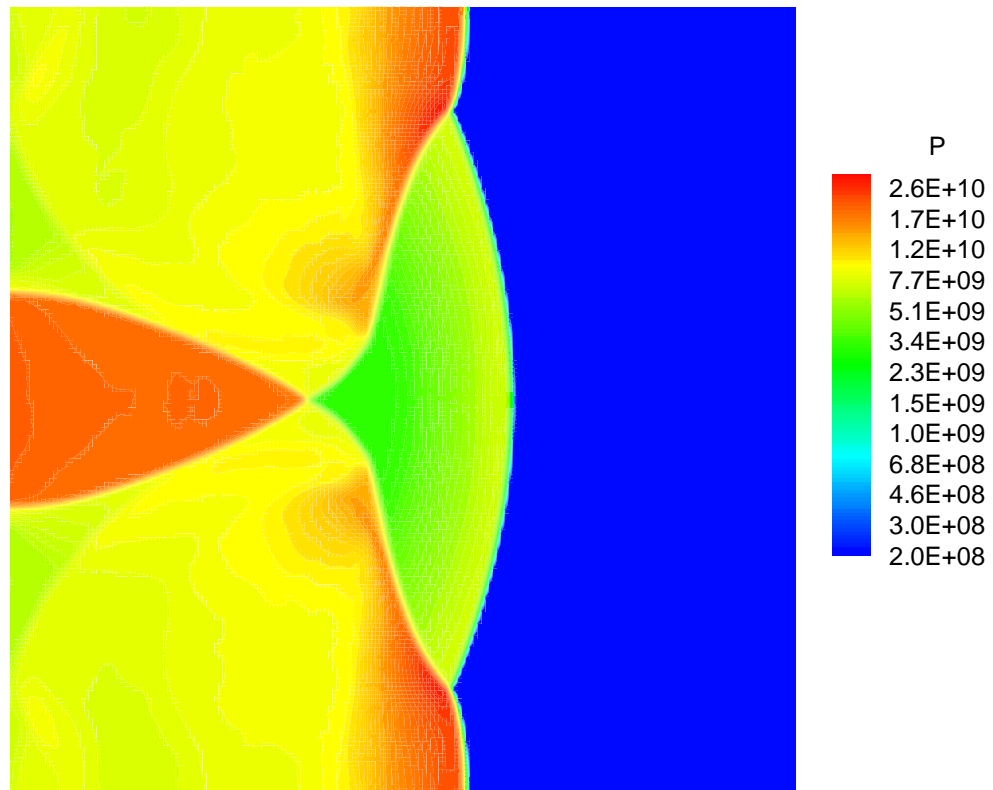


Figure 4.14: Pressure (Pa) contour at an instance just before the incident shock contacts the second material interface of a Blatz-Ko elastic plate. Grid of 400 by 400 points spans a physical domain of 3 cm by 3 cm.

Chapter 5

High Resolution Multi-Material Impact: Inert (Metal)

In this chapter, we describe a specialized version of the multi-material hydrodynamic code that we have discussed in the previous chapter. In particular, the governing equations are essentially the Eulerian equations of a compressible gas with additional evolution equations that govern the physics of elasto–plastic solid deformation in the high-speed impact events. Detailed discussion of this specialized methodology is found in Ref. [80], and a complete discussion on a subject of metal plasticity can be found in [44], [9], [30], [37], and [43].

In order to simulate the dynamic deformation of ductile materials, we need an additional constitutive model of metal plasticity. Before we present a mathematical formulation of the multi-material impact involving elasto–plasticity, we first describe the evolution equations for the dynamic deformation of metals. An additional scalar called the effective plastic strain is introduced and its evolution law is derived based on the classical small-strain theory [5]. The Cauchy stress as it is defined in the spatial coordinate, consists of two terms—the volumetric term and the deviatoric term. Because the theory is based on the classical strain assumption, one does not explicitly calculate the elastic strain field during the dynamic deformation event; instead, the total rate of strain or the velocity gradient is calculated to update the history of deformation in the plastic constitutive relations. In the sections below, we will elaborate on the derivation of the additional evolution laws that are required when considering the material plasticity.

5.1 Elastic–plastic solid modeling

The constitutive relation for the Cauchy stress tensor is that the dilatational response is governed by the equation of state (EOS) while the deviatoric response follows classical plastic flow theory. In particular, the ideal EOS of a compressible reactive binary mixture is used for the explosive gas as our projectile, while the Mie–Gruneisen EOS is used to represent the hydrostatic pressure of an elasto–plastic metal such as copper. In this section, preliminaries related to the subject of elasto–plastic material modeling will be addressed. Both experimental and numerical benchmark results of Taylor–impact testing of a copper cylinder validate the results obtained through the present code.

5.1.1 Preliminaries

The linear elastic constitutive law suggests the Cauchy stress of a Hookean solid by

$$\boldsymbol{\sigma} = \lambda \hat{\epsilon}_{kk} \mathbf{I} + 2\mu \hat{\boldsymbol{\epsilon}}, \quad (5.1)$$

where we have assumed the ideal linear elastic solid without viscosity. Unlike the non-linear elastic material (e.g. Blatz–Ko) formulation of the previous section, we here concentrate on the small-strain deformation represented through the small-strain tensor,

$$\begin{aligned} \hat{\boldsymbol{\epsilon}} &= \frac{1}{2}(\mathbf{H} + \mathbf{H}^\top) \\ &= \frac{1}{2} \left(\frac{\partial \mathbf{u}}{\partial X_1} + \frac{\partial \mathbf{u}}{\partial X_1}^\top \right). \end{aligned} \quad (5.2)$$

Also, we may express $\boldsymbol{\sigma}$ in terms of its deviatoric part and the volumetric part:

$$\boldsymbol{\sigma} = \mathbf{s} + \frac{1}{3} \text{tr} \boldsymbol{\sigma} \mathbf{I} \quad (5.3)$$

$$= \mathbf{s} - p \mathbf{I} \quad (\text{using } p = -\frac{1}{3} \sigma_{kk}) \quad (5.4)$$

where we have used the hydrostatic pressure p to represent the volumetric part of the Cauchy stress in this idealized case. For later use, we define the velocity gradient or the deformation rate tensor

D as

$$\begin{aligned} \mathbf{D} &= \frac{1}{2}(\nabla \mathbf{v} + \nabla \mathbf{v}^\top) \\ &= \frac{1}{2} \left(\frac{\partial \mathbf{v}}{\partial x} + \frac{\partial \mathbf{v}^\top}{\partial x} \right). \end{aligned}$$

Making a substitution for $\boldsymbol{\sigma}$ in (5.4) by the expression in (5.1), we may express the deviatoric stress in terms of elastic strain, namely,

$$\begin{aligned} s_{ij} &= 2\mu(\hat{\epsilon}_{ij} - \frac{1}{3}\hat{\epsilon}_{kk}\delta_{ij}) \\ &= 2\mu\hat{\epsilon}'_{ij}, \end{aligned} \tag{5.5}$$

where we have introduced the primed (') notation to represent the deviatoric part of the argument. Furthermore, we define the total strain increment $d\boldsymbol{\epsilon}$ as a sum of elastic and plastic strain:

$$d\boldsymbol{\epsilon} = d\hat{\boldsymbol{\epsilon}} + d\boldsymbol{\epsilon}^p. \tag{5.6}$$

Then, the corresponding deviatoric incremental strain can be expressed as

$$d\boldsymbol{\epsilon}' = d\hat{\boldsymbol{\epsilon}}' + d\boldsymbol{\epsilon}^p \tag{5.7}$$

where we use the plastic flow rule to replace $d\boldsymbol{\epsilon}^{p'}$ with $d\boldsymbol{\epsilon}^p$ using the fact that $\epsilon_{kk}^p = 0$. We will elaborate on the flow rule shortly. From (5.5), we can express the incremental deviatoric stress as

$$ds = 2\mu(d\boldsymbol{\epsilon}' - d\boldsymbol{\epsilon}^p). \tag{5.8}$$

5.1.2 Derivation of evolution laws of plasticity

There are many ways to reach the plastic flow and material plastic deformation. The overall goal is to determine the stress or rate of change of stress given the current stress, some measure of current deformation or deformation rate, and some measure of the history of deformation.

We start the derivation of evolution equations of plasticity by defining a yield surface $f(\boldsymbol{\sigma}, \bar{\epsilon}^p)$

$$f = \bar{\sigma}(\boldsymbol{\sigma}) - H(\bar{\epsilon}^p) = 0$$

where $\bar{\sigma}$ and H represent the effective stress and hardening function, respectively. This function describes a surface in stress space, where the inside of the surface (i.e. $f < 0$) is the elastic region. Yield and subsequent plastic flow take place on the surface. Along this surface of yield, we can infer that the small change in f is also zero; in other words, the derivative of f can be evaluated so that

$$\begin{aligned} df &= \frac{\partial f}{\partial \boldsymbol{\sigma}} : d\boldsymbol{\sigma} + \frac{\partial f}{\partial \bar{\epsilon}^p} d\bar{\epsilon}^p \\ &= \frac{\partial \bar{\sigma}}{\partial \boldsymbol{\sigma}} : d\boldsymbol{\sigma} - \frac{\partial H}{\partial \bar{\epsilon}^p} d\bar{\epsilon}^p = 0. \end{aligned}$$

Upon rearranging, we have the condition for incipient plastic loading

$$\frac{\partial \bar{\sigma}}{\partial \boldsymbol{\sigma}} : d\boldsymbol{\sigma} = \frac{\partial H}{\partial \bar{\epsilon}^p} d\bar{\epsilon}^p. \quad (5.9)$$

In order to evaluate the derivative of effective stress with respect to the Cauchy stress, the von Mises criterion is used to define $\bar{\sigma} = \sqrt{\frac{3}{2} \mathbf{s} : \mathbf{s}}$, so that upon evaluating the derivative, $\frac{\partial \bar{\sigma}}{\partial \boldsymbol{\sigma}}$, (5.9) becomes

$$\frac{3}{2\bar{\sigma}} \mathbf{s} : d\boldsymbol{\sigma} = H' d\bar{\epsilon}^p \quad (\text{using } H' = dH/d\bar{\epsilon}^p). \quad (5.10)$$

Using the fact that $\mathbf{s} : d\boldsymbol{\sigma} = \mathbf{s} : d\mathbf{s}$, we may write (5.10) as

$$\frac{3}{2\bar{\sigma}} \mathbf{s} : d\mathbf{s} = H' d\bar{\epsilon}^p. \quad (5.11)$$

Using (5.8), we find

$$\frac{3}{2} \frac{s_{ij}}{\bar{\sigma}} 2\mu (d\epsilon'_{ij} - d\epsilon^p_{ij}) = H' d\bar{\epsilon}^p. \quad (5.12)$$

In order to derive an equation for an incremental effective plastic strain $d\bar{\epsilon}^p$, we now need to introduce the plastic flow rule based on the plastic potential theory by von Mises. Similar to the elastic potential theory, where the elastic strain is obtained by the derivative of strain energy U with respect to the Cauchy stress $\boldsymbol{\sigma}$, the incremental plastic strain, or equivalently the material derivative of it can be expressed by

$$\dot{\epsilon}_{ij}^p = \dot{\bar{\epsilon}}^p \frac{\partial Q(\sigma_{ij})}{\partial \sigma_{ij}}, \quad (\text{analogy, } \hat{\epsilon}_{ij} = \frac{\partial U}{\partial \sigma_{ij}})$$

where von Mises has proposed a plastic potential function $Q(\sigma_{ij})$ whose gradient is proportional to the plastic strain by a factor of $\dot{\bar{\epsilon}}^p$. A common approach in plasticity theory is to assume that $Q(\sigma_{ij}) = f(\sigma_{ij}, \bar{\epsilon}^p)$, a yield surface. This says then, the plastic strain increment is in the direction normal to the yield surface f (since $\frac{\partial f}{\partial \boldsymbol{\sigma}}(\boldsymbol{\sigma}) \perp f(\boldsymbol{\sigma})$). Evaluating $\frac{\partial f}{\partial \sigma_{ij}}$, we find

$$\dot{\epsilon}_{ij}^p = \frac{3}{2\bar{\sigma}} s_{ij} \dot{\bar{\epsilon}}^p$$

which is also an empirically determined plastic flow rule (Levy–Mises equation).

The Levy–Mises equation based on experiments or plastic potential flow theory can be viewed as giving a ‘direction’ to a scalar, $\dot{\bar{\epsilon}}^p$, so that \mathbf{R} , as defined by

$$\mathbf{R} = \frac{3}{2} \frac{\mathbf{s}}{\bar{\sigma}},$$

may represent a direction tensor. Thus we can express the incremental plastic strain $d\epsilon_{ij}^p$ in terms of the effective plastic strain $d\bar{\epsilon}^p$, a scalar, by giving a direction normal to the yield surface $f = 0$:

$$\frac{3}{2} \frac{s_{ij}}{\bar{\sigma}} 2\mu (d\epsilon'_{ij} - \frac{3}{2} \frac{s_{ij}}{\bar{\sigma}} d\bar{\epsilon}^p) = H' d\bar{\epsilon}^p. \quad (5.13)$$

Finally, solving for $d\bar{\epsilon}^p$, we may write

$$d\bar{\epsilon}^p = \frac{1}{1 + \frac{H'}{3\mu}} \frac{\mathbf{s} : d\boldsymbol{\epsilon}'}{\bar{\sigma}}. \quad (5.14)$$

In summary, we have derived evolution equations for $\bar{\epsilon}^p$ and \mathbf{s} by replacing the increments with

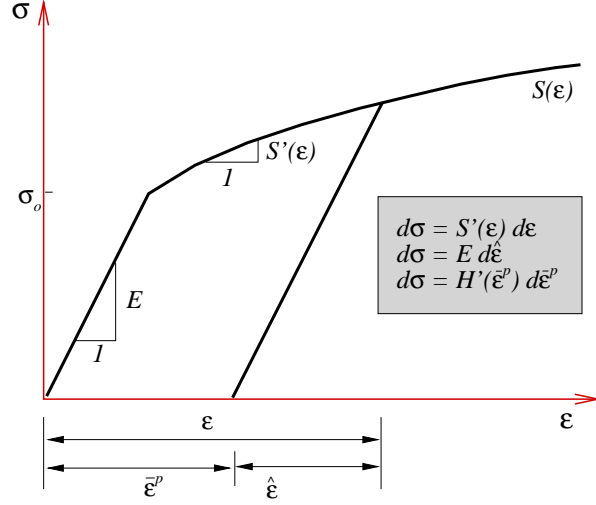


Figure 5.1: Universal stress–strain curve from a simple tension test.

material derivative, such that

$$\begin{aligned}
 \dot{\mathbf{s}} &= 2\mu\dot{\hat{\boldsymbol{\epsilon}}}^{\prime} + \boldsymbol{\Omega}\mathbf{s} - \mathbf{s}\boldsymbol{\Omega} \\
 &= 2\mu(\dot{\boldsymbol{\epsilon}}^{\prime} - \dot{\boldsymbol{\epsilon}}^p) + \boldsymbol{\Omega}\mathbf{s} - \mathbf{s}\boldsymbol{\Omega} \quad (\text{Using } \dot{\boldsymbol{\epsilon}}^{\prime} = \mathbf{D}^{\prime}) \\
 &= 2\mu(\mathbf{D}^{\prime} - \frac{3}{2}\frac{\mathbf{s}}{\bar{\sigma}}\dot{\boldsymbol{\epsilon}}^p) + \boldsymbol{\Omega}\mathbf{s} - \mathbf{s}\boldsymbol{\Omega}
 \end{aligned} \tag{5.15}$$

$$\dot{\boldsymbol{\epsilon}}^p = \frac{1}{1 + \frac{H'}{3\mu}} \frac{\mathbf{s} : \mathbf{D}^{\prime}}{\bar{\sigma}}, \tag{5.16}$$

where Ω_{ij} are the components of spin tensor, defined by

$$\Omega_{ij} = \frac{1}{2}(v_{i,j} - v_{j,i}).$$

The Ω_{ij} terms in (5.15) arise because constitutive laws based on Hooke's law are formulated from objective stress rates as observed in the material frame rotated back to the laboratory frame [23, 38].

5.1.3 Hardening laws

According to Fig. 5.1, simple tension test result is used to illustrate the distinction between the elastic strain $\hat{\epsilon}$ and the plastic strain $\bar{\epsilon}^p$ and that summation of the two represents the total natural strain ϵ . Experiment provides a plastic response function $S(\epsilon)$ whose derivative represents a slope of the stress-strain curve $\frac{d\sigma}{d\epsilon}$. As before, a constant elastic slope is denoted E as in Fig. 5.1. The function $H(\bar{\epsilon}^p)$ is called a hardening function which, in our case of copper, follows an isotropic hardening law. In other words, we assume

$$H(\bar{\epsilon}^p) = \sigma_o + E_p(\bar{\epsilon}^p) \bar{\epsilon}^p \quad (5.17)$$

where σ_o is a constant yield stress and $H'(\bar{\epsilon}^p)$ represents the slope of the stress versus effective plastic strain $\bar{\epsilon}^p$ curve. In particular, in this case of simple hardening, $H'(\bar{\epsilon}^p) = E_p(\bar{\epsilon}^p)$, a plastic modulus. Noting that S' and E are the slopes of σ - ϵ and σ - $\hat{\epsilon}$ curves, respectively, we can express H' in terms of S' and E :

$$\begin{aligned} H'(\bar{\epsilon}^p) &= \frac{1}{\frac{1}{S'(\epsilon)} - \frac{1}{E}} \\ &= \frac{S'(\epsilon)E}{E - S'(\epsilon)}. \end{aligned} \quad (5.18)$$

For the Taylor impact testing of copper, it is sufficient to assume linear hardening. This simplifying assumption allows us to replace $S'(\epsilon)$ with a constant tangent modulus E_t and $H'(\bar{\epsilon}^p)$ with a constant plastic modulus E_p . Table 5.5.4 lists the elasto-plastic response properties for a typical copper.

In some extreme ballistic penetration events, a linear hardening of the previous section may not be suitable where the flow stress may exhibit a strong rate-sensitivity. We consider a power law where

$$H(\bar{\epsilon}^p) = \sigma_o \left(1 + \frac{\bar{\epsilon}^p}{\bar{\epsilon}_o^p} \right)^{1/n}. \quad (5.19)$$

Here, $\bar{\epsilon}_o^p$ is an initial yield strain of a material, and n is the hardening exponent. Johnson and Cook [35] suggest adding the effect of thermal softening to this conventional power law as less plastic

behavior is expected of a metal as its temperature is close to the melting point. In other words, the hardening law that we use, in addition to the linear relation in (5.17), takes the following form:

$$H(\bar{\epsilon}^p) = \sigma_o \left[1 - \left(\frac{T - T_o}{T_m - T_o} \right)^\alpha \right] \left(1 + \frac{\bar{\epsilon}^p}{\bar{\epsilon}_o^p} \right)^{1/n}, \quad (5.20)$$

where T_o and T_m are a reference temperature and a melting temperature respectively, and α is the softening exponent. The derivative of the hardening law can be found as

$$H'(\bar{\epsilon}^p) = \frac{\sigma_o}{n\bar{\epsilon}_o^p} \left(1 + \frac{\bar{\epsilon}^p}{\bar{\epsilon}_o^p} \right)^{1/n-1} \left[1 - \left(\frac{T - T_o}{T_m - T_o} \right)^\alpha \right]. \quad (5.21)$$

5.2 Mathematical formulation

5.2.1 Two-dimensional equations of fluid–solid interaction with reaction

The flux form of the governing equations of the conservative variables is expressed by

$$\frac{\partial \mathbf{U}}{\partial t} + \frac{\partial \mathbf{F}}{\partial x} + \frac{\partial \mathbf{G}}{\partial y} = \mathbf{S}(\mathbf{U}) \quad (5.22)$$

where the variables \mathbf{U} and two fluxes \mathbf{F}, \mathbf{G} are defined as

$$\mathbf{U} = \begin{bmatrix} \rho \\ \rho v_1 \\ \rho v_2 \\ \rho E \\ \rho \lambda \end{bmatrix}, \mathbf{F} = \begin{bmatrix} \rho v_1 \\ \rho v_1^2 + p \\ \rho v_1 v_2 \\ v_1(\rho E + p) \\ \rho v_1 \lambda \end{bmatrix}, \mathbf{G} = \begin{bmatrix} \rho v_2 \\ \rho v_1 v_2 \\ \rho v_2^2 + p \\ v_2(\rho E + p) \\ \rho v_2 \lambda \end{bmatrix}. \quad (5.23)$$

The source terms are defined as

$$\mathbf{S} = \begin{bmatrix} 0 \\ \frac{\partial s_{xx}}{\partial x} + \frac{\partial s_{xy}}{\partial y} \\ \frac{\partial s_{xy}}{\partial x} + \frac{\partial s_{yy}}{\partial y} \\ \frac{\partial}{\partial x}(v_1 s_{xx} + v_2 s_{xy}) + \frac{\partial}{\partial y}(v_1 s_{xy} + v_2 s_{yy}) \\ \rho A(1 - \lambda)^{1/2} \end{bmatrix}, \quad (5.24)$$

where we have used the definition of Cauchy stress, $\boldsymbol{\sigma} = \mathbf{s} - p\mathbf{I}$. If the material is a gas, the deviatoric stress becomes zero such that the components of source vector \mathbf{S} are zeroes with the reaction rate term. In other words, the governing system of equations represents the reactive Euler equations with the equation of state stated as

$$\rho e = \frac{p}{(\gamma - 1)} - \rho Q_c \lambda. \quad (5.25)$$

Here, $\gamma = 3$, $Q_c = 4 \times 10^6 \text{ m}^2/\text{s}^2$, and $A = 2.5147 \times 10^6 \mu\text{sec}^{-1}$.

In the case of a solid, the components of a deviatoric stress must be computed using the evolution laws defined previously. First, the pressure of an elasto-plastic metal is obtained by the Mie-Gruneisen EOS, namely

$$p(e, \rho) = \frac{c_o^2(V_o - V)}{[V_o - s(V_o - V)]^2} + \Gamma_o \rho_o V \left\{ \rho e - \frac{\rho}{2} \left(\frac{c_o(V_o - V)}{V_o - s(V_o - V)} \right)^2 \right\}, \quad (5.26)$$

where $V = 1/\rho$, c_o is the speed of sound at ambience, s is the coefficients of Hugoniot data from a shock test, and Γ_o is the constant Mie-Gruneisen coefficient for a typical copper. The three equations of deviatoric stress are

$$\frac{\partial s_{xx}}{\partial t} + v_1 \frac{\partial s_{xx}}{\partial x} + v_2 \frac{\partial s_{xx}}{\partial y} = 2\mu \left(D'_{xx} - \frac{3}{2} \frac{s_{xx}}{\bar{\sigma}} \dot{\epsilon}^p \right) + \Omega_{xm} s_{mx} - s_{xm} \Omega_{mx}, \quad (5.27)$$

$$\frac{\partial s_{yy}}{\partial t} + v_1 \frac{\partial s_{yy}}{\partial x} + v_2 \frac{\partial s_{yy}}{\partial y} = 2\mu \left(D'_{yy} - \frac{3}{2} \frac{s_{yy}}{\bar{\sigma}} \dot{\epsilon}^p \right) + \Omega_{ym} s_{my} - s_{ym} \Omega_{my}, \quad (5.28)$$

$$\frac{\partial s_{xy}}{\partial t} + v_1 \frac{\partial s_{xy}}{\partial x} + v_2 \frac{\partial s_{xy}}{\partial y} = 2\mu \left(D'_{xy} - \frac{3}{2} \frac{s_{xy}}{\bar{\sigma}} \dot{\epsilon}^p \right) + \Omega_{xm} s_{my} - s_{xm} \Omega_{my}, \quad (5.29)$$

with $s_{xy} = s_{yx}$. And the evolution of effective plastic strain is governed by

$$\frac{\partial \bar{\epsilon}^p}{\partial t} + v_1 \frac{\partial \bar{\epsilon}^p}{\partial x} + v_2 \frac{\partial \bar{\epsilon}^p}{\partial y} = \frac{1}{1 + \frac{H'}{3\mu}} \frac{(s_{xx} D'_{xx} + s_{yy} D'_{yy} + 2s_{xy} D'_{xy})}{\bar{\sigma}}. \quad (5.30)$$

5.2.2 Level set for interface tracking

We use the level-set equation,

$$\frac{\partial \phi}{\partial t} + v_1 \frac{\partial \phi}{\partial x} + v_2 \frac{\partial \phi}{\partial y} = 0, \quad (5.31)$$

to track the location of the material interface represented by the zero-level curve of $\phi(x, y)$. Initially, ϕ starts out as a distance function, and in time the function will be evolved with the local velocity $\mathbf{v} = (v_1, v_2)$. This advection of ϕ suggests that the location of material interfaces and contact surfaces will be exactly tracked by the position of the moving distance function in time. As we will discuss how other jumps of the flow field are treated, the material interfaces will be treated with the level-set function.

5.3 Numerics

The discretized version of the system of PDEs in (5.22) can be solved in steps of space and time methods. For our two-dimensional system, two fluxes in x and y directions are treated with the fourth-order convex ENO scheme, which is a version of high-order shock capturing methods for advection terms of the Euler equation. Once the two advection terms are treated a priori, the remaining system represents a system of ODEs rather than PDEs as its initial form, and can be solved in time with a high-order stable method. We use the third-order TVD Runge–Kutta scheme, which is guaranteed to be total-variation diminishing in the sense of Ref. [64]. This standard approach in using shock capturing schemes to pre-process the advection terms of the hyperbolic PDE is called a method of lines since per fixed spatial node, one marches in time. When depicted on a graph of space versus time, this process of time marching per a fixed spatial grid, i or j , shows straight lines parallel to the time axis. Among other reasons, this method-of-lines approach is often favored over the space–time method in that the method can achieve order greater than three

without any complicated coupling between space and time advancement. In fact, the space–time representation of the PDE solver is a mesh, not straight lines, and thus it is called the method of meshes instead.

For a thorough discussion on the subject of essentially non-oscillatory shock capturing schemes, we refer the reader to [64, 42]. In the calculations shown in this work, we have used the fourth-order convex ENO scheme by Liu and Osher [42]. As for the TVD Runge–Kutta method for advancing in time after the spatial discretization has been completed via ENO, we use the following three-stage scheme for the third-order integration:

$$\begin{aligned} \mathbf{k}_1 &= \mathbf{k}_0 + \Delta t[\mathbf{f}(\mathbf{k}_0) + \mathbf{g}(\mathbf{k}_0)], \\ \mathbf{k}_2 &= \mathbf{k}_0 + \frac{1}{4}\Delta t[\mathbf{f}(\mathbf{k}_0) + \mathbf{g}(\mathbf{k}_0)] + \frac{1}{4}\Delta t[\mathbf{f}(\mathbf{k}_1) + \mathbf{g}(\mathbf{k}_1)], \\ \mathbf{k}_3 &= \mathbf{k}_0 + \frac{1}{6}\Delta t[\mathbf{f}(\mathbf{k}_0) + \mathbf{g}(\mathbf{k}_0)] + \frac{1}{6}\Delta t[\mathbf{f}(\mathbf{k}_1) + \mathbf{g}(\mathbf{k}_1)] + \frac{2}{3}\Delta t[\mathbf{f}(\mathbf{k}_2) + \mathbf{g}(\mathbf{k}_2)], \end{aligned} \quad (5.32)$$

where \mathbf{f} and \mathbf{g} represent the discretized spatial fluxes and the source terms of (5.22), respectively.

5.4 Interface tracking using level sets

A level-set function as previously defined provides a simple way to track material interfaces and contact surfaces that divide two different media (or materials). In fact, almost everything we see on a daily basis is exposed to this multi-material setting where either fluid–solid, solid–solid, solid–void, or void–fluid are at all times in close contact. Two gases of different ratios of specific heat in a Sod’s experiment can be easily handled by the use of level-set functions. A gas in contact with a free-moving piston (or a vacuum) can also be modeled using a variational approach to the level-set method. In this section, we will consider two main types of multi-material interfaces. First, we consider the material–material contact, and second, we explain how we treat the material–void (or vacuum) interface using a level-set function.

5.4.1 Material–material interface tracking

A detailed description can be inferred from references [51], [49]. Across the contact surface of any two fluids or solids, pressure and velocity are smooth while entropy (likewise density or internal

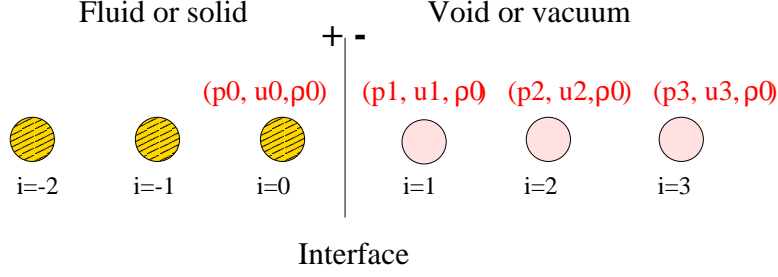


Figure 5.2: Schematic of material–void interface.

energy) and material properties may change sharply. This is especially over-burdening when numerically solving the equations of motion at this internal boundary. Either the computed density profile is widely dissipated or some spurious oscillations typically occur near the jump where well known ‘over-heating’ effects are seen in most finite-differencing schemes. A level-set function, denoted ϕ , is taken positive outside of material and negative inside. Therefore, the material interface is the zero level set of ϕ , since ϕ is initialized as the signed normal distance from the material interface. In this case of any two materials (either fluid or solid) in contact, we use the standard method of pressure update in each region based on the signs of the level-set function. Recall that equation

$$\phi_t + \mathbf{u} \cdot \nabla \phi = 0$$

will move the zero level of ϕ exactly as the actual material interface moves. Since ϕ is a smooth function, unlike the variables of the equations of motion, the level-set equation is solved easily.

The basic idea in tracking a material interface is to evolve the PDE in ϕ along with the full motion of the two regions with distinctly varying material properties. Since only a single system of conservation laws is needed to represent the motions of two materials in contact, additional equations are needed to characterize the two materials. The equation of state in the form of $p(e, \rho)$ or $e(p, \rho)$ is used to define the unknown of the system. In the case of a gas in contact with a metal as shown in this work, we use the ideal EOS with the ratio of specific heats γ as the main parameter in the gas, and Mie–Gruneisen EOS is used in elasto–plastic metal with the Gruneisen coefficient Γ as the main parameter.

5.4.2 Material–void stress-free interface tracking

Some examples of material–void contact include the interface between gas and a vacuum, gas and a free-moving piston, and solid and a void. In all these cases, the stress-free condition must be satisfied at the interface. Ideally, the zero density and stress characterize a vacuum. However, the resulting large density ratio between vacuum and a material puts a significant constraint on any solver, oftentimes leading to an early termination of computation and/or a very unstable marching in both space and time.

We find a modified version of the ghost-fluid-method for the general two-material interface very useful in the material–void contact [27]. Experience tells us that a typical density variation across this type of interface is on the order of 10^3 . Either large oscillations or a smeared out profiles of density are usually observed in a standard application of a level-set curve to update the pressure on each side. Instead, one can avoid these inaccuracies associated with ill-conditioned methods by a one-sided extrapolation of density (or entropy) inside the solid out to the vacuum region. Fig. 5.2 shows how a band of ghost nodes (e.g. $i = 1 \dots 3$) are populated by the first order extrapolation in one dimension. Using the fact that both pressure and velocity across the material interface (or equivalently a contact line in gas) are smooth and continuous while the density or the entropy usually jumps, we extrapolate the discontinuous density field by assigning $\rho_{i=0}$ into $\rho_{i=1\dots3}$. The new field, called ghost zones, now have the pressure and velocity of voids (zeros if vacuum) while their density is assigned as the extrapolated density value of the material in contact. Clearly, solving the equation of motion in the new material-ghost zones is much easier as the entire field is smooth without any discontinuities. As the level-set function is solved, the interface at $\phi = 0$ position is advected with the particle velocity, while the exact location of material contact line is accurately tracked.

At first, this simple technique might seem troublesome because the resulting flow field looks different from the actual physical situation where a solid is in contact with a void. The ideal equation of state for gas or Mie–Gruneisen equation of state for elasto–plastic metals as they are plotted on e – ρ axes represents a hyperbola for a specified pressure. These curves with constant pressures are essentially isobars representing different states—either gas or metal can exist given a pressure state. So the idea of ‘modifying’ the density or the internal energy of voids while the

pressure is remained constant suggest that we are shifting a point on this isobar to a different point with density of actual material with corresponding internal energy. This technique, an isobaric fix, as it is called in the fixing of the well known ‘over-heating’ problems of piston–gas interface is also used in the material–void contact cases with its justification discussed extensively in Ref. [28].

In multi-dimensions, the one-sided extrapolation involves solving the PDE

$$\frac{\partial I}{\partial t} \pm n_x \frac{\partial I}{\partial x} \pm n_y \frac{\partial I}{\partial y} = 0, \quad (5.33)$$

where I may be ρ or e depending on the equations formulated. We note that the two components of the unit normal vector \mathbf{n} at every grid point can be found by

$$\mathbf{n} = \frac{\nabla \phi}{|\nabla \phi|}. \quad (5.34)$$

Furthermore, the signs in the PDE of the isobaric fix variable are chosen positive for normal pointing from positive material (i.e. positive distanced level-set function) into the negative material. In other words, we choose the $+$ sign in the PDE to populate the ghost nodes in the region where $\phi < 0$ with the values of I from the region where $\phi > 0$. Similarly, we choose the $-$ sign in the PDE to populate the ghost nodes in the region where $\phi \geq 0$. As it turns out, the equation needs to be solved for only a few pseudo-time steps to populate a thin band of ghost nodes ($i = 1 \dots 3$) needed for the extrapolation.

5.5 Code validations

In this section, we describe special forms of equations representing an Euler gas, a condensed high explosive (HE), and elasto–plastic metals.

The reactive Euler equations are the hyperbolic equation (5.22) whose fluxes are

$$\mathbf{U} = \begin{bmatrix} \rho \\ \rho v_1 \\ \rho v_2 \\ \rho E \\ \rho \lambda \end{bmatrix}, \mathbf{F} = \begin{bmatrix} \rho v_1 \\ \rho v_1^2 + p \\ \rho v_1 v_2 \\ v_1(\rho E + p) \\ \rho v_1 \lambda \end{bmatrix}, \mathbf{G} = \begin{bmatrix} \rho v_2 \\ \rho v_1 v_2 \\ \rho v_2^2 + p \\ v_2(\rho E + p) \\ \rho v_2 \lambda \end{bmatrix}. \quad (5.35)$$

The source term vector is defined as

$$\mathbf{S} = \begin{bmatrix} 0 \\ 0 \\ 0 \\ 0 \\ \rho A(1 - \lambda)^{1/2} \end{bmatrix}. \quad (5.36)$$

The ideal EOS for reactive gas with λ representative of the extent of chemical reaction is given by

$$p = (1 - \gamma(\phi)) \left\{ \rho E - \frac{\rho}{2} (v_1^2 + v_2^2) + \rho Q_c \lambda \right\}, \quad (5.37)$$

where the gamma-law scalar is a function of the level set such that

$$\gamma(\phi) = \begin{pmatrix} \gamma_1 & \phi > 0 \\ \gamma_2 & \phi < 0 \\ \bar{\gamma} & \phi = 0 \end{pmatrix}. \quad (5.38)$$

In the limit of high pressure, these hyperbolic PDEs without λ can also represent a metal under a large deformation and hydrostatic stress. This dynamic modeling of elasto-plastic metals using Euler equations is especially useful for multi-material calculation of explosive and inerts, and it benefits from a vast resource of computing technique already developed for high-speed compressible gas dynamics. The equation of state (EOS) chosen to represent the pressure behavior of high-strength ductile materials at an elevated pressure range of 10^9 Pa is the experimentally

	Gas1 (50 cm)	Gas2 (50 cm)
γ	1.4	1.2
ρ (kg/m ³)	1	0.125
p (Pa)	1.5×10^5	1.0×10^4
v (m/s)	0	0

Table 5.1: Initial parameters of shock tube Case A.

validated fitting curve called the Mie–Gruneisen equation. To illustrate the plastic model of our code, we show how the source vector of the Euler equations is modified. From (5.22), the new source representative of a metal becomes

$$\mathbf{S} = \begin{bmatrix} 0 \\ \frac{\partial s_{xx}}{\partial x} + \frac{\partial s_{xy}}{\partial y} \\ \frac{\partial s_{xy}}{\partial x} + \frac{\partial s_{yy}}{\partial y} \\ \frac{\partial}{\partial x}(v_1 s_{xx} + v_2 s_{xy}) + \frac{\partial}{\partial y}(v_1 s_{xy} + v_2 s_{yy}) \\ 0 \end{bmatrix}, \quad (5.39)$$

where we have used the definition of Cauchy stress $\boldsymbol{\sigma} = \mathbf{s} - p\mathbf{I}$ and the total energy $\rho E = \rho e + \frac{\rho}{2}(v_1^2 + v_2^2)$. Instead of the ideal EOS, we use the Mie–Gruneisen EOS for metals so that

$$p = \frac{c_o^2(V_o - V)}{[V_o - s(V_o - V)]^2} + \Gamma_o \rho_o V \left\{ \rho e - \frac{\rho}{2} \left(\frac{c_o(V_o - V)}{V_o - s(V_o - V)} \right)^2 \right\}, \quad (5.40)$$

where $V = 1/\rho$, c_o is the speed of sound at ambience, s is the coefficient of Hugoniot data from a shock test, and Γ_o is the constant Mie–Gruneisen coefficient. Table 5.5.4 summarizes these constants for a specific metal, a copper.

5.5.1 Verification of order of convergence

Here we consider two different Euler gases initially brought to contact. Upon the removal of the diaphragm between the gases with different γ 's, an expansion wave and a normal shock propagate in the opposite direction and a contact surface (or material interface) follows the right-running shock. Listed below are the initial conditions of this experiment. Results shown in Fig. 5.3 are calculated with 100 points spanning 1 meter in the x direction. We used the fourth-order convex

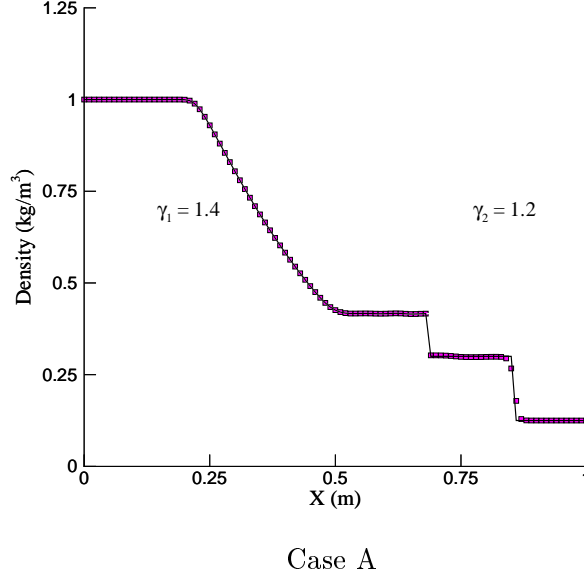


Figure 5.3: Riemann problem involving two different gases used in the validation of rate of numerical convergence.

ENO scheme with a third-order Runge–Kutta scheme. The material interface or the contact line between the gases are tracked via the level-set approach using the one-sided extrapolation density update as discussed previously. We note that there is absolutely no smearing across the material interface.

We analyze the spatial accuracy by measuring the relative error E_1 in the L_1 norm during the time integration to estimate the order of convergence as shown in Ref. [79]. The eight data points (e.g. density) between $x = 0.52$ to $x = 0.59$ in increments of $\Delta x = 0.01$ are compared with the double grid data points at the same locations at time $t = 0.0007$. The discrete L_1 norm is defined as

$$E_1 = \sum_i |\rho^{\text{exact}} - \rho_i| \Delta x. \quad (5.41)$$

If a method is of r th order, then for a uniform mesh with N grid points, the error should satisfy

$$E_1^N = O(\Delta x^{r_c}).$$

N	E_1	r_c
100	9.0×10^{-5}	—
200	1.68×10^{-5}	2.4
400	2.7×10^{-6}	2.8
800	1.8×10^{-7}	3.9

Table 5.2: Results of numerical test of convergence. In the table, N denotes grid points, E_1 is the L_1 norm of error measured between the grids of size N and $2N$ points, and r_c is the rate of convergence.

When the uniform mesh is refined by doubling the grid points, we should have

$$E_1^{2N} = O\left(\left(\frac{\Delta x}{2}\right)^{r_c}\right).$$

Then, one can solve for the rate of convergence, r_c , and finds

$$r_c = \frac{\ln E_1^N - \ln E_1^{2N}}{\ln 2}. \quad (5.42)$$

The L_1 error and the rate of convergence based on density are displayed in Table 5.5.1. The rate of convergence is calculated using the formula in (5.42). The fourth-order convex ENO scheme is tested in this 1-D shock tube exercise with level-set technique treating the multi-material interface. Clearly, as the number of grids approaches ∞ , we observe that the computed rate of convergence approaches the theoretical value of 4. Here, we make sure that Δt is kept small compared with Δx to make sure that no additional errors are coming from the third-order temporal scheme, which will hinder achieving the theoretical convergence rate of 4 as tabulated.

5.5.2 Validation 1: 1-D shock reflection of two different gases

In the second shock-tube test, we start from a right-running shock that reflects off a contact line at the center of a shock tube consisting of two gases of different γ . A part of the incident shock running from left to right will be transmitted as there will be a right-moving interface separating the two different shocks running in the opposite direction. The initial conditions are summarized in Table 5.5.2.

Figure 5.4 shows the wave structures inside the tube after some period of time. Upon the incidence of initial shock on the interface originally at $x = 0.5$ m, a part gets transmitted to

	Gas1 (5 cm)	Gas1 (45 cm)	Gas2 (50 cm)
γ	1.4	1.4	1.67
ρ (kg/m ³)	1.333	1.0	0.1379
p (Pa)	1.5×10^5	1.0×10^5	1.0×10^5
v (m/s)	$0.3535\sqrt{10^5}$	0	0

Table 5.3: Initial parameters of shock tube Case B.

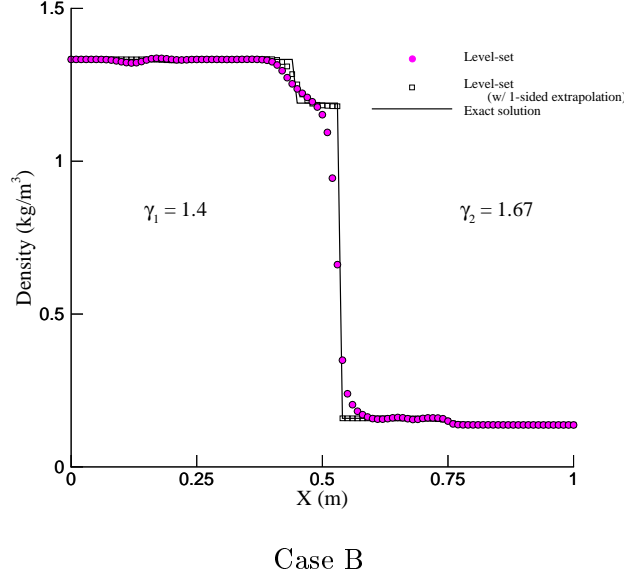


Figure 5.4: Shock-tube test of shock reflection and transmission of two different gases.

the right-side gas, and part gets reflected while the interface between the two follows the local particle velocity, moving to the right. Both the level-set method with and without the one-sided extrapolation accurately captures the location of shocks in opposite directions. Noticeably, the material interface between the two gases is resolved without any smearing in the one-sided extrapolated method while the transmitted and reflected shocks are a bit smeared out by the fourth-order convex ENO scheme.

5.5.3 Validation 2: ZND structure

We test our multi-dimensional reactive Euler code by numerically obtaining a reaction-zone structure. A planar steady detonation wave with a Chapman–Jouguet (CJ) state at the burnt side is initiated in a planar channel. The initial detonation profile in the high explosive condensed gas is

	Burnt	Fresh
p (GPa)	32	10^{-5}
ρ (g/cc)	8/3	2
v (m/s)	2000	0
γ	3	3
λ	1	0

Table 5.4: Initial end states of CJ detonation wave in a typical high explosive.

taken from the Aslam–Bdzil–Stewart (ABS) model from Ref. [2]. The value of γ of HE is 3 and the heat of chemical reaction Q_c is $4 \times 10^6 \text{ m}^2/\text{s}^2$, while frequency rate of reaction A is given as $2.5147 \times 10^6 \text{ sec}^{-1}$.

The two end states of the CJ detonation are defined in Table 5.5.3. Given the end states as listed, the resulting Neumann’s peak is approximately 60 GPa with a reaction zone thickness of 4 mm, and the steady CJ detonation propagates at a speed 8000 m/s.

Shown in Fig. 5.5 are the pressure and λ profiles along a single spatial axis. A theoretical peak value of 60 GPa is reached in the current resolution of approximately 40 points covering the reaction zone. Certainly, it would be beneficial to use extensive meshes in all regions of the flow field without any adaptive meshing effort; however, we carry out our multi-dimensional computations of this thesis with only a limited number of points—about 10 points across the reaction zone. This level of resolution is tested to be sufficient to capture accurately the physics of fluid–solid interface dynamics and behaviors of ductile metals during the ballistic penetration/impact events as shown in the forthcoming sections.

5.5.4 Validation 3: Copper rod impact

A cylindrical rod of initial radius of 3.2 mm and a length of 32.4 mm strikes head-on a rigid wall at a flying velocity of 227 m/s. The rod is made of copper, whose material properties in both elastic and plastic limits are well known. We chose this impact experiment to validate our model and numerics against the large resource of benchmark results both experimentally and computationally obtained by others (see [87], [74], [36]). Table 5.5.4 summarizes the material properties of a copper. For simplicity, we assumed a linear hardening law with a plastic modulus $E_p = 100 \text{ MPa}$. The final deformed shape, length, and radius are compared with the benchmark results. Further, we expect the effective plastic field to match with other calculated results. The calculation is run up to 80

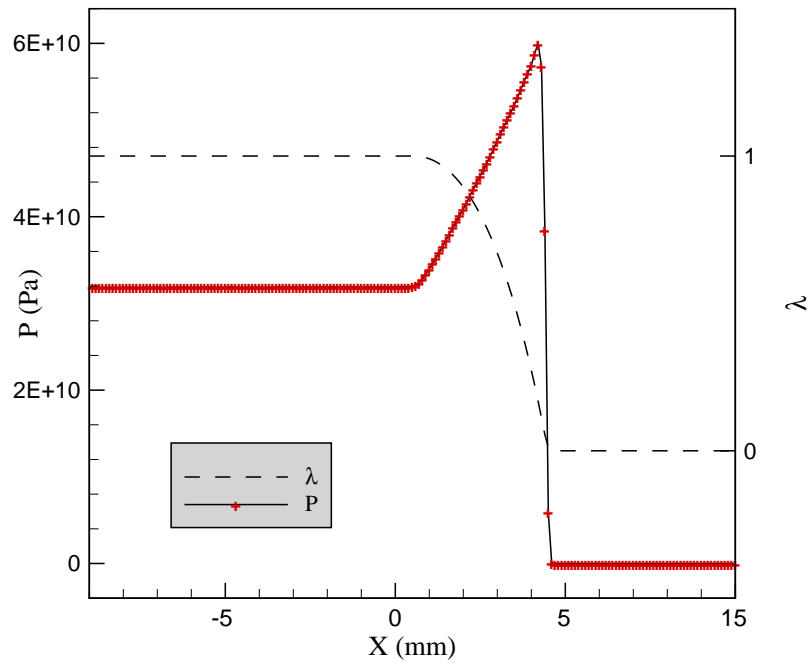


Figure 5.5: ZND detonation structure obtained through the multi-dimensional reactive Euler solver. Δx is 0.1 mm and consequently 40 points are placed in the 4 mm reaction zone.

Material property	Value
Density of copper	8.930 g/cc
Shear modulus (μ)	43.222 GPa
Poisson's ratio (ν)	0.35
Young's modulus (E)	117 GPa
Plastic modulus (E_p)	100 MPa
Yield stress (σ_o)	400 MPa
Mie-Gruneisen coefficient, Γ_o	2.0
Mie-Gruneisen coefficient, s	1.49
Speed of sound, c_o	3.94 km/s

Table 5.5: Material properties typical of copper.

μsec . For this run and all other computing in this thesis, we rely on our in-house eight-processor SGI Origin.

In Fig. 5.6, we show a representative fixed Cartesian grid used in our Eulerian calculation. The Lagrangian mesh used in the benchmark numerical result [19] is shown at the final time, $t = 80 \mu\text{sec}$. In Fig. 5.7, the computed result of copper rod impact at a crushing velocity of 227 m/s directed downward is shown with a scaled image from Ref. [19]. Both figures are representative of the final (i.e. $t = 80 \mu\text{sec}$) deformed shape of the initially 6.4 mm by 32.4 mm in diameter and length. The run on the left by Camacho and Ortiz (1997) is obtained from the FEM-based Lagrangian solver with the finite-strain plasticity model. Based on the high-order ENO scheme with the level-set functions tracking the material interface, the computed Eulerian result on the right-hand side is strikingly similar to this benchmark numerical result. In fact, the plasticity model on the Eulerian code is based on a small-strain theory with a linear hardening law; yet, the computed plastic strain field is quantitatively in agreement with the result compared with the maximum value nearing 3.

5.5.5 Validation 4: Rate-stick experiment

As our last validation of the multi-material scheme, we consider the rate-stick experiment where a ‘stick’ of HE of length 36 cm, width 1.2 cm, is initially placed in an inert medium surrounding the stick at x and y thicknesses of 0.4 cm and 2.4 cm, respectively. In [1], Aslam and Bdzil computed this rate-stick experiment using *Amrita*, an adaptive grid algorithm for computational shock dynamics [55]. Fig. 5.8 depicts the initial setup of the experiment where density, extent of reaction, and pressure fields are shown. A complete detail of the start-up problem are summarized

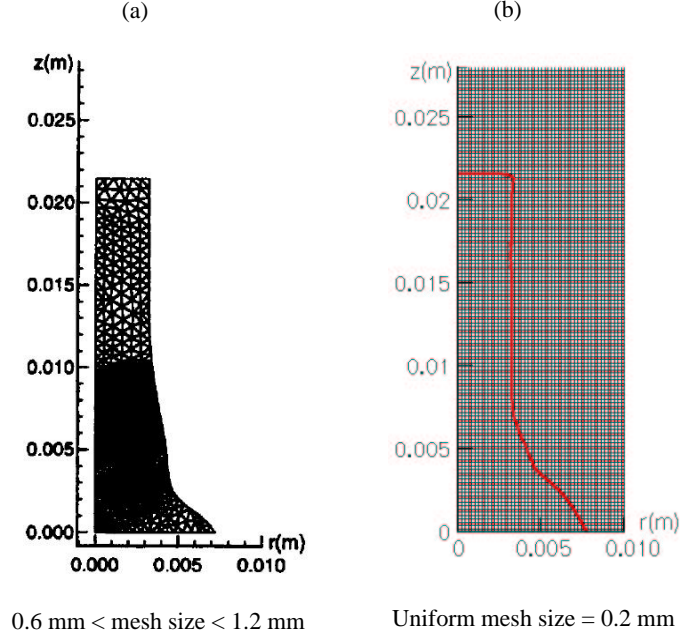


Figure 5.6: Grid comparison: (a) deformed grid at time $t = 80 \mu\text{sec}$ used in the Lagrangian FEM calculation by [19]; (b) uniform grid used in the current work.

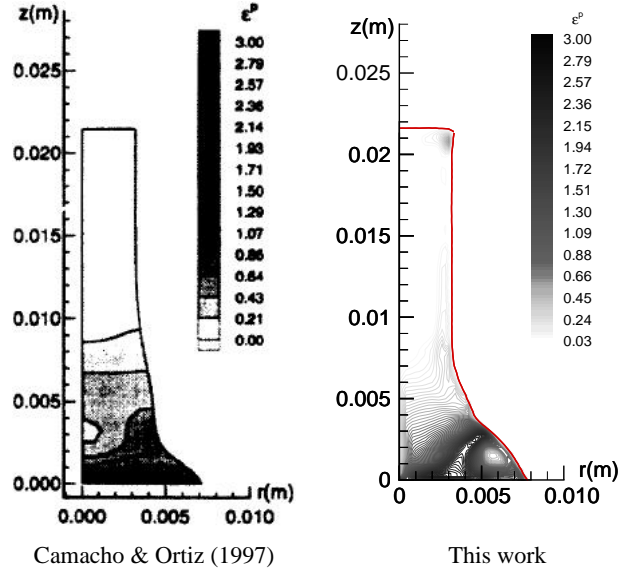


Figure 5.7: Comparison of effective plastic strain distribution at $80 \mu\text{s}$. A 50×170 grid spans the r and z directions ($\Delta r = \Delta z = 2.0 \times 10^{-4} \text{ m}$).

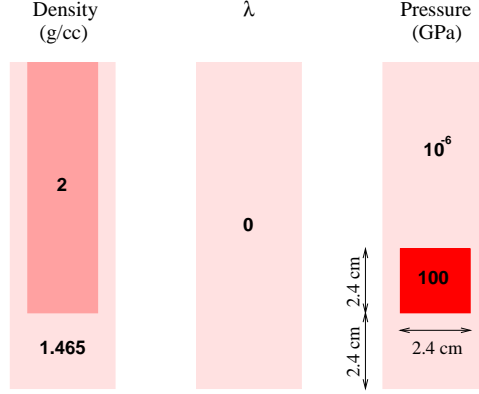


Figure 5.8: Schematic of rate-stick experiment in [1].

	HE	HE (Booster)	Inert
Density (kg/m ³)	2000	2000	1465
Pressure (Pa)	10 ⁵	100 × 10 ⁹	10 ⁵
γ	3	3	1.4
λ	0	0	0

Table 5.6: Running parameter of rate-stick experiment of Ref. [1].

in Table 5.5.5. We note that a pocket of high-pressured HE of dimension 2.4 by 2.4 cm initiates a steady detonation wave in the y direction and the hot gas pushes the HE–Inert interface outward in the x direction. The rate law used in the HE is also based on the ABS model [2], which is stated here again:

$$\dot{\lambda} = AH(p^*)(1 - \lambda)^\nu.$$

With $A = 2.5 \times 10^6 \text{ sec}^{-1}$, the reaction zone length of 4 mm is observed while $\nu = 0.5$, and the threshold pressure $p^* = 10^9 \text{ Pa}$ is used in the Heaviside function $H(p)$ to prevent any unwanted pre-ignition events from happening in the unreacted HE. The interface between HE and the inert (HE–Inert) is described by a level-set curve represented by

$$\phi = \min(b - x, y - a), \quad (5.43)$$

where constants a and b are 1.2 cm and 2.4 cm, respectively.

Depicted in Fig. 5.9 is the comparison of two calculated results of rate-stick; left figures are from Aslam et al. [1] while on the right, the result of this work is shown. Aslam’s results were computed based on the adaptive grids, which give $\Delta x = \Delta y = 0.0074$ cm or 54 points in the complete reaction zone of thickness 4 mm. The results in the right column are based on the uniform mesh of size 0.027 cm, allowing 15 points across the reaction zone. In both fields of λ and ρ , we see an excellent agreement of the detonation front and the angle of shock transmitted in the inert. On top of geometric shape comparison, we have also matched the steady detonation speed of 0.69 cm/ μ s with the speed obtained from the reference calculation of [1].

Even at the coarse grid resolution (i.e. approximately 1/4th of that in Ref. [1]), our multi-material numerics are accurately reproducing the fine-grid results of Aslam. Next, we attempt to simulate multi-material problems of higher complexity, namely interaction between HE and metals. In the following section, we will describe the applications to which our new code has been applied where analytical solution (or experimentally validating data) are not available.

5.6 Applications

5.6.1 HE–Cu–Void (a “challenging” rate-stick) problem

The interface treatment technique as discussed earlier in the thesis is concerned with material–void or material–vacuum contact. We extend this approach to incorporate the generic material–material interface with a simple use of level sets. By tracking two different interfaces, namely a contact between a high explosive–copper and copper–void, we can use the unified fluid–solid code for complex impact and penetration problems.

A plane steady Chapman–Jouguet (CJ) detonation wave is used as the initial solution at the bottom of a rate-stick shown in the schematic, Fig. 5.10. Experimental observations on the rate-stick suggest that the steady, curved detonation wave propagates down the axis more slowly than a planar detonation. The wave speed varies with the diameter of the stick and also depends on the type of confinement. To understand the effect of metal confinement in place of the condensed gas used in the validation rate-stick experiment in the previous section, we use the fluid–solid hydrodynamic formulation to place a copper layer in contact with HE. With a finite thickness

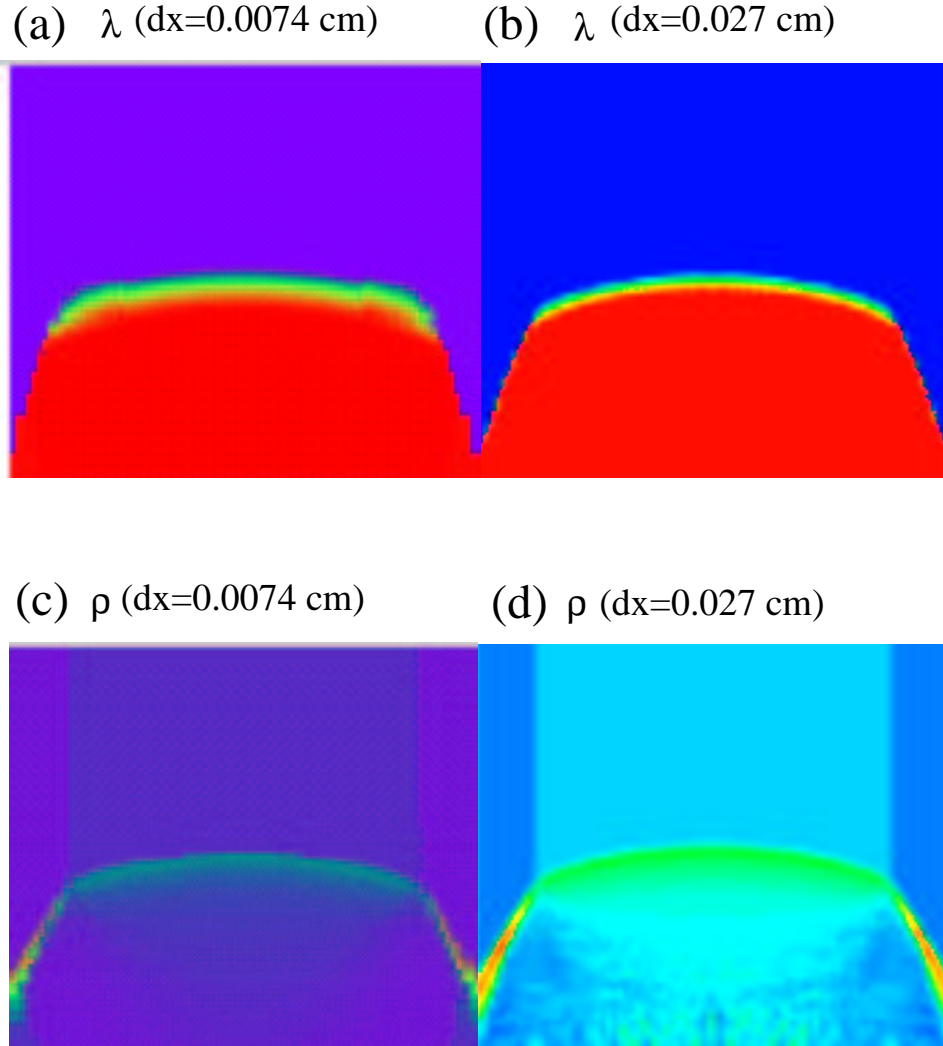


Figure 5.9: Comparison of rate-stick experiment. Shown on the left are extent of reaction and density from Ref. [1] with $\Delta x = \Delta y = 0.0074$ cm or 54 points in the reaction zone. Computed results on the right column are based on $\Delta x = \Delta y = 0.027$ cm or 15 points covering the reaction zone.

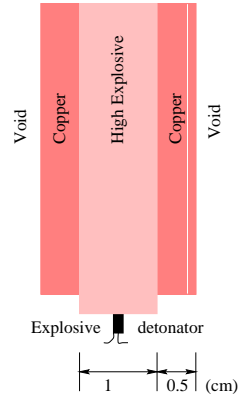


Figure 5.10: Schematic of a “challenging” rate-stick experiment.

of the copper-band confinement, we can observe the shock angle in the steady propagating wave system and the constant speed.

Shown in Fig. 5.11 are the transients of initial planar wave developing into a system of steady propagating detonation. The propagating pressure peak is approximately 60 GPa. The time elapsed between the frames shown in the figure is approximately 5 μsec .

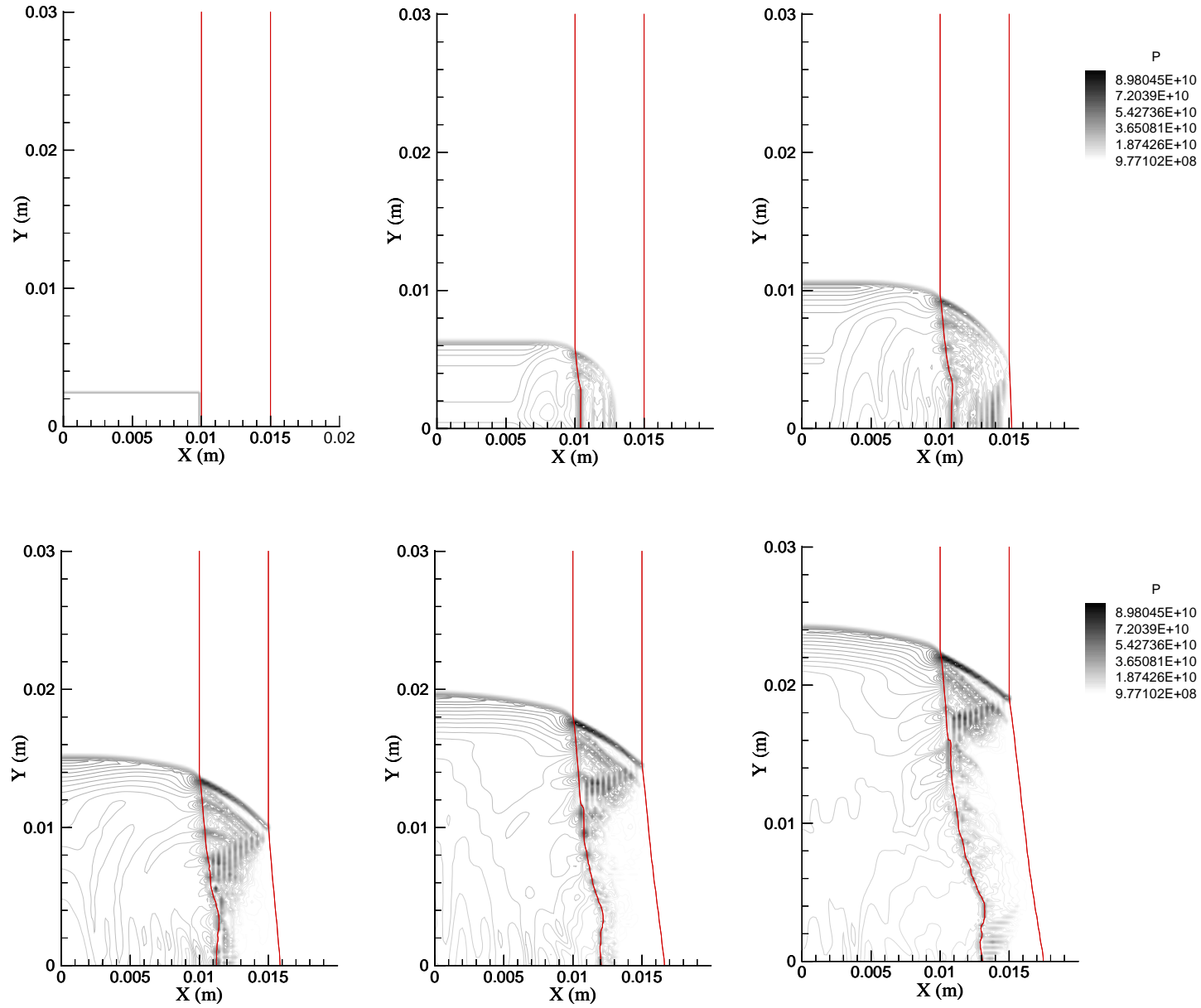


Figure 5.11: Rate-stick experiment simulated on 100 by 150 grid with 0.5 cm initial thickness of copper plate. Shown are the pressure fields (taken at every 5 μ sec) of 2 cm-thick cylinder of HE confined in a 5 mm-thick copper tube. The outer end of the copper band is a free surface.

Material property	Value
Density	7.85 g/cc
Shear modulus (μ)	77.5 GPa
Poisson's ratio (ν)	0.29
Young's modulus (E)	200 GPa
Yield stress (σ_o)	1500 MPa
Softening exponent, α	1.17
Hardening exponent, n	22
Melting temperature, T_m	1777 Kelvin
Reference temperature, T_o	300 Kelvin

Table 5.7: Material properties of high-strength steel.

5.6.2 Explosive welding

Fig. 5.13 shows a cartoon representing the basic idea of how explosive welding works. Initially separated by a small gap, one of two metal plates is coated with a layer of high explosive (HE). As the detonator initiates a planar shock wave, which is transmitted through a layer of copper plate and further through a steel layer, the two plates come in at a shearing velocity at a sizable fraction of the detonation speed of 8000 m/s and at a normal velocity of $D_{CJ} \sin \beta$. Here, β is the small angle formed by the closing of initial gap between the plates (see Table 5.6.2 for properties of steel).

To simulate the HE–Copper–Steel contact problem in the welding setting, we modify the initial setup slightly. First, the two plates are assumed in contact initially. Then, to mimic the resultant skew contact velocity with its components V_p and V_c , we assume the rectangular hot spot has velocity V_c initially. In this way, the interface between the HE and the copper plate experience both the shearing and normal velocity just as in the actual experiment shown in Fig. 5.13. Numerical results are shown in Figs. 5.14 and 5.15. The overlaid lines of the level-set functions on the pressure and the density figure represent the material interfaces between the metals and HE. Initially positioned at 1 cm and 1.5 cm, two interfaces have translated downward about 2.5 mm at the $x = 0$ location while the detonation front has reached the $x = 3$ cm location. Tremendous ringing is observed in the copper plate when the strong shock wave first penetrates and becomes weaker as it transmitted through the less-dense steel. Since the plastic yielding occurs at a much lower stress state in copper, the hardening behavior (seen with perturbations or ‘ringings’) is very pronounced in the copper layer. Although the unstable shearing motions are not easily observable in the copper–

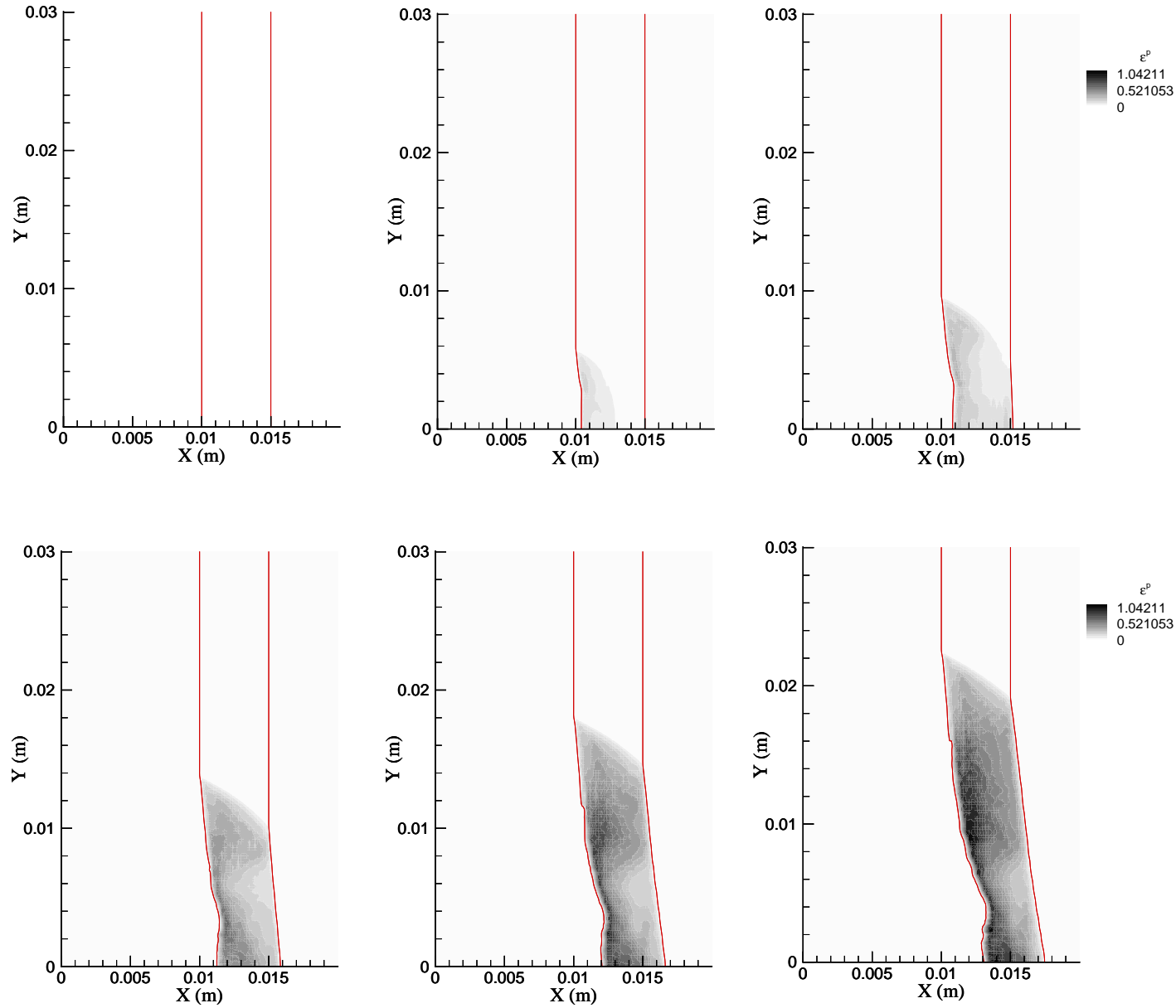


Figure 5.12: Rate-stick experiment simulated on 100 by 150 grid with 0.5 cm initial thickness of copper plate. Shown are the effective plastic strain fields (taken at every 5 μ sec) of 2 cm-thick cylinder of HE confined in a 5 mm-thick copper tube. The outer end of the copper band is a free surface.

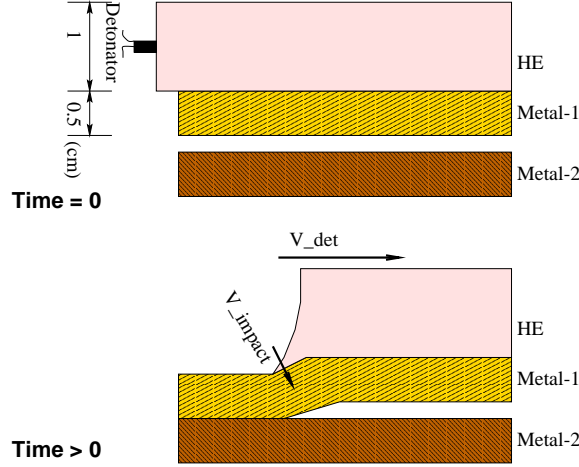


Figure 5.13: Schematic of explosive welding of two metal plates.

steel interface, this slip line can start the Kelvin–Helmholtz instability, resulting in rolling up of the contact lines. In Chapter 4, we considered the shear-induced melting of two plates in contact (see Fig. 4.9). The liquid interface between the plates became unstable as the plates experienced a shearing motion. By allowing the copper and steel of the welding simulation to undergo phase transformations, we can melt the interface and further observe a coherent wavy structure as the unstable interface starts to roll up as shown in the shear-induced melting of Chapter 4.

5.6.3 Penetration of copper plate target by spherical detonation

First the initial shape and location of two material interfaces are prescribed by a single distance function for each interface:

$$\begin{aligned}\phi_1 &= 1 \text{ cm} - x \\ \phi_2 &= (1 \text{ cm} + \text{width}) - x\end{aligned}$$

where the distance from the left inlet to a first interface is assigned a distance 1 cm, and the width is set 0.5 cm of the initial copper plate thickness. As the hot spot initiates a spherical detonation wave in a radial direction, chemical reaction instantly consumes the fuel ($\lambda = 0$) and a thin (in a continuum sense) reaction front is coupled to a shock approaching the first interface between the HE–Copper. As the shock penetrates the copper, we see an incipient plastic deformation in the

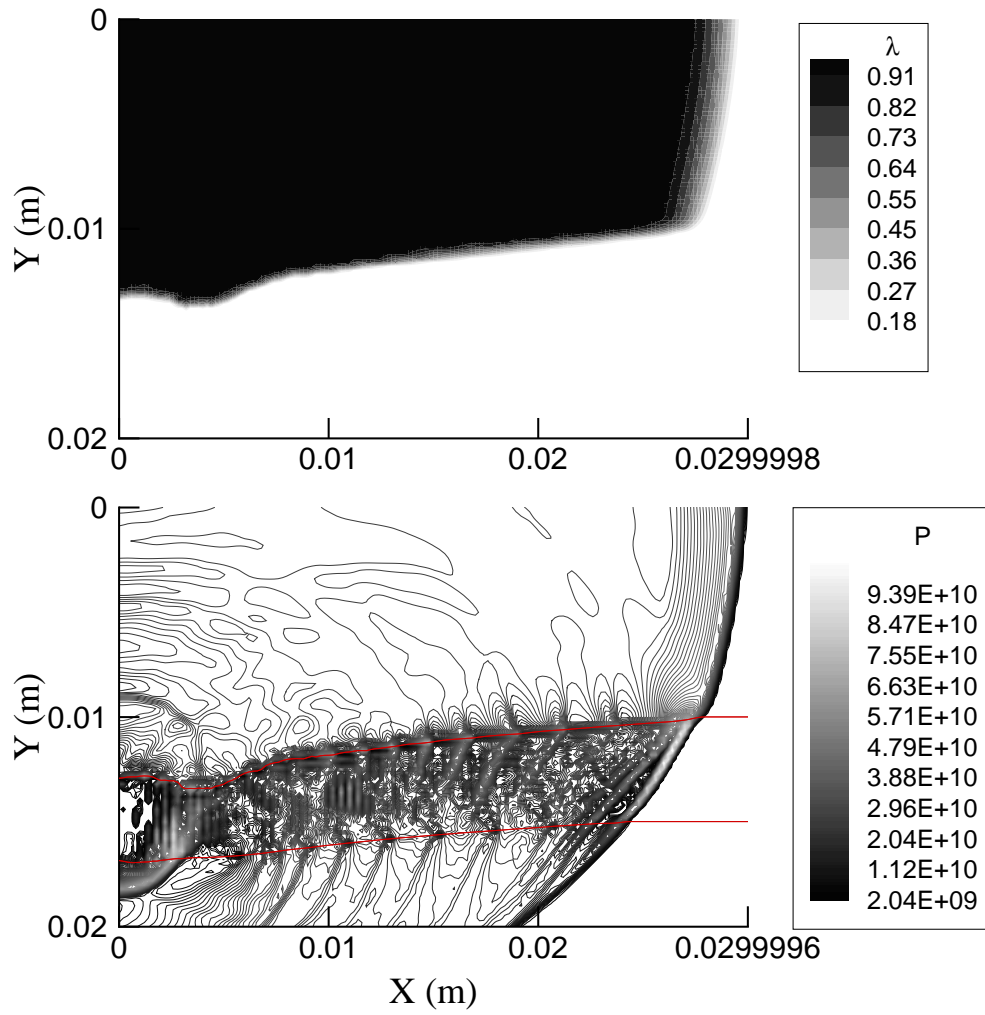


Figure 5.14: Explosive welding of copper (8.93g/cc) and high-strength steel (7.85g/cc). Shown are the extent of reaction and the pressure (Pa). Simulated on a 150 by 100 grid.

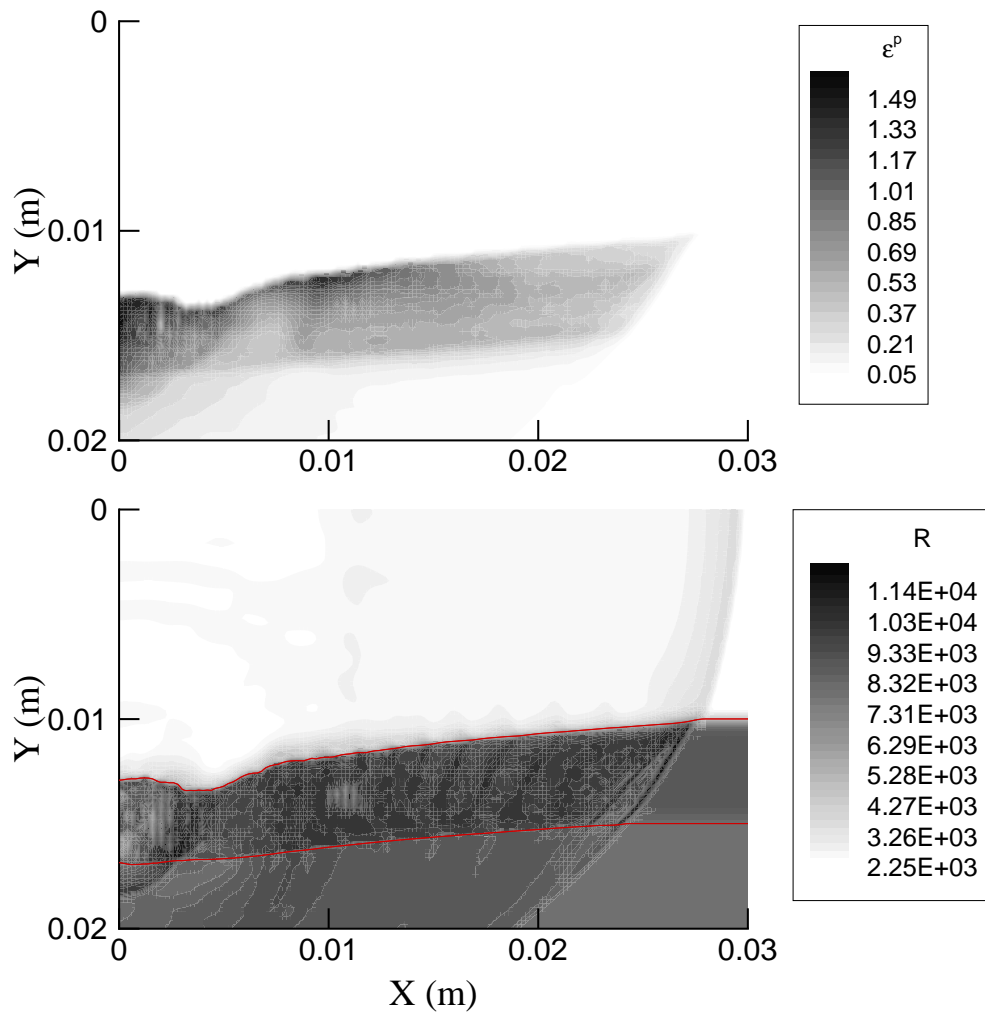


Figure 5.15: Explosive welding of copper (8.93g/cc) and high-strength steel (7.85g/cc). Shown are the effective plastic strain and the density (kg/m^3). Simulated on a 150 by 100 grid.

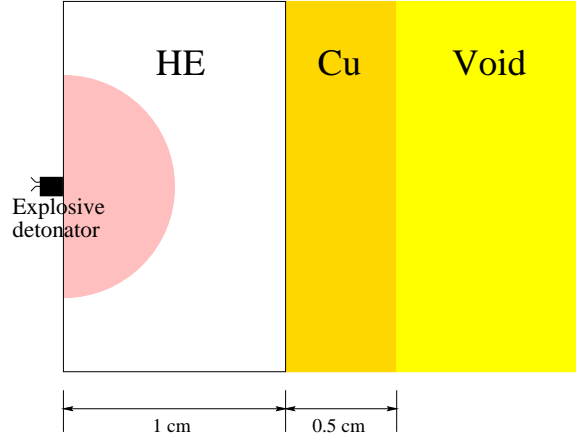


Figure 5.16: Schematic of copper plate penetration by a point source (detonation).

metal through Fig. 5.17. The highest effective plastic strains are observed where extreme bending occurs right at the center and the upper and lower ends. Since the second interface between the copper and a void is modeled by a free-moving piston, we expect the entrapment of waves between these two interfaces, resulting in a rich wave interaction in the metal layer.

Fig. 5.18 shows the pressure contours of spherical detonation wave penetrating into the first copper interface and pushing out the second interface. The first snapshot taken at $t = 1.02 \mu\text{sec}$ shows a complex wave structure at the interface, where reflections of the incident waves are clearly observed. As the incident spherical wave reaches the second interface, a translational motion of the free boundary is seen from the $t = 2.77 \mu\text{sec}$ figure, where part of the incident shock is reflecting back toward the first interface. As the process of plastic deformation takes place inside the copper layer, the deformed shape of the plate suggests that the pressure distribution plays an important role in the changing the shape of the metal layer. The reflecting shocks off the upper and lower walls of the domain cause the two ends of the plate to start bending as in the last figure ($t = 5.23 \mu\text{sec}$). This bending of the two ends might suggest a pinching-off mechanism by which a metal of finite thickness may break open upon a detonation wave.

Fig. 5.19 describes how the initially unreacted HE is completely burnt as the hot product gas pushes the copper plate in the direction outward. The reflecting boundary on the top and the bottom of the domain allows for a translational motion of the metal strip. A more realistic boundary would have been to fix the metal ends while all flows in the field are allowed to leave the

domain. In any event, the present numerical simulations explain the kind of damage a spherical detonation wave can do to a metal plate. One may also find regions of a high tensile stress where an onset of ‘tearing’ may occur, causing the plate to break up in pieces.

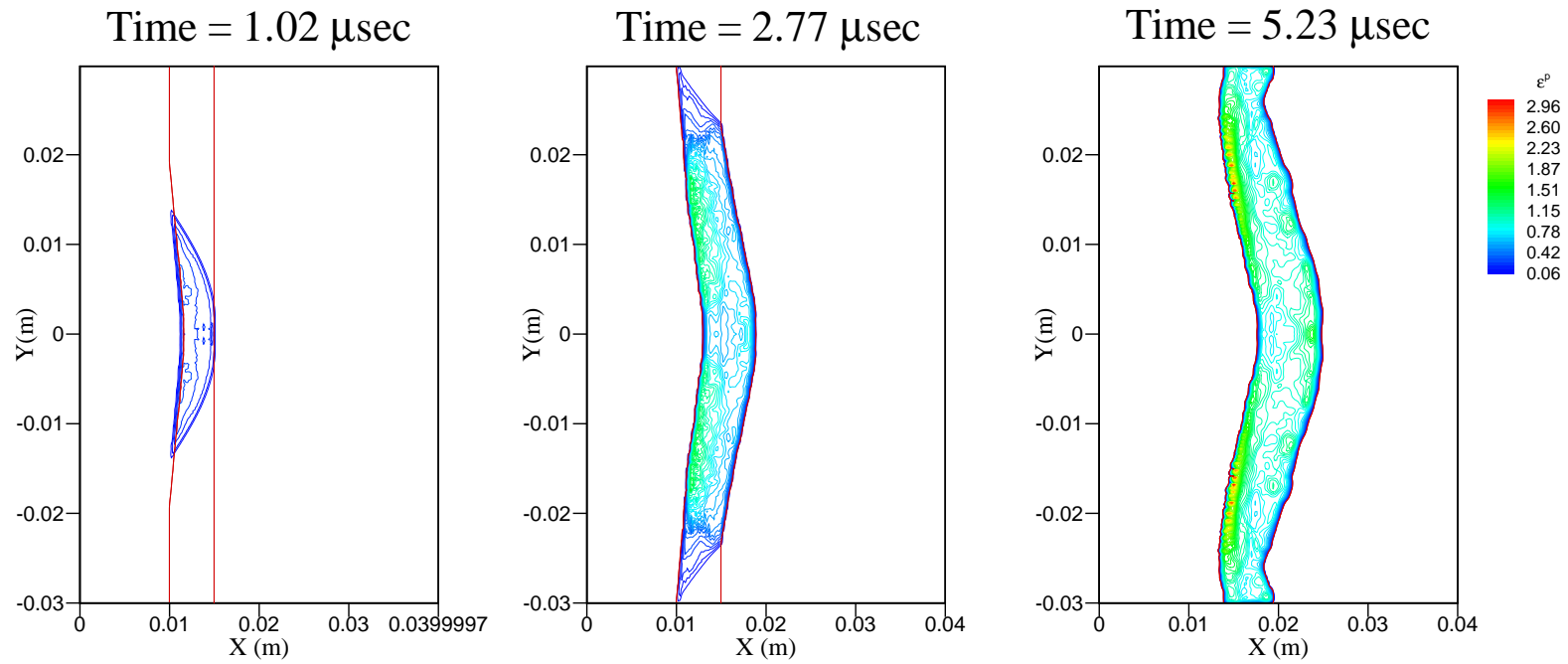


Figure 5.17: Spherical detonation wave (ABS model) initiated at a point source located at $(x,y) = (0,0)$ penetrating the copper plate target located at 1 cm. The right edge of the plate is at 1.5 cm, where the copper-void interface boundary is enforced. Dynamic deforming motion of the plate is illustrated through a series of snapshots at different times. Shown are the effective plastic strain field as calculated on 200 by 600 grid.

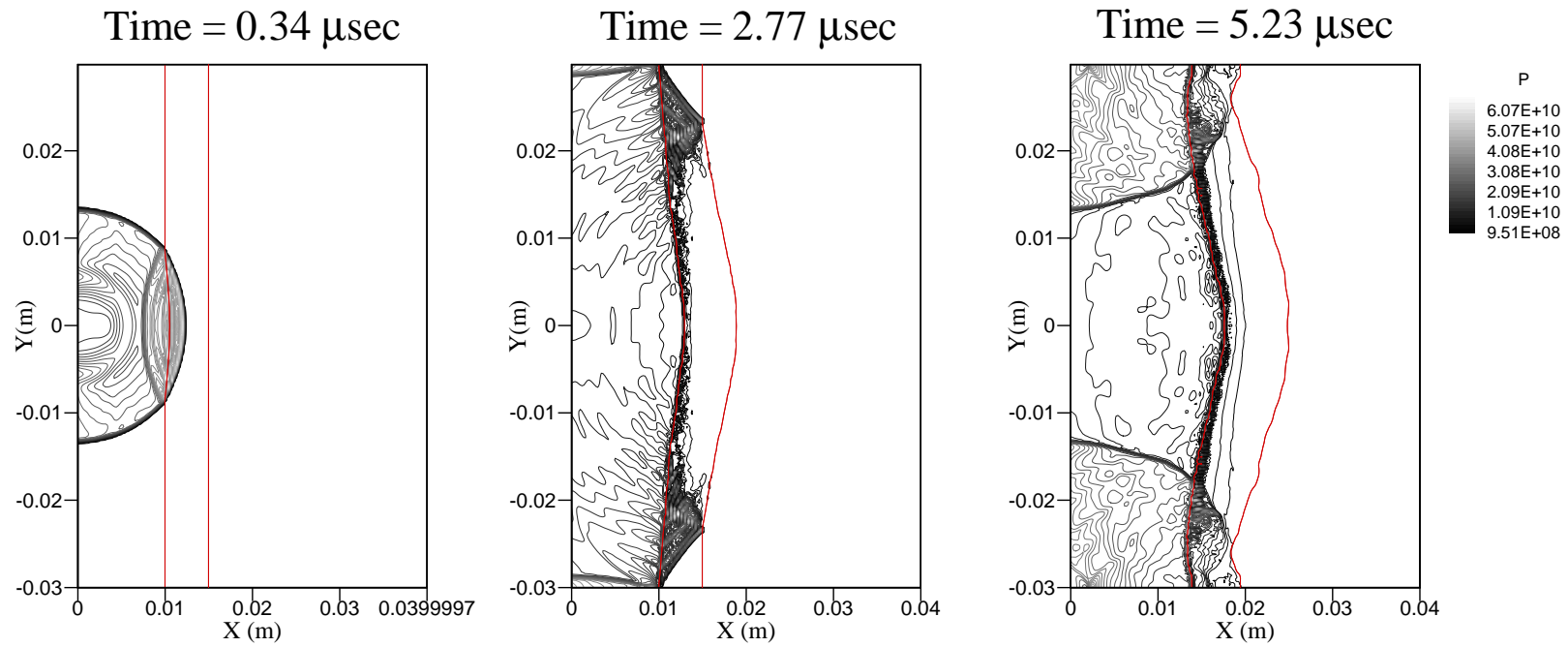


Figure 5.18: Spherical detonation wave (ABS model) initiated at a point source located at $(x, y) = (0, 0)$ penetrating the copper plate target located at 1 cm. The right edge of the plate is at 1.5 cm, where the copper-void interface boundary is enforced. Dynamic deforming motion of the plate is illustrated through a series of snapshots at different times. Shown are the pressure fields as calculated on 200 by 600 grid.

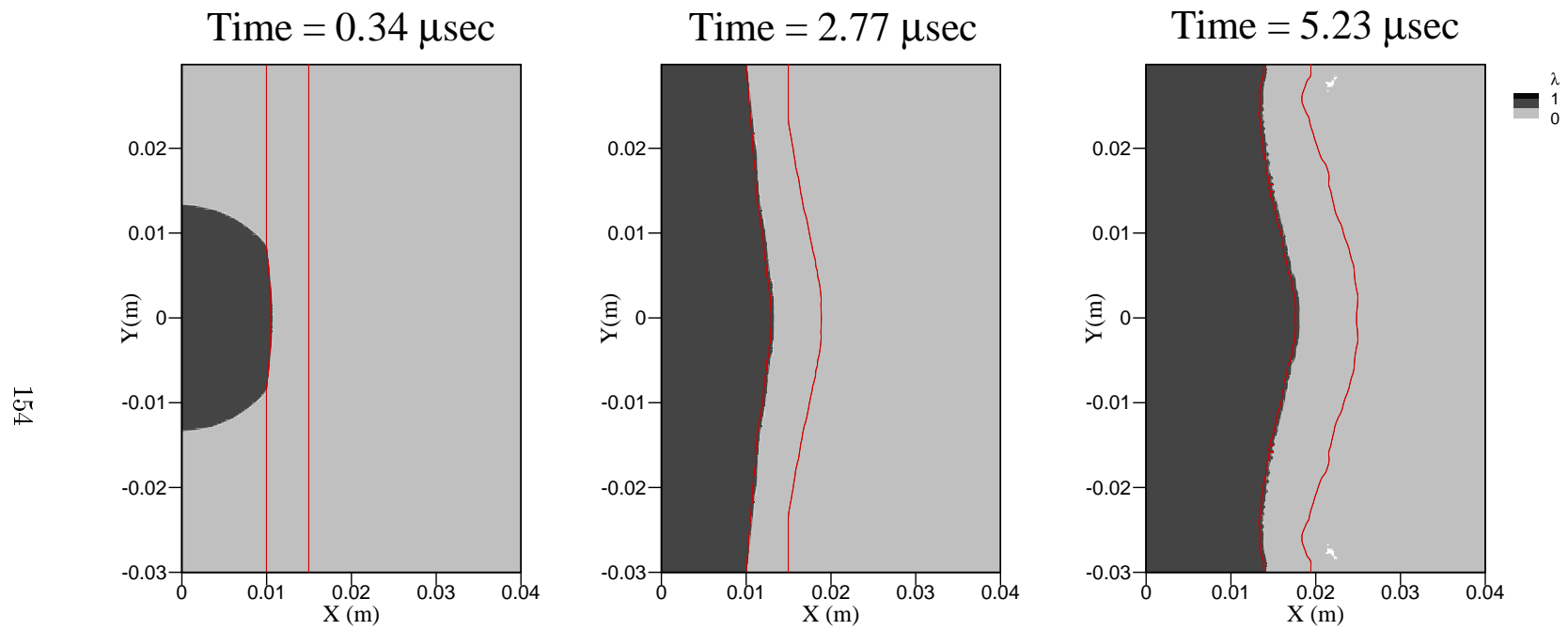


Figure 5.19: Spherical detonation wave (ABS model) initiated at a point source located at $(x,y) = (0,0)$ penetrating the copper plate target located at 1 cm. The right edge of the plate is at 1.5 cm, where the copper-void interface boundary is enforced. Dynamic deforming motion of the plate is illustrated through a series of snapshots at different times. The reaction progress variable is shown on 200 by 600 grid.

Chapter 6

Conclusions

We have derived a three-dimensional model for a representative energetic materials with two independent state variables that represent the change of phase from solid to liquid to gas and the extent of exothermic reaction. The model corrects the errors found in the work of Ruderman [61] so that the equations are consistent with the combustion theory of binary mixtures while the entropy principle is satisfied. We have fit the model to HMX, a base-line energetic material, and have given interpretations of the model relating to classical phase transitions. Also, we have carried out detailed computations of classical simple motions.

In the second half of the thesis, we have developed a comprehensive numerical frame to compute multi-material interactions for the same energetic material and such other inerts as copper and an elastic solid. The numerical methods used in the spatial discretization are ENO schemes with level sets to treat the sharp material interface. The level sets track the motions of the material–material or material–void (or vacuum) interfaces so as to minimize any spurious oscillations associated with the smearing of entropy profiles across a sharp material interface. The high-resolution simulation tool for the multi-material impact has been carefully validated through a series of one-dimensional and multi-dimensional tests and has produced both qualitative and quantitative comparisons with benchmark results.

Possible topics for future research using the present framework of the theory and the numerics are: (i) micro-explosion of a hydrocarbon fuel droplet, (ii) explosive welding with phase changes, (iii) ignition of HE in contact with hot-spots and voids, and (iv) miniaturization of energetic materials and HE devices.

Appendix A

List of φ -dependent functions

$$\mathcal{F}(\varphi) = [\varphi(\varphi - 1)(\varphi - 2)]^2$$

$$\mathcal{F}'(\varphi) = 2\varphi(4 - 18\varphi + 26\varphi^2 - 15\varphi^3 + 3\varphi^4)$$

$$\beta'_m(\varphi) = \begin{cases} 6\varphi(1 - \varphi) & \text{for } 0 \leq \varphi \leq 1 \\ 0 & \text{otherwise} \end{cases}$$

$$\beta'_v(\varphi) = \begin{cases} 6(\varphi - 1)(2 - \varphi) & \text{for } 1 \leq \varphi \leq 2 \\ 0 & \text{otherwise} \end{cases}$$

$$\mu_s(\varphi) = \begin{cases} 2(\mu_{sol} - \mu_{liq})\varphi^3 - 3(\mu_{sol} - \mu_{liq})\varphi^2 + \mu_{sol} & \text{for } 0 \leq \varphi \leq 1 \\ 2(\mu_{liq})(\varphi - 1)^3 - 3(\mu_{liq})(\varphi - 1)^2 + \mu_{liq} & \text{for } 1 \leq \varphi \leq 2 \end{cases}$$

$$\mu'_s(\varphi) = \begin{cases} 6(\mu_{sol} - \mu_{liq})\varphi^2 - 6(\mu_{sol} - \mu_{liq})\varphi & \text{for } 0 \leq \varphi \leq 1 \\ 6(\mu_{liq})(\varphi - 1)^2 - 6(\mu_{liq})(\varphi - 1) & \text{for } 1 \leq \varphi \leq 2 \\ 0 & \text{otherwise} \end{cases}$$

$$R(\varphi) = \begin{cases} 2(-R_v)(\varphi - 1)^3 - 3(-R_v)(\varphi - 1)^2 & \text{for } 1 \leq \varphi \leq 2 \\ 0 & \text{for } \varphi < 1 \\ R_v & \text{for } \varphi > 2 \end{cases}$$

$$R'(\varphi) = \begin{cases} 6(-R_v)(\varphi - 1)^2 - 6(-R_v)(\varphi - 1) & \text{for } 1 \leq \varphi \leq 2 \\ 0 & \text{otherwise} \end{cases}$$

$$\alpha(\varphi) = \begin{cases} 2(\alpha_s)(\varphi - 1)^3 - 3(\alpha_s)(\varphi - 1)^2 & \text{for } 1 \leq \varphi \leq 2 \\ \alpha_s & \text{for } \varphi < 1 \\ 0 & \text{for } \varphi > 2 \end{cases}$$

$$\alpha'(\varphi) = \begin{cases} 6(\alpha_s)(\varphi - 1)^2 - 6(\alpha_s)(\varphi - 1) & \text{for } 1 \leq \varphi \leq 2 \\ 0 & \text{otherwise} \end{cases}$$

$$\rho\gamma_\varphi(\varphi) = \begin{cases} 6(-\rho\gamma_\varphi)\varphi^2 - 6(-\rho\gamma_\varphi)\varphi & \text{for } 0 \leq \varphi \leq 1 \\ 6(-\rho\gamma_\varphi)(\varphi - 1)^2 - 6(-\rho\gamma_\varphi)(\varphi - 1) & \text{for } 1 \leq \varphi \leq 2 \\ 0 & \text{otherwise} \end{cases}$$

$$c_v(\varphi) = c_v$$

Appendix B

Special Forms of Equations

B.1 Lagrangian equations (in terms of X_1)

Mass balance:

$$\frac{\partial \rho}{\partial t} + \rho \left(1 + \frac{\partial u_1}{\partial X_1}\right)^{-1} \frac{\partial v_1}{\partial X_1} = 0$$

Momentum balance:

$$\begin{aligned} \rho_o \frac{\partial v_1}{\partial t} = & \frac{\partial}{\partial X_1} \left\{ \bar{\mu}_1 \left(1 + \frac{\partial u_1}{\partial X_1}\right) - \bar{\mu}_2 \left(1 + \frac{\partial u_1}{\partial X_1}\right)^{\frac{-1}{1-2\nu}} - \rho RT - \rho \gamma_\varphi \left(1 + \frac{\partial u_1}{\partial X_1}\right)^{-1} \frac{\partial \varphi}{\partial X_1} \right\} \\ & (\nu_f + 2\mu_f) \frac{\partial v_1}{\partial X_1} \left(1 + \frac{\partial u_1}{\partial X_1}\right)^{-1} \end{aligned}$$

Displacement:

$$\frac{\partial u_1}{\partial t} = v_1$$

Energy balance:

$$\begin{aligned}
\rho c_v \frac{\partial T}{\partial t} = & K(1 + \frac{\partial u_1}{\partial X_1})^{-1} \frac{\partial}{\partial X_1} \left((1 + \frac{\partial u_1}{\partial X_1})^{-1} \frac{\partial T}{\partial X_1} \right) \\
& + (\nu_f + 2\mu_f) \left(\frac{\partial v_1}{\partial X_1} (1 + \frac{\partial u_1}{\partial X_1})^{-1} \right)^2 \\
& + B_\varphi \left(\frac{\partial \varphi}{\partial t} \right)^2 + B_\lambda \left(\frac{\partial \lambda}{\partial t} \right)^2 + T \rho \left(\beta_m' \frac{Q_m}{T_m} + \beta_v' \frac{Q_v}{T_v} \right) \frac{\partial \varphi}{\partial t} + \rho Q_c \frac{\partial \lambda}{\partial t} \\
& + \bar{\mu}_1 \frac{\partial v_1}{\partial X_1} - \bar{\mu}_2 (1 + \frac{\partial u_1}{\partial X_1})^{-\frac{1}{1-2\nu}} \frac{\partial v_1}{\partial X_1} - \rho R T (1 + \frac{\partial u_1}{\partial X_1})^{-1} \frac{\partial v_1}{\partial X_1} \\
& + \frac{1}{2} \frac{\partial \bar{\mu}_1}{\partial \varphi} (1 + \frac{\partial u_1}{\partial X_1})^{-1} \left((1 + \frac{\partial u_1}{\partial X_1})^2 - 1 \right) \frac{\partial \varphi}{\partial t} \\
& + \frac{1-2\nu}{2\nu} \frac{\partial \bar{\mu}_2}{\partial \varphi} (1 + \frac{\partial u_1}{\partial X_1})^{-1} \left((1 + \frac{\partial u_1}{\partial X_1})^{-\frac{2\nu}{1-2\nu}} - 1 \right) \frac{\partial \varphi}{\partial t}
\end{aligned}$$

Microforce balance:

$$\begin{aligned}
B_\varphi \frac{\partial \varphi}{\partial t} = & (1 + \frac{\partial u_1}{\partial X_1})^{-1} \frac{\partial}{\partial X_1} \left(\rho \gamma_\varphi (1 + \frac{\partial u_1}{\partial X_1})^{-1} \frac{\partial \varphi}{\partial X_1} \right) \\
& - \mu_s'(\varphi) \frac{\rho}{2\rho_o} \left((1 + \frac{\partial u_1}{\partial X_1})^2 - 1 \right) \\
& - \bar{\mu}_2'(\varphi) \frac{\rho(1-2\nu)}{2\rho_o \nu} \left((1 + \frac{\partial u_1}{\partial X_1})^{\frac{-2\nu}{1-2\nu}} - 1 \right) \\
& + \rho c_v'(\varphi) \left(T \ln \frac{T}{T_o} - (T - T_o) \right) - \rho \frac{1}{2} \Psi^{well} \frac{\partial}{\partial \varphi} \left(\{(\varphi)(\varphi-1)(\varphi-2)\}^2 \right) \\
& - \rho \beta_m'(\varphi) \frac{T - T_m}{T_m} Q_m - \rho \beta_v'(\varphi) \frac{T - T_v}{T_v} Q_v
\end{aligned}$$

B.2 Eulerian equations (in terms of x_1)

Mass balance:

$$\frac{\partial \rho}{\partial t} + v_1 \frac{\partial \rho}{\partial x_1} + \rho \frac{\partial v_1}{\partial x_1} = 0$$

Momentum balance:

$$\begin{aligned}
\rho \left(\frac{\partial v_1}{\partial t} + v_1 \frac{\partial v_1}{\partial x_1} \right) = & \frac{\partial}{\partial x_1} \left\{ \mu_s (1 + H) - \mu_s (1 + H)^{\frac{-1}{1-2\nu}} - \rho R T \gamma_\varphi \left(\frac{\partial \varphi}{\partial x_1} \right)^2 \right. \\
& \left. + (\nu_f + 2\mu_f) \frac{\partial v_1}{\partial x_1} \right\}
\end{aligned}$$

Displacement gradient, $H = \frac{\partial u_1}{\partial X_1}$:

$$\frac{\partial H}{\partial t} = \frac{\partial v_1}{\partial x}(1 + H)$$

Energy balance:

$$\begin{aligned} \rho c_v \left(\frac{\partial T}{\partial t} + v_1 \frac{\partial T}{\partial x} \right) &= K \frac{\partial^2 T}{\partial x_1^2} + (\nu_f + 2\mu_f) \left(\frac{\partial v_1}{\partial x} \right)^2 \\ &+ B_\varphi \left(\frac{\partial \varphi}{\partial t} + v_1 \frac{\partial \varphi}{\partial x} \right)^2 + B_\lambda \left(\frac{\partial \lambda}{\partial t} + v_1 \frac{\partial \lambda}{\partial x} \right)^2 \\ &+ T \rho \left(\beta_m' \frac{Q_m}{T_m} + \beta_v' \frac{Q_v}{T_v} \right) \left(\frac{\partial \varphi}{\partial t} + v_1 \frac{\partial \varphi}{\partial x} \right) + \rho Q_c \left(\frac{\partial \lambda}{\partial t} + v_1 \frac{\partial \lambda}{\partial x} \right) \\ &+ \bar{\mu}_1 (1 + H) \frac{\partial v_1}{\partial x} - \bar{\mu}_2 (1 + H)^{-\frac{1}{1-2\nu}} \frac{\partial v_1}{\partial x} - \rho R T \frac{\partial v_1}{\partial x} \\ &+ \frac{1}{2} \frac{\partial \bar{\mu}_1}{\partial \varphi} (1 + H)^{-1} ((1 + H)^2 - 1) \left(\frac{\partial \varphi}{\partial t} + v_1 \frac{\partial \varphi}{\partial x} \right) \\ &+ \frac{1 - 2\nu}{2\nu} \frac{\partial \bar{\mu}_2}{\partial \varphi} (1 + H)^{-1} \left((1 + H)^{-\frac{2\nu}{1-2\nu}} - 1 \right) \left(\frac{\partial \varphi}{\partial t} + v_1 \frac{\partial \varphi}{\partial x} \right) \end{aligned}$$

Microforce balance:

$$\begin{aligned} B_\varphi \left(\frac{\partial \varphi}{\partial t} + v_1 \frac{\partial \varphi}{\partial x} \right) &= \frac{\partial}{\partial x} \left(\rho \gamma_\varphi \frac{\partial \varphi}{\partial x} \right) \\ &- \mu_s'(\varphi) \frac{1}{2} (1 + H)^{-1} ((1 + H)^2 - 1) \\ &- \bar{\mu}_2'(\varphi) \frac{(1 - 2\nu)}{2\nu} (1 + H)^{-1} \left((1 + H)^{-\frac{2\nu}{1-2\nu}} - 1 \right) \\ &+ \rho c_v'(\varphi) \left(T \ln \frac{T}{T_o} - (T - T_o) \right) - \rho \frac{1}{2} \Psi^{well} \frac{\partial}{\partial \varphi} \left(\{(\varphi)(\varphi - 1)(\varphi - 2)\}^2 \right) \\ &- \rho \beta_m'(\varphi) \frac{T - T_m}{T_m} Q_m - \rho \beta_v'(\varphi) \frac{T - T_v}{T_v} Q_v \end{aligned}$$

B.3 Conservation in Eulerian framework

Spherically symmetric coordinate

The basic difference is in the divergence operator:

$$\begin{aligned} \nabla \cdot \mathbf{u} &= \frac{1}{r^2} \frac{\partial}{\partial r} (r^2 \mathbf{u}) \\ \nabla \cdot \nabla \mathbf{u} &= \frac{1}{r^2} \frac{\partial}{\partial r} \left(r^2 \frac{\partial \mathbf{u}}{\partial r} \right) \end{aligned}$$

Mass balance:

$$\frac{\partial}{\partial t}(\rho) + \frac{1}{r^2} \frac{\partial}{\partial r}(r^2 \rho v_r) = 0$$

or

$$\frac{\partial}{\partial t}(\rho) + \frac{\partial}{\partial r}(\rho v_r) = -\frac{2}{r} \rho v_r$$

Momentum balance:

$$\begin{aligned} \frac{\partial}{\partial t}(\rho v_r) + \frac{\partial}{\partial r}(\rho v_r^2) &= \frac{\partial}{\partial r} \sigma + \frac{2}{r}(\sigma - \rho v_r^2) \\ \text{where } \sigma &= \left\{ \bar{\mu}_1(1+H) - \bar{\mu}_2(1+H)^{\frac{-1}{1-2\nu}} - \rho R T - \rho \gamma_\varphi \left(\frac{\partial \varphi}{\partial r} \right)^2 \right. \\ &\quad \left. + (\nu_f + 2\mu_f) \frac{\partial v_r}{\partial r} \right\} \end{aligned}$$

Displacement gradient, $H = \frac{\partial u_r}{\partial X_1}$:

$$\frac{\partial H}{\partial t} = \frac{\partial v_r}{\partial r}(1+H)$$

Energy balance:

$$\begin{aligned} \frac{\partial}{\partial t}(\rho c_v T) + \frac{\partial}{\partial r}(\rho c_v T v_r) &= K \frac{\partial^2 T}{\partial r^2} + \frac{2}{r} \left(K \frac{\partial T}{\partial r} - \rho c_v T v_r \right) + (\nu_f + 2\mu_f) \left(\frac{\partial v_r}{\partial r} \right)^2 \\ &\quad + B_\varphi \left(\frac{\partial \varphi}{\partial t} + v_r \frac{\partial \varphi}{\partial r} \right)^2 + B_\lambda \left(\frac{\partial \lambda}{\partial t} + v_r \frac{\partial \lambda}{\partial r} \right)^2 \\ &\quad + T \rho \left(\beta_m' \frac{Q_m}{T_m} + \beta_v' \frac{Q_v}{T_v} \right) \left(\frac{\partial \varphi}{\partial t} + v_r \frac{\partial \varphi}{\partial r} \right) + \rho Q_c \left(\frac{\partial \lambda}{\partial t} + v_r \frac{\partial \lambda}{\partial r} \right) \\ &\quad + \bar{\mu}_1(1+H) \frac{\partial v_r}{\partial r} - \bar{\mu}_2(1+H)^{-\frac{1}{1-2\nu}} \frac{\partial v_r}{\partial r} - \rho R T \frac{\partial v_r}{\partial r} \\ &\quad + \frac{1}{2} \frac{\partial \bar{\mu}_1}{\partial \varphi} (1+H)^{-1} ((1+H)^2 - 1) \left(\frac{\partial \varphi}{\partial t} + v_r \frac{\partial \varphi}{\partial r} \right) \\ &\quad + \frac{1-2\nu}{2\nu} \frac{\partial \bar{\mu}_2}{\partial \varphi} (1+H)^{-1} \left((1+H)^{-\frac{2\nu}{1-2\nu}} - 1 \right) \left(\frac{\partial \varphi}{\partial t} + v_r \frac{\partial \varphi}{\partial r} \right) \end{aligned}$$

Microforce balance:

$$\begin{aligned}
\frac{B_\varphi}{\rho} \left(\frac{\partial}{\partial t} (\rho\varphi) + \frac{\partial}{\partial r} (\rho\varphi v_r) \right) &= \frac{\partial}{\partial r} \left(\rho\gamma_\varphi \frac{\partial \varphi}{\partial r} \right) + \frac{2}{r} \left(\rho\gamma_\varphi \frac{\partial \varphi}{\partial r} - \rho\varphi v_r \right) \\
&\quad - \mu'_s(\varphi) \frac{1}{2} (1+H)^{-1} ((1+H)^2 - 1) \\
&\quad - \bar{\mu}'_2(\varphi) \frac{(1-2\nu)}{2\nu} (1+H)^{-1} \left((1+H)^{\frac{-2\nu}{(1-2\nu)}} - 1 \right) \\
&\quad + \rho c'_v(\varphi) \left(T \ln \frac{T}{T_o} - (T - T_o) \right) - \rho \frac{1}{2} \Psi^{well} \frac{\partial}{\partial \varphi} \left(\{(\varphi)(\varphi-1)(\varphi-2)\}^2 \right) \\
&\quad - \rho \beta'_m(\varphi) \frac{T - T_m}{T_m} Q_m - \rho \beta'_v(\varphi) \frac{T - T_v}{T_v} Q_v
\end{aligned}$$

Level-set function:

$$\frac{\partial}{\partial t} (\rho\phi) + \frac{\partial}{\partial r} (\rho\phi v_r) = -\frac{2}{r} (\rho\phi v_r)$$

B.4 Euler equations in spherical coordinates

$$\begin{aligned}
\frac{\partial(\rho)}{\partial t} + \frac{\partial}{\partial r} (\rho v_r) + \frac{2}{r} (\rho v_r) &= 0 \\
\frac{\partial(\rho v_r)}{\partial t} + \frac{\partial}{\partial r} (\rho v_r^2 + p) + \frac{2}{r} (\rho v_r^2) &= 0 \\
\frac{\partial(\rho e)}{\partial t} + \frac{\partial}{\partial r} ((\rho e + p)v_r) + \frac{2}{r} (\rho e v_r) &= 0
\end{aligned}$$

Appendix C

Structure Analysis of Steady Phase Transformation Waves

In this chapter, we consider the structure of steady wave system which is admitted by the continuum equations described earlier in this work. In particular, we compute the shock structures in pure phases of solid and gas, and the phase front structure of melting/freezing and vaporization/condensation.

C.1 Shock structures

In the continuum theory, a shock is interpreted as a thin region, rather than a discontinuity, in which rapid changes of the flow quantities occur. Two uniform end states of a typical shock are related through a smooth structure of finite length in microns where the conservation of mass, momentum and energy is achieved. In this section, we will consider the shock structures of compressible Navier–Stokes equations, gas-phase HMX equations, and solid-phase HMX equations.

C.1.1 Continuum structure of compressible N–S equations

The shocked state is the unstable equilibrium. The integration of the structure starts from this point to a stable point on the unshocked state. Fig. C.1 shows the steady shock coordinate where $\xi = x - Dt, U = u - D$ so that in this frame, velocities both upstream and downstream are negative, pointing to the left. Here D is the steady wave speed, directed in the negative ξ direction

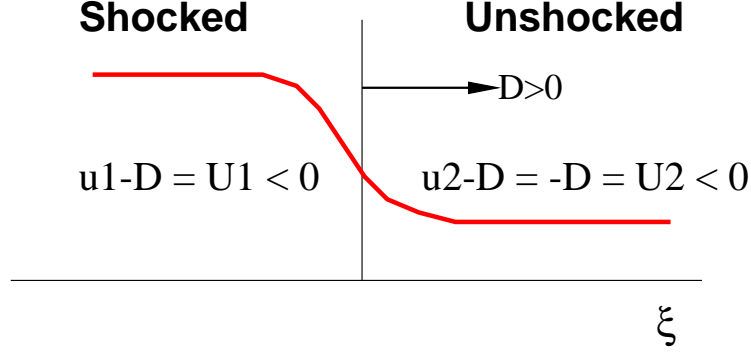


Figure C.1: Schematic of shock-attached frame.

(i.e. $D < 0$). The derivatives with respect to x and t now become

$$\frac{\partial}{\partial t} = \frac{\partial \xi}{\partial t} \frac{d}{d\xi} = -D \frac{d}{d\xi} \quad ; \quad \frac{\partial}{\partial x} = \frac{d}{d\xi}$$

and, in particular, the velocity gradient becomes

$$\frac{\partial u}{\partial x} = \frac{dU}{d\xi}$$

Thus the equations of motions for the ideal gas are as follows:

$$\rho U = m, \quad (U = D - u) \tag{C.1}$$

$$\frac{dU}{d\xi} = \frac{3}{4\mu_f} \left\{ mU_{-\infty} + \frac{m}{U_{-\infty}} RT_1 - mU - \frac{m}{U} RT \right\} \tag{C.2}$$

$$\frac{dT}{d\xi} = \frac{1}{K} \left\{ \frac{\gamma}{\gamma - 1} mRT_1 + \frac{1}{2} mU_{-\infty}^2 - \frac{4}{3} \mu_f U U_\xi - \frac{\gamma}{\gamma - 1} mRT - \frac{1}{2} mU^2 \right\} \tag{C.3}$$

where we have used $m = \rho U$ and $p = \rho RT$. Using the constants standard of air, so that $\mu = 1.95 \times 10^{-5}$ N s/m², $K = 0.0276$ W/m K, and $R = 287$ m²/s²K, we can integrate from a shocked state as shown in Fig. C.2 into an ambient side.

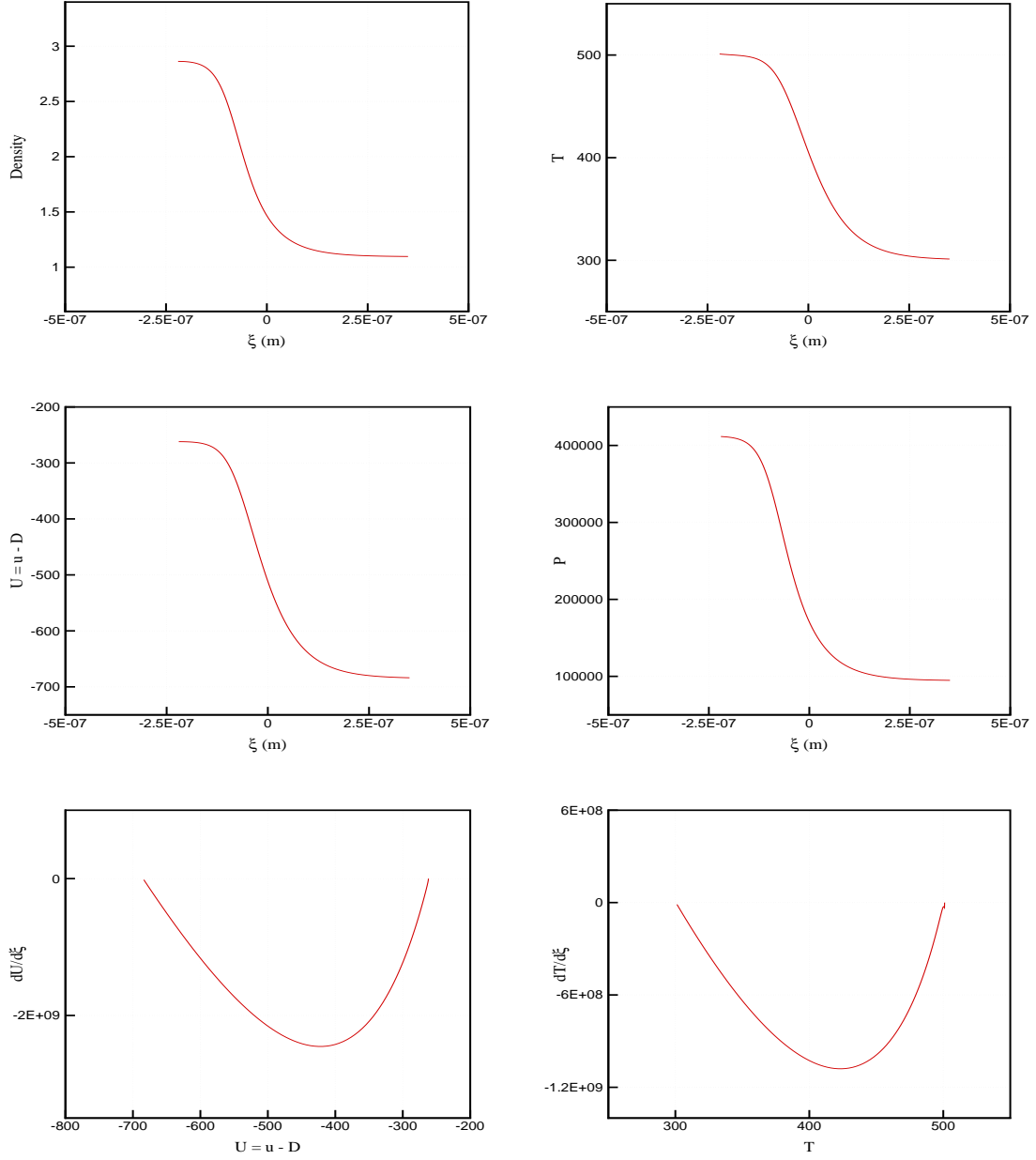


Figure C.2: Computed shock structure of compressible viscous Euler gas.

C.1.2 Continuum structure of gas-phase HMX equations

When $\varphi = 2$, the continuum equations for HMX represent a set of condensed gas phase equations. Expressed in terms of transformed coordinate ξ , the equations become

$$\frac{dU}{d\xi} = \frac{3}{4\mu_f} \{mU + \rho RT - mU_{-\infty} - \rho_{-\infty} RT_{-\infty}\} \quad (\text{C.4})$$

$$\frac{dH}{d\xi} = \frac{1}{K} \left\{ mc_v H - \frac{4}{3} \mu_f \left(\frac{dU}{d\xi} \right)^2 + \rho RT \frac{dU}{d\xi} \right\} \quad (\text{C.5})$$

$$\frac{dT}{d\xi} = H. \quad (\text{C.6})$$

As in the case of compressible N-S equations, we fix the far left shocked state and start the integration toward the positive ξ direction.

Shown in Fig. C.3 is the computed shock structures of HMX vapor where the phase field variable is stationary at a value of 2. Based on the constants of HMX properties, the resulting shock thickness is about 4 mm, a thickness much thicker than the ideal gas structure thickness of $0.5 \mu\text{m}$.

C.1.3 Continuum structure of solid-phase HMX equations

In this exercise, we consider a shock in solid, namely non-reacting HMX solid whose phase is fixed at $\varphi = 0$. The governing equations as follows:

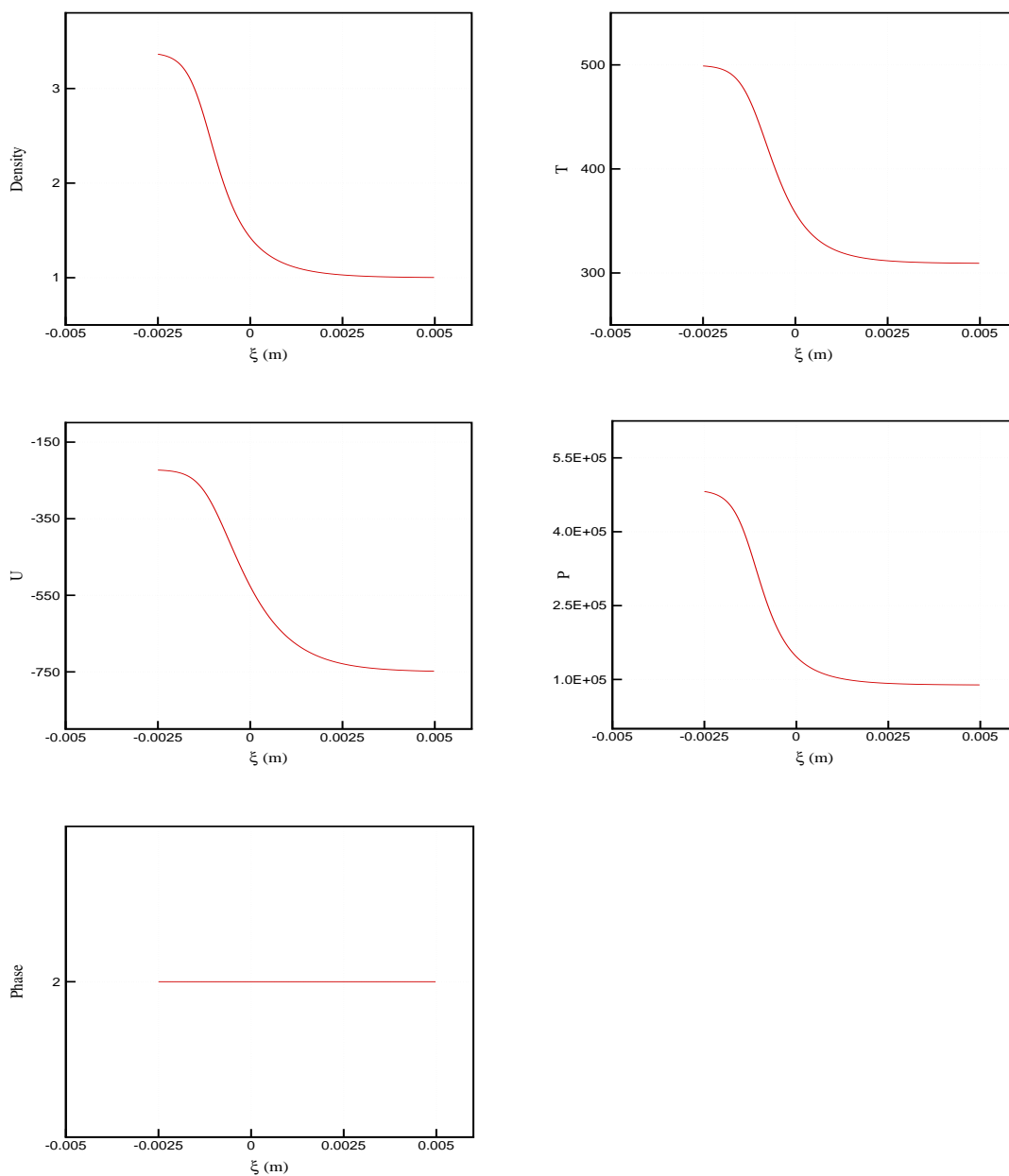
$$\begin{aligned} \frac{dU}{d\xi} = \frac{3}{4\mu_f} \left\{ mU + \mu_s \left(\frac{\rho}{\rho_o} \right) \left[\left(\frac{\rho}{\rho_o} \right)^{2\nu_s/(1-2\nu_s)} - \left(\frac{\rho}{\rho_o} \right)^{-2} \right] \right. \\ \left. + \alpha_s \kappa \frac{\rho}{\rho_o} (T - T_o) - mU_{-\infty} + \sigma_{-\infty} \right\} \end{aligned} \quad (\text{C.7})$$

$$\frac{dH}{d\xi} = \frac{1}{K} \left\{ mc_v H - \frac{4}{3} \mu_f \left(\frac{dU}{d\xi} \right)^2 + \alpha_s \kappa \frac{\rho}{\rho_o} T \frac{dU}{d\xi} \right\} \quad (\text{C.8})$$

$$\frac{dT}{d\xi} = H \quad (\text{C.9})$$

Having fixed the far left end state, the integration starts from negative to positive in ξ to obtain the stable equilibrium at the far right.

In Fig. C.4, we see a solid shock structure in the HMX where the observed thickness is on the



HMX-Equations (gas)

Figure C.3: Computed shock structure of gas-phase HMX.

order of $1\ \mu\text{m}$. The stress as shown in the figure is the equilibrium stress comprised of the Blatz-Ko elastic part and the thermal softening part.

As we have obtained the shock structures of the HMX equations of the earlier chapters, the limiting forms at solid or gas are consistent with the classical equations of motions which genuinely admit structures of shocks as found in the solid or gas phase of materials.

C.2 Structure of phase front

Two uniform end states of a typical phase front are related through a smooth structure of finite length in microns where the conservation of mass, momentum and energy is achieved. Resembling the structure of a classical shock wave of gas dynamics, evaporation/condensation front and melting/freezing front are carefully studied by considering their structures in the special case of a transition between two uniform states. An estimated thickness of evaporation/condensation front of *n*-heptane is on the order of 10^{-1} micron while the HMX melting/freezing front thickness is seen to be on the order of 1 micron.

C.2.1 Continuum structure of evaporation/condensation front

The details of shock profile between the end states at $\pm\infty$ are provided by transforming the unsteady equations into the steady flow equations in a frame of reference moving with the shock using $\xi = x - Dt$, $U = u - D$. Here D is the steady wave speed, directed in the negative ξ direction (i.e. $D < 0$). The derivatives with respect to x and t now become

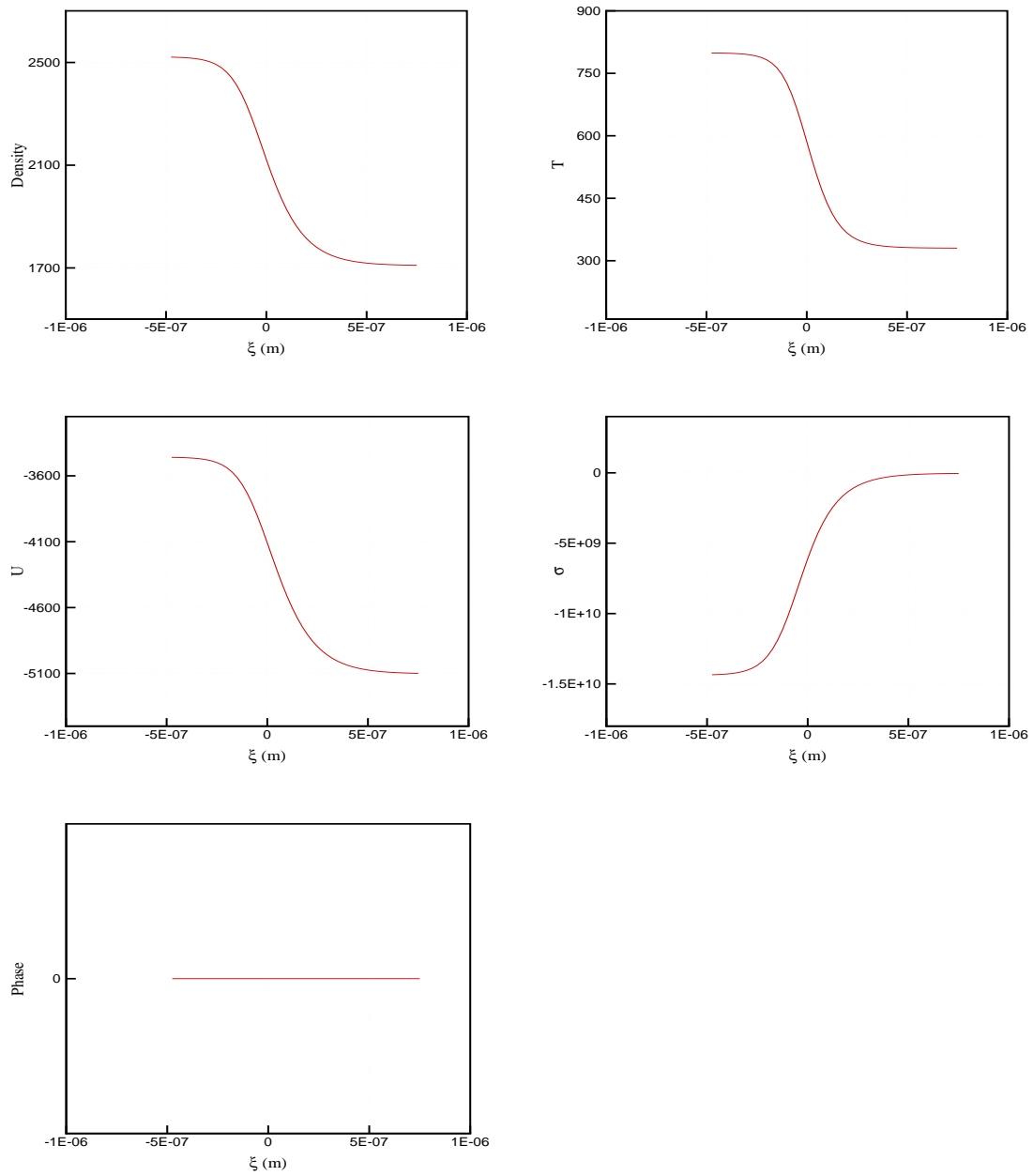
$$\frac{\partial}{\partial t} = \frac{\partial \xi}{\partial t} \frac{d}{d\xi} = -D \frac{d}{d\xi} \quad ; \quad \frac{\partial}{\partial x} = \frac{d}{d\xi}$$

and, in particular, the velocity gradient becomes

$$\frac{\partial u}{\partial x} = \frac{dU}{d\xi}$$

Thus the mass and momentum equations transform as follows:

$$\rho U = m$$



HMX-Equations (solid)

Figure C.4: Computed shock structure of solid-phase HMX.

and

$$\rho U \frac{dU}{d\xi} = \frac{d}{d\xi} \left(\sigma + \frac{4}{3} \mu_f \frac{dU}{d\xi} \right)$$

Since we are interested in the shock structure, we integrate the momentum equation once with respect to ξ to arrive at a first-order ODE in the form

$$mU - \sigma - \frac{4}{3} \mu_f \frac{dU}{d\xi} = \beta$$

where β is a constant of integration which can be evaluated at $\xi \rightarrow -\infty$. As for the energy and phase-field structure equations, the partials with respect to x and t are replaced with the derivative in ξ , and the total derivative $\dot{\phi}$ transforms to $U \frac{d\phi}{d\xi}$ where ϕ is either T or φ .

In summary, the structure equations for evaporation phenomena are derived, and they are described as follows. With mass flux defined constant, m , the structure momentum equation reads

$$\frac{dU}{d\xi} = \frac{3}{4\mu_f} \{mU + p + \rho\mu_\varphi G^2 - mU_k - p_k\} \quad (\text{C.10})$$

In order to write the energy equation with the highest derivative in a first-order, a new variable H is introduced such that

$$\begin{aligned} \frac{dH}{d\xi} = \frac{1}{\kappa} \left\{ m c_v H - \frac{4}{3} \mu_f \left(\frac{dU}{d\xi} \right)^2 + \rho R T \frac{dU}{d\xi} - B_\varphi (UG)^2 - \rho T \beta'_v(\varphi) \frac{Q_v}{T_v} UG \right. \\ \left. + \rho c'_v T \ln \frac{T}{T_k} + \beta'_v(\varphi) Q_k \right\} \end{aligned} \quad (\text{C.11})$$

where H is defined

$$\frac{dT}{d\xi} = H \quad (\text{C.12})$$

and the index k equals one in the evaporation case and two in the condensation case. As for the

phase equation, we also introduce a variable G such that

$$\begin{aligned} \frac{dG}{d\xi} = & \frac{1}{\mu_\varphi} \left\{ UB_\varphi G + \frac{1}{2} \Psi \frac{\partial}{\partial \varphi} \{(\varphi(\varphi - 1)(\varphi - 2))^2\} + \beta'_v(\varphi) \frac{T - T_v}{T_v} Q_v \right. \\ & \left. - c'_v \left(T \ln \frac{T}{T_k} - (T - T_k) \right) \right\} \end{aligned} \quad (\text{C.13})$$

with G defined as

$$\frac{d\varphi}{d\xi} = G \quad (\text{C.14})$$

Note that we have allowed the dependence of c_v , R , and β_v on the phase field variable φ . This generalization of phase dependent coefficients brings in an added complexity to the equations with their derivatives becoming non zero. Our choice of φ -dependent coefficients conforms the structure of evaporation wave. In other words, we introduce the φ -dependence in the form of

$$\alpha(\varphi) = \frac{1}{2} \left[\alpha_1 \left\{ \tanh\left(\frac{\varphi^* - \varphi}{\epsilon}\right) + 1 \right\} + \alpha_2 \left\{ \tanh\left(\frac{\varphi - \varphi^*}{\epsilon}\right) + 1 \right\} \right]$$

whose derivative with respect to φ is

$$\alpha'(\varphi) = \frac{1}{2\epsilon} \alpha_2 \text{sech}^2\left(\frac{\varphi - \varphi^*}{\epsilon}\right) - \frac{1}{2\epsilon} \alpha_1 \text{sech}^2\left(\frac{\varphi^* - \varphi}{\epsilon}\right)$$

Here, α can be any of c_v , c_p , β_v , β_m , or R with appropriate end states specified. φ^* is $(3 + \sqrt{3})/3$ for vaporization/condensation and $(3 - \sqrt{3})/3$ for melting/freezing. With ϵ chosen appropriately, the resulting transport function works like a switch between the two end state values. With these switch functions, we can proceed to solve the governing equations, once we specify all other parameters relating the properties of n -heptane as listed in Table C.1.

Integrating these autonomous ODEs, we use a high-order low-storage semi-implicit Runge–Kutta scheme [84], [77], [78], [67] to march in ξ . In the case of evaporation, in particular, we fix

Property	Value
c_v^{liquid}	$2.136 \times 10^3 \text{ J/kg K}$
c_v^{vapor}	$2.136 \times 10^1 \text{ J/kg K}$
R_{liquid}	3.0 J/kg K
R_{vapor}	$3.0 \times 10^2 \text{ J/kg K}$
$\mu_{f-liquid}$	$5.4 \times 10^{-4} \text{ kg/m s}$
$\mu_{f-vapor}$	$5.4 \times 10^{-4} \text{ kg/m s}$
B_φ	3.5×10^{-2}
μ_φ	2.0×10^{-12}
Ψ	40.0×10^{-6}
$T_{vaporization}$	371.4 K

Table C.1: Dimensional parameters for n -heptane evaporation/condensation [56], [72].

the liquid state at $k = 1$ (i.e. $\xi = -\infty$) with the following set of quantities.

$$\left. \begin{array}{l} \rho_1 = 675 \text{ kg/m}^3 \\ m = 0.7315515 \text{ kg/m}^2\text{s} \\ D = 1.08378 \times 10^{-3} \text{ m/s} \\ u_1 = 0 \text{ m/s} \\ T_1 = 300 \text{ K} \\ p_1 = 6.07500 \times 10^5 \text{ Pa} \\ \varphi_1 = 1.0000001 \\ H = G = 0 \\ Q_1 = +3.35 \times 10^{15} \text{ J} \end{array} \right\} \quad \xi = -\infty$$

We start our numerical integration from state 1 (liquid side) at $-\infty$ to state 2 (gas side) at $+\infty$. Fig. C.5 represents the structure of an evaporation wave admitted by the equations. As the initial state is perturbed, the solution of the structure equation is described by the integration path, going through a particular structure-stable point on the far right side. The velocity profile is such that initial 10^{-3} m/s jumps to 10^{-1} m/s at a stable state where the corresponding density jump is that of a typical n -heptane evaporation [66], [41], [21], [57], [59], [63], [65]. As the phase-field changes from 1 to 2, the representative thickness of a phase front is observed to be on the order of tenth of a micron. Considering an experimentally measured thickness of a shock in helium on the orders of millimeters [71], the suggested evaporation front thickness is much smaller, yet lying

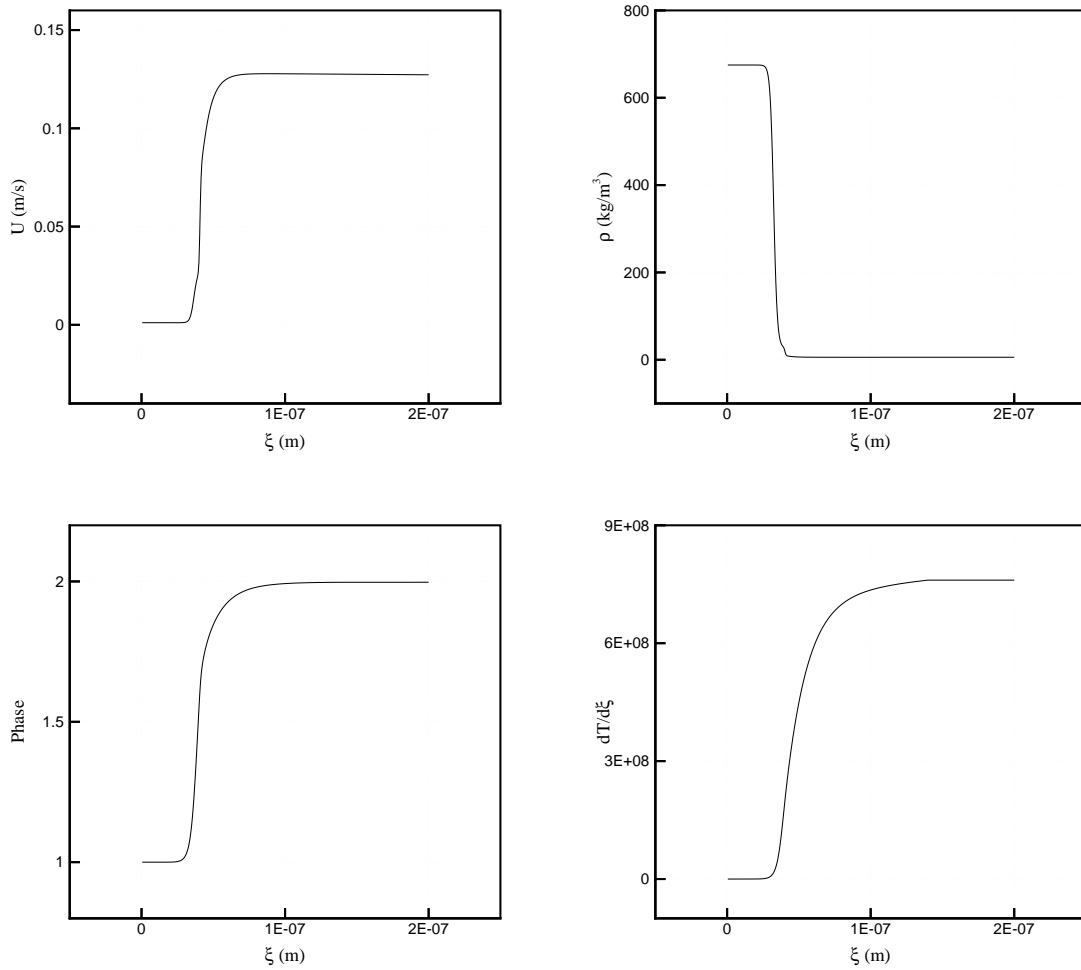


Figure C.5: Evaporation wave structure based on the transformed velocity, density, phase, temperature gradient field of n -heptane.

significantly within the range of length scale at which the continuum approximation holds. The temperature gradient as seen on Fig. C.5 at each end is uniform such that $T(-\infty)$ is a constant and $T(+\infty)$ is linear with respect to ξ , representing a far-field constant thermal-gradient condition for an evaporation process [76], [66].

In the case of condensation, the vapor state-2 is fixed at $-\infty$, and we integrate into the liquid

side at $+\infty$. The initial conditions of integration for condensation is listed below:

$$\left. \begin{aligned} \rho_2 &= 5 \text{ kg/m}^3 \\ U_2 &= 0.11 \text{ m/s} \\ m &= 0.7315515 \text{ kg/m}^2\text{s} \\ T_2 &= 480 \text{ K} \\ \varphi_2 &= 1.9999991 \\ H &= G = 0 \\ Q_2 &= -4.35 \times 10^{14} \text{ J} \end{aligned} \right\} \quad \xi = -\infty$$

Here, we essentially reverse the integration from the fixed state at $k = 2$ to a new state at 1. Fig. C.6 represents the structure of a condensation wave admitted by the equations described with fixing $k = 2$. The structure is nearly identical to that of evaporation, except the direction of integration is reversed. With a proper value assigned to a heat of condensation, Q , we integrate the ODE from a vapor side into a liquid zone through a thin region of 10^{-1} micron. The velocity field and the corresponding density in Fig. C.6 resembles a typical observation of fuel-droplet condensation; in particular, the end state density is about 675 kg/m^3 , prototypical of a hydrocarbon liquid fuel [41], [72]. While the reverse heat is added to drive the vapor state back to a liquid, the far end state temperature gradients remain uniform, such that $T(-\infty)$ is constant and $T(+\infty)$ is linearly decreasing with respect to ξ .

C.2.2 Continuum structure of melting/freezing front

The structure equations, in the case of solid to liquid or liquid to solid transition, are obtained in an analogous way as in the evaporation/condensation case of previous section. Major distinction in terms of equations arises due to the fact that there now is an additional dependence of conservative variables on the deformation field. A variable, F , is the one-dimensional deformation gradient which is introduced into momentum, energy, and phase-field equations. Again with mass flux remaining a constant, m , the momentum structure equation, after integrated from $-\infty$ to some position in ξ ,

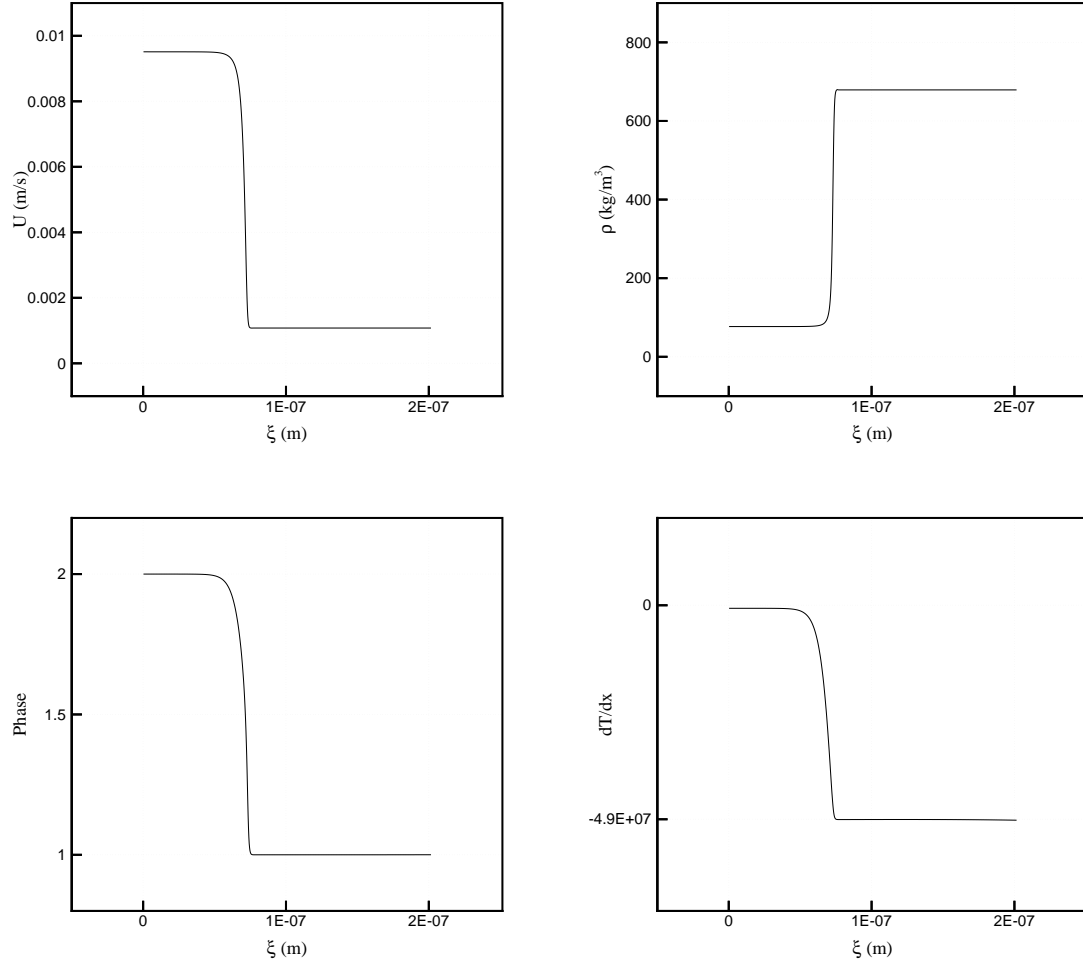


Figure C.6: Condensation wave structure based on the transformed velocity, density, phase, temperature gradient field of *n*-heptane.

becomes

$$\frac{dU}{d\xi} = \frac{3}{4\mu_f} \left\{ mU + p + \rho\mu_\varphi G^2 - \mu_s F + \mu_l F^{-\frac{1}{1-2\nu_s}} - mU_k - p_k \right\} \quad (\text{C.15})$$

Here, basically two additional terms of elasticity appears as a deformation stress term inside the bracket modeling the total Cauchy stress of a material under phase transition. The equation represents melting if $k = 1$ or freezing if $k = 2$. The energy equation reads

$$\begin{aligned} \frac{dH}{d\xi} = \frac{1}{\kappa} & \left\{ mc_v H - \frac{4}{3}\mu_f \left(\frac{dU}{d\xi} \right)^2 + \rho RT \frac{dU}{d\xi} + \mu_s F \frac{dU}{d\xi} - \mu_l F^{-\frac{1}{1-2\nu_s}} \frac{dU}{d\xi} \right. \\ & - B_\varphi (UG)^2 - \rho T \beta'_m(\varphi) \frac{Q_m}{T_m} UG + \rho c'_v T \ln \frac{T}{T_k} + \beta'_m(\varphi) Q_k \\ & \left. - \frac{1}{2} \mu'_s F^{-1} (F^2 - 1) (UG) - \frac{1 - 2\nu_s}{2\nu_s} \mu'_l F^{-1} (F^{-\frac{2\nu_s}{1-2\nu_s}} - 1) (UG) \right\} \end{aligned} \quad (\text{C.16})$$

where, like in the evaporation/condensation case, a new variable, H was introduced to split the original energy equation into a set of two first-order ODEs with

$$\frac{dT}{d\xi} = H \quad (\text{C.17})$$

Likewise, the phase field equation reads

$$\begin{aligned} \frac{dG}{d\xi} = \frac{1}{\mu_\varphi} & \left\{ UB_\varphi G + \frac{1}{2} \Psi \frac{\partial}{\partial \varphi} \{ (\varphi(\varphi - 1)(\varphi - 2))^2 \} + \beta'_m(\varphi) \frac{T - T_m}{T_m} Q_m \right. \\ & - c'_v (T \ln \frac{T}{T_k} - (T - T_k)) + \mu'_s \frac{1}{2} F^{-1} (F^2 - 1) \\ & \left. + \mu'_l \frac{1 - 2\nu_s}{2\nu_s} F^{-1} (F^{-\frac{2\nu_s}{1-2\nu_s}} - 1) \right\} \end{aligned} \quad (\text{C.18})$$

with

$$\frac{d\varphi}{d\xi} = G, \quad (\text{C.19})$$

making a set of first-order ODEs for structure analysis. Lastly, we need to close the system with additional equation which relates the deformation gradient field with the velocity field via the

Property	Value
c_v^{solid}	$1.06 \times 10^3 \text{ J/kg K}$
c_v^{liquid}	$2.1 \times 10^3 \text{ J/kg K}$
R_{solid}	1.1 J/kg K
R_{liquid}	3.0 J/kg K
$\mu_{f-solid}$	$1.0 \times 10^{-3} \text{ kg/m s}$
$\mu_{f-liquid}$	$1.0 \times 10^{-3} \text{ kg/m s}$
B_φ	3.5×10^{-2}
μ_φ	2.0×10^{-12}
Ψ	40.0×10^{-6}
$T_{melting}$	558.0 K

Table C.2: Dimensional parameters for HMX melting/freezing

identity

$$\frac{dF}{d\xi} = -\frac{F}{U_k} \frac{dU}{d\xi} \quad (\text{C.20})$$

or

$$F = e^{-\frac{U}{U_k} + 1} \quad (\text{C.21})$$

We choose HMX as the candidate for the phase structure analysis for which a significant amount of material data is compiled a priori [10], [24], [54], [60], [70], [86], [88]. Table C.2 quantifies several parameters of HMX in the calculation of structure equations of melting and freezing. Again, we use the high-order low-storage Runge–Kutta method to solve the system of non-linear ODEs. In the case of melting, we are fixing the solid state of HMX and setting $k = 1$ at $\xi = -\infty$ with the

following set of initial data:

$$\left. \begin{aligned} \rho_1 &= 2000 \text{ kg/m}^3 \\ m &= 2.0 \times 10^3 \text{ kg/m}^2\text{s} \\ D &= 1.0 \text{ m/s} \\ u_1 &= 0 \text{ m/s} \\ T_1 &= 300 \text{ K} \\ p_1 &= 6.07500 \times 10^5 \text{ Pa} \\ \varphi_1 &= 0.0000001 \\ F &= 1.00000001 \\ H &= G = 0 \\ Q_1 &= +3.3 \times 10^{14} \text{ J} \end{aligned} \right\} \quad \xi = -\infty$$

It must be mentioned here that, since there are no reported sets of data for the rate of melting for the highly explosive HMX, we simply select a value of D in the range of 10^{-3} to 10^3 m/s. The minimum in this range corresponds to a typical deflagration speed while the maximum represents a typical detonation speed [29], [76], [68], [39]. A natural choice is to take the mean value, approximately 1 m/s. Fig. C.7 depicts the structure of a melting front admitted by the equations addressed in this section. In particular, the initial density of 2000 kg/m^3 , typical of solid explosive such as HMX, decreases by a factor of two. The system of ODE of melting is integrated from a slightly perturbed initial state into a new state representative of melt HMX. The thickness of the phase front is on the order of microns, supporting the observation that explosive melting front is approximately ten times thicker than the evaporation/condensation front of liquid fuel. There is also a new property that rapidly changes across the melting fronts in the phase transition of a non-linearly elastic solid. Fig. C.7 shows the deformation gradient field across the melting front of HMX; in particular, the initial state of solid is essentially unstressed (i.e. $F = 1$) while the end state of the integration is at a compression state with $F \sim 0.3$. In fact, the wave, a compression wave, on the far right side, propagate into an unstressed material on the left side at a steady melting speed of D . This observation is consistent with the principles of energy transfer from a higher state to a lower state. The temperature field as shown from Fig. C.7 also supports this observation that uniform state

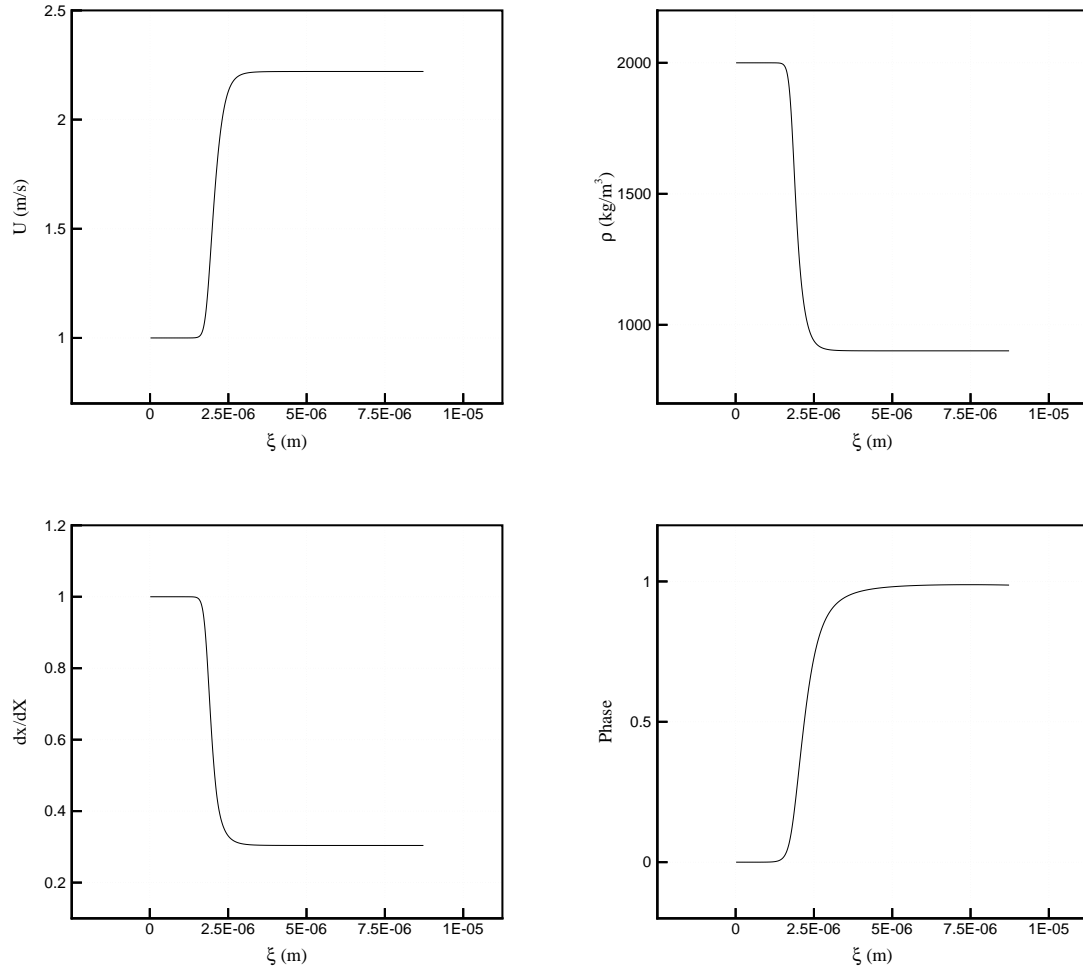


Figure C.7: Melting front structure observed from the transformed velocity, density, deformation gradient, and phase field of solid HMX.

on the left is balanced by a linearly increasing thermal field on the far right, causing the energy transfer to go from liquid to solid, essentially a melting process by definition [58], [53], [18], [54].

In the case of freezing, the liquid state-2 is fixed at $-\infty$, and the integration starts from the far left in the liquid region to a position in the solid at $+\infty$. Listed below are the initial conditions of

integration of which the liquid state is assumed uniform:

$$\left. \begin{aligned} \rho_2 &= 1580 \text{ kg/m}^3 \\ U_2 &= 1.4 \text{ m/s} \\ m &= 2.0 \times 10^3 \text{ kg/m}^2\text{s} \\ T_2 &= 700 \text{ K} \\ \varphi_2 &= 0.99999991 \\ F &= 1.00000001 \\ H &= G = 0 \\ Q_2 &= -4.2 \times 10^{14} \text{ J} \end{aligned} \right\} \quad \xi = -\infty$$

Fig. C.8 represents the structure of a freezing front, admitted by the equations described in this section with setting $k = 2$. Previous investigation of thermodynamic properties of HMX suggests that the material can undergo a liquid-solid transition at a temperature 550 K and a pressure above 50×10^5 Pa. So the process of ‘freezing’, in principle, is realizable at this melting temperature with an elevated pressure of 50×10^5 Pa or above. typical melt explosive density of 10^3 kg/m^3 makes a rapid transition to a new state, a solid state as shown in Fig. C.8 of density structure. Again, the thickness of numerically obtained freezing front is in the order of microns, which is about ten times the thickness of condensation front of hydrocarbon liquid fuel. As the phase field changes from 1 to 0, the deformation field as depicted in Fig. C.8 goes from an unstressed liquid at $F(-\infty) \approx 1$ to a tensional state at $F(+\infty) \approx 1.3$. The front again moves from right to left with a steady propagating speed of $D \approx 1.26 \text{ m/s}$. The temperature gradient field, shown from Fig. C.8, also describes the uniform states at both ends, making the T field uniform at $-\infty$ and linearly decreasing at $+\infty$ suggesting a release of heat upon the process of freezing.

C.3 Algebraic theory

C.3.1 Derivation of Rankine–Hugoniot relations

In the previous section, we have derived a set of equations which describes the structure of phase shock as one state is perturbed to make a smooth transition into another structure-stable state. In

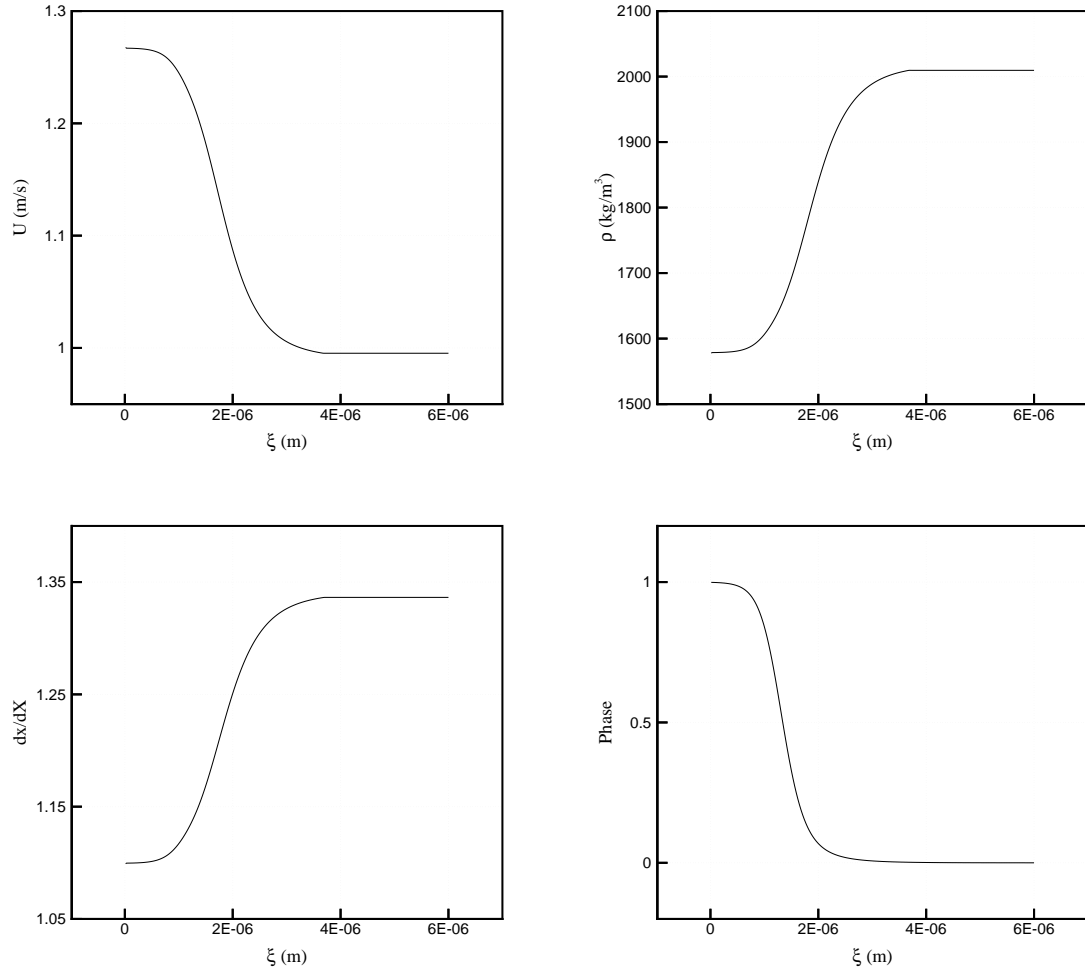


Figure C.8: Freezing front structure observed from the transformed velocity, density, deformation gradient, phase temperature gradient, and temperature field of liquid-HMX.

this section, we will look, in a more elaborate fashion, at the two end states of a shock, a phase shock, and arrive at a new algebraic theory of phase transition which possesses many similitude to that of a classical R-H theory of shock wave [75], [71], [40].

Integrating the steady mass and momentum equations of previous section with respect to x from $-\infty$ to $+\infty$, we have

$$\rho_1 u_1 = \rho_2 u_2 \quad (\text{C.22})$$

and

$$\rho_1 u_1^2 + \sigma_1 = \rho_2 u_2^2 + \sigma_2$$

where the total stress term is

$$\sigma = -\rho RT - \rho \mu_\varphi \left(\frac{\partial \varphi}{\partial x} \right)^2 + \frac{4}{3} \mu_f \frac{\partial u}{\partial x} + \mu_s F - \mu_l (F)^{-\frac{1}{1-2\nu_s}}$$

Now we assume a constant deformation gradient and zero gradient for all other variables at two end states, such that

$$(\text{at } -\infty) \quad \frac{\partial \varphi}{\partial x} = \frac{\partial u}{\partial x} = 0; F = 1 \quad \text{and} \quad (\text{at } +\infty) \quad \frac{\partial \varphi}{\partial x} = \frac{\partial u}{\partial x} = 0; F = \hat{C}$$

and that the difference between two lame parameters, $\mu_s - \mu_l$ is zero at two end states. Then, the resulting relation for momentum conservation states

$$\rho_1 u_1^2 + p_1 = \rho_2 u_2^2 + p_2 \quad (\text{C.23})$$

which is identical to the R-H relation for shock wave [75].

For the energy relation, we convert our evolution equation for T into a total energy form. First, the internal energy equation reads

$$\rho \dot{e} = \frac{\partial}{\partial x} \left(\kappa \frac{\partial T}{\partial x} \right) + \sigma \frac{\partial u}{\partial x} + G(\rho, u, T, \varphi, F)$$

where

$$G = B_\varphi (U \frac{\partial \varphi}{\partial x})^2 + mT\beta'_m(\varphi) \frac{Q_m}{T_m} \frac{\partial \varphi}{\partial x} + \frac{1}{2} \frac{\partial \mu_s}{\partial \varphi} (F)^{-1} \left((F)^2 - 1 \right) \dot{\varphi} + \frac{1 - 2\nu_s}{2\nu_s} \frac{\partial \mu_c}{\partial \varphi} (F)^{-1} \left(F^{-\frac{2\nu_s}{1-2\nu_s}} - 1 \right) \dot{\varphi}$$

By multiplying the momentum equation by u results in a mechanical energy equation:

$$\rho \left(\frac{\dot{u}^2}{2} \right) = u \frac{\partial \sigma}{\partial x}$$

Summing up these two equations, we obtain the total energy equation

$$\rho(\dot{e} + \left(\frac{\dot{u}^2}{2} \right)) = \frac{\partial}{\partial x} \left(\kappa \frac{\partial T}{\partial x} \right) + \frac{\partial}{\partial x} (\sigma u) + G$$

Now assuming steady-state, we can integrate the total energy equation with respect to x from $-\infty$ to $+\infty$ giving the jump relation

$$\begin{aligned} m \left(e + \frac{u^2}{2} \right) \Big|_{-\infty}^{\infty} &= \sigma u \Big|_{-\infty}^{\infty} + \int_{-\infty}^{\infty} G dx + C \\ &= \left(-p + \frac{4}{3} \mu_f \frac{\partial u}{\partial x} \right) u \Big|_{-\infty}^{\infty} + \int_{-\infty}^{\infty} G dx + C \end{aligned}$$

where we have assumed constant temperature gradient and deformation gradient at farfield and zero gradient for all other variables at two end states, such that

$$(\text{at } -\infty) \quad \frac{\partial T}{\partial x} = \frac{\partial \varphi}{\partial x} = \frac{\partial u}{\partial x} = 0; F = 1 \quad \text{and} \quad (\text{at } +\infty) \quad \frac{\partial T}{\partial x} = C; \frac{\partial \varphi}{\partial x} = \frac{\partial u}{\partial x} = 0; F = \hat{C}$$

and that the difference between the two Lamé parameters, $\mu_s - \mu_l$ is zero at two end states. Dividing by m , we find that energy jump becomes

$$\left(e + \frac{u^2}{2} \right) \Big|_{-\infty}^{\infty} = \left(-\frac{p}{\rho} + \frac{4}{3} \frac{\mu_f}{\rho} \frac{\partial u}{\partial x} \right) \Big|_{-\infty}^{\infty} + \frac{1}{m} \int_{-\infty}^{\infty} G dx + \frac{C}{m}$$

And using the definition of enthalpy, $h = e + p/\rho$, we obtain the desired expression for the enthalpy

evolution equation as

$$h_1 + \frac{u_1^2}{2} = h_2 + \frac{u_2^2}{2} - \frac{1}{m} \int_{-\infty}^{\infty} G(\rho, u, T, \varphi, F) dx - \frac{C}{m}$$

C.3.2 Algebraic theory of phase transition wave

The Rankine–Hugoniot relations for general phase transition can be summarized in the following form:

$$\rho_1 U_1 = \rho_2 U_2 \equiv m \quad (\text{C.24})$$

$$\rho_1 U_1^2 + p_1 = \rho_2 U_2^2 + p_2 \quad (\text{C.25})$$

$$c_{p1} T_1 + \frac{U_1^2}{2} = c_{p2} T_2 + \frac{U_2^2}{2} + Q \quad (\text{C.26})$$

If the two end states are representing liquid and vapor states, Q plays essentially a role of heat of evaporation or condensation, and it is uniquely defined for our model by

$$Q(\rho, U, T, \varphi) = -\frac{1}{m} \int_{-\infty}^{\infty} \left\{ B_\varphi \left(U \frac{\partial \varphi}{\partial \xi} \right)^2 + m T \beta'_v(\varphi) \frac{Q_v}{T_v} \frac{\partial \varphi}{\partial \xi} \right\} d\xi - \frac{C}{m}$$

with

$$\beta'_v(\varphi) = \begin{cases} 6(\varphi - 1)(2 - \varphi) & \text{if } 1 \leq \varphi \leq 2 \\ 0 & \text{otherwise} \end{cases}$$

where $Q > 0$ represents evaporation and $Q < 0$ represents condensation.

In the case of the melting/freezing process, Q involves two additional terms from the theory of linear elasticity. Basically, Q , in the solid to liquid or liquid to solid transition, depends also on deformation gradient F , and it reads

$$\begin{aligned} Q(\rho, U, T, \varphi, F) = & -\frac{1}{m} \int_{-\infty}^{\infty} \left\{ B_\varphi \left(U \frac{\partial \varphi}{\partial \xi} \right)^2 + m T \beta'_m(\varphi) \frac{Q_m}{T_m} \frac{\partial \varphi}{\partial \xi} \right. \\ & \left. + \frac{1}{2} \frac{\partial \mu_s}{\partial \varphi} (F)^{-1} \left((F)^2 - 1 \right) \dot{\varphi} + \frac{1 - 2\nu_s}{2\nu_s} \frac{\partial \mu_c}{\partial \varphi} (F)^{-1} \left(F^{-\frac{2\nu_s}{1-2\nu_s}} - 1 \right) \dot{\varphi} \right\} d\xi - \frac{C}{m} \end{aligned}$$

with

$$\beta'_m(\varphi) = \begin{cases} 6\varphi(1-\varphi) & \text{if } 0 \leq \varphi \leq 1 \\ 0 & \text{otherwise} \end{cases}$$

where $Q > 0$ is for melting and $Q < 0$ is for freezing. These jump relations are identical to a classical shock relations in the theory of gas dynamics, except that we have added an enthalpy change due to phase transformation. One objective of the derivation of algebraic theory for our full continuum model, has to do with determining U_1, U_2 , and ρ_2 . What follows is thus specifically aimed at solving the algebraic relations for those unknowns.

First the ideal equation of state (EOS) and the definition of U are substituted into the RH-relations (C.24-C.26), resulting in the following:

$$\begin{aligned} \rho_1 D &= \rho_2 (D - u_2) \\ \rho_1 D^2 + \rho_1 R_1 T_1 &= \rho_2 (D - u_2)^2 + \rho_2 R_2 T_2 \\ c_{p1} T_1 + \frac{D^2}{2} &= c_{p2} T_2 + \frac{(D - u_2)^2}{2} + Q \end{aligned}$$

Using specific volume, $v = 1/\rho$, to rewrite the continuity, we have

$$m v_2 = D - u_2,$$

and momentum and energy equation become

$$m^2 v_2^2 = m^2 v_1 v_2 + \frac{R_1 T_1}{v_1} v_2 - R_2 T_2 \quad (\text{C.27})$$

$$\frac{m^2 v_2^2}{2} = c_{p1} T_1 - c_{p2} T_2 - Q + \frac{D^2}{2} \quad (\text{C.28})$$

Substituting $m^2 v_2^2$ from (C.27) into (C.28), we can express v_2 as a function only of one unknown, D^2 :

$$v_2 = \frac{c_{p1} T_1 - c_{p2} T_2 - Q + \frac{D^2}{2} + \frac{1}{2} R_2 T_2}{\frac{1}{2} (m^2 v_1 + \frac{R_1 T_1}{v_1})} \quad (\text{C.29})$$

Then, we use this expression for v_2 in (C.28) to arrive at a single quadratic equation for $D^2 = \phi$ as a function of all known quantities:

$$\phi^2(2\alpha + 2\Gamma) + \phi(4\alpha^2 + 4\alpha\Gamma + \Gamma^2 + 2\Gamma R_1 T_1) - 2\alpha(R_1 T_1)^2 = 0 \quad (\text{C.30})$$

For convenience, we have introduced two new variables in (C.30), namely,

$$\begin{aligned} \Gamma &\equiv R_2 T_2 - R_1 T_1 \\ \alpha &\equiv c_{p1} T_1 - c_{p2} T_2 - Q \end{aligned}$$

The quadratic relation admits two possible solutions, such that

$$D^2 = \frac{-b \pm \sqrt{b^2 - 4ac}}{2a} \quad (\text{C.31})$$

where

$$\begin{aligned} a &= 2(\alpha + \Gamma) \\ b &= 4\alpha^2 + 4\alpha\Gamma + \Gamma^2 + 2\Gamma R_1 T_1 \\ c &= -2\alpha(R_1 T_1)^2 \end{aligned}$$

Once D^2 is determined, the specific volume of gas, v_2 , can be obtained through

$$v_2^2 = v_1^2 \left(1 + \frac{2\alpha}{D^2} \right) \quad (\text{C.32})$$

and the gas velocity is further determined by

$$u_2 = D \left(1 - \frac{v_2}{v_1} \right) \quad (\text{C.33})$$

Both (C.31) and (C.32) are subject to constraints, namely, $D^2 > 0$ and $v_2^2 > 0$. First, the

quantity within the square root must be positive definite such that the inequality

$$(2\alpha + \Gamma)^2(4\alpha^2 + 4\alpha\Gamma + (\Gamma + 2R_1T_1)^2) \geq 0 \quad (\text{C.34})$$

holds for all α, Γ , and R_1T_1 . Assuming the constraint $b^2 - 4ac \geq 0$ is satisfied, we consider the condition

$$\frac{-b \pm \sqrt{\Omega}}{2a} > 0$$

where Ω is $b^2 - 4ac$. In terms of α and Γ , this inequality becomes

$$-\alpha + \frac{-\Gamma^2 - 2\Gamma R_1T_1 \pm \sqrt{\Omega}}{4(\alpha + \Gamma)} > 0 \quad (\text{C.35})$$

As it turns out, only the positive square root (i.e. the sign in front of the square root operator) fulfills this inequality, and the allowed region on the Γ vs. α plot are drawn in Fig. C.9. In both cases with setting $R_1T_1 = 900$, upper and lower left quadrants on the $\alpha - \Gamma$ plane represent a region of unacceptable solutions of D^2 . Upper right quadrant represent possible solutions of evaporation in Fig. C.9a and possible solutions of melting in Fig. C.9b. Likewise, the condensation and freezing solutions, as constrained by the inequality, are bound to lie in the lower right quadrant in Figs. C.9a and C.9b, respectively.

The third inequality emerges from (C.32). Unlike the previous two constraints imposed by (C.31), this one simply places an lower bound on the variable α which essentially quantifies the net enthalpy change in the system. That is,

$$\alpha > -\frac{1}{2}D^2 \quad (\text{C.36})$$

C.3.3 Solution of algebraic theory

So far, we have derived a general theory of jump relations between the two uniform conditions across a phase shock. By specifying the knows of the system, we can determine the phase front propagating speed, D , the density jump, $\Delta\rho$, and the velocity jump, Δu of phase shock wave. For

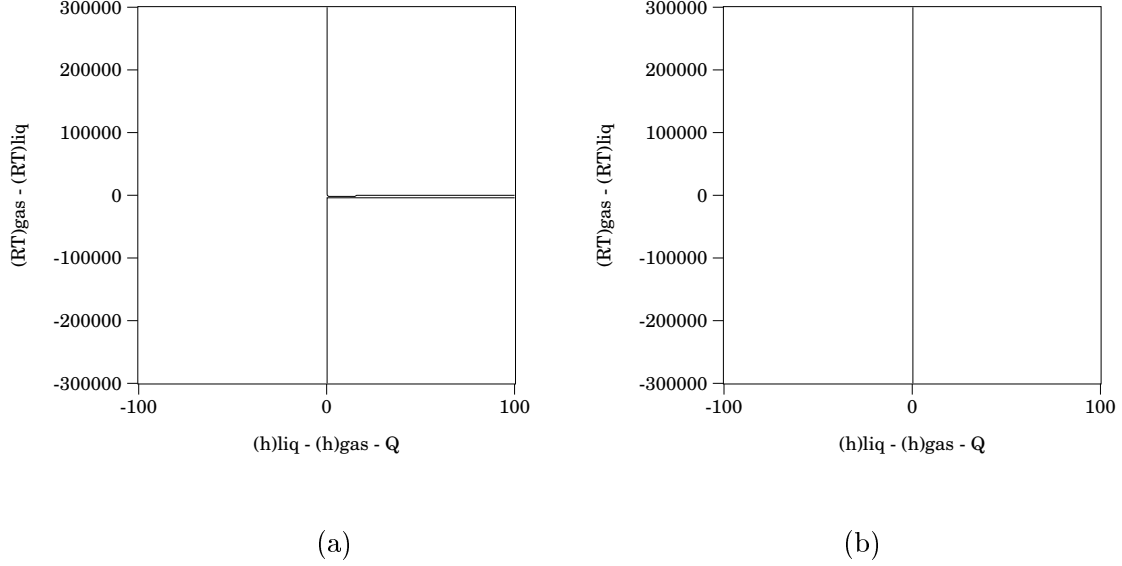


Figure C.9: (a) Plot of $(-b + \sqrt{b^2 - 4ac})/2a$ as a function of α and Γ in the case of n -heptane evaporation/condensation. (b) Plot of $(-b + \sqrt{b^2 - 4ac})/2a$ as a function of α and Γ in the case of HMX melting/freezing.

example, we consider the case of evaporation where the fixed state is described as follows:

$$\left. \begin{array}{l} \rho_1 = 675 \text{ kg/m}^3 \\ u_1 = 0 \text{ m/s} \\ c_{p1} = 2139 \text{ J/kg K} \\ T_1 = 300 \text{ K} \\ p_1 = 607500 \text{ Pa} \end{array} \right\} \xi = -\infty \quad \left. \begin{array}{l} Q = 320,000 \text{ J/kg} \\ c_{p2} = 321.36 \text{ J/kg K} \\ T_2 = 1001.0578 \text{ K} \\ p_2 = 607499.9344 \text{ Pa} \end{array} \right\} \xi = +\infty$$

Then (C.31), (C.32), and (C.33) can be solved for the unknowns, namely, D , ρ_2 , and u_2 . One possible solution reveals that

$$D = 0.00108378 \text{ m/s} \quad (\text{C.37})$$

$$\rho_2 = 2.02286 \text{ kg/m}^3 \quad (\text{C.38})$$

$$u_2 = 0.361642 \text{ m/s} \quad (\text{C.39})$$

Promisingly, these results are quantitatively consistent with those of the end state prediction by the evaporation shock structure analysis in the previous section. In particular, the steady rate of

evaporation, D , is approximately 1 mm/sec which is consistent with the experimentally observed n -heptane regression rate in the droplet ignition [41]. Of course, the surprisingly good agreement between the algebraic theory and the experiment was mainly possible because of the parameter, Q in the model which acts as a ‘tuning’ device for producing a desired end state solution.

Appendix D

Thermodynamics of Energetic Materials

In this chapter, we describe how a P - V - T diagram of HMX is constructed. Based on a semi-empirically generated P - V - T diagram, we will be able to characterize the melting and vaporization of HMX upon thermomechanical loadings. Furthermore, we will explain the hydrostatic pressure of HMX, whose distinct expressions at each of three phases are properly understood.

D.1 Constructing a P - V - T diagram of HMX

Study of high explosives (HE) is a challenging subject not only because of the underlying rich behavior of an initially solid material undergoing phase transformation to a detonated gas, but also because of the scarcity of the available chemico-thermo data available in wide range of pressure and temperature. We choose to analyze the mechanical and thermodynamic behavior of HMX, whose reported experimental data are reasonably easy to find in many places. For the purpose of our interrogation of HMX, material properties are reported in the Table 3.1, We based these values from the references [10], [24], [70], [60], [85], [69], [47], [4].

Pressure-volume-temperature (P - V - T) surfaces of HMX has not been constructed based on any empirical attempt due to the reason mentioned earlier. In our work, we were motivated to look into how the classical theory of thermomechanical phase transition can predict the properties of this explosive in the situations where there are no known data. At this time, we take the fundamental approach in predicting the melting/freezing regime and the vaporization/condensation regime via the Clausius–Clapeyron relations and some of the empirical relations like the Kraut–

Kennedy melting law [54]. As for the sublimation region, several experimentalists of late 60's and 70's have measured the log of vapor pressure versus the reciprocal of temperature. In particular, Rosen and Dickinson [60] obtained the following pressure relation in pascals for the HMX in the temperature range of $370 \sim 402.3$ K:

$$\log p(T) = 16.18 - \frac{9154}{T} \quad (\text{D.1})$$

As for the range of $461 \sim 486$ Kelvin, Taylor and Crookes [70] suggest using the following log relationship between p and T at phase equilibrium:

$$\log p(T) = 14.732 - \frac{8296}{T} \quad (\text{D.2})$$

We note here that the original relations were written down in mm Hg (or Torr), and thus we have made the unit conversion for pressure, such as $1 \text{ mm Hg} = 1 \text{ torr} = 1.333 \times 10^2 \text{ Pa}$.

With a measured triple point of HMX at $(T_o, p_o) = (558 \text{ K}, 50 \text{ Pa})$, we perform a one-sided extrapolation from the curve of Taylor and Crookes which ends at a temperature of 486 Kelvin. Thus the points on the resulting curve cover all possible thermodynamic states in which both solid and vapor phase can coexist. Based on both empirical data available and theoretical arguments made on the basis of Gibbs free energy, we can draw a phase diagram as in Fig. D.1, which depicts all three states of HMX with phase-equilibrium curves of solid–liquid and liquid–vapor constructed from the semi-empirical relations. Dividing the solid–liquid phases, we use the well-known Kraut–Kennedy melt curve, which takes the form

$$T_m(p) = T_o + bp \quad (\text{D.3})$$

where the empirical coefficient, $b = 58 \text{ K/GPa}$, and p, T in pascals and Kelvin, respectively. As for the vaporization curve on P – T plane, we use the classical argument based on the Clausius–Clapeyron relation that change in chemical potential energy is negligible across the phase boundary.

This invokes the following general expression for liquid-vapor phase transition curve,

$$T_v(p) = \left(\frac{R}{Q_v} \ln \frac{p}{p_o} + \frac{1}{T_o} \right)^{-1} \quad (\text{D.4})$$

with temperature in Kelvin and pressure in pascals. The gas constant R and the heat of vaporization Q_v corresponds to values for HMX.

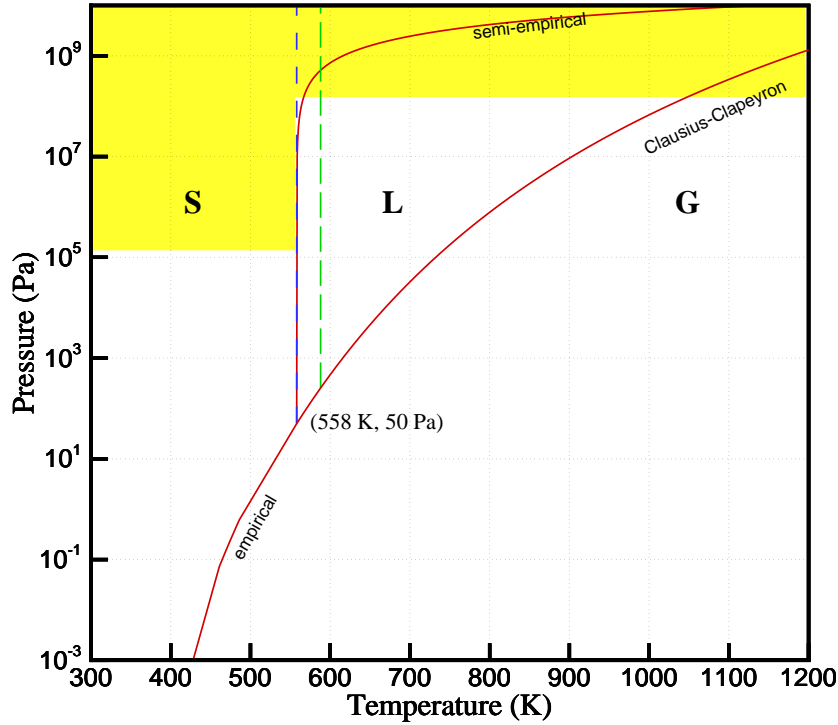


Figure D.1: Sublimation curve drawn based upon the empirical data of Rosen & Dickinson [60] and Taylor & Crookes [70]. Melt curve is estimated by semi-empirical Kraut–Kennedy law. Vapor curve is drawn from equilibrium thermodynamics using the Clausius–Clapeyron relation for idealized β -HMX vapor.

In the forthcoming sections, we will elaborate on the constructing of these phase boundaries based on thermodynamic and empirical data. According to these expressions, melt and vaporization temperatures are explicitly dependent on corresponding melt and vaporization pressure. However, in most of our simulations, we assume that T_m and T_v are independent of pressure, just for sake of simplicity. In the future, we can replace the melting and vaporization curve with those discussed

in detail in the forthcoming sections.

D.2 Equation of state (EOS)

D.2.1 Experimental isothermal data for solid HMX

In 1978, Bedrov et al. [4] measured hydrostatic stress of HMX by suspending small crystals in a methanol–ethanol medium and then placing the sample in a Bridgman anvil. Recently, Yoo and Cynn [85] made use of diamond–anvil cell (DAC) technologies to achieve hydrostatic compression of β -HMX at high pressures and temperatures. The sample is prepared from Argon pressure medium instead, whose bulk modulus (or, stiffness) is about 1.4 GPa, substantially smaller than that of any hydrocarbon substance at 20 GPa. Since the stiffness of any typical high explosive (HE) is close to 20 GPa, one would expect a lower compressive stress on the HMX sample placed on the Bridgman anvil cell.

Isothermal data of HMX in a hydrostatic condition using the DAC technique of Yoo et al. is obtained for pressures up to 43 GPa. In particular, their p – V relations shows a (first-order) jump in specific volume at about 27 GPa. The well-known β – δ solid phase transition explained the observation where the volume change (increase) due to transition is about 4%. A best fit was attempted for the p – V isotherm below this transition pressure of 27 GPa. They used the third-order Birch–Murnaghan (BM) equation of state, such that

$$p(\eta) = \frac{3}{2}B_o[\eta^{-7/3} - \eta^{-5/3}][1 - 3(1 - B'/4)(\eta^{-2/3} - 1)], \quad (\text{D.5})$$

where $\eta = V/V_o$, the bulk modulus B_o is 12.4 GPa, and its pressure derivative B' is 10.4. The pressure is given in GPa.

D.2.2 Jones–Wilkins–Lee equation for vapor HMX

The Jones–Wilkins–Lee (JWL) EOS has been used to describe explosives in applications involving metal acceleration [24]:

$$p(\eta) = A\left(1 - \frac{0.3}{4.2\eta}\right)e^{-4.2\eta} + B\left(1 - \frac{0.3}{\eta}\right)e^{-\eta} + \frac{0.3}{\eta}E_o \quad (\text{D.6})$$

where A , B are the linear coefficients with $A = 7.783 \times 10^2$ GPa and $B = 7.071$ GPa. Here, E_o is the detonation energy per unit volume and $E_o = 10.5$ GPa-m³/m³. As in the BM EOS, pressure is given in GPa.

D.2.3 Hydrostatic pressure for our model

In order to simulate high explosive undergoing phase transition from solid, liquid, and vapor, to reacted product, we need to develop an equation of state that can effectively represent all phases of material in an accurate fashion. As we have previously discussed in detail in the thermomechanical derivation of continuum laws, we have made use of the Blatz–Ko strain-energy density to come up with the Cauchy stress definition related to elastic deformation of a solid material. In addition, we have also considered the stress due to the thermal expansion on both solid and liquid of energetic materials. However, when the material undergoes phase transition to a gaseous state, both deformational stress and thermal stress should contribute nothing to the hydrostatic component (or non-deviatoric part) of the Cauchy stress; instead, we would then model this spherical part of the stress as an ideal gas with ideal EOS. With proper transfer functions which are explicitly dependent on the phase variable, φ , EOS of the energetic material as reflected through our continuum model is capable of representing all phases of a material from solid, liquid, vapor, and to reacted product gas.

The hydrostatic pressure of our model can be described by an isotropic compression on a material. In terms of the components of stress tensors

$$p = -\frac{1}{3}(\sigma_{rr} + \sigma_{\theta\theta} + \sigma_{\phi\phi}),$$

the Cauchy stress, as defined in the Eulerian description of the model, consists of two terms, namely the equilibrium part and the dissipative part. This equilibrium part of the stress can be further divided into a spherical part and a trace-less part or a deviatoric part. This spherical part of the stress is what we consider a pressure in our model [12], [3], and it basically represents a mean average of diagonal components of equilibrium stress, or simply stated, $\sigma^{sph} = \frac{1}{3}\sigma_{ii}^{eq} = \frac{1}{3}\text{tr } \boldsymbol{\sigma}^{eq}$.

Starting from the equilibrium stress tensor, we recall that

$$\boldsymbol{\sigma}^{eq} = \mu_s \frac{\rho}{\rho_o} \mathbf{B} - \mu_s \frac{\rho}{\rho_o} \text{III}_B^{-\frac{\nu_s}{1-2\nu_s}} \mathbf{1} - \rho RT \mathbf{1} - \frac{\rho}{\rho_o} \alpha \kappa (T - T_o) \mathbf{1} - \rho \gamma_\varphi \nabla \varphi \otimes \nabla \varphi$$

Now, we may write this expression in terms of spherical and deviatoric part such that

$$\begin{aligned} \boldsymbol{\sigma}^{eq} &= \boldsymbol{\sigma}^{sph} + \boldsymbol{\sigma}^{dev} \\ &= \left(-\mu_s \frac{\rho}{\rho_o} \text{III}_B^{-\frac{\nu_s}{1-2\nu_s}} - \rho RT - \frac{\rho}{\rho_o} \alpha \kappa (T - T_o) + \mu_s \frac{\rho}{\rho_o} \frac{1}{3} \text{tr} \mathbf{B} - \rho \gamma_\varphi \frac{1}{3} \text{tr} (\nabla \varphi \otimes \nabla \varphi) \right) \mathbf{1} \\ &\quad + \mu_s \frac{\rho}{\rho_o} \left(\mathbf{B} - \frac{1}{3} \text{tr} \mathbf{B} \mathbf{1} \right) - \rho \gamma_\varphi \left(\nabla \varphi \otimes \nabla \varphi - \frac{1}{3} \text{tr} (\nabla \varphi \otimes \nabla \varphi) \mathbf{1} \right) \end{aligned}$$

Clearly, the deviatoric part of the equilibrium stress has the property, $\text{tr} \boldsymbol{\sigma}^{dev} = 0$. So the pressure can be related to the negative of the spherical part of the equilibrium stress:

$$-p = -\mu_s \frac{\rho}{\rho_o} \text{III}_B^{-\frac{\nu_s}{1-2\nu_s}} + \mu_s \frac{\rho}{\rho_o} \frac{1}{3} \text{tr} \mathbf{B} - \rho RT - \frac{\rho}{\rho_o} \alpha \kappa (T - T_o) - \rho \gamma_\varphi \frac{1}{3} \text{tr} (\nabla \varphi \otimes \nabla \varphi) \quad (\text{D.7})$$

Limiting forms

Equation D.7 is a generalized form of spherical stress component, representing a ‘press’ of our model. In a classical sense, the hydro-pressure is a static measure, which does not include any instantaneous changes in phase. In this spirit, we specialize the expression above to a specific deformational mapping and distinguish its limiting forms corresponding to $\varphi = 0, 1$ and 2 .

We first assume a homogeneous volume compression (expansion) on a material, whose left Cauchy–Green tensor is given by $\mathbf{B} = (\rho_o/\rho)^{2/3} \mathbf{1}$. Consequently the first invariant of \mathbf{B} reads $I_B = \text{tr} \mathbf{B} = 3(\rho_o/\rho)^{2/3}$, and the third invariant $\text{III}_B = \det \mathbf{B} = (\rho_o/\rho)^2$. Under these conditions, the pressure becomes

$$p = -\mu_c \left(\frac{\rho}{\rho_o} \right)^{\frac{1}{3}} + \mu_s \left(\frac{\rho}{\rho_o} \right)^{\frac{1}{1-2\nu_s}} - \rho RT + \frac{\rho}{\rho_o} \alpha \kappa (T - T_o) \quad (\text{D.8})$$

where $\mu_c(\varphi) = \mu_s(\varphi) + \mu_l(\varphi)$ such that $\mu_s(0) = \mu_{solid}$ and zero for all $\varphi > 1$, and $\mu_l(1) = \mu_{liquid}$ and $\mu_l(0) = \mu_l(2) = 0$. Of course, the gas phase will support neither deformation nor thermal

expansion, such that $p = \rho RT$ is recovered when φ reaches $\varphi = 2$, the vapor phase.

One- and two-dimensional cases for simulations

Numerical simulations are performed in one and two dimensions. Corresponding expressions for pressures are discussed here. In one-dimensional deformation, the generalized spherical portion of the Cauchy stress becomes

$$p = \mu_s(1 + f')^{-\frac{1}{1-2\nu_s}} + \rho RT + \frac{\rho}{\rho_o} \alpha \kappa (T - T_o) - \frac{\mu_s(1 + f')^{-1}}{3} ((1 + f')^2 + 2) + \rho \gamma_\varphi \frac{1}{3} \left(\frac{\partial \varphi}{\partial x} \right)^2 \quad (\text{D.9})$$

Similarly in the two-dimensional coordinates, the pressure can be expressed as

$$p = \mu_s \left(\frac{\rho}{\rho_o} \right)^{\frac{1}{1-2\nu_s}} + \rho RT + \rho \gamma_\varphi \frac{1}{3} \left(\left(\frac{\partial \varphi}{\partial x} \right)^2 + \left(\frac{\partial \varphi}{\partial y} \right)^2 \right) \quad (\text{D.10})$$

$$- \frac{1}{3} \mu_s \frac{\rho}{\rho_o} [(1 + H_{11})^2 + (1 + H_{22})^2 + H_{12}^2 + H_{21}^2 + 1] \quad (\text{D.11})$$

As before, we consider the expressions of pressure in a classical sense: limiting forms at each distinct phases φ of 0, 1, and 2 are considered. The pressure, expressed in pascals, in the solid phase is deduced from assigning $\varphi = 0$ such that in one-dimension it becomes

$$p(\eta) = \mu_{sol} \eta^{-\frac{1}{1-2\nu_s}} - \frac{\mu_{sol}}{3} \eta^{-1} (\eta^2 + 2) + \frac{\alpha_s \kappa}{\eta} (T - T_o) \quad (\text{D.12})$$

where μ_{sol} and α_s are the shear modulus corresponding to the solid phase and expansion coefficient corresponding to a solid phase. As before, $\eta = V/V_o$. As for the liquid phase, we allow only the volumetric change with zero deformation and maintain the thermal expansion of liquid. Further, one would expect that the liquid-state isotherm should reflect a 4% volume increase upon solid to liquid phase change, and thus the corresponding form of the pressure in the liquid case becomes,

$$p(\eta) = \mu_{liq} \eta^{-\frac{1}{1-2\nu_s}} - \frac{\mu_{liq}}{3} \eta^{-1} (\eta^2 + 2) + \frac{\alpha_s \kappa}{\eta} (T - T_o) \quad (\text{D.13})$$

where μ_{liq} is a modeled liquid shear modulus, and α_s is chosen the same as the solid case. When

$\varphi = 2$, we recover the ideal EOS for vapor HE and reacted product, such that

$$p(\eta) = \frac{\rho_o RT}{\eta} \tag{D.14}$$

with pressure expressed in pascals.

Appendix E

Eulerian–Lagrangian Configurations

The continuum laws of energetic materials was derived in the spatial configuration such that the Cauchy stress tensor is related to the Eulerian variable \mathbf{x} as well as the Lagrangian variable \mathbf{X} . A complete listing of governing continuum equations in ‘both’ configurations is desired as it will provide a foundation for performing a robust numerical simulation of thermomechanical behavior of HMX under large deformation. The stress response function of a material undergoing a phase transition from solid to fluid may suggest that

$$\begin{aligned}\boldsymbol{\sigma}(\mathbf{f}(\mathbf{X}, t), t) &= \rho(\mathbf{f}(\mathbf{X}, t), t) \mathbf{F}(\mathbf{X}, t) \left(\frac{\partial \psi}{\partial \mathbf{F}(\mathbf{X}, t)} \right)^\top + {}^4\mathbf{CL}(\mathbf{f}(\mathbf{X}, t), t) \\ &\quad - \nabla \phi_i(\mathbf{f}(\mathbf{X}, t), t) \otimes \boldsymbol{\xi}_i(\mathbf{f}(\mathbf{X}, t), t),\end{aligned}$$

where $\mathbf{f}(\mathbf{X}, t)$ is a deformation that maps a point \mathbf{X} in reference configuration into a position \mathbf{x} in spatial configuration. Moreover, the deformation tensor \mathbf{F} is $\frac{\partial \mathbf{f}(\mathbf{X}, t)}{\partial \mathbf{X}}$, the velocity gradient \mathbf{L} is $\frac{\partial \mathbf{v}(\mathbf{f}(\mathbf{X}, t), t)}{\partial \mathbf{x}}$, and ∇ is the spatial gradient operator $\frac{\partial}{\partial \mathbf{x}}$. As we find out, an additional equation for the displacement gradient \mathbf{H} must be solved with the balance laws simultaneously in the spatial formulation of the problem. In the referential description of continuum laws, it is the displacement $\mathbf{u}(\mathbf{X}, t)$ that is determined additionally to the unknowns of calculation (i.e. $\rho(\mathbf{X}, t)$, $\mathbf{v}(\mathbf{X}, t)$, $T(\mathbf{X}, t)$, $\varphi(\mathbf{X}, t)$, and $\lambda(\mathbf{X}, t)$). A distinct advantage of formulating the problem in the Lagrangian context is that the advection terms that arise in the spatial description of the material time derivative of each material property vanish. Because the computational grid is literally fixed to the particle, the treatment of the impact-loading boundary is also trivial in the Lagrangian formulation. In the following sections, continuum laws are revisited and explicitly writ-

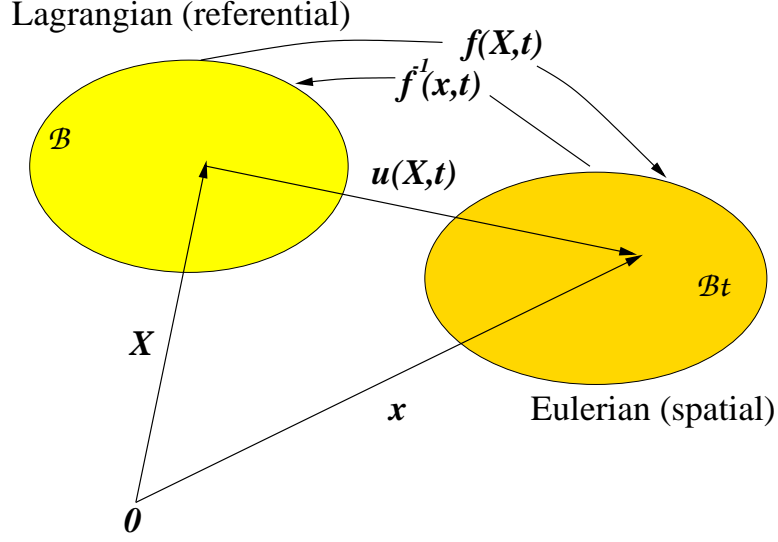


Figure E.1: Lagrangian and Eulerian frames.

ten out in both the Eulerian and the Lagrangian configurations in such a fashion that the resulting set of equations are suitable for the high-order accurate direct numerical simulation of the HMX thermochemical behaviors.

E.1 Eulerian description of balance laws

In the following collection of equations, the material time derivative (total derivative) of a physical material property $\phi(\mathbf{X}, t)$ (equivalently, $\widehat{\phi}(\mathbf{f}(\mathbf{X}, t), t)$), will be denoted by $\dot{\phi}$, where

$$\dot{\phi} = \frac{\partial \widehat{\phi}(\mathbf{f}(\mathbf{X}, t), t)}{\partial t} + \widehat{\mathbf{v}}(\mathbf{f}(\mathbf{X}, t), t) \cdot \nabla \widehat{\phi}(\mathbf{f}(\mathbf{X}, t), t) \quad (\text{E.1})$$

As for a vector quantity $\boldsymbol{\phi}(\mathbf{X}, t)$, the material time derivative becomes

$$\dot{\boldsymbol{\phi}} = \frac{\partial \widehat{\boldsymbol{\phi}}(\mathbf{f}(\mathbf{X}, t), t)}{\partial t} + (\nabla \widehat{\boldsymbol{\phi}}(\mathbf{f}(\mathbf{X}, t), t)) \widehat{\mathbf{v}}(\mathbf{f}(\mathbf{X}, t), t) \quad (\text{E.2})$$

Starting with the balance of mass, we have

$$\dot{\rho} + \rho \nabla \cdot \widehat{\mathbf{v}}(\mathbf{f}(\mathbf{X}, t), t) = 0 \quad (\text{E.3})$$

The linear momentum balance gives

$$\rho \dot{\mathbf{v}} = \nabla \cdot \boldsymbol{\sigma}(\mathbf{f}(\mathbf{X}, t), t) + \widehat{\mathbf{b}}(\mathbf{f}(\mathbf{X}, t), t) \quad (\text{E.4})$$

where $\boldsymbol{\sigma}$ is the Cauchy stress tensor which is described by the constitutive relations in the following manner:

$$\boldsymbol{\sigma}(\mathbf{f}(\mathbf{X}, t), t) = \mu_s \frac{\rho}{\rho_o} B - \mu_s \frac{\rho}{\rho_o} \text{III}_B^{-(\nu_s/1-2\nu_s)} \mathbf{1} - \rho RT \mathbf{1} - \rho \gamma_\varphi \nabla \varphi \otimes \nabla \varphi + \nu_f (\text{tr } D) \mathbf{1} + 2\mu_f L \quad (\text{E.5})$$

Combining the momentum balance with this definition for stress, we have

$$\rho \dot{\mathbf{v}} = \nabla \cdot \left\{ \mu_s \frac{\rho}{\rho_o} B - \mu_s \frac{\rho}{\rho_o} \text{III}_B^{-(\nu_s/1-2\nu_s)} \mathbf{1} - \rho RT \mathbf{1} - \rho \gamma_\varphi \nabla \varphi \otimes \nabla \varphi + \nu_f (\text{tr } D) \mathbf{1} + 2\mu_f L \right\} + \widehat{\mathbf{b}} \quad (\text{E.6})$$

The angular momentum balance implies that

$$\boldsymbol{\sigma}(\mathbf{f}(\mathbf{X}, t), t) = \boldsymbol{\sigma}^\top(\mathbf{f}(\mathbf{X}, t), t) \quad (\text{E.7})$$

This implies that (E.6) can alternatively be written with \mathbf{D} in place of \mathbf{L} using the symmetry property of the Cauchy stress, $\boldsymbol{\sigma}$. Energy balance is

$$\rho c_v \dot{T} = \nabla \cdot (K \nabla T) + \boldsymbol{\sigma}^{dis} \cdot D - \pi_i^{dis} \dot{\phi}_i + T \left(-\frac{\partial \pi_i^{eq}}{\partial T} \dot{\phi}_i + \frac{\partial \xi_i}{\partial T} \cdot \nabla(\dot{\phi}_i) + \frac{\partial \boldsymbol{\sigma}^{eq}}{\partial T} \cdot D \right) \quad (\text{E.8})$$

With constitutive equations properly introduced, the energy equation yields

$$\begin{aligned} \rho c_v \dot{T} = & \nabla \cdot (K \nabla T) + \nu_f (\text{tr } D)^2 + 2\mu_f D \cdot D + B_\varphi \dot{\varphi}^2 + B_\lambda \dot{\lambda}^2 \\ & + \left\{ -\rho c'_v(\varphi) T \ln \frac{T}{T_o} + \rho \left(\beta'_m(\varphi) \frac{T}{T_m} Q_m + \beta'_v(\varphi) \frac{T}{T_v} Q_v \right) \right\} \dot{\varphi} \\ & + \rho Q_c \Omega - (\rho RT \mathbf{1}) \cdot D \end{aligned} \quad (\text{E.9})$$

The phase change equation, after substituting the relations for microforces and microstresses, becomes

$$\begin{aligned}
B_\varphi \dot{\varphi} = & \nabla \cdot (\rho \gamma_\varphi \nabla \varphi) - \mu'_s(\varphi) \frac{\rho}{2\rho_o} (I_B - 3) - \mu'_s(\varphi) \frac{\rho(1-2\nu_s)}{2\rho_o\nu_s} \left(\mathbb{I}_B^{-\nu_s/(1-2\nu_s)} - 1 \right) \\
& + \rho c'_v(\varphi) \left\{ T \ln \frac{T}{T_o} - (T - T_o) \right\} - \rho \frac{1}{2} \Psi^{well} \frac{\partial}{\partial \varphi} \left(\{(\varphi)(\varphi-1)(\varphi-2)\}^2 \right) \\
& - \rho \beta'_m(\varphi) \frac{T - T_m}{T_m} Q_m - \rho \beta'_v(\varphi) \frac{T - T_v}{T_v} Q_v
\end{aligned} \tag{E.10}$$

E.1.1 Equation for displacement gradient

The description of balance laws in the spatial configuration as discussed above requires an independent determination of the extra unknown, the left Cauchy–Green tensor, \mathbf{B} . As we will see in the balance laws written in the reference configuration, one additionally computes the displacement $\mathbf{u}(\mathbf{X}, t)$. Here, however, we can either treat the deformational gradient \mathbf{F} or the displacement gradient \mathbf{H} as the extra unknown, and together we can solve the balance laws in a well-posed manner. The well-known relation between the time derivative of deformation tensor and the spatial variables (\mathbf{x}, t) is used to solve for \mathbf{F} , such that

$$\begin{aligned}
\dot{\mathbf{F}} &= \mathbf{L}\mathbf{F}, \text{ or} \\
\frac{\partial \mathbf{F}}{\partial t} &= \frac{\partial \widehat{\mathbf{v}}(\mathbf{f}(\mathbf{X}, t), t)}{\partial \mathbf{x}} \mathbf{F}
\end{aligned} \tag{E.11}$$

Alternatively, we can solve for the displacement gradient by using $\mathbf{F} = \mathbf{I} + \mathbf{H}$, or

$$\frac{\partial \mathbf{H}}{\partial t} = \frac{\partial \widehat{\mathbf{v}}(\mathbf{f}(\mathbf{X}, t), t)}{\partial \mathbf{x}} (\mathbf{I} + \mathbf{H}) \tag{E.12}$$

E.1.2 Displacement gradient based numerical formulation

Equations (E.3), (E.6), (E.9), (E.10), and (E.12) are solved simultaneously via the high-order accurate and robust numerical schemes. In particular, fourth-order convex ENO schemes are used to discretize the advection terms and all first derivative terms while the fourth-order central difference schemes are used to treat the second derivative terms of diffusive nature. Once the system of equations in the previous section are spatially discretized, the resulting semi-discretized equations

are solved in a method of line approach. Here, we have chosen to discretize in time via the low-storage third-order semi-implicit Runge–Kutta (LSSIRK–3) schemes.

E.2 Relations between spatial and referential operators

In order to reformulate balance laws in terms of the Lagrangian variables (\mathbf{X}, t) , we first convert the spatial operators, which appear explicitly in the balance laws, into their referential counterparts. We basically perform the coordinate transformation of $(x_1, x_2, x_3, t) \mapsto (X_1, X_2, X_3, t)$. Starting from the spatial description of material time derivative, the Lagrangian description is a simple time derivative such that

$$\frac{\partial \hat{\phi}(\mathbf{f}(\mathbf{X}, t), t)}{\partial t} + \hat{\mathbf{v}}(\mathbf{f}(\mathbf{X}, t), t) \cdot \nabla \hat{\phi}(\mathbf{f}(\mathbf{X}, t), t) = \frac{\partial}{\partial t} \phi(\mathbf{X}, t) \quad (\text{E.13})$$

As for gradient operators, we have the following relation via chain rule:

$$\nabla \hat{\phi}(\mathbf{f}(\mathbf{X}, t), t) = \mathbf{F}^{-\top} \mathbf{Grad} \phi(\mathbf{X}, t) \quad (\text{E.14})$$

Similarly, when the gradient operates on a vector, the relation becomes

$$\nabla \hat{\phi}(\mathbf{f}(\mathbf{X}, t), t) = \mathbf{Grad} \phi(\mathbf{X}, t) \mathbf{F}^{-1} \quad (\text{E.15})$$

Divergence of a vector becomes

$$\nabla \cdot \hat{\phi}(\mathbf{f}(\mathbf{X}, t), t) = \frac{\partial \hat{\phi}_i}{\partial x_i} = \frac{\partial \phi_i}{\partial X_l} \frac{\partial X_l}{\partial x_i} = \frac{\partial \phi_i}{\partial X_l} F_{li}^{-1} = \mathbf{Grad} \phi(\mathbf{X}, t) \cdot \mathbf{F}^{-\top} \quad (\text{E.16})$$

As it appears in the linear momentum balance, the divergence of a tensor quantity will also be expressed in the reference configuration. For simplicity, we will use the Cauchy stress tensor $\boldsymbol{\sigma}(\mathbf{f}(\mathbf{X}, t), t)$ as an example of some physical tensoral material property under transformation:

$$\nabla \cdot \boldsymbol{\sigma}(\mathbf{f}(\mathbf{X}, t), t) = \frac{\partial \sigma_{ij}}{\partial x_j} \mathbf{e}_i = \frac{\partial \sigma_{ij}}{\partial X_k} \frac{\partial X_k}{\partial x_j} \mathbf{e}_i \quad (\text{E.17})$$

Now, if we multiply the result in (E.17) by the Jacobian J , an expression involving a divergence of a new tensor quantity called the first Piola–Kirchhoff (PK-1) stress emerges. This new tensor quantity, which is defined by the product of the Jacobian, the Cauchy stress, and the inverse deformation tensor, is the engineering stress as recorded from the undeformed coordinate. In other words, we claim to express (E.17) as

$$J \frac{\partial \sigma_{ij}}{\partial X_k} \frac{\partial X_k}{\partial x_j} \mathbf{e}_i = \mathbf{Div} \left(J \boldsymbol{\sigma}(\mathbf{f}(\mathbf{X}, t), t) \mathbf{F}^{-\top} \right) \quad (\text{E.18})$$

$$= \mathbf{Div} \tilde{\boldsymbol{\sigma}}(\mathbf{X}, t) \quad (\text{E.19})$$

where we use the symbol, $\tilde{\boldsymbol{\sigma}}$, to denote the PK-1 stress. Now, it remains to prove the statement in (E.18). Expressed in the component notations, the right-hand side of (E.18) is

$$\frac{\partial}{\partial X_j} \left(J \sigma_{ik} \frac{\partial X_j}{\partial x_k} \right) = \frac{\partial}{\partial X_j} \left(J \frac{\partial X_j}{\partial x_k} \right) \sigma_{ik} + \left(J \frac{\partial X_j}{\partial x_k} \right) \frac{\partial \sigma_{ik}}{\partial X_j} \quad (\text{E.20})$$

Here, the first term emerging as a result of applying the divergence operator via chain rule is identically zero due to the theorem of *Piola's identity*. It basically states that $\mathbf{Div} (J \mathbf{F}^{-\top}) = 0$ thus (E.20) consists only of the last term, such that

$$\begin{aligned} \frac{\partial}{\partial X_j} \left(J \sigma_{ik} \frac{\partial X_j}{\partial x_k} \right) &= \left(J \frac{\partial X_j}{\partial x_k} \right) \frac{\partial \sigma_{ik}}{\partial X_j} \\ &= J \frac{\partial \sigma_{ij}}{\partial X_k} \frac{\partial X_k}{\partial x_j} \end{aligned} \quad (\text{E.21})$$

with some relabeling of indices j and k . This result is identical to what we intended to prove earlier on the left-hand side of (E.18).

The Laplacian operator, $\nabla \cdot (\nabla \hat{\phi}(\mathbf{f}(\mathbf{X}, t), t))$, as it appears in the energy conduction term is transformed next. Recall from (E.14) how the gradient of scalar $\hat{\phi}(\mathbf{f}(\mathbf{X}, t), t)$ transformed, and for simplicity its component notation will be stated here:

$$\frac{\partial \hat{\phi}}{\partial x_i} = \frac{\partial X_j}{\partial x_i} \frac{\partial \phi}{\partial X_j} \quad (\text{E.22})$$

Now, taking the divergence on the above vector quantity, one obtains the following:

$$\begin{aligned}
\nabla \cdot (\nabla \hat{\phi})_i &= \frac{\partial}{\partial x_i} (\nabla \hat{\phi})_i \\
&= \frac{\partial (\nabla \hat{\phi})_i}{\partial X_l} \frac{\partial X_l}{\partial x_i} \\
&= \frac{\partial X_l}{\partial x_i} \frac{\partial}{\partial X_l} \left\{ \frac{\partial X_j}{\partial x_i} \frac{\partial \phi}{\partial X_j} \right\} \\
&= F_{li}^{-1} \left(\frac{\partial}{\partial X_l} \left\{ F_{ij}^{-\top} \frac{\partial \phi}{\partial X_j} \right\} \right) \\
&= F_{il}^{-\top} \left(\frac{\partial}{\partial X_l} \left\{ F_{ij}^{-\top} \frac{\partial \phi}{\partial X_j} \right\} \right)
\end{aligned}$$

Thus, the Laplacian of $\hat{\phi}(\mathbf{f}(\mathbf{X}, t), t)$ transforms as

$$\nabla \cdot (\nabla \hat{\phi}(\mathbf{f}(\mathbf{X}, t), t)) = \mathbf{F}^{-\top} \cdot \mathbf{Grad} \left(\mathbf{F}^{-\top} \mathbf{Grad} \phi(\mathbf{X}, t) \right) \quad (\text{E.23})$$

Furthermore, we will list some of the useful expressions of a velocity gradient as they appear in numerous parts of the balance laws:

$$\mathbf{L} = \nabla \hat{\mathbf{v}}(\mathbf{f}(\mathbf{X}, t), t) = \mathbf{Grad} \mathbf{v}(\mathbf{X}, t) \mathbf{F}^{-1} \quad (\text{E.24})$$

$$\mathbf{D} = \frac{1}{2} \left(\mathbf{Grad} \mathbf{v}(\mathbf{X}, t) \mathbf{F}^{-1} + (\mathbf{Grad} \mathbf{v}(\mathbf{X}, t) \mathbf{F}^{-1})^\top \right) \quad (\text{E.25})$$

$$\begin{aligned}
\text{tr } \mathbf{D} = \text{tr } \mathbf{L} &= \text{tr} \left(\mathbf{Grad} \mathbf{v}(\mathbf{X}, t) \mathbf{F}^{-1} \right) \\
&= \text{tr} \left\{ \frac{1}{2} \left(\mathbf{Grad} \mathbf{v}(\mathbf{X}, t) \mathbf{F}^{-1} + (\mathbf{Grad} \mathbf{v}(\mathbf{X}, t) \mathbf{F}^{-1})^\top \right) \right\} \quad (\text{E.26})
\end{aligned}$$

E.3 Lagrangian description of balance laws

The balance of mass, linear momentum, angular momentum, energy, microforces, and reaction species in (E.3) through (E.12) now take the following forms in the Lagrangian configuration:

$$\frac{\partial \rho(\mathbf{X}, t)}{\partial t} + \rho(\mathbf{X}, t) \frac{\partial \mathbf{v}(\mathbf{X}, t)}{\partial \mathbf{X}} \cdot \mathbf{F}^{-\top} = 0 \quad (\text{E.27})$$

$$\rho_o \frac{\partial \mathbf{v}(\mathbf{X}, t)}{\partial t} = \mathbf{Div} \tilde{\boldsymbol{\sigma}}(\mathbf{X}, t) + \rho_o \mathbf{b}(\mathbf{X}, t) \quad (\text{E.28})$$

where the PK-1 stress does not satisfy the stress symmetry by the angular momentum such that $\tilde{\boldsymbol{\sigma}} \neq \tilde{\boldsymbol{\sigma}}^\top$. Expressing $\tilde{\boldsymbol{\sigma}}$ in terms of constitutive relations, we have then

$$\begin{aligned}
\tilde{\boldsymbol{\sigma}}(\mathbf{X}, t) &= J\boldsymbol{\sigma}(\mathbf{f}(\mathbf{X}, t), t)\mathbf{F}^{-\top} \\
&= \frac{\rho_o}{\rho} \left\{ \mu_s \frac{\rho}{\rho_o} \mathbf{B} - \mu_s \frac{\rho}{\rho_o} \mathbb{I}_B^{-(\nu_s/1-2\nu_s)} \mathbf{1} - \rho RT \mathbf{1} - \rho \gamma_\varphi \nabla \varphi \otimes \nabla \varphi + \nu_f (\text{tr } \mathbf{D}) \mathbf{1} + 2\mu_f \mathbf{D} \right\} \mathbf{F}^{-\top} \\
&= \left\{ \mu_s \mathbf{B} - \mu_s \mathbb{I}_B^{-(\nu_s/1-2\nu_s)} \mathbf{1} - \rho_o RT \mathbf{1} - \rho_o \gamma_\varphi \left(\mathbf{F}^{-\top} \frac{\partial \varphi}{\partial \mathbf{X}} \right) \otimes \left(\mathbf{F}^{-\top} \frac{\partial \varphi}{\partial \mathbf{X}} \right) \right. \\
&\quad \left. + \frac{\rho_o}{\rho} \nu_f \left(\text{tr } \left(\frac{\partial \mathbf{v}}{\partial \mathbf{X}} \mathbf{F}^{-1} \right) \right) \mathbf{1} + \frac{\rho_o}{\rho} \mu_f \left(\frac{\partial \mathbf{v}}{\partial \mathbf{X}} \mathbf{F}^{-1} + \left(\frac{\partial \mathbf{v}}{\partial \mathbf{X}} \mathbf{F}^{-1} \right)^\top \right) \right\} \mathbf{F}^{-\top} \quad (\text{E.29})
\end{aligned}$$

Energy balance, under the Lagrangian transformation, becomes

$$\begin{aligned}
\rho c_v \frac{\partial T}{\partial t} &= K \mathbf{F}^{-\top} \cdot \left(\frac{\partial}{\partial \mathbf{X}} (\mathbf{F}^{-\top} \frac{\partial T}{\partial \mathbf{X}}) \right) + \nu_f (\text{tr } \mathbf{D})^2 + 2\mu_f \mathbf{D} \cdot \mathbf{D} \\
&\quad + B_\varphi \left(\frac{\partial \varphi}{\partial t} \right)^2 + B_\lambda \left(\frac{\partial \lambda}{\partial t} \right)^2 \\
&\quad + \left\{ -\rho c'_v(\varphi) T \ln \frac{T}{T_o} + \rho \left(\beta'_m(\varphi) \frac{T}{T_m} Q_m + \beta'_v(\varphi) \frac{T}{T_v} Q_v \right) \right\} \frac{\partial \varphi}{\partial t} \\
&\quad + \rho Q_c \frac{\partial \lambda}{\partial t} - (\rho RT \mathbf{1}) \cdot \mathbf{L} \quad (\text{E.30})
\end{aligned}$$

where \mathbf{D} , \mathbf{L} , and $\text{tr}(\mathbf{D})$ are defined in (E.24) through (E.26). Similarly, the equation of phase change takes the following form:

$$\begin{aligned}
B_\varphi \frac{\partial \varphi}{\partial t} &= \mathbf{F}^{-\top} \cdot \left(\frac{\partial}{\partial \mathbf{X}} (\rho \gamma_\varphi \mathbf{F}^{-\top} \frac{\partial \varphi}{\partial \mathbf{X}}) \right) - \mu'_s(\varphi) \frac{\rho}{2\rho_o} (I_B - 3) \\
&\quad - \mu'_s(\varphi) \frac{\rho(1-2\nu_s)}{2\rho_o \nu_s} \left(\mathbb{I}_B^{-\nu_s/(1-2\nu_s)} - 1 \right) + \rho c'_v(\varphi) \left(T \ln \frac{T}{T_o} - (T - T_o) \right) \\
&\quad - \rho \frac{1}{2} \Psi^{well} \frac{\partial}{\partial \varphi} \left(\{(\varphi)(\varphi-1)(\varphi-2)\}^2 \right) \\
&\quad - \rho \beta'_m(\varphi) \frac{T - T_m}{T_m} Q_m - \rho \beta'_v(\varphi) \frac{T - T_v}{T_v} Q_v \quad (\text{E.31})
\end{aligned}$$

Finally, the displacement field is determined via solving the following equation

$$\frac{\partial \mathbf{u}(\mathbf{X}, t)}{\partial t} = \mathbf{v}(\mathbf{X}, t) \quad (\text{E.32})$$

E.3.1 Longitudinal problem

For a longitudinal impact problem, the generalized Lagrangian formulation of continuum theory as developed above becomes a set of non-linear PDE which is solved using high-order temporal scheme to capture the transients and high-order spatial schemes to resolve all of the scales in the continuum field. The three fundamental invariants of \mathbf{B} now simplify to

$$\begin{aligned} I_B &= \text{tr}(\mathbf{B}) = 2 + \left(1 + \frac{\partial u_1}{\partial X_1}\right)^2 \\ II_B &= \frac{1}{2} ((\text{tr} \mathbf{B})^2 - \text{tr} \mathbf{B}^2) = 1 + 2\left(1 + \frac{\partial u_1}{\partial X_1}\right)^2 \\ III_B &= \det \mathbf{B} = \left(\frac{\rho_o}{\rho}\right)^2 = \left(1 + \frac{\partial u_1}{\partial X_1}\right)^2 \end{aligned} \quad (\text{E.33})$$

and

$$J = \frac{\rho_o}{\rho} = 1 + \frac{\partial u_1}{\partial X_1} \quad (\text{E.34})$$

$$F_{11}^{-1} = \left(1 + \frac{\partial u_1}{\partial X_1}\right)^{-1} = F_{11}^{-\top} \quad (\text{E.35})$$

First, the equation of mass balance becomes

$$\frac{\partial \rho}{\partial t} + \rho \left(1 + \frac{\partial u_1}{\partial X_1}\right)^{-1} \frac{\partial v_1}{\partial X_1} = 0 \quad (\text{E.36})$$

The linear momentum balance becomes

$$\begin{aligned} \rho_o \frac{\partial v_1}{\partial t} &= \frac{\partial}{\partial X_1} \left\{ \mu_s \left(1 + \frac{\partial u_1}{\partial X_1}\right) - \mu_s \left(1 + \frac{\partial u_1}{\partial X_1}\right)^{\frac{-1}{1-2\nu_s}} - \rho RT \right. \\ &\quad \left. - \rho \gamma_\varphi \left(1 + \frac{\partial u_1}{\partial X_1}\right)^{-1} \frac{\partial \varphi}{\partial X_1} \right\} + (\nu_f + 2\mu_f) \frac{\partial v_1}{\partial X_1} \left(1 + \frac{\partial u_1}{\partial X_1}\right)^{-1} \end{aligned} \quad (\text{E.37})$$

where the quantity in the curly bracket is the referential stress quantity (PK-1 stress) as discussed previously. The displacement is related to velocity via

$$\frac{\partial u_1}{\partial t} = v_1 \quad (\text{E.38})$$

The balance of energy takes a simpler form as

$$\begin{aligned}
\rho c_v \frac{\partial T}{\partial t} = & K \left(1 + \frac{\partial u_1}{\partial X_1}\right)^{-1} \frac{\partial}{\partial X_1} \left(\left(1 + \frac{\partial u_1}{\partial X_1}\right)^{-1} \frac{\partial T}{\partial X_1} \right) \\
& + (\nu_f + 2\mu_f) \left(\frac{\partial v_1}{\partial X_1} \left(1 + \frac{\partial u_1}{\partial X_1}\right)^{-1} \right)^2 \\
& + B_\varphi \left(\frac{\partial \varphi}{\partial t}\right)^2 + B_\lambda \left(\frac{\partial \lambda}{\partial t}\right)^2 + T \rho \left(\beta_m' \frac{Q_m}{T_m} + \beta_v' \frac{Q_v}{T_v} \right) \frac{\partial \varphi}{\partial t} + \rho Q_c \frac{\partial \lambda}{\partial t} \\
& + \mu_s \frac{\partial v_1}{\partial X_1} - \mu_s \left(1 + \frac{\partial u_1}{\partial X_1}\right)^{-\frac{1}{1-2\nu_s}} \frac{\partial v_1}{\partial X_1} - \rho R T \left(1 + \frac{\partial u_1}{\partial X_1}\right)^{-1} \frac{\partial v_1}{\partial X_1} \\
& + \frac{1}{2} \frac{\partial \mu_s}{\partial \varphi} \left(1 + \frac{\partial u_1}{\partial X_1}\right)^{-1} \left(\left(1 + \frac{\partial u_1}{\partial X_1}\right)^2 - 1 \right) \frac{\partial \varphi}{\partial t} \\
& + \frac{1-2\nu_s}{2\nu_s} \frac{\partial \mu_s}{\partial \varphi} \left(1 + \frac{\partial u_1}{\partial X_1}\right)^{-1} \left(\left(1 + \frac{\partial u_1}{\partial X_1}\right)^{-\frac{2\nu_s}{1-2\nu_s}} - 1 \right) \frac{\partial \varphi}{\partial t}
\end{aligned} \tag{E.39}$$

The phase equation also takes on a simpler form:

$$\begin{aligned}
B_\varphi \frac{\partial \varphi}{\partial t} = & \left(1 + \frac{\partial u_1}{\partial X_1}\right)^{-1} \frac{\partial}{\partial X_1} \left(\rho \gamma_\varphi \left(1 + \frac{\partial u_1}{\partial X_1}\right)^{-1} \frac{\partial \varphi}{\partial X_1} \right) \\
& - \mu_s'(\varphi) \frac{\rho}{2\rho_o} \left(\left(1 + \frac{\partial u_1}{\partial X_1}\right)^2 - 1 \right) \\
& - \mu_s'(\varphi) \frac{\rho(1-2\nu_s)}{2\rho_o \nu_s} \left(\left(1 + \frac{\partial u_1}{\partial X_1}\right)^{\frac{-2\nu_s}{(1-2\nu_s)}} - 1 \right) \\
& + \rho c_v'(\varphi) \left(T \ln \frac{T}{T_o} - (T - T_o) \right) - \rho \frac{1}{2} \Psi^{well} \frac{\partial}{\partial \varphi} \left(\{(\varphi)(\varphi-1)(\varphi-2)\}^2 \right) \\
& - \rho \beta_m'(\varphi) \frac{T-T_m}{T_m} Q_m - \rho \beta_v'(\varphi) \frac{T-T_v}{T_v} Q_v
\end{aligned} \tag{E.40}$$

E.4 Two-Dimensional generalization of continuum laws

The continuum theory as discussed in this thesis are general in that two dimensional extensions can be presumed in a straightforward manner. Before developing the corresponding balance laws, we first state some of the usual expressions which are called upon readily. The displacement gradient tensor \mathbf{H} is such that

$$\mathbf{H} = \begin{bmatrix} \frac{\partial u_1}{\partial X_1} & \frac{\partial u_1}{\partial X_2} \\ \frac{\partial u_2}{\partial X_1} & \frac{\partial u_2}{\partial X_2} \end{bmatrix} \quad (\text{E.41})$$

and the left Cauchy–Green tensor ($\mathbf{B} = \mathbf{B}^\top$) becomes

$$\mathbf{B} = \begin{bmatrix} (1 + H_{11})^2 + H_{12}^2 & (1 + H_{11})H_{21} + H_{12}(1 + H_{22}) & 0 \\ (1 + H_{11})H_{21} + H_{12}(1 + H_{22}) & H_{21}^2 + (1 + H_{22})^2 & 0 \\ 0 & 0 & 1 \end{bmatrix} \quad (\text{E.42})$$

Thus, by means of \mathbf{B}^2 , we have the following expression:

$$\begin{aligned} \text{tr } \mathbf{B}^2 &= B_{11}^2 + B_{22}^2 + B_{33}^2 \\ &= (1 + H_{11})^4 + 2H_{12}^2(1 + H_{11})^2 + H_{12}^4 \\ &\quad + H_{21}^4 + 2H_{21}^2(1 + H_{22})^2 + (1 + H_{22})^4 + 1. \end{aligned} \quad (\text{E.43})$$

Likewise, we further obtain the following:

$$\begin{aligned} (\text{tr } \mathbf{B})^2 &= ((1 + H_{11})^2 + (1 + H_{22})^2 + (H_{12}^2 + H_{21}^2 + 1))^2 \\ &\quad + 2((1 + H_{11})^2 + (1 + H_{22})^2)(H_{12}^2 + H_{21}^2 + 1) \end{aligned} \quad (\text{E.44})$$

We also find that

$$\begin{aligned}
\mathbf{B} \cdot \mathbf{L} &= \begin{bmatrix} (1 + H_{11})^2 + H_{12}^2 & (1 + H_{11})H_{21} + H_{12}(1 + H_{22}) & 0 \\ (1 + H_{11})H_{21} + H_{12}(1 + H_{22}) & H_{21}^2 + (1 + H_{22})^2 & 0 \\ 0 & 0 & 1 \end{bmatrix} \cdot \begin{bmatrix} \frac{\partial v_1}{\partial x} & \frac{\partial v_1}{\partial y} & 0 \\ \frac{\partial v_2}{\partial x} & \frac{\partial v_2}{\partial y} & 0 \\ 0 & 0 & 0 \end{bmatrix} \\
&= ((1 + H_{11})^2 + H_{12}^2) \frac{\partial v_1}{\partial x} + ((1 + H_{11})H_{21} + H_{12}(1 + H_{22})) \frac{\partial v_1}{\partial y} \\
&\quad + ((1 + H_{11})H_{21} + H_{12}(1 + H_{22})) \frac{\partial v_2}{\partial x} + (H_{21}^2 + (1 + H_{22})^2) \frac{\partial v_2}{\partial y}
\end{aligned}$$

and

$$\mathbf{L} \cdot \mathbf{1} = \frac{\partial v_1}{\partial x} + \frac{\partial v_2}{\partial y} \quad (\text{E.45})$$

Further, we list the invariants of \mathbf{B} as follows:

$$\begin{aligned}
I_B &= \text{tr}(\mathbf{B}) \\
&= (1 + H_{11})^2 + (1 + H_{22})^2 + H_{12}^2 + H_{21}^2 + 1
\end{aligned} \quad (\text{E.46})$$

$$\begin{aligned}
III_B &= \det \mathbf{B} = \left(\frac{\rho_o}{\rho} \right)^2 \\
&= ((1 + H_{11})^2 + H_{12}^2)(H_{21}^2 + (1 + H_{22})^2) \\
&\quad - ((1 + H_{11})H_{21} + H_{12}(1 + H_{22}))^2
\end{aligned} \quad (\text{E.47})$$

Recall the constitutive expression for the equilibrium stress,

$$\boldsymbol{\sigma}^{eq} = \mu_s \frac{\rho}{\rho_o} \mathbf{B} - \mu_s \frac{\rho}{\rho_o} III_B^{-\frac{\nu_s}{1-2\nu_s}} \mathbf{1} - \rho RT \mathbf{1} - \frac{\rho}{\rho_o} \alpha \kappa (T - T_o) - \rho \gamma_\varphi \nabla \varphi \otimes \nabla \varphi$$

where

$$\sigma_{11}^{eq} = \mu_s \frac{\rho}{\rho_o} [(1 + H_{11})^2 + H_{12}^2] - \mu_s \left(\frac{\rho}{\rho_o} \right)^{\frac{1}{1-2\nu_s}} - \rho RT - \alpha \kappa \frac{\rho}{\rho_o} (T - T_o) - \rho \gamma_\varphi \left(\frac{\partial \varphi}{\partial x} \right)^2 \quad (\text{E.48})$$

$$\sigma_{12}^{eq} = \mu_s \frac{\rho}{\rho_o} [(1 + H_{11})H_{21} + H_{12}(1 + H_{22})] - \rho \gamma_\varphi \frac{\partial \varphi}{\partial x} \frac{\partial \varphi}{\partial y} \quad (\text{E.49})$$

$$\sigma_{21}^{eq} = \sigma_{12}^{eq} \quad (\text{E.50})$$

$$\sigma_{22}^{eq} = \mu_s \frac{\rho}{\rho_o} [H_{21}^2 + (1 + H_{22})^2] - \mu_s \left(\frac{\rho}{\rho_o} \right)^{\frac{1}{1-2\nu_s}} - \rho RT - \alpha \kappa \frac{\rho}{\rho_o} (T - T_o) - \rho \gamma_\varphi \left(\frac{\partial \varphi}{\partial y} \right)^2 \quad (\text{E.51})$$

As before, the dissipative part of the stress reads

$$\boldsymbol{\sigma}^{dis} = \nu_f (\text{tr } \boldsymbol{D}) \boldsymbol{I} + 2\mu_f \boldsymbol{D}$$

where

$$\boldsymbol{D} = \frac{1}{2} \begin{bmatrix} 2\frac{\partial v_1}{\partial x} & \frac{\partial v_1}{\partial y} + \frac{\partial v_2}{\partial x} & 0 \\ \frac{\partial v_2}{\partial x} + \frac{\partial v_1}{\partial y} & 2\frac{\partial v_2}{\partial y} & 0 \\ 0 & 0 & 0 \end{bmatrix} \quad (\text{E.52})$$

and

$$\text{tr } \boldsymbol{D} = \left(\frac{\partial v_1}{\partial x} + \frac{\partial v_2}{\partial y} \right) \quad (\text{E.53})$$

We also note that

$$\begin{aligned} \boldsymbol{D} \cdot \boldsymbol{D} &= D_{ij} D_{ij} \\ &= \left(\frac{\partial v_1}{\partial x} \right)^2 + \frac{1}{2} \left(\frac{\partial v_1}{\partial y} + \frac{\partial v_2}{\partial x} \right)^2 + \left(\frac{\partial v_2}{\partial y} \right)^2 \end{aligned} \quad (\text{E.54})$$

Thus,

$$\boldsymbol{\sigma}^{dis} = \nu_f \left(\frac{\partial v_1}{\partial x} + \frac{\partial v_2}{\partial y} \right) \begin{bmatrix} 1 & 0 & 0 \\ 0 & 1 & 0 \\ 0 & 0 & 1 \end{bmatrix} + \mu_f \begin{bmatrix} 2\frac{\partial v_1}{\partial x} & \frac{\partial v_1}{\partial y} + \frac{\partial v_2}{\partial x} & 0 \\ \frac{\partial v_2}{\partial x} + \frac{\partial v_1}{\partial y} & 2\frac{\partial v_2}{\partial y} & 0 \\ 0 & 0 & 0 \end{bmatrix} \quad (\text{E.55})$$

In the conservative form, the momentum equations thus become

$$\frac{\partial}{\partial t} \begin{pmatrix} \rho v_1 \\ \rho v_2 \end{pmatrix} + \frac{\partial}{\partial x} \begin{pmatrix} \rho v_1^2 - \sigma_{11} \\ \rho v_1 v_2 - \sigma_{21} \end{pmatrix} + \frac{\partial}{\partial y} \begin{pmatrix} \rho v_1 v_2 - \sigma_{12} \\ \rho v_2^2 - \sigma_{22} \end{pmatrix} = \begin{pmatrix} 0 \\ 0 \end{pmatrix}$$

where the Cauchy stress components are given by

$$\begin{aligned} \sigma_{11} = & \mu_s \frac{\rho}{\rho_o} [(1 + H_{11})^2 + H_{12}^2] - \mu_s \left(\frac{\rho}{\rho_o} \right)^{\frac{1}{1-2\nu_s}} - \rho R T - \alpha \kappa \frac{\rho}{\rho_o} (T - T_o) - \rho \gamma_\varphi \left(\frac{\partial \varphi}{\partial x} \right)^2 \\ & + \nu_f \left(\frac{\partial v_1}{\partial x} + \frac{\partial v_2}{\partial y} \right) + 2\mu_f \frac{\partial v_1}{\partial x} \end{aligned} \quad (\text{E.56})$$

$$\sigma_{12} = \mu_s \frac{\rho}{\rho_o} [(1 + H_{11})H_{21} + H_{12}(1 + H_{22})] - \rho \gamma_\varphi \frac{\partial \varphi}{\partial x} \frac{\partial \varphi}{\partial y} + \mu_f \left(\frac{\partial v_1}{\partial y} + \frac{\partial v_2}{\partial x} \right) \quad (\text{E.57})$$

$$\sigma_{21} = \sigma_{12} \quad (\text{E.58})$$

$$\begin{aligned} \sigma_{22} = & \mu_s \frac{\rho}{\rho_o} [H_{21}^2 + (1 + H_{22})^2] - \mu_s \left(\frac{\rho}{\rho_o} \right)^{\frac{1}{1-2\nu_s}} - \rho R T - \alpha \kappa \frac{\rho}{\rho_o} (T - T_o) - \rho \gamma_\varphi \left(\frac{\partial \varphi}{\partial y} \right)^2 \\ & + \nu_f \left(\frac{\partial v_1}{\partial x} + \frac{\partial v_2}{\partial y} \right) + 2\mu_f \frac{\partial v_2}{\partial y} \end{aligned} \quad (\text{E.59})$$

The displacement gradients assume the following relationship:

$$\frac{\partial H_{11}}{\partial t} + v_1 \frac{\partial H_{11}}{\partial x} + v_2 \frac{\partial H_{11}}{\partial y} = \frac{\partial v_1}{\partial x} (1 + H_{11}) + \frac{\partial v_1}{\partial y} (H_{21}) \quad (\text{E.60})$$

$$\frac{\partial H_{12}}{\partial t} + v_1 \frac{\partial H_{12}}{\partial x} + v_2 \frac{\partial H_{12}}{\partial y} = \frac{\partial v_1}{\partial x} (H_{12}) + \frac{\partial v_1}{\partial y} (1 + H_{22}) \quad (\text{E.61})$$

$$\frac{\partial H_{21}}{\partial t} + v_1 \frac{\partial H_{21}}{\partial x} + v_2 \frac{\partial H_{21}}{\partial y} = \frac{\partial v_2}{\partial y} (H_{21}) + \frac{\partial v_2}{\partial x} (1 + H_{11}) \quad (\text{E.62})$$

$$\frac{\partial H_{22}}{\partial t} + v_1 \frac{\partial H_{22}}{\partial x} + v_2 \frac{\partial H_{22}}{\partial y} = \frac{\partial v_2}{\partial y} (1 + H_{22}) + \frac{\partial v_2}{\partial x} (H_{12}) \quad (\text{E.63})$$

The energy balance becomes

$$\begin{aligned} \frac{\partial}{\partial t} (\rho T) + \frac{\partial}{\partial x} (\rho v_1 T) = & \frac{1}{c_v} \left\{ K \left(\frac{\partial^2 T}{\partial x_1^2} + \frac{\partial^2 T}{\partial y^2} \right) + \nu_f \left(\frac{\partial v_1}{\partial x} + \frac{\partial v_2}{\partial y} \right)^2 \right. \\ & + \frac{\partial}{\partial y} (\rho v_2 T) + 2\mu_f \left(\left(\frac{\partial v_1}{\partial x} \right)^2 + \frac{1}{2} \left(\frac{\partial v_1}{\partial y} + \frac{\partial v_2}{\partial x} \right)^2 + \left(\frac{\partial v_2}{\partial y} \right)^2 \right) + B \dot{\varphi}^2 \\ & \left. + \rho (\beta'_m \frac{T}{T_m} Q_m + \beta'_v \frac{T}{T_v} Q_v) \dot{\varphi} - \rho R T \left(\frac{\partial v_1}{\partial x} + \frac{\partial v_2}{\partial y} \right) - \alpha \kappa \frac{\rho}{\rho_o} T \left(\frac{\partial v_1}{\partial x} + \frac{\partial v_2}{\partial y} \right) \right\} \end{aligned}$$

The phase-field equation now reads

$$\begin{aligned}
\frac{\partial}{\partial t}(\rho\varphi) + \frac{\partial}{\partial x}(\rho\varphi v_1) + \frac{\partial}{\partial y}(\rho\varphi v_2) = & \frac{\rho}{B} \left\{ \rho\gamma_\varphi \left(\frac{\partial^2 \varphi}{\partial x_1^2} + \frac{\partial^2 \varphi}{\partial y^2} \right) - \mu'_s \frac{\rho}{2\rho_o} (I_B - 3) \right. \\
& - \mu'_s \frac{\rho(1 - 2\nu_s)}{2\rho_o\nu_s} (\text{III}_B^{-\frac{\nu_s}{1-2\nu_s}} - 1) \\
& - \frac{\rho}{2} \Psi^{well} \frac{\partial}{\partial \varphi} \{ (\varphi(\varphi - 1)(\varphi - 2))^2 \} \\
& \left. - \rho\beta'_m \frac{T - T_m}{T_m} Q_m - \rho\beta'_v \frac{T - T_v}{T_v} Q_v \right\}
\end{aligned}$$

Appendix F

Derivation of Classical Sharp Interface Problems as Asymptotic Limits of the Phase-Field Equations

F.1 Introduction

Using detailed asymptotic analyses of the dynamics of the phase-field model as presented in this thesis, we show that the major sharp-interface models (Stefan, modified Stefan, and Hele-Shaw) are recovered as limiting cases of the temperature and phase evolution equations. Distinct physical parameters of the model are first recognized, and then the proper scaling of these microscopic parameters allows us to derive a set of macroscopic sharp-interface models of solidification. We close follow Caginalp^[15].

F.2 Preliminaries

F.2.1 Sharp interface model problems

A set of macroscopic equations that incorporate latent heat across an interface, heat diffusion, and surface tension on the interface, can be described as follows. It is assumed that the continuity and the momentum balance are satisfied and that the material undergoes only a single phase transition from solid to liquid with zero deformation and chemical reaction. The function $u(x, y, t)$ represent

temperature and a surface $\Gamma(t)$ represents a time dependent interface such that

$$\frac{\partial u}{\partial t} = K \nabla^2 u \quad \text{in } \Omega/\Gamma(t) \quad (\text{F.1})$$

$$lv = -K [\nabla u]_{\Gamma_-}^+ \quad \text{in } \Gamma(t) \quad (\text{F.2})$$

$$u = -\frac{\sigma}{\Delta s}(\kappa + \alpha v) \quad \text{in } \Gamma(t) \quad (\text{F.3})$$

where l is the latent heat, v is the interfacial velocity in the direction normal to the surface $\Gamma(t)$, σ is the surface tension, α is a nonzero constant, κ is the local interfacial curvature ($\nabla^2 r$), and Δs is the entropy difference of the two phases ($\Delta s = l/T_m$). By allowing $\sigma \rightarrow 0$, we obtain the classical Stefan problem.^[15] If σ is finite, the modified Stefan solidification problem emerges. Further, the condition $\kappa = 0$ describes plane-front solidification.

Another limit, known as the quasi-static approximation in phase boundary problems arising from condensed matter physics,^[16] is described as follows:

$$0 = K \nabla^2 u \quad \text{in } \Omega_1, \Omega_2/\Gamma(t) \quad (\text{F.4})$$

$$lv = -K [\nabla u]_{\Gamma_-}^+ \quad \text{in } \Gamma(t) \quad (\text{F.5})$$

$$u = -\frac{\sigma}{\Delta s}(\kappa + \alpha v) \quad \text{in } \Gamma(t) \quad (\text{F.6})$$

where the heat diffusion occurs so rapidly in the interface such that the process is steady state. In some context, namely in fluid mechanics, u may represent the pressure between two immiscible fluids. Such a problem is called the Hele-Shaw model.^[17]

F.2.2 Phase-field model problems

Unlike the macroscopic description of the interface as in the sharp interface models (e.g. modified Stefan, classical Stefan, and Hele-Shaw), the phase-field model arises as a microscopic counterpart such that there is an order-parameter φ , which takes a value of 0 in the solid phase and a value of unity in the liquid phase. With zero deformation and absence of chemical reaction, one conservative equation for the temperature (u) field and a non-conservative evolution equation for φ are derived

earlier as follows:

$$\rho C_p \dot{u} = \nabla \cdot (K \nabla u) + B_\varphi \dot{\varphi}^2 + \rho \left(z'_m(\varphi) \frac{u}{T_m} Q_m \right) \dot{\varphi} \quad (\text{F.7})$$

$$B_\varphi \dot{\varphi} = \nabla \cdot (\rho \mu_\varphi \nabla \varphi) - \rho \frac{1}{2} \Psi^{\text{well}} \frac{\partial}{\partial \varphi} \left(\{(\varphi)(\varphi - 1)\}^2 \right) - \rho z'_m(\varphi) \frac{u - T_m}{T_m} Q_m \quad (\text{F.8})$$

where the material derivative (dot) in this context becomes a simple time derivative and the heat of melt Q_m is by definition the negative of latent heat l in the sharp interface models. The interface $\Gamma(t)$ in this phase-field model is defined as

$$\Gamma(t) = \{\mathbf{x} \in \Omega; u(\mathbf{x}, t) = T_m, \varphi(\mathbf{x}, t) = 1/2\}.$$

It is the intent of this thesis that as we take the asymptotic limits of the phase-field model equations, the sharp interface models are recovered. In particular, the asymptotic treatment of the evolution equations for u and φ is justified if the interface thickness scale (B_φ, μ_φ) and the potential well depth scale $(a \sim 1/\Psi^{\text{well}})$ approach zero in the Stefan limits, and the condition $K/\rho C_p \rightarrow \infty$ describes the Hele-Shaw limits. For the sake of simplicity, we assume $\rho C_p = 1$ and $\rho \mu_\varphi = \text{constant}$ such that ρ is also considered constant. The forthcoming sections will discuss the details of recovering the classical solidification models upon taking the matched asymptotic limits on the governing phase-field equations in (F.7), (F.8). As a reference, we will follow the procedure as outlined in Caginalp^[15] in taking the asymptotic limits of our phase-field model.

F.3 Sharp interface limit with finite surface tension (Modified Stefan model)

In the limit $B_\varphi, \mu_\varphi, a \rightarrow 0$ with $(B_\varphi/a)^{1/2}$ and $(\mu_\varphi/a)^{1/2}$ remaining fixed, there exists a formal asymptotic solution of the phase-field model (F.7), (F.8) that is governed by the modified Stefan

model (F.1)-(F.3). We start the analysis by introducing the following scales:

$$B_\varphi \sim \mu_\varphi \sim \epsilon, \quad c_1 \equiv \sqrt{\epsilon/a}$$

Assuming $\rho C_p = 1$, we can write (F.7) as

$$u_t = K \nabla^2 u + \epsilon \varphi_t^2 + \rho z_m' u \frac{Q_m}{T_m} \varphi_t \quad (\text{F.9})$$

As for the phase equation, we allow that $\rho \mu_\varphi$ be pulled out of the divergence operator and let $a = 1/\Psi^{\text{well}}$, such that the resulting equation reads

$$B_\varphi \varphi_t = \rho \mu_\varphi \nabla^2 \varphi - \rho \frac{1}{2a} g(\varphi) - \rho z_m' \frac{u - T_m}{T_m} Q_m \quad (\text{F.10})$$

where we have introduced a new function

$$g(\varphi) \equiv \frac{\partial}{\partial \varphi} \{ [\varphi(\varphi - 1)]^2 \}$$

After properly introducing the scales, the resulting phase equation becomes

$$\frac{2}{\rho} \epsilon^2 \varphi_t = 2 \epsilon^2 \nabla^2 \varphi - f(\varphi) - 2 \epsilon z_m' \frac{Q_m}{T_m} (u - T_m) \quad (\text{F.11})$$

where we also introduce a notation

$$\frac{\epsilon}{a} g(\varphi) = c_1^2 g(\varphi) \equiv f(\varphi)$$

In order to carry out an asymptotic expansion on (F.9) and [F.11], we first expand the variables u and φ in their original coordinates (i.e. outer expansion) as

$$\begin{aligned} u(x, y, t, \epsilon) &= u^{(0)}(x, y, t) + \epsilon u^{(1)}(x, y, t) + O(\epsilon^2) \\ \varphi(x, y, t, \epsilon) &= \varphi^{(0)}(x, y, t) + \epsilon \varphi^{(1)}(x, y, t) + O(\epsilon^2) \end{aligned}$$

As for the inner expansion, we introduce a moving coordinate system (r, s) where r is defined normal

to the interfacial surface $\Gamma(t)$ so that it is positive from the solid ($\varphi < 1/2$) to liquid ($\varphi > 1/2$). Let s be a measure of arc length from some fixed point. Further we introduce a stretched coordinate

$$z = \frac{r}{\epsilon}$$

so the expansion with the inner variables U and ϕ are given by

$$\begin{aligned} u(x, y, t, \epsilon) &= U(z, s, t, \epsilon) = U^{(0)}(z, s, t) + \epsilon U^{(1)}(z, s, t) + O(\epsilon^2) \\ \varphi(x, y, t, \epsilon) &= \phi(z, s, t, \epsilon) = \phi^{(0)}(z, s, t) + \epsilon \phi^{(1)}(z, s, t) + O(\epsilon^2) \\ r(x, y, t, \epsilon) &= r^{(0)} + \epsilon r^{(1)} + O(\epsilon^2) \\ s(x, y, t, \epsilon) &= s^{(0)} + \epsilon s^{(1)} + O(\epsilon^2) \end{aligned}$$

Furthermore, the interface $\Gamma(t)$ may be described as the set of points at which (x, y, t) vanishes.

In the neighborhood of Γ , the following is true:

$$|\nabla r| = 1, \quad \nabla^2 r = \kappa$$

The potential well function $f(\varphi)$ may also be expanded in ϵ such that

$$f(\varphi) = f(\varphi^{(0)}) + \epsilon f'(\varphi^{(0)})\varphi^{(1)} + \epsilon^2 \left[f'(\varphi^{(0)})\varphi^{(2)} + f''(\varphi^{(0)})\frac{(\varphi^{(1)})^2}{2} \right] + O(\epsilon^3)$$

for the outer variables, and as for the inner variable the expansion becomes

$$f(\phi) = f(\phi^{(0)}) + \epsilon f'(\phi^{(0)})\phi^{(1)} + \epsilon^2 \left[f'(\phi^{(0)})\phi^{(2)} + f''(\phi^{(0)})\frac{(\phi^{(1)})^2}{2} \right] + O(\epsilon^3)$$

Outer Expansion

$O(1)$:

$$u_t^{(0)} = K \nabla^2 u^{(0)} + \rho z_m' u^{(0)} \frac{Q_m}{T_m} \varphi_t^{(0)} \quad (\text{F.12})$$

$$f(\varphi^{(0)}) = 0 \quad (\text{F.13})$$

Equating the phase equation, we find that

$$\begin{aligned} f(\varphi^{(0)}) &= c_1^2 \frac{\partial}{\partial \varphi^{(0)}} \left\{ [\varphi^{(0)}(\varphi^{(0)} - 1)]^2 \right\} \\ &= c_1^2 2\varphi^{(0)}(\varphi^{(0)} - 1)(2\varphi^{(0)} - 1) = 0 \end{aligned}$$

where the system admits three roots of which $\varphi^{(0)} = 0, 1$ are the two solutions of the outer limits.

Thus the temperature evolution equation for $u^{(0)}$ becomes a classical heat diffusion equation

$$u_t^{(0)} = K \nabla^2 u^{(0)} \quad (\text{F.14})$$

Inner Expansion In the moving coordinate system, the Laplacian operator can be written as

$$\begin{aligned} \nabla^2 u &= u_{rr} + \nabla^2 r u_r + |\nabla s|^2 u_{ss} + \nabla^2 s u_s \\ &= \frac{1}{\epsilon^2} U_{zz} + \frac{1}{\epsilon} \nabla^2 r U_z + |\nabla s|^2 U_{ss} + \nabla^2 s U_s \end{aligned}$$

and the time derivative becomes

$$\begin{aligned} \frac{d}{dt} u(r, s, t) &= u_t + r_t u_r + s_t u_s \\ &= U_t + \frac{1}{\epsilon} r_t U_z + s_t U_s \end{aligned}$$

Then (F.9) and (F.11) are expressed in the new coordinate system as

$$K U_{zz} + \epsilon \left[K \nabla^2 r U_z - r_t U_z + \rho z'_m U \frac{Q_m}{T_m} r_t \phi_z \right] + \epsilon^2 [\dots] + \epsilon^3 [\dots] = 0 \quad (\text{F.15})$$

As for the phase equation, we obtain

$$2\phi_{zz} - f(\phi) + \epsilon \left[2\nabla^2 r \phi_z - \frac{2}{\rho} r_t \phi_z - 2z'_m \frac{Q_m}{T_m} (U - T_m) \right] + \epsilon^2 [\dots] = 0 \quad (\text{F.16})$$

The first order problems are

$$O(1) :$$

$$U_{zz}^{(0)} = 0 \quad (\text{F.17})$$

$$2\phi_{zz}^{(0)} - f(\phi^{(0)}) = 0 \quad (\text{F.18})$$

The solution to (F.17) is $U^{(0)} = \alpha z + \beta$. Using the matching condition at $z \rightarrow \infty$, α must be zero for the solution to be bounded. Then the unknown β is independent of z such that $\beta = \beta(s, t)$. Thus the first order temperature solution is independent of the stretched coordinate z . As for the phase solution, the matching condition suggests that

$$\begin{aligned} \phi^{(0)}(z \rightarrow \pm\infty, t) &= \varphi^{(0)}(\Gamma_{\pm}^{(0)}, t) \\ &= 0 \text{ or } 1 \end{aligned} \quad (\text{F.19})$$

And recalling the interface definition such that $\phi^{(0)}(0, t) = 1/2$ specifies the surface $\Gamma(t)$, we may deduce the following:

$$\phi^{(0)}(z, s, t) \rightarrow \phi^{(0)}(z) \quad (\text{F.20})$$

In summary, the first order phase equation admits a set of homogeneous boundary value problem:

$$L\phi^{(0)} \equiv 2\phi_{zz}^{(0)} - f(\phi^{(0)}) = 0 \quad (\text{F.21})$$

$$\phi^{(0)}(\pm\infty) = 0 \text{ or } 1 \quad (\text{F.22})$$

$$\phi^{(0)}(0) = 1/2 \quad (\text{F.23})$$

The $O(\epsilon)$ problems of the inner solution becomes

$O(\epsilon)$:

$$\begin{aligned} KU_{zz}^{(1)} &= r_t^{(0)} U_z^{(0)} - K \nabla^2 r^{(0)} U_z^{(0)} - \rho z_m' \frac{Q_m}{T_m} U^{(0)} r_t^{(0)} \phi_z^{(0)} \\ &= + \rho z_m' \frac{Q_m}{T_m} U^{(0)} v \phi_z^{(0)} \end{aligned} \quad (\text{F.24})$$

$$2\phi_{zz}^{(1)} - f'(\phi^{(0)})\phi^{(1)} + 2\nabla^2 r^{(0)}\phi_z^{(0)} - \frac{2}{\rho}r_t^{(0)}\phi_z^{(0)} - 2z'_m \frac{Q_m}{T_m}(U^{(0)} - T_m) = 0 \quad (\text{F.25})$$

The jump condition or the latent heat condition of the modified Stefan problem can be derived from considering (F.24). Integrating from $-\infty$ to $+\infty$, one finds

$$KU_z^{(1)} \Big|_{-\infty}^{+\infty} = -\rho z'_m \frac{l}{T_m} \beta v \phi^{(0)} \Big|_{-\infty}^{+\infty}$$

where we have made substitutions for $l = -Q_m$ and $\beta = U^{(0)}$. Applying the Neumann matching condition gives

$$U_z^{(1)}(z \rightarrow \pm\infty, t) = u_r^{(0)}(\Gamma_{\pm}^{(0)}, t) \quad (\text{F.26})$$

So the jump condition at the interface becomes the following:

$$\left[Ku_r^{(0)} \right]_{\Gamma_{\pm}} = -\frac{\rho z'_m}{T_m} l v (1 - 0) \quad (\text{F.27})$$

$$= -\frac{\rho z'_m}{T_m} l v \quad (\text{F.28})$$

Now it remains to recover the third equation of the sharp interface model, namely the temperature profile within the interface $\Gamma(t)$. Rewriting the $O(\epsilon)$ equation for the phase in (F.25) as

$$L\phi^{(1)} \equiv 2\phi_{zz}^{(1)} - f'(\phi^{(0)})\phi^{(1)} = -\frac{2}{\rho}v\phi_z^{(0)} - 2\kappa\phi_z^{(0)} - \frac{2z'_m l}{T_m}(U^{(0)} - T_m) \quad (\text{F.29})$$

with the solution of $L\phi^{(0)}$, we may construct a solvability condition as

$$\int_{-\infty}^{+\infty} \phi_z^{(0)} \left[\frac{2}{\rho}v\phi_z^{(0)} + 2\kappa\phi_z^{(0)} + \frac{2z'_m l}{T_m}(U^{(0)} - T_m) \right] dz = 0$$

Since $U^{(0)}$ is independent of z , we may perform the integral operator further such that

$$\frac{2z'_m l}{T_m}(U^{(0)} - T_m)(1 - 0) + \left(\frac{2}{\rho}v + 2\kappa\right) \int_{-\infty}^{+\infty} (\phi_z^{(0)})^2 dz = 0 \quad (\text{F.30})$$

If we introduce a surface tension which is defined by the integral, $\sigma \equiv \int_{-\infty}^{+\infty} (\phi_z^{(0)})^2 dz$, the equation

above further simplifies to

$$\frac{z'_m l}{T_m} (U^{(0)} - T_m) = -\left(\frac{v}{\rho} + \kappa\right) \sigma$$

Using the matching condition

$$U^{(0)}(\pm\infty) = u^{(0)}(\Gamma_{\pm}^{(0)})$$

we finally recover (closely) the temperature profile within the interface region for the modified Stefan sharp interface model:

$$z'_m (u^{(0)}|_{\Gamma_{\pm}} - T_m) = -\frac{\sigma}{\Delta s} \left(\frac{v}{\rho} + \kappa \right) \quad (\text{F.31})$$

where we have used the definition of the entropy difference of the two phases, namely $\Delta s \equiv l/T_m$.

In the asymptotic limit as $\epsilon, a \rightarrow 0$ while holding $\sqrt{\epsilon/a} = \text{constant}$, we have successfully recovered the first of the three sharp interface model of condensed matter physics, namely the modified Stefan solidification problem. In summary, equations (F.14), (F.28), and (F.31) are identical to the model equations in (F.1)–(F.3). In the subsequent sections, two other classical sharp interface models will be derived using the similar matched asymptotic expansion technique as discussed in this section.

F.4 Sharp interface limit with zero surface tension (Classical Stefan model)

We choose a particular scaling such that there is only one parameter (ϵ) in the asymptotic limit.

$$B_{\varphi} \sim \mu_{\varphi} \sim \epsilon^4, \quad a \equiv \epsilon^2 c_o^{-2}$$

Thus in the limit $\epsilon^2 \rightarrow 0$ holding $c_o = \sqrt{\epsilon^2/a}$ fixed, the asymptotic expansions of (F.7) and (F.8) will be justified and they resemble the following expressions:

$$u_t = K\nabla^2 u + \epsilon^4 \varphi_t^2 + \rho z_m' u \frac{Q_m}{T_m} \varphi_t \quad (\text{F.32})$$

$$\frac{2}{\rho} \epsilon^6 \varphi_t = 2\epsilon^6 \nabla^2 \varphi - f(\varphi) - 2\epsilon^2 z_m' \frac{Q_m}{T_m} (u - T_m) \quad (\text{F.33})$$

where we have used the definition $f(\varphi) = c_o^2 g(\varphi)$ as in the previous analysis. Both outer and inner expansions of the variables u and φ remain unchanged from the previous section except that we now introduce a different stretching of the normal coordinate z such that

$$z = \frac{r}{\epsilon^3}$$

Outer Expansion

$O(1)$:

$$u_t^{(0)} = K\nabla^2 u^{(0)} + \rho z_m' u^{(0)} \frac{Q_m}{T_m} \varphi_t^{(0)} \quad (\text{F.34})$$

$$f(\varphi^{(0)}) = 0 \quad (\text{F.35})$$

This is identical to the case of modified Stefan such that we clearly recover the classical heat diffusion equation as

$$u_t^{(0)} = K\nabla^2 u^{(0)} \quad (\text{F.36})$$

Inner Expansion In the interior, the Laplacian and the time derivative on the inner variables are written as follows:

$$\begin{aligned}
\nabla^2 u &= u_{rr} + \nabla^2 r u_r + |\nabla s|^2 u_{ss} + \nabla^2 s u_s \\
&= \frac{1}{\epsilon^6} U_{zz} + \frac{1}{\epsilon^3} \nabla^2 r U_z + |\nabla s|^2 U_{ss} + \nabla^2 s U_s \\
\frac{d}{dt} u(r, s, t) &= u_t + r_t u_r + s_t u_s \\
&= U_t + \frac{1}{\epsilon^3} r_t U_z + s_t U_s
\end{aligned}$$

In the transformed coordinate system $((x, y, t) \rightarrow (z, s, t))$, we may rewrite (F.32) and (F.33) as follows:

$$K U_{zz} + \epsilon^3 \left[K \nabla^2 r U_z - r_t U_z + \rho z'_m U \frac{Q_m}{T_m} r_t \phi_z \right] + O(\epsilon^6) = 0 \quad (\text{F.37})$$

As for the phase, (F.33) becomes

$$2\phi_{zz} - f(\phi) + \epsilon^2 \left[2z'_m \frac{Q_m}{T_m} (U - T_m) \right] + \epsilon^3 \left[-\frac{2}{\rho} r_t \phi_z + 2\nabla^2 r U_z \right] + O(\epsilon^6) = 0 \quad (\text{F.38})$$

$O(1)$:

$$U_{zz}^{(0)} = 0 \quad (\text{F.39})$$

$$2\phi_{zz}^{(0)} - f(\phi^{(0)}) = 0 \quad (\text{F.40})$$

The solution boundedness on U requires U to be a constant in z such that $U^{(0)} = \beta(s, t)$ as before. Similarly the phase order parameter $\phi^{(0)}$ is function only of z , following the same argument as in the previous section. In short,

$$U^{(0)} = \beta(s, t) \quad (\text{F.41})$$

$$\phi^{(0)} = \phi^{(0)}(z) \quad (\text{F.42})$$

In order to recover the classical Stefan limit, one needs to show that $\beta(s, t) = 0$ such that the interfacial temperature profile is identically zero (i.e. $u|_{\Gamma_{\pm}} = 0$). To do so, we need higher-order expansions in ϵ :

$O(\epsilon)$:

$$\begin{aligned} U_{zz}^{(1)} &= 0 \\ L\phi^{(1)} &\equiv 2\phi_{zz}^{(1)} - f'(\phi^{(0)})\phi^{(1)} = 0 \end{aligned}$$

$O(\epsilon^2)$:

$$\begin{aligned} U_{zz}^{(2)} &= 0 \\ L\phi^{(2)} &\equiv 2\phi_{zz}^{(2)} - f'(\phi^{(0)})\phi^{(2)} = \frac{2z'_m Q_m}{T_m}(U^{(0)} - T_m) + f''(\phi^{(0)})\frac{(\phi^{(1)})^2}{2} \end{aligned}$$

Solving the homogeneous system in $O(\epsilon)$, we discover that

$$\phi^{(1)} = \phi_z^{(0)} \tag{F.43}$$

and thus we may arrive at a solvability condition on the $O(\epsilon^2)$ system such that

$$\int_{-\infty}^{+\infty} \phi_z^{(0)} \left[f''(\phi^{(0)})\frac{(\phi_z^{(1)})^2}{2} + \frac{2z'_m Q_m}{T_m}(U^{(0)} - T_m) \right] dz = 0$$

Here, we argue that f, f'' are odd, and $f', \phi^{(1)}$ are even. Thus the condition becomes

$$\frac{2z'_m Q_m}{T_m}(U^{(0)} - T_m) \int_{-\infty}^{+\infty} \phi_z^{(0)} dz = 0$$

Since the integral reduces to a unity, the condition is held true if the temperature in the interface is identical to the melting temperature such that we recover the second equation of the classical

Stefan solidification problem:

$$u(\Gamma_{\pm}) = T_m \quad (\text{F.44})$$

It is noted that in the dimensionless theory of Stefan model problems, the melting temperature is assumed to be zero with a proper introduction of scalings. For generality, we will assign a finite value of that melting temperature as T_m for the remainder of the discussions.

The third equation of the classical Stefan limit is the latent heat condition identical to (F.28) in the modified Stefan limit. To consider it, we need the $O(\epsilon^3)$ expansion of temperature:

$O(\epsilon^3)$:

$$KU_{zz}^{(3)} + K\nabla^2 r U_z^{(0)} - r_t^{(0)} U_z^{(0)} + \rho z_m' \frac{U^{(0)}}{T_m} lv \phi_z^{(0)} = 0$$

Since $U^{(0)} = T_m$ on Γ_{\pm} , we may further simplify the expression such that

$$KU_{zz}^{(3)} = -\rho z_m' lv \phi_z^{(0)}$$

Upon integrating and observing the jump condition on the gradient, we obtain

$$KU_z^{(3)} \Big|_{-\infty}^{+\infty} = -\rho z_m' lv$$

With the matching condition

$$U^{(3)}(z \rightarrow \pm\infty, t) = u_r^{(0)}(\Gamma_{\pm}, t)$$

we finally recover the latent heat condition of the classic Stefan problem:

$$K \left[u_r^{(0)} \right]_{\Gamma_{\pm}} = -\rho z_m' lv \quad (\text{F.45})$$

In summary, equations (F.36), (F.44), and (F.45) are the asymptotic limiting solutions of the phase-field model equations and they are in fact the classical Stefan limits of the sharp interface models in (F.1)–(F.3) with zero surface tension.

F.5 Quasi-static limit (Hele-Shaw model)

In the quasi-static limit, the constants (l, K, α) have different meanings from the earlier sense. Further, we expect to associate the variable u as the hydrodynamic pressures with σ being the interfacial tension between two fluids. We first list the scaling of the parameters as

$$B_\varphi \sim \mu_\varphi \sim \epsilon, \quad K \sim 1/\epsilon \quad c_1 = \sqrt{\epsilon/a}, \quad c_2 = \sqrt{\epsilon l}$$

In addition, we further require the scaling

$$(u - T_m) \sim \epsilon u$$

such that heat diffuses very rapidly in the interface such that the quasi-static approximation will hold justified. Assuming $\rho C_p = 1$ again, we rewrite (F.7) as

$$\epsilon u_t = \nabla^2 u + \epsilon^2 \varphi_t^2 - \rho z'_m \frac{u}{T_m} c_2^2 \varphi_t \quad (\text{F.46})$$

and the phase equation in (F.8) becomes

$$\frac{2}{\rho} \epsilon^2 \varphi_t = 2\epsilon^2 \nabla^2 \varphi - f(\varphi) + 2\epsilon \frac{z'_m}{T_m} c_2^2 u \quad (\text{F.47})$$

where we have used the fact that $(u - T_m) \sim u$ and $c_1^2 g(\varphi) = f(\varphi)$.

Outer Expansion

$O(1)$:

$$\nabla^2 u^{(0)} = \rho z'_m \frac{u^{(0)}}{T_m} c_2^2 \varphi_t^{(0)} \quad (\text{F.48})$$

$$f(\varphi^{(0)}) = 0 \quad (\text{F.49})$$

Since $\varphi^{(0)} = 1$ or 0 in the outer layer, we recover the first condition of the Hele-Shaw limit, namely the pressure Laplacian equation,

$$\nabla^2 u^{(0)} = 0 \quad (\text{F.50})$$

Inner Expansion Along with transforming the coordinate from $(x, y, t) \rightarrow (r, s, t)$, we use a stretching scales of the form

$$z = \frac{r}{\epsilon}$$

which is the same stretching as in the modified Stefan problem. Now, the Laplacian and time derivative operators transform to

$$\nabla^2 u = \frac{1}{\epsilon^2} U_{zz} + \frac{1}{\epsilon} \nabla^2 r U_z + |\nabla s|^2 U_{ss} + \nabla^2 s U_s$$

and the time derivative becomes

$$\frac{d}{dt} u(r, s, t) = U_t - \frac{v}{\epsilon} U_z + s_t U_s$$

Then the resulting equations for U and ϕ after transforming (F.46) and (F.47) become the following:

$$\begin{aligned} \epsilon^3 U_t - \epsilon^2 v U_t + \epsilon^3 s_t U_s &= U_{zz} + \epsilon \nabla^2 r U_z + \epsilon^2 |\nabla s|^2 U_{ss} + \epsilon^2 (\nabla^2 s) U_s \\ &\quad + \epsilon^4 \varphi_t^2 - \epsilon^2 \rho \frac{z'_m}{T_m} u c_2^2 \left(\varphi_t - \frac{v}{\epsilon} \varphi_z + s_t \varphi_s \right) \end{aligned} \quad (\text{F.51})$$

$$\begin{aligned} \frac{2}{\rho} (\epsilon^2 \varphi_t - \epsilon v \varphi_z + \epsilon^2 s_t \varphi_s) &= 2 (\varphi_{zz} + \epsilon \nabla^2 r \varphi_z + \epsilon^2 |\nabla s|^2 \varphi_{ss} + \epsilon^2 \nabla^2 s \varphi_s) \\ &\quad - \epsilon f(\varphi) + \frac{2z'_m}{T_m} c_2^2 u \end{aligned} \quad (\text{F.52})$$

The first order problems are

$O(1)$:

$$U_{zz}^{(0)} = 0 \quad (\text{F.53})$$

$$2\phi_{zz}^{(0)} - f(\phi^{(0)}) = 0 \quad (\text{F.54})$$

Following the argument in the modified Stefan limit, we obtain $U^{(0)} = \beta(s, t)$. We also obtain the governing boundary value problem for the phase:

$$L\phi^{(0)} \equiv 2\phi_{zz}^{(0)} - f(\phi^{(0)}) = 0 \quad (\text{F.55})$$

$$\phi^{(0)}(\pm\infty) = 0 \text{ or } 1 \quad (\text{F.56})$$

$$\phi^{(0)}(0) = 1/2 \quad (\text{F.57})$$

The $O(\epsilon)$ problems of the inner solution becomes

$O(\epsilon)$:

$$U_{zz}^{(1)} = -\rho \frac{z'_m}{T_m} U^{(0)} c_2^2 v \phi_z^{(0)} \quad (\text{F.58})$$

$$-\frac{2}{\rho} v \phi_z^{(0)} = 2\phi_{zz}^{(1)} + 2\nabla^2 r^{(0)} \phi_z^{(0)} - f'(\phi^{(0)}) \phi^{(1)} + 2 \frac{z'_m}{T_m} c_2^2 U^{(0)} \quad (\text{F.59})$$

Recalling $c_2^2 = l/K$, we find the latent heat condition from integrating the above equation for u such that

$$\left[u_r^{(0)} \right]_-^+ = -\frac{l}{\bar{K}} v \quad (\text{F.60})$$

where we have used the matching condition of

$$U_z^{(1)}(\pm\infty, t) = u_r^{(0)}(\Gamma_\pm, t)$$

As for the third condition of the Hele-Shaw limit, we consider the phase equation in (F.59):

$$L\phi^{(1)} \equiv 2\phi_{zz}^{(1)} - f'(\phi^{(0)}) \phi^{(1)} = -\frac{2}{\rho} v \phi_z^{(0)} - 2\kappa \phi_z^{(0)} - \frac{2z'_m}{T_m} c_2^2 U^{(0)} \quad (\text{F.61})$$

The solvability condition gives

$$\int_{-\infty}^{+\infty} \phi_z^{(0)} \left[\frac{2}{\rho} v \phi_z^{(0)} + 2\kappa \phi_z^{(0)} + \frac{2z_m'}{T_m} c_2^2 U^{(0)} \right] dz = 0$$

Using the surface tension σ as defined earlier, we arrive at the expression for the pressure distribution in the interface,

$$u^{(0)}|_{\Gamma_{\pm}} = -\tilde{\beta} \frac{\sigma}{\Delta s} \left(\frac{v}{\rho} + \kappa \right) \quad (\text{F.62})$$

where we have used the matching condition,

$$U^{(0)}(\pm\infty) = u^{(0)}|_{\Gamma_{\pm}}$$

and the fact that $\Delta s = l/T_m$.

Clearly, we have successfully recovered the Hele-Shaw model of solidification upon taking the asymptotic limits on the phase-model equations in [F.7] and [F.8].

Appendix G

Code Index

We list all codes used to generate the numerical simulation results contained in the thesis. A brief description of each code is given. Available on a CD-ROM disc is a copy of the codes in different folders with makefiles and subsidiary input files needed to compile and generate the executable.

Solvers of Chapter 3

- *longitudinal.f* (1-D): One-dimensional code of HMX model used in the longitudinal motion analysis.
- *shear.f* (1-d): One-dimensional code of HMX model used in the shearing motion analysis.

Multi-material solvers of Chapter 4 (EM)

- *ring-up.f* (1-D): One-dimensional code based on the ghost-fluid-method (GFM) to simulate a piston driven laminate of two different gases.
- *hot-spot.f* (1-D, spherically symmetric): One-dimensional code based on GFM to simulate the hot-spot formation in solid HMX.
- *shear-induced-melting.f* (2-D): Two-dimensional code used to generate a wavy interface between two Blatz–Ko solids with phase change in a shearing motion.
- *plate-cutter-I.f* (2-D): Two-dimensional code using GFM to simulate the HE/Blatz–Ko plate/fluid interactions.

Multi-material solvers of Chapter 5 (Metal)

- *shocktube.f* (1-D): One-dimensional code using a level-set to calculate the standard shock-tube test involving two gases of different γ 's.
- *Taylor-rod-impact.f* (2-D): Two-dimensional code used to reproduce the standard rod-impact test of copper.
- *rate-stick-I.f* (2-D): Two-dimensional code built to reproduce the rate-stick result of Aslam and Bdzil using *Amrita*.
- *rate-stick-II.f* (2-D): Two-dimensional code used to simulate a rate-stick with a copper confinement.
- *explosive-welding.f* (2-D): Two-dimensional code built to simulate the welding of a copper and steel plates.
- *plate-cutter-II.f* (2-D): Two-dimensional code using two level-sets to simulate the HE/Cu/Void interactions upon penetration of a spherical detonation wave into the copper plate.

References

- [1] T. D. Aslam and J. B. Bdzil. Private communication. Los Alamos National Laboratory, 2001.
- [2] T. D. Aslam, J. B. Bdzil, and D. S. Stewart. Level Set Methods Applied to Modeling Detonation Shock Dynamics. *Journal of Computational Physics*, 126:390–409, 1996.
- [3] G. K. Batchelor. *An Introduction to Fluid Dynamics*. Cambridge: Cambridge University Press, 1967.
- [4] D. Bedrov, G. D. Smith, and T. D. Sewell. Temperature Dependent Shear Viscosity Coefficients of HMX, a Molecular Dynamics Simulation Study. *Journal of Chemical Physics*, 112:7203–7208, 2000.
- [5] D. M. Belk. Class notes. U. S. Air Force Research Laboratory, Eglin Air Force Base, Fla., 1999.
- [6] D. J. Benson. Computational Methods in Lagrangian and Eulerian Hydrocodes. *Computer Methods in Applied Mechanics and Engineering*, 99:235–394, 1992.
- [7] D. J. Benson. A Multi-Material Eulerian Formulation for the Efficient Solution of Impact and Penetration Problem. *Computational Mechanics*, 15:558–571, 1995.
- [8] D. J. Benson. Eulerian Finite Element Methods for the Micromechanics of Heterogeneous Materials: Dynamic Prioritization of Material Interfaces. *Computer Methods in Applied Mechanics and Engineering*, 151:343–360, 1998.
- [9] E. W. Billington and A. Tate. *The Physics of Deformation and Flow*. New York: McGraw-Hill, Inc., 1981.

- [10] T. L. Boggs. The Thermal Behavior of Cyclotrimethylenetrinitramine (RDX) and Cyclotetramethylenetetranitramine (HMX). *Progress in Astro. and Aero*, 90:121–175, 1984.
- [11] R. M. Bowen. Part I: Theory of Mixtures, in *Continuum Physics, Vol III Mixtures and Electromagnetic Field Theories*. A. C. Eringen, ed. Academic Press, 1976.
- [12] R. M. Bowen. *Introduction to Continuum Mechanics for Engineers*. Plenum Press, 1989.
- [13] T. B. Brill. Multiphase chemistry considerations at the surface of burning nitramine monopropellants. *Journal of Propulsion and Power*, 11:740–750, 1995.
- [14] J. D. Buckmaster and G. S. S. Ludford. *Theory of Laminar Flames*. Cambridge: Cambridge University Press, 1982.
- [15] G. Caginalp. Stefan and Hele-Shaw Type Models as Asymptotic Limits of the Phase-Field Equations. *Physical Review A*, 39:5887–5896, 1989.
- [16] G. Caginalp. A Microscopic Derivation of Macroscopic Sharp Interface Problems Involving Phase Transitions. *Journal of Statistical Physics*, 59:869–884, 1990.
- [17] G. Caginalp and E. A. Socolovsky. Computation of Sharp Phase Boundaries by Spreading: The Planar and Spherically Symmetric Cases. *Journal of Computational Physics*, 95:85–100, 1991.
- [18] Herbert B. Callen. *Thermodynamics: an Introduction to the Physical Theories of Equilibrium Thermostatistics and Irreversible Thermodynamics*. New York: John Wiley & Sons, Inc., 1985.
- [19] G. T. Camacho and M. Ortiz. Adaptive Lagrangian modelling of ballistic penetration of metallic targets. *Computer Methods in Applied Mechanics and Engineering*, 142:269–301, 1997.
- [20] D. Chakraborty, R. P. Muller, S. Dasgupta, and W. A. Goddard. The Mechanism for Unimolecular Decomposition of RDX (1,3,5-Trinitro-1,3,5-triazine), an ab Initio Study. *Journal of Physical Chemistry*, 104:2261–2272, 2000.

- [21] C. H. Chiang, M. S. Raju, and W. A. Sirignano. Numerical Analysis of Convecting, Vaporizing Fuel Droplet with Variable Properties. *International Journal of Heat and Mass Transfer*, 5:1307–1324, 1992.
- [22] B. D. Coleman and W. Noll. The Thermodynamics of Elastic Materials with Heat Conduction and Viscosity. *Archive of Rational Mechanics*, 13:245–261, 1963.
- [23] R. F. Davidson and P. J. Maudlin. A continuum code investigation of stress integration using exact and approximate material rotation. Technical Report LA-12380-MS, Los Alamos National Laboratory, NM, 1992.
- [24] B. M. Dobratz and P. C. Crawford. *LLNL Explosive Handbook*. Lawrence Livermore National Laboratory, 1985.
- [25] A. D. Drozdov. *Finite Elasticity and Viscoelasticity*. New Jersey: World Scientific, 1996.
- [26] B. E. Engquist and B. Sjögren. Robust difference approximations of stiff inviscid detonation waves. CAM Report 91-03, University of California at Los Angeles, 1991.
- [27] R. P. Fedkiw, T. Aslam, B. Merriman, and S. Osher. A Non-Oscillatory Eulerian Approach to Interfaces in Multimaterial Flows (The Ghost Fluid Method). *Journal of Computational Physics*, 152:457–492, 1999.
- [28] R. P. Fedkiw, A. Marquina, and B. Merriman. An Isobaric Fix for the Overheating Problem in Multimaterial Compressible Flows. *Journal of Computational Physics*, 148:545–578, 1999.
- [29] W. Fickett and W. C. Davis. *Detonation*. Berkeley, Calif.: University of California Press, 1979.
- [30] J. J. Goodier and P. G. Hodge. *Elasticity and Plasticity*. New York: John Wiley and Sons, Inc., 1958.
- [31] D. J. Grove and A. M. Rajendran. Simulation of Flyer Plate-Rod Target Impact Experiment. *Shock Waves in Condensed Matter*, 737–740, 1987.
- [32] M. E. Gurtin. *Configurational Forces as Basic Concepts of Continuum Physics*. Mathematical Sciences, vol. 137, New York: Springer, 2000.

- [33] M. E. Gurtin. A Mechanical Theory for Crystallization of a Rigid Solid in a Liquid Melt: Melting–Freezing Waves. *Archive of Rational Mechanics and Analysis*, 110:287–312, 1990.
- [34] K. S. Holian and B. L. Holian. Hydrodynamic Simulations of Hypervelocity Impacts. *Int. J. Impact Engineering*, 8:115–132, 1989.
- [35] G. R. Johnson and W. H. Cook. Fracture characteristics of three metals subjected to various strains, strain rates, temperatures and pressures. *Engrg. Fract. Mech.*, 21:31–48, 1985.
- [36] A. Kamoulakos. A simple benchmark for impact. *Bench Mark*, 31–35, 1990.
- [37] A. S. Khan and S. Huang. *Contiuum Theory of Plasticity*. New York: John Wiley and Sons, Inc., 1995.
- [38] D. B. Kothe, J. R. Baumgardner, J. H. Cerutti, B. J. Daly, K. S. Holian, E. M. Kober, S. J. Mosso, J. W. Painter, R. D. Smith and M. D. Torrey. PAGOSA: A Massively-Parallel, Multi-Material Hydrodynamics Model for Three-Dimensional High-Speed Flow and High-Rate Material Deformation. *High Performance Computing Symposium*, 9–14, 1993.
- [39] K. K. Kuo. *Principles of Combustion*. New York: Wiley-Interscience, 1986.
- [40] L. D. Landau and E. M. Lifshitz. *Fluid Mechanics*. Oxford: Pergamon Press, 1989.
- [41] C. K. Law. Recent Advances in Droplet Vaporization and Condensation. *Progress in Energy and Combustion Science*, 88:171–201, 1982.
- [42] X.-D. Liu and S. Osher. Convex ENO High Order Multi-Dimensional Schemes without Field by Field Decomposition or Staggered Grids. *Journal of Computational Physics*, 142:304–330, 1998.
- [43] J. Lubliner. *Plasticity Theory*. New York: Collier Macmillan, 1990.
- [44] L. E. Malvern. *Introduction to the Mechanics of a Continuous Medium*. New Jersey: Prentice-Hall, Inc., 1969.
- [45] J. M. McGlaun, S. L. Thompson, and M. G. Elrick. CTH: A Three-Dimensional Shock Wave Physics Code. *Int. J. Impact Engineering*, 10:351–360, 1990.

- [46] J. M. McGlaun, F. J. Zeigler, and S. L. Thompson. CTH: A Three-Dimensional, Large Deformation, Shock Wave Physics Code. *Shock Waves in Condensed Matter*, 717–720, 1987.
- [47] R. Menikoff and T. D. Sewell. Constituent Properties of HMX Needed for Meso-Scale Simulations. Submitted to *Applied Physics Reviews*, 2001.
- [48] M. A. Meyers. *Dynamic Behavior of Materials*. New York: John Wiley & Sons, Inc, 1994.
- [49] W. Mulder, S. Osher, and J. A. Sethian. Computing Interface Motion in Compressible Gas Dynamics. *Journal of Computational Physics*, 100:209–228, 1992.
- [50] I. Muller. *Thermodynamics*. New York: Pittman, 1985.
- [51] S. Osher and J. A. Sethian. Fronts Propagating with Curvature-Dependent Speed: Algorithms Based on Hamilton-Jacobi Formulations. *Journal of Computational Physics*, 79:12–49, 1988.
- [52] J. C. Oxley. *Explosive Effects and Applications*. J. A. Zuckas and W. P. Walters eds., Springer, 1997.
- [53] A. B. Pippard. *Elements of Classical Thermodynamics for Advanced Students of Physics*. Cambridge: Cambridge University Press, 1966.
- [54] J.-P. Poirier. *Introduction to the Physics of the Earth's Interior*. Cambridge: Cambridge University Press, 1991.
- [55] J. Quirk. A Parallel Adaptive Grid Algorithm for Computational Shock Hydrodynamics. *Appl. Numer. Math.*, 20:427–453, 1996.
- [56] D. R. Dick. *Engineering Sciences Data Unit Index*. Engineering Sciences Data Unit Ltd., 1975.
- [57] M. S. Raju and W. A. Sirignano. Spray Computations in a Centerbody Combustor. *Transactions of ASME*, 111:710–718, 1989.
- [58] F. Reif. *Fundamentals of Statistical and Thermal Physics*. New York: McGraw-Hill Book Company, 1985.
- [59] M. Renksizbulut and M. C. Yuen. Experimental Study of Droplet Evaporation in a High-Temperature Air Stream. *Transactions of ASME*, 105:384–388, 1983.

- [60] J. M. Rosen and C. Dickinson. Vapor Pressures and Heats of Sublimation of Some High Melting Organic Explosives. *Journal of Chemical and Engineering Data*, 14:120–124, 1969.
- [61] G. A. Ruderman. A Continuum Thermomechanical Model for Energetic Materials. PhD thesis, Department of Mechanical and Industrial Engineering, University of Illinois at Urbana-Champaign, 1998.
- [62] G. A. Ruderman, D. S. Stewart, and J. J. Yoh. A Thermomechanical Model for Energetic Materials with Phase Transformations. Submitted to *SIAM J. Appl. Math*, 2001.
- [63] D. Scherrer. Combustion of a Non-Moving Droplet: Numerical Study of the Influence of the Assumptions Leading to the D^2 Law. *Recherche Aero*, 25–37, 1985.
- [64] C.-W. Shu and S. Osher. Efficient Implementation of Essentially Non-oscillatory Schemes II. *Journal of Computational Physics*, 83:32–78, 1989.
- [65] J. S. Shuen, V. Yang, and C. C. Hsia. Combustion of Liquid-Fuel Droplets in Supercritical Conditions. *Combustion and Flame*, 89:299–319, 1992.
- [66] W. A. Sirignano. *Fluid Dynamics and Transport of Droplets and Sprays*. Cambridge: Cambridge University Press, 1999.
- [67] P. R. Spalart, R. D. Moser, and M. M. Rogers. Spectral Methods for the Navier-Stokes Equations with One Infinite and Two Periodic Directions. *Journal of Computational Physics*, 96:297–324, 1991.
- [68] R. Strehlow. *Fundamentals of Combustion*. New York: Kreiger, 1978.
- [69] C. M. Tarver, S. K. Chidester, and A. L. Nichols III. Critical Conditions for Impact- and Shock-Induced Hot Spots in Solid Explosives. *Journal of Physical Chemistry*, 100:5794–5799, 1996.
- [70] J. W. Taylor and R. J. Crookes. Vapour Pressure and Enthalpy of Sublimation of 1,3,5,7-tetranitro-1,3,5,7-tetra-azacyclo-octane (HMX). *Journal of Chemical Society. Faraday Transactions I*, 72:723–728, 1976.

- [71] P. A. Thompson. *Compressible-Fluid Dynamics*. Advanced Engineering Series, 1988.
- [72] J. Timmermans. *Physico-chemical Constants of Pure Organic Compounds, v. 1, 2*. New York: Elsevier Publishing Co., 1965.
- [73] A. A. Wheeler, W. J. Boettinger, and G. B. McFadden. Phase-Field Model for Isothermal Phase Transitions in Binary Alloys. *Physical Review A*, 45:7424–7439, 1992.
- [74] R. G. Whirley and J. O. Hallquist. DYNA-3D User Manual. Technical Report UCRL-MA-107254, Lawrence Livermore National Laboratory, 1991.
- [75] G. B. Whitham. *Linear and Nonlinear Waves*. New York: Wiley-Interscience, 1999.
- [76] F. A. Williams. *Combustion Theory*. Redwood City, California: Addison-Wesley, 1985.
- [77] J. H. Williamson. Low-Storage Runge-Kutta Schemes. *Journal of Computational Physics*, 35:48–56, 1995.
- [78] A. A. Wray. Very Low Storage Time-Advancement Schemes. Internal Report Moffet Field, Califo., NASA, 1986.
- [79] S. Xu, T. Aslam, and D. S. Stewart. High Resolution Numerical Simulation of Ideal and Non-ideal Compressible Reacting Flows with Embedded Internal Boundaries. *Combust. Theory Modelling*, 1:113–142, 1997.
- [80] J. J. Yoh and D. S. Stewart. High Resolution Multi-Material Hydrodynamics Model for High-Rate Deformation with Detonating Explosives. To be submitted to *Combust. Theory Modelling*, 2001.
- [81] J. J. Yoh, D. S. Stewart, and G. A. Ruderman. A Thermomechanical Model for Energetic Materials with Phase Transformations: Analysis of Simple Motions. Submitted to *SIAM J. Appl. Math*, 2001.
- [82] J. J. Yoh and X. Zhong. Low-Storage Semi-Implicit Runge-Kutta Schemes for Chemically Reacting Flow Computations. Submitted to *Journal of Computational Physics*, 2000.

- [83] J. J. Yoh and X. Zhong. Semi-Implicit Runge-Kutta Schemes for Stiff Multi-Dimensional Reacting Flows. Paper 97-0803, AIAA, 1997.
- [84] J. J. Yoh and X. Zhong. Low-Storage Semi-Implicit Runge-Kutta Methods for Reactive Flow Computations. Paper 98-0130, AIAA, 1998.
- [85] C. Yoo and H. Cynn. Equation of State, Phase Transition, Decomposition of β -HMX (Octahydro-1,3,5,7-Tetranitro-1,3,5,7-Tetrazonine) at High Pressures. *Journal of Chemical Physics*, 111:10229–10235, 1999.
- [86] A. Zenin. HMX and RDX: Combustion Mechanism and Influence on Modern Double-Base Propellant Combustion. *Journal of Propulsion and Power*, 11:752–758, 1995.
- [87] Y. Y. Zhu and S. Cescotto. Unified and mixed formulation of the 4-node quadrilateral elements by assumed strain method: Application to thermomechanical problems. *Int. J. Numer. Methods Engrg.*, 38:685–716, 1995.
- [88] J. Zinn and R. N. Rogers. Thermal Initiation of Explosives. *Journal of Physical Chemistry*, 66:2646–2653, 1962.

Vita

Jack Jai-ick Yoh was born in Seoul, Korea, on March 4th, 1970. He began his education in the United States in August 1986, attending Miramonte High School in Orinda, California. In May 1992, he received his B.S. in Mechanical Engineering from the University of California, Berkeley. He then joined the Korean Army as a soldier. Returning to the United States, he entered the University of California, Los Angeles, and completed his M.S. in Mechanical Engineering in June 1995. While pursuing the doctoral degree, he transferred to the Department of Theoretical and Applied Mechanics at the University of Illinois at Urbana-Champaign, where he began working as a research assistant for Professor D. Scott Stewart in Spring 1998. Parts of his research work have been submitted to the *SIAM Journal of Applied Mathematics*, *Combustion Theory and Modelling*, and *Journal of Computational Physics*.